UNIVERSIDAD COMPLUTENSE DE MADRID

FACULTAD DE CIENCIAS QUIMICAS
Departamento de Química Física I

MOJADO Y EVAPORACIÓN DE DISOLUCIONES DE TENSIOACTIVOS Y NANOEMULSIONES

MEMORIA PARA OPTAR AL GRADO DE DOCTOR
PRESENTADA POR

Hezekiah O. Agogo

Bajo la dirección de los doctores

Ramón González Rubio
Francisco Ortega Gómez
Manuel García Velarde

Madrid, 2013

UNIVERSIDAD COMPLUTENSE DE MADRID
FACULTAD DE CIENCIAS QUÍMICAS
DEPARTAMENTO DE QUÍMICA FÍSICA I

MOJADO Y EVAPORACIÓN DE DISOLUCIONES DE TENSIOACTIVOS Y NANOEMULSIONES.

Memoria para optar al Grado de Doctor presentada por

Hezekiah O. Agogo

DIRECTORES:
Ramón González Rubio
Francisco Ortega Gómez
Manuel García Velarde

MADRID, Abril 2013

Declaration of Originality

I hereby declare that the research recorded in this thesis and the thesis itself was composed and originated entirely by myself in the Department of Physical Science I at Universidad Complutense de Madrid.

Hezekiah O. Agogo.

Dedication

I dedicate this work to my father …**Daniel Ijogo Agogo (1947-2006).**

Acknowlegdements

I would like to acknowlegde and appreciate the contribution and assistance of Professor Ramon G. Rubio, who provided the laboratories where this research has been carried out, I would also like to appreciate his patient guidiance, contributions and discussions in this research work. I would also like to appreciate the contribution of Professor Francisco Ortega for being available to share ideas and in the analysis of the experimental results presented here. Prof. Manuel G. Velarde has been a very important guide for understanding the fundamentals of the Physics of Fluids, and the current theories of spreading. I would also like to appreciate the contribution of Professor Victor Starov, for fruitful discussions, and his key contribution to the development of the theory of evaporation of liquid droplets onto hydrophobic substrates. Most of the theoretical analysis of the evaporation results were done in close collaboration with Dr. Sergey Semenov. I thank Dr Natasha Ivanova her assistance and training in the calibration of the spreading technique.

I would like to appreciate immensely my mother Mrs. Comfort Agogo, my siblings Marai, Emmanuel, Steven, Naomi and their families, and David, for their prayers, support and encouragement through the duration of this research to achieve this personal dream. I would also like to appreciate Retsat Maina for her encouragement and support. I will also like to acknowlegde my friends and colleagues, specially my labmates Marta, Sara, Alma, Nuria and Fernando, for their assistance in words and presence.

I would like to appreciate the financial support of the MULTIFLOW ITN of the Marie Curie program of the European Union (VII Framework Program). The opportunity to work and learn within the research network, and to interact with the researchers participating on it has been an awesome experience.

Table of Contents

List of Figures

List of Tables

List of Publications

1. S. Semenov, V.M. Starov, R.G. Rubio, H. Agogo, M.G. Velarde, Evaporation of sessile water droplets: Universal behaviour in presence of contact angle hysteresis, Colloids and Surfaces A: Physicochem. Eng. Aspects 391 (2011) 135– 144.
2. A. Tribala, A. Okoye, S. Semenov, H. Agogo, R.G. Rubio, F. Ortega, V.M. Starov, Evaporation kinetics of sessile droplets of aqueous nanosuspensions of inorganic nanoparticles, Accepted J. Colloid Interf. Sci. (2013)
3. H.Agogo, R. G. Rubio, S. Semenov, V.M. Starov, M.G. Velarde, Effects of concentration, temperature and relative humidity on evaporation of surfactant solution droplets, Submitted to Langmuir, (2013).
4. A. Trybala, A. Okoye, S. Semenov, H. Agogo, R.G. Rubio, F. Ortega, V.M. Starov, Simultaneous spreading and evaporation of nanosuspensions, Submitted to Langmuir (2013).

Summary

Introduction.

Wetting and Evaporation are important phenomena that are of immense use in several applications in science and technology such as in heat transfer devices, drug delivery applications, coating processes and numerous biological and geophysical processes. Wetting can be described as the expansion of a liquid droplet in contact with a solid surface, the expansion is a result of the chemical structure of the liquid and the solid surface, while evaoration can be described as a surface diffusive phenomenon that describes the transfer of molecules from solid-liquid to liguid-gas interface. Understanding these phenomena is important in the use and application of detergents, textile processing chemicals, herbicides, pesticides, cosmetics emulsifiers, painting (or coating operations), ink jet printing and in wetting agents. Other applications where wetting and spreading are also useful are in the manufacture and operation of semi conductors (where cleaning and drying semi conductor wafers is important), oil recovery in oil exploration operations and heat transfer processes where the presence of fluid drops or films can have an altering effect on the overall heat transfer rates. Considering sessile drops three distinct phases interact simultaneously; solid (substrate), liquid (drop) and gas (surrounding), and to understand the force dynamics and controlling mechanisms for spreading and evaporating droplets the heat and mass transfer across interfaces has to be analysed thoroughly. Wetting, spreading and evaporation are also relevant in the medical and cosmetic areas. For the sake of example, it is well known that the stability of the tear film in the eyes is crucial to avoid the Dry Eye illness. To avoid this problem one has to ensure good wetting and spreading of the tear film and that dewetting does not occur in the time elapsed between two consecutive blinks. Another example is the formation of a continuous fims of the fatty component of sweat onto the front of humans, specially those from South Asia, which is an important problem for the cosmetic industry.

The phenomena of wetting and evaporation have been of immense interest in the recent years, several researches have been carried out to give insight to the dynamics of the wetting process and spreading and evaporation dynamics of pure fluids of different and varying chemical compositions. In the case of pure fluids it was concluded that a temperature gradient was a driving force for evaporation. The evaporation of volatile

hydrocarbon mixtures have also been studied and it was concluded that the process of evaporation was dependent on the more volatile component of the mixture. In any case, despite the technologycal interest, very little is known about the spreading and evaporation kinetics of complex fluids, such as surfactant and polymer solutions and nanosuspensions, and no accepted theoretical description exists that can be used for doing accurate predictions that can be used for the design of industrial processes.

Aims of the project.

The overall goal of this research is to carry out experimental and theoretical analysis on the kinetics of spreading and evaporation of aqueous surfactant solutions and nanoparticle dispersions onto hydrophobic substrates, and to study the influence of surfactant concentration and nanoparticle volume fraction on the three phase contact line to promote or inhibit evaporation. We will focus on hydrophobic substrates because the behavior of aqueous fluids onto hydrophilic substrates (complete wetting condition) has already been described in the literature.

In this research the focus will be on the spreading and evaporation kinetics of sessile droplets of surfactant solutions (Silwet L-77) and nanoparticle dispersions, the adsorption kinetics of these complex liquids will also be measured to determine the contribution of adsorption to evaporation. The effect of concentration, relative humidity and temperature on the spreading and evaporation kinetics of droplets of surfactant solutions and nano-particle suspensions has also been studied with a focus on the interaction at the three phase contact line. The profile of a droplet undergoing spreading and evaporation proceeds through four (4) stages, (i) spreading: characterised by reduction of contact angle, increase in droplet base radius with a constant volume, (ii) evaporation with reducing contact angle with constant droplet radius, (iii) constant contact angle and a reduction in droplet radius and (iv) simultaneous reduction in contact angle and droplet base radius until the droplet disappears. We have chosen Silwet L-77 because it is a well known superspreader surfactant for which the adsorption kinetics at the air-liquid interface has already been studied in our research group. In addition, due to the fast spreading, it is expected that the interference between spreading and evaporation will be minimized. The latex nanoparticles have been used because, contrary to other inorganic particles frequently used, they slightly adsorbe both

at the liquid/air and on the solid/liquid interfaces, thus showing a qualitative similarity to the surfactant solutions.

Chapter one includes an explanation to the physics of the phenomena of spreading and evaporation of a sessile droplet and the interacting surface forces at the three-phase contact line. It also includes a bibliographic review of the different theoretical postulations on the spreading of a sessile droplet, such as the Autophlic Theory proposed by Starov et al. and E. Ruckenstein, the theory proposed by Blake and Haynes, and the Rate Theory proposed by Slavchov et al. The wetting transistion and the influence of surface topography has also been discussed. The second part of chapter one focuses on the stages of evaporation, a theoretical description of the evaporation process for volatile liquids. Finally a we have carried out a detailed review of the recent literature on spreading and evaporation fluids in the presence gradients of temperature and concentration, and as a function of the relative humidity.

Results

1.- Chapter two gives a description of the experimental equipments and materials used during this research. In the course of this project measurements have been made for surface tension, using a plate tensiometer, and the adsorption kinetics of surfactant and nanoparticles has been measured using a dissipative quartz crystal microbalance. Pattern formation after evaporation has been measured using the scanning electron microscope. The methods used in the preparation of samples and the composition of samples used is also discussed. A main part of the project has been the design and set up of an experimental technique for measuring the spreading and evaporation kinetics of fluid droplets. The equipment includes two CCD cameras for imaging the drops both from the side and from the top. The description of the chamber used to measure the spreading and evaporation evolution over time is described in detail. An important point is that the chamber allows to measure at constant temperature and relative humidity. A brief description of the software used in analysing images and how the variables are calculated is also explained. A description of the components for other equipments used in this research have been outlined.

2.- Chapter three presents the experimental results obtained for the spreading and evaporating kinetics of surfactant solutions and nanoparticle dispersions onto hydrophobic substrates for a wide range of surfactant concentration and particle volume

fractions measured at varied temperatures and relative humidities. The results for the kinetics of adsorption of surfactant solutions and nanoparticle dispersions onto the substrate are also presented herein. The results show that it is possible to observe the four stages of the spreading-evaporation process, although in the second stage of evaporation the constant angle does not remain constant as time increases. This is an important difference with respect to the case of pure fluids.

Discussion

In Chapter four we present a detailed comparison of the experimental results with the available theories. More specifically, the experimental results for the spreading of surfactants and nanoparticle dispersions have been compared with the predictions of the Autophilic Theory, Blake's Theory and the Rate Theory. Furthermore a model to describe the first two stages of evaporation of pure fluids is developed. An important result is that the model predicts two universal behaviors, one for each of the two first evaporation stages, when the time evolution of the contact angle, the radius of the base of the droplet, and time are expressed as reduced variables. The model is satisfactory for the evaporation of pure fluids. The same model is used to predict the evaporation dynamics of surfactant solutions and nanoparticle dispersions, and disagreements between theory and experiment have been found for the second stage in the very low concentration range. The theory has been extended to account for the contributions of the adsorption at the liquid/air and solid/liquid interfaces, as well as for the increase of concentration as evaporation proceeds. The theory is able to capture semi-quantitatively the experimental behavior.

Conclusions

Chapter five presents the conclusions based on all the exeperimental results and theories described herein, with recommendations and proposed further studies. The main conclusions are as follows:

a) The experimental equipment build in the laboratory is suitable for the study of spreading and evaporation of complex fluids under controlled ambient conditions.

b) The Autophilic and Blake's theories are able to describe satisfactorily the spreading results of both the surfactant solutions and the nanosuspensions. However, the Rate theory does not capture the qualitative behavior of the systems studied.

c) The theory proposed for pure fluids predicts universal behaviors for the contact angle and the reduced radius of the droplet as a function of reduced time. It works satisfactorily for pure fluids.

d) For mixtures and suspensions, the above theory has been modified to take into account the adsorption at the liquid/air and the solid/liquid interfaces, as well as the increase of concentration as evaporation proceeds. The theory has been able to describe semi-quantitatively the behavior of the systems even at the low concentration range.

Most relevant references.

-.R. Holdich, V.M. Starov, P. Prokopovich, D.O. Njobuenwua, R.G. Rubio, S. Zhdanov, M.G. Velarde, Spreading of liquid drops from a source, Colloids Surf. A, 2006, 282-283, 247-255

-. S. Rafai, D. Bonn, Spreading of Newtonian fluids and surfactant solutions on solid surfaces, Physica A, 2005, 358, 58-67

-. S. Rafai, D. Bonn, E. Bertrand, J. Meunier, Long-range critical wetting: Observation of a critical end point, Phys. Rev. Lett., 2004, 92, 245701.

-.K.S. Lee, V.M. Starov, T.J.P. Muchatuta, S.I.R, Srikantha, Spreading of trisiloxanes over thin aqueous layers, Colloid J., 2009, 71, 365-369.

-.M. J. de Ruijter, M. Charlot, M. Voue, J. De Coninck, Experimental evidence of several time scales in rop spreading, Langmuir 2000, 16, 2363-2368.

- N. Ivanova, V.M. Starov, R. Rubio, H. Ritacco, N. Hilal, D. Johnson, Critical wetting concentrations of trisiloxane surfactants, Colloids Surf. A: Physicochem. Eng. Aspects 2010, 354, 143–148

- S. Sikalo, C. Tropea, E.N. Ganic, Dynamic wetting angle of a spreading droplet, Exp. Thermal Fluid Sci. 2005, 29, 795–802.

- M. Ghosh, K. J. Stebe, Spreading and retraction as a function of drop size, Adv. in Colloid Interf. Sci. 2010, 161, 61–76.

- K.Y. Chan, A. Borhan, Surfactant-assisted spreading of a liquid drop on a smooth solid surface, J. Colloid Interf. Sci. 2005, 287, 233–248.

- Y. Zhang, F. Han, The spreading behaviour and spreading mechanism of new glucosamide-based trisiloxane on polystyrene surfaces, J. Colloid Interf. Sci. 2009, 337, 211–217.
- J. Venzmer, S.P. Wilkowski, Trisiloxane surfactants-Mechanism of spreading and wetting, Amer. Soc. Testing and Mater., 1998, 18, 140-151.
- V. Slavchov, K.G. Sabbatovskiy, M. Stolz, K. Grundke, V.M. Rudoy, Unusual wetting dynamics of aqueous surfactant solutionson polymer surfaces, J. Colloid Interf. Sci. 2003, 267, 456–462.
- K. Sefiane, M. E.R. Shanahan, M. Antoni, Wetting and phase change: Opportunities and challenges, Cur. Opinion Colloid Interf. Sci. 2011, 16, 317–325.

Resumen

Introducción

Tanto el mojado y esparcimiento ("spreading") como la evaporación de líquidos son fenómenos presentes en gran número de problemas científicos y tecnológicos que abarcan desde la Química, la Física, la Biología, la Geología a la Ingeniería. El esparcimiento puede ser definido de forma breve como el aumento del radio de la base de una gota líquida tras haber sido depositada sobre una superficie sólida. La evaporación es un fenómeno íntimamente ligado al esparcimiento y no es sino la transferencia de materia desde el líquido al vapor que lo rodea. Un aspecto común al esparcimiento y a la evaporación de gotas es que su comportamiento está determinado por tres interfases: sólido/líquido, sólido/vapor y líquido/vapor, así como por la naturaleza química del líquido y del sólido y la topología del mismo.

La comprensión y el modelado de estos fenómenos son de gran importancia para el diseño de procesos tales como la detergencia, el procesado de textiles, la deposición de herbicidas y pesticidas, cosmética, pintura y recubrimientos o la escritura con chorro de tinta. También para la construcción y uso de semiconductores, en los que el limpiado y secado de las obleas de Si son pasos clave, la recuperación de petróleo, los intercambiadores de calor y la construcción de nanoestructuras es preciso poder entender y controlar el mojado, esparcimiento y evaporación de fluidos. El mojado, esparcimiento y evaporación de líquidos es también de gran importancia en Medicina y Cosmética. A modo de ejemplo, la estabilidad de la capa de fluido lacrimal en los ojos es de crucial importancia para evitar la enfermedad del Ojo Seco. Para evitar este serio problema, es necesario asegurar óptimas condiciones de mojado y esparcimiento del fluido lacrimal y que no tiene lugar su ruptura durante el tiempo comprendido entre dos parpadeos. Otro ejemplo, en el campo cosmético, es la formación de una película continua del componente graso del sudor en la frente de humanos, especialmente en individuos del sur de Asia.

A pesar de la importancia científica y tecnológica del mojado, esparcimiento y evaporación de fluidos sobre superficies sólidas, no existe aún ningún esquema teórico o fenomenológico que permita predecir el comportamiento de fluidos hidrofílicos o hidrofóbicos sobre sustratos hidrofóbicos. Más aún, debe tenerse en cuenta que, en muchos casos de interés práctico, las superficies sólidas no son pulidas sino rugosas y/o estructuradas química o físicamente. Además, tanto el esparcimiento como la

evaporación tienen lugar generalmente en condiciones fuera del equilibrio, por ejemplo en presencia de gradientes de temperatura o de densidad del vapor. La situación se complica aún más cuando se trata de fluidos multicomponentes, ya que existe adsorción competitiva de los componentes en las superficies líquido/vapor y sólido/líquido, así como diferente volatilidad de los distintos componentes.

Objetivos

El objetivo global de la investigación realizada es llevar a cabo un estudio detallado, tanto experimental como teórico, de las cinéticas de esparcimiento y de evaporación de disoluciones de acuosas de tensioactivos y nanodispersiones sobre superficies hidrofóbicas. La razón para esta elección es que el comportamiento de fluidos acuosos sobre sustratos hidrofílicos en condiciones de mojado completo ya se ha descrito en la bibliografía. Se discutirán en profundidad los efectos de la concentración, la humedad relativa y la temperatura.

De manera más específica, el tensioactivo elegido ha sido el Silwet L-77, bien conocido por su comportamiento de esparcimiento muy rápido ("super-spreading"), y nanopartículas de látex de poliestireno estabilizadas por repulsión Coulómbica (las partículas contienen grupos sulfato en la superficie); se estudiarán tres tamaños de nanopartícula. El interés del esparcimiento muy rápido es que se espera que la interferencia entre el proceso de esparcimiento y la primera etapa de la evaporación sea menor. El uso de partículas de látex se debe a que, contrariamente a las nanopartículas inorgánicas usadas frecuentemente, presentan una pequeña adsorción tanto en la interfase líquido/aire como en la sólido/líquido.

El Capítulo uno contiene una descripción detallada de los procesos de esparcimiento y de evaporación, así como una revisión del trabajo publicado en los últimos años. Se describen brevemente algunas de las teorías existentes para describir el esparcimiento de fluidos puros y mezclas sobre superficies hidrofóbicas. Entre dichas teorías se encuentran la de esparcimiento autofílico propuesta por Starov et al. y por Ruckenstein, la teoría propuesta por Blake y Haynes, y la teoría de velocidades propuesta por Slavchov et al. La segunda parte del Capítulo se centra en la descripción de las distintas etapas de la evaporación y se describe un modelo teórico. Finalmente, se presenta una revisión detallada de la bibliografía reciente sobre esparcimiento y evaporación,

incluyendo la existencia de gradientes de temperatura y concentración y el efecto de la humedad relativa.

Resultados

1.- El Capítulo dos describe los métodos experimentales utilizados, así como las sustancias usadas en este proyecto. En el curso de la investigación se han realizado medidas de tensión superficial usando un tensiómetro de placa, y de cinética de adsorción de tensioactivos y nanopartículas usando una microbalanza de cuarzo disipativa. La morfología de los depósitos formados tras la evaporación se ha estudiado mediante microscopía electrónica. Se discuten los protocolos seguidos para la preparación de las muestras. La parte más importante se ha dedicado a la descripción del equipo experimental puesto a punto para los experimentos de esparcimiento y evaporación de gotas sustentadas por sólidos. El equipo incluye dos cámaras CCD para la obtención de las imágenes de las gotas, tanto desde el lateral como desde arriba. Se describe en detalle la celda de medida usada para los estudios de esparcimiento como de evaporación. Un aspecto importante es que la celda permite realizar los experimentos a temperatura y humedad relativa constantes. Se describe también el software usado para el análisis de imagen del perfil de la gota.

2.- El Capítulo tres presenta los resultados experimentales utilizados para las disoluciones de tensioactivos y las nanosuspensiones. En el caso de las disoluciones de Silwet L-77 el intervalo de concentraciones estudiado ha cubierto desde disoluciones muy diluidas (muy por debajo de la concentración crítica de agregación) hasta concentradas (por encima de la concentración crítica de mojado). Para cada composición se han estudiado tres temperaturas y tres humedades relativas. En el caso de las nanosuspensiones se han estudiado tres fracciones en volumen a dos temperaturas y una humedad relativa. También se incluyen los resultados de adsorción en la interfase sólido/líquido. Los resultados muestran que es posible observar las cuatro etapas del proceso completo de esparcimiento – evaporación, aunque en la segunda etapa de evaporación el ángulo de contacto no permanece constante a medida que el tiempo aumenta. Esta es una diferencia muy importante con respecto al caso de los fluidos puros.

Discusión

Finalmente, el Capítulo 4 incluye una discusión detallada de los resultados experimentales obtenidos, así como de otros disponibles en la bibliografía. Más concretamente, los resultados de la cinética de esparcimiento se han comparado con las predicciones de las teorías presentadas por Ivanova et al., Blake, y Slavchov et al. También se presenta un modelo teórico para las dos primeras etapas de la evaporación de fluidos puros. Un resultado importante de este modelo es que predice dos comportamientos universales, uno para cada etapa, cuando la evolución del ángulo de contacto, el radio de la base de la gota y el tiempo se expresan como magnitudes reducidas. El modelo da resultados satisfactorios para fluidos puros. En el caso de los resultados correspondientes a las de las disoluciones de Silwet L-77 y de SDS, los resultados se han comparado con las predicciones de la teoría desarrollada para fluidos puros y se han encontrado discrepancias para la segunda etapa de evaporación, especialmente en la región muy diluida. Cuando se extiende dicha teoría teniendo en cuenta las adsorciones en las interfases líquido/aire y sólido/líquido, así como el aumento de concentración a medida que el fluido se evapora, se obtiene un acuerdo semicuantitativo con los resultados experimentales en todo el intervalo de concentraciones.

Conclusiones

El Capítulo cinco resume las conclusiones obtenidas a partir de los resultados experimentales y su comparación con las diferentes teorías. Las principales conclusiones son:

El equipo experimental construido en el laboratorio es adecuado para el estudio del esparcimiento y la evaporación de fluidos complejos en condiciones ambientales controladas.

Las teorías de esparcimiento autofílico y de Blake describen satisfactoriamente los resultados de esparcimiento de las disoluciones tensioactivas y de las nanosuspensiones. Sin embargo, la teoría de velocidades no describe el comportamiento cualitativo de los sistemas estudiados.

La teoría propuesta para fluidos puros predice comportamientos universales para el ángulo de contacto y el radio de la base de la gota reducido como función del tiemo reducido. Los resultados son buenos para fluidos puros.

Para mezclas y nanosuspensiones la teoría anteriormente mencionada ha tenido que ser modificada para incluir la adsorción en las interfases líquido/aire y sólido/líquido, así como el aumento de concentración durante la evaporación. La teoría describe semicuantitativamente el comportamiento observado, incluso en el intervalo de bajas concentraciones.

Bibliografía más relevante

-. R. Holdich, V.M. Starov, P. Prokopovich, D.O. Njobuenwua, R.G. Rubio, S. Zhdanov, M.G. Velarde, Spreading of liquid drops from a source, Colloids Surf. A, 2006, 282-283, 247-255

-. S. Rafai, D. Bonn, Spreading of Newtonian fluids and surfactant solutions on solid surfaces, Physica A, 2005, 358, 58-67

-. S. Rafai, D. Bonn, E. Bertrand, J. Meunier, Long-range critical wetting: Observation of a critical end point, Phys. Rev. Lett., 2004, 92, 245701.

-. K.S. Lee, V.M. Starov, T.J.P. Muchatuta, S.I.R, Srikantha, Spreading of trisiloxanes over thin aqueous layers, Colloid J., 2009, 71, 365-369.

-. M. J. de Ruijter, M. Charlot, M. Voue, J. De Coninck, Experimental evidence of several time scales in rop spreading, Langmuir 2000, 16, 2363-2368.

- N. Ivanova, V.M. Starov, R. Rubio, H. Ritacco, N. Hilal, D. Johnson, Critical wetting concentrations of trisiloxane surfactants, Colloids Surf. A: Physicochem. Eng. Aspects 2010, 354, 143–148
- S. Sikalo, C. Tropea, E.N. Ganic, Dynamic wetting angle of a spreading droplet, Exp. Thermal Fluid Sci. 2005, 29, 795–802.
- M. Ghosh, K. J. Stebe, Spreading and retraction as a function of drop size, Adv. in Colloid Interf. Sci. 2010, 161, 61–76.
- K.Y. Chan, A. Borhan, Surfactant-assisted spreading of a liquid drop on a smooth solid surface, J. Colloid Interf. Sci. 2005, 287, 233–248.
- Y. Zhang, F. Han, The spreading behaviour and spreading mechanism of new glucosamide-based trisiloxane on polystyrene surfaces, J. Colloid Interf. Sci. 2009, 337, 211–217.

- J. Venzmer, S.P. Wilkowski, Trisiloxane surfactants-Mechanism of spreading and wetting, Amer. Soc. Testing and Mater., 1998, 18, 140-151.
- V. Slavchov, K.G. Sabbatovskiy, M. Stolz, K. Grundke, V.M. Rudoy, Unusual wetting dynamics of aqueous surfactant solutionson polymer surfaces, J. Colloid Interf. Sci. 2003, 267, 456–462.
- K. Sefiane, M. E.R. Shanahan, M. Antoni, Wetting and phase change: Opportunities and challenges, Cur. Opinion Colloid Interf. Sci. 2011, 16, 317–325.

Chapter One

1.0 Introduction

1.1 Wetting and Spreading

Spreading is the expansion of the contact baseline of a spherical droplet, it is property exhibited by various liquids and it is dependent on the inherent physical properties of the liquid droplet and the type of substrate in contact with the liquid. The spreading of a liquid droplet is either gravity or capillary controlled, the volume of the droplet determines the influence of gravity and the capillary number (usually in small droplets) determines capillary controlled spreading [1-3]. The spreading ability of a liquid was used as a criterion to determine the efficiency of a surface active material, [4]. Solid substrates can be classified in terms of their susceptibility to water as hydrophobic and hydrophilic substrates which will be discussed alongside the different transitions of spreading. Wetting (or spreading) is an important phenomenon that is of immense importance and has several industrial applications and every day activities. The efficient deposition of droplets was critical in painting, coating and solution delivery applications, and the addition of surfactants improved the wettability of most liquids, [2-13]. Spreading is important in emerging technologies where the control of precisely metered small droplets is required such as lab-on-a-chip devices, [8], heat pipes, micro-array assays for control schemes of MEMS and NEMS devices by capillary bridge actuators and colloidal deposition from evaporating drops, understanding the spreading kinetics is of utmost importance, [10, 11]. Wetting is also important in agricultural processes where aqueous solutions are required to spread out on hard-to-wet surfaces, a classic example is the application of pesticides to plant leaves whose waxy coating make them highly hydrophobic, the addition surface active agents or surfactants immensely reduced the interfacial tensions and improved the wettability of the surface, [12-16]. Another direct application the study of wetting principles in oil recovery where there is need to increase the speed and uniformity of wetting on normally hydrophobic substrates, surfactants and surface active polymers are used to improve the spreading properties of the liquids on hydrophobic substrates, [5, 17, 18]. The role of surfactants in oil recovery processes being specifically important in oil recovery where surfactants are used to extract oil trapped in the pores of rocks through the injection of surfactants to reduce the interfacial

tension between the oil and water phases, allowing the extraction of oil from small pores [19]. Understanding the wetting properties of liquids is also important in the manufacture of windshields, solar panels and self -cleaning surfaces, the mode of interaction between the liquid and the surface goes a long way in determining the modelling of these devices for optimum efficiency [6, 20]. Pharmaceutical and cosmetics products depend on the wetting characteristics of surfactants to increase their wettability and improve their efficiency in the applications, with improved wetting a larger surface area is covered in real time [3, 5, 12-15, 21-23]. Another important application of wetting is in the manufacture of semi-conductor devices where it affects the growth of crucial film layers and also the working principles of more simple applications such as paints, dyes and detergents [9, 12, 13, 24]. Wetting plays an important role in several applications ranging from micro-fluidic devices to fuel cells and inkjet printing the efficient and effective control of the drop dynamics is highly desirable, and this relies upon understanding the internal fluid motion of the drop, [25]. In recent years there has been a growing interest in modifying surface properties of inorganic oxides, polymer films, and other solid substrates with tethered polymers applications of such surfaces include, colloid stabilization, adhesion promotion or reduction, wetting, lubrication, biocompatibility, size exclusion chromatography and reducing fouling of ultra-filtration membranes and it is important to understand the hydrophilicity of the surface, DNA chain elongation for disease diagnosis analysing the coffee ring structure formation in the case of blood [8, 18, 23, 26, 27]. Droplet impact also comes into play also in food engineering when a spray technology is used to apply a coating on food substances, [28]. Electro-wetting is another emerging area with applications for spreading, when an external voltage is applied across a wetting interface the result is termed electro-wetting this has been used in low energy surfaces with tremendous results as it is possible to control liquid movement and change the state of a system with no mechanical parts, the applications include but are not limited to electronic paper, cooling of electronic circuits by transport of cold drops across them, transport of micro-drops, suction of liquids in micro-tube and lab-on-a-chip applications for analysis of the chemical composition of liquids, [29].

Wetting (or spreading) of a droplet can be described in terms of the behaviour of the droplet and the interaction with the substrate. Generally solid substrates when in contact with liquid droplets that form contact angles less than 90º (θ <90º) or allow complete wetting of fluids on their surfaces are referred to as hydrophilic and substrates when in

contact with liquids form contact angles greater than 90º (θ >90º) are referred to as hydrophobic substrates.

(a) (b)

Figure 1.1: Scheme of (a) non-wetting hydrophobic substrate and (b) a partially wetting hydrophilic substrate.

It is possible to explain the behaviour of substrate in terms of the contact angle (using the Young's Equation) and surface tension, these parameters that influence the spreading and wetting behaviours of liquid droplets will be discussed.

1.1.1 Surface Tension

Surface tension results from an imbalance of molecular forces in a liquid. Due to the imbalance found at the solid-liquid, liquid-air and the solid-air interface the molecules are attracted to each other and exert a net force pulling molecules together. The addition of components can alter the surface tension of fluids and solid substrates in either direction. A schematic of the molecular interaction is shown in Figure 1.2.

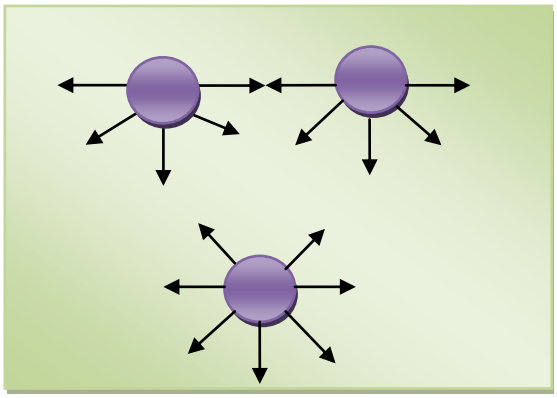

Figure 1.2: Molecular interaction of molecules in the bulk fluid and surface.

Surface tension can also be defined in terms of work done per unit area to increase the surface area of the liquid film spanned over a surface, the liquid moves through a distance *dx*, and work is done. This is shown in the Figure 1.3 below.

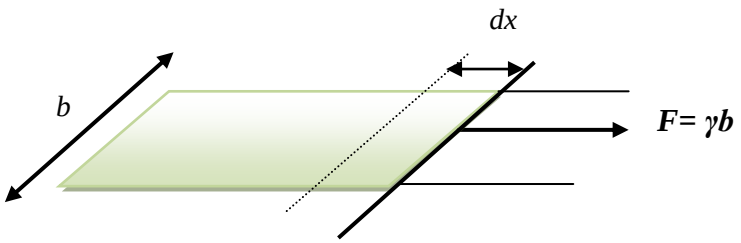

Figure 1.3: Surface tension in terms of work done.

From Figure 1.3 above the work done (surface tension) to increase the surface area by *dA* is given by;

$$dW = \gamma dA \qquad 1.1$$

Where *W* and *A* are the work done and surface area respectively and γ is the surface tension, it must be considered that the work done at constant temperature and pressure, excluding the volumetric one, is the change of Gibbs energy, therefore, in the case of fluids, γ can also be defined of the Gibbs energy per unit of area, which is very important because this concept makes it easy to derive the Thermodynamics of fluid interfaces, and define variables such as surface entropy, enthalpy, heat capacity, etc. In the case of liquid-liquid, solid-liquid and solid-vapour interfaces it is also possible to define the corresponding interfacial tensions, though for solid/vapour it is frequent to refer to surface energy instead to surface tension. Moreover, in the case of a solid surface it is not always possible to define the surface tension as the Gibbs energy per unit of area, surface tension is measured $N.m^{-1}$, [30].

1.1.2 Young's Equation

From a macroscopic point of view a droplet forms a three phase contact line on deposition unto a solid substrate (solid-liquid, liquid-vapour and solid-vapour). The ratio of these interfacial forces can be used to determine the contact angle of the droplet. From the value of the contact angle we can classify substrates and also wetting patterns of liquids. The Young's Eq. is a representation of the surface forces along the three phase contact line given by the equation below.

$$\gamma_{sv} = \gamma_{sl} + \gamma_{lv} cos\theta_{eq} \qquad 1.2$$

where γ_{sv} represents the surface force along the solid-vapour interface, γ_{sl} the surface force along the solid-liquid interface and $\gamma_{lv}$the surface force along the liquid-vapour interface, $\theta_{eq}$is the equilibrium contact angle which in real sense cannot be measured but estimated, Figure 1.4 shows the schematic of the interacting surface forces.

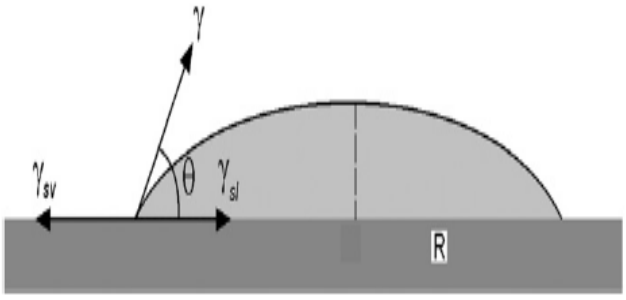

Figure 1.4: Scheme of the three phase contact line interaction showing the direction of the surface forces.

The Young's Eq. can also be derived from thermodynamic principles assuming a change in the triple line corresponding to a change in wetted area will result in a variation of the free surface energy, where:

$$\Delta G = \Delta A(\gamma_{sl} + \gamma_{sv}) + \Delta A\gamma_{lv}\cos(\theta - \Delta\theta) \qquad 1.3$$

At equilibrium;

$$lim\Delta A \rightarrow 0 \frac{\Delta G}{\Delta A} = 0 \qquad 1.4$$

$\frac{\Delta\theta}{\Delta A}$, takes the form of a second order differential, we obtain the Eq.1.3 in the form:

$$\gamma_{sv} = \gamma_{sl} + \gamma_{lv}cos\theta \qquad 1.5$$

Wenzel, described the advancing contact angle by illustrating a situation where the three phase contact line is in competition with the gas phase (reduction of contact angle) while the receding contact angle can be described as a contraction at the triple phase contact line, [30-32], shown in Figure 1.5.

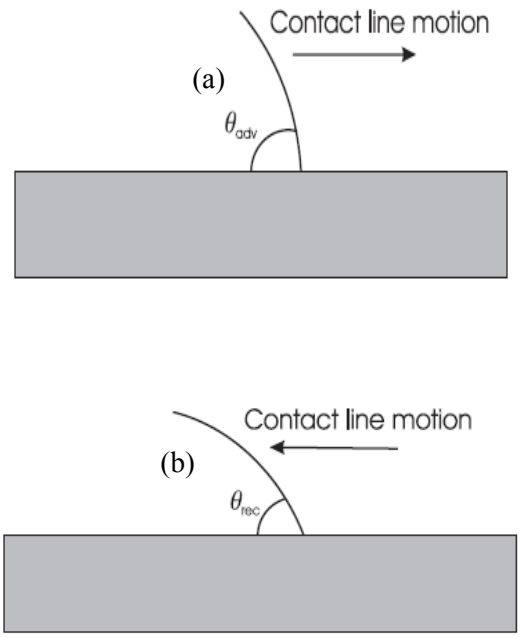

Figure 1.5: Scheme for (a) advancing contact angle, and (b) receding contact angle.

The dynamic contact angle is dependent on the structure of the substrate, surface tension the adsorption at the solid-liquid interface and temperature of the fluid. For non-wetting scenarios (e.g. water on Teflon AF) the advancing and receding contact angles may be considered constant with respect to the adsorption at the solid-liquid interface and surface tension. In reality the equilibrium contact angle is never measured due to chemical non-homogeneities and irregular surfaces result in contact angle hysteresis. The equilibrium contact angle takes a value intermediate angle between the advancing contact angle θ_a and the receding contact angle θ_r. The advancing contact angle for a sessile drop is the angle at which the contact line begins to move while the receding contact angle refers to the angle at which the contact line begins to recede. For consistency defined the equilibrium contact angle was defined as the angle that corresponded to the maximum surface energy, [33].

1.1.3 Wetting Transitions

Wetting transitions are of fundamental interest in order to study long-range interactions between different media,[18].The idea of wetting transitions was first proposed in 1977 by John Cahn, the difference between a liquid forming film or a droplet when in contact with a surface was due to thermodynamic differences of phases. He found the phase transition from partial to complete wetting was as a result of the singular behaviour of

surface rather than bulk thermodynamic functions. It was predicted that the wetting transition should take place below the bulk critical temperature where it is impossible to distinguish liquid and vapour phases, [24].

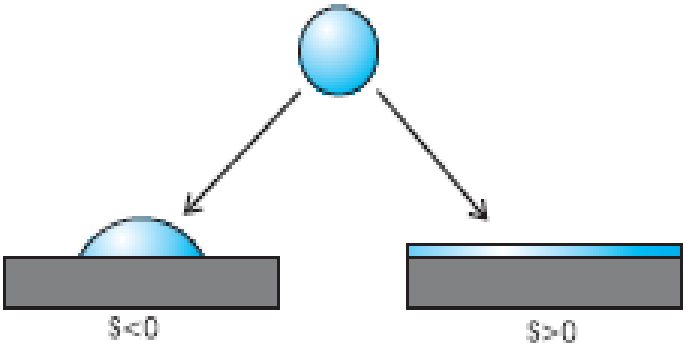

Figure 1.6: Scheme for a case of wetting and complete wetting

In a case where a liquid is in contact with a solid surface two distinct phenomena are observed as shown in Figure 1.6, the liquid spreads and forms a film over the surface or it does not spread and forms droplets (partial wetting). In essence the behaviour of the system depends on S, for cases where S is positive a complete wetting profile is observed and where S is negative the wetting profile is partial. Assuming the three interfacial surface tensions are known, the wetting potential of a fluid can be determined. When there is low surface tension, free energy is minimized by a droplet with a finite contact angle which leads to partial wetting, [33].

Sferrazza et al. described the phenomenon of dewetting as the process where an initially uniform liquid film on a non-wetting substrate breaks into droplets, the importance of dewetting in thin films and coating applications has made its study important experimentally and theoretically, [34].

The spreading coefficient of a fluid is denoted by S, which is can be defined as the difference in free energy between partial and complete wetting. We can represent S by

$$S = \gamma_{sv} - \gamma_{sl} - \gamma_{lv} \qquad 1.6$$

When $S \geq 0$, the wetting profile corresponds to complete wetting while when $S < 0$ the profile corresponds to a non-wetting case, the finite contact angle which is formed may be determined by the expression in Eq.1.7.

$$cos\theta_{eq} = \frac{\gamma_{sv} - \gamma_{sl}}{\gamma_{lv}} \qquad 1.7$$

The wetting transition induced by electric fields they found that saturation prevents partial to complete wetting transitions of water on solid. Their focus was on dewetting transitions where the initial state was complete wetting for oil a reverse transition from complete wetting of oil on polymer was triggered by the applied field between water and a counter-electrode beneath the polymer.In most cases dewetting is a result of nucleation of dry zones, either heterogeneous nucleation where dewetting is due to a defect into the film or thermal nucleation where dewetting is a result of a temperature gradient, [18].

Reiter and Khanna [33] andSferrazza et al [34] studied the dynamics of dewetting in thin polymer films,, and they concluded that dewetting involved the dissipation mechanisms occurring at the solid-liquid interface as a result of viscoelastic effects and properties of the interface. In polymer layers an interesting phenomenon referred to as slippage, is due to the friction between the confined film and the substrate. In reality solid surfaces are always rough, and this roughness influences the ability of a liquid to wet a surface. The stability of the liquid film formed on a surface has been related to its thickness by de Gennes et al. [35] in the monograph for wetting which they proposed.

Brochard-Wyart studied theoretically and experimentally the rim „birth' kinetics for hole nucleation within the supported film on a solid slipping substrate, the model was based on the visco-elastic properties of the system and the friction at the wall surface. An exponential law was modelled for the growth of the hole as a function of time where dissipation was low in the direction of the film around the hole, a linear law where the viscous dissipation was dominant as the dewetting velocity remained constant and a power law where the wetting velocity decreased as the capillary force remained constant while the dissipation increased due to the friction at the rim. For polymers dewetting near its glass transition an important asymmetry for the rim was observed, the elastic behaviour of the poly was responsible for this morphology. They suggested that between the first stage I, where capillary forces govern dewetting, and the hole velocity follows an exponential law and the final stage, IV, where velocity follows the -1/3 power law governed by viscous dissipation in the rim, two other regimes (II and III) were observed, and they proposed that dissipation which controlled the rim size controlled the these regimes (II and II) as shown in Figure 1.7, [34].

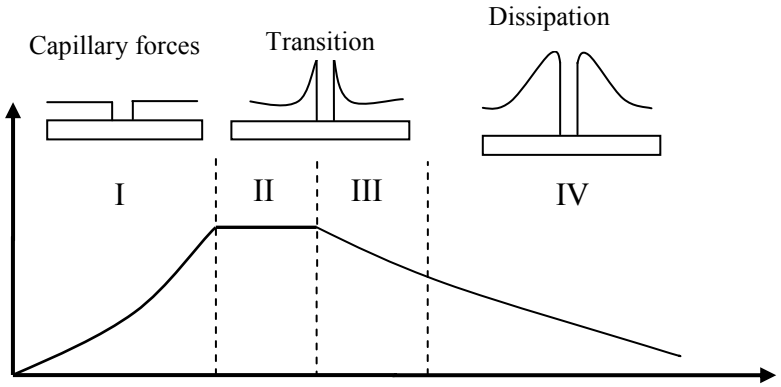

Figure 1.7: Schematic showing the dewetting stages of a polystyrene film on a PDMS brush at the glass transition, redrawn from [34].

Weiss [36], analysed the wetting transition in alkanes studying the influence of temperature and salinity on the different components of the disjoining pressure that drive the wetting transition. The transition from partial wetting to complete wetting in thin films to thick films were analysed based on the Derjaguin-Frumkin theory which takes into account the behaviour of the disjoining pressure and the excess free energy isotherms, and it was observed that for a stable wetting film that co-exists with the drop and oversaturated vapour will have a negative disjoining pressure.

Ping et al. carried out experiments with trisiloxane surfactants on hydrophobic substrates to determine the wetting transition [37], and they found that the transition from partial wetting to complete wetting was at the critical wetting concentration. The critical wetting concentration was described by Ivanova et al [6], as a concentration above which a transition from partial wetting to complete wetting occurs for spreading over moderately hydrophobic surfaces from which they inferred that the CWC was associated with the beginning of the superspreading.

Svitova et al. [38] analyzed the spreading behavior of aqueous solutions of a number of non-ionic surfactants on graphite as a function of surfactant concentration. They found that the transition from partial wetting to complete spreading for surfactant solutions similar to that for other hydrophobic solid and liquid substrates and the transition occurred at the critical wetting concentration which was considerably higher than the critical aggregation concentration.

Macdonald et al. [39], showed that after the evaporation of n-dodecane on graphite they was a formation of patterns which were attributed to two different dewetting scenarios; where there was heterogeneous and thermal nucleation of „dry' spots and spinodal-like

dewetting at nanometer-size film thicknesses due to combination of a polar long-range repulsive forces and restructuring/layering-induced density variations.

Bonn and co-workers [40] concluded that the transition from partial to complete wetting occurred in three different ways as a result of the subtle interplay between short-range forces and long-range van der Waals force, and that critical wetting transitions were peculiar to systems dominated by both long- and short-range forces. For specific cases an interface potential can be formulated describing the net effect of the intermolecular forces as an interaction between two surfaces as shown in Figure 1.8, where T_w is the wetting temperature with respect to the thickness of the film.

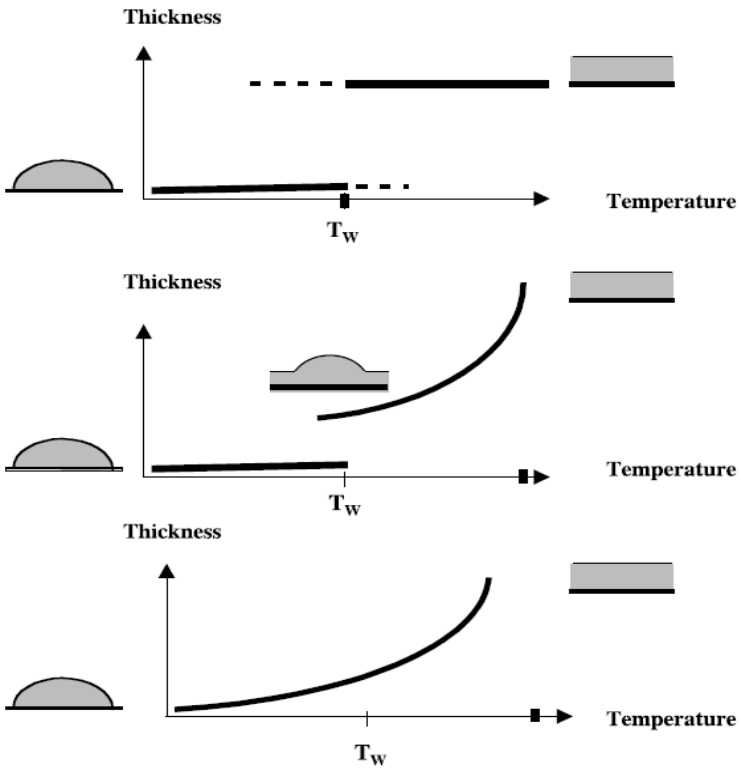

Figure 1.8: Schematic of the possible wetting transitions as described by Bonn et al, redrawn from [40].

Masutubara et al. used line tension measurement using interference microscopy and applied to hexadecane lenses they found that the line tension changes from positive to negative simultaneously with the transition from partial wetting to pseudo-partial wetting. This was the first experimental evidence of the theoretical prediction of the behavior of the line tension at the wetting transition previously developed, [41].

Changera et al. studied aqueous solutions of non-ionic surfactant on graphite as a function of concentration by AFM using tapping mode for imaging and contact mode

for force measurements was carried out, [42]. They found that the a transition from partial wetting to complete spreading for surfactant solutions occurred at the critical wetting concentration which was similar to other hydrophobic solids, an that the wetting transition was as a result of multilayer adsorption at the solid-liquid interface.

Kajiya et al [43], analyzed the wetting transition on parafilm gel, and they concluded that the surface deformation at the contact line is caused by the balance between the surface tension of the liquid and elastic resistance of the gel. However, as the SBS–paraffin gel is visco-elastic, when the contact line stays close to its initial position, the elastic resistance of the gel gradually relaxes and the gel creeps to evolve a surface, and after long time the surface ridge changes its shape to a gradual surface rise like the capillary ridge formed at the contact line of liquid on the surface of another liquid.

1.1.4 Wetting over Smooth and Rough Surfaces

A droplet in contact with a substrate will usually create a contact angle hysteresis which was described simply as the difference between the advancing contact angle and the receding contact angle, [9]. The wetting dynamics of trisiloxane surfactants on hydrophobic surfaces had been undertaken on parafilm and polystyrene surfaces and the wetting was described as Wenzel wetting with respect to contact angle hysteresis, [19].

Surfaces can be classified based on the interaction at the liquid-solid interface, a review by Matsubara et al. [41] classified solid substrates into hydrophobic (or oloephobic i.e. because they possess a stronger affinity for water than oil based liquids) and hydrophobic (or oleophilic i.e. they possess high affinity for oil based liquids). These surfaces possess high surface energies and form contact angles larger than ninety (greater than 90º) contact angles when in contact with liquids are called hydrophobic (low affinity for water interaction) e.g. polystyrene, Teflon. Super-hydrophobic surfaces are substrates on which spreading is more difficult and in some cases impossible and the possibility of the droplet rolling off the surface can be expected e.g. dry lotus leaves or modified surfaces. The surface topography of solid surfaces can be altered to increase or reduce the surface energy, fumed silica particles and fluorinated polymer coatings to create super-hydrophobic surfaces i.e. contact angles $\pi/2 > 90º$, [9, 41, 44]. Erbil et al. [45] precipitated polypropylene from a good solvent with a non-solvent and cast a fine reticulated structure which gave a water contact angle of 160º.

Cheng et al [46], formulated superhydrophobic surfaces with aligned polystyrene (PS) nano tubes using the porous alumina membrane covering method. The unique nano-tube

topography endowed the film surface with not only considerable roughness which contributeed not only to the superhydrophobicity, but also to a strong adhesive effect on the water droplet, due to the capillary force and the capillarity-induced negative pressure.

The wetting dynamics on a lotus leaf was analysed and two distinct levels roughness were identified, the wetting dynamics was consistent with Wenzel mode [32] on wet surfaces and wetting dynamics described by Cassie- Baxter [47] on dry surfaces for water droplets. The inclusion of Silwet facilitated the permeation of liquid into the spaces between the pillars of the lotus leaves leading to the transition from Cassie-Baxter wetting to Wenzel wetting on the dry lotus surface, the transition point was related to the surfactant concentration and deposition time, [22, 41].

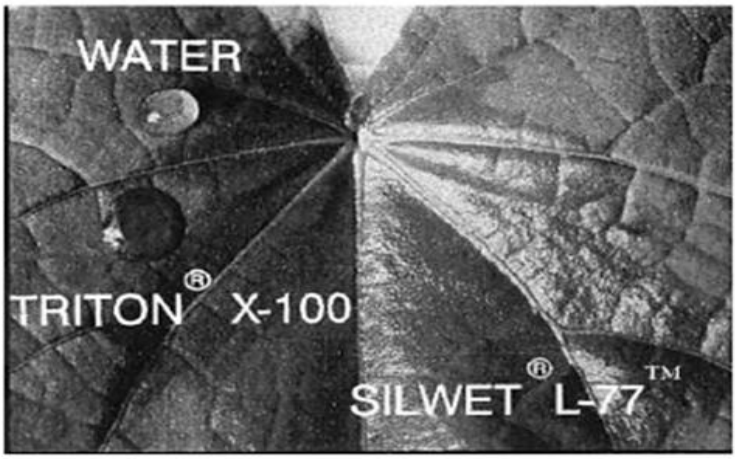

Figure 1.9: Photograph depicting the spreading of: (a). water droplets and a drop of 0.25% Triton X-100 solution, (b) 0.1% Silwet L-77 solution on a velvet leaf surface, redrawn from [48].

Tang et al. carried out experiments to determine the influence of hydrophobicity in spreading experiments on dry and wet lotus leaves using surfactant solutions of Silwet, [49]. They analysed the the surface of the lotus leaf with an scanning electron microscope, shown in Figure 1.10 and they found micrometer scale bumps and nanometer scale hair-like structures covering the surface of the leaf, these structures were seen to enhance hydrophobicity on a dry leaf surface but became hydrophilic on a wet surface. They observed a variation of contact angles with time on the dry surfaces indicating the contribution of surface structure to the wetting transition.

Feng et al. [50], experimentally studied the surface of the lotus leaf, they found that the presence of hierarchical micro-nanostructures and hydrophobic epicuticular wax are critical for the formation of the super-hydrophobicity. Therefore, artificial superhydrophobic surfaces with self-cleaning properties can be designed and prepared based on the principle of combining hierarchical roughness with low surface energy materials.

Starov et al. [51], proposed that the transfer of surfactant molecules in the water droplet onto the hydrophobic surfaces changes the wetting characteristics in front of the drop at the three-phase contact line was responsible for the spreading of surfactant solutions onto hydrophobic Teflon substrates. The surfactant molecules reduced the solid-vapor interfacial tension and hydrophilized the initially hydrophobic solid substrate just in front of the spreading drop (at the three phase contact line) causing the liquid to spread over time.

Figure 1.10: Pure water drop on (a) dry lotus leaf (a) and (b) wet leaf redrawn from [46].

Wetting dynamics remains an active subject of research, in the case of gel like surfaces because of the need to patch up classical hydrodynamics near the contact line. On gels, the situation would be more complex as the wetting liquid causes a large deformation on the gel surface which successively affects the statics and dynamics of the contact line. The deformation of the gel surface is caused by two mechanisms: by the balance between the interfacial tensions and elastic resistance of the gel and by the volume exchange between the liquid and gel. Intuitively, the behavior of the contact line on gels might be understood in analogy with the wetting on soft surfaces like an elastomer or with the wetting on permeable surfaces like porous media, [43].

The equilibrium contact angle is not unique; surface irregularities and non-homogeneous chemical composition of surfaces results in contact angle hysteresis as a

result of differences in surface energy over a given substrate. The role of surface roughness on the wettability properties of a solid surface have been interpreted using the Wenzel model and the Cassie–Baxter model which are derived by modifying the Young's Equation [32, 47].

The Wenzel approach was analyzed by considering a liquid filling the space of the surface grooves and linking the experimental apparent contact angle (θ′) and the thermodynamic equilibrium contact angle (θ_{eq}) as follows [32]:

$$cos\theta' = r_s cos\theta_{eq} \quad 1.8$$

Given that r_s is the ratio between the true surface area and its horizontal projected area ($r \geq 1$), with this condition the surface roughness reduces the equilibrium contact angle to less than 90º, and it does not give rise to super-hydrophobicity.

Applying the Cassie–Baxter approach to explain the interaction between the liquid and solid substrate, where air is assumed filling the hollow spaces of the rough surface and the relationship between the contact angles is given by:

$$cos\theta' = f_1 cos\theta_{eq} - f_2 \quad 1.9$$

Given that f_1 is the fraction of liquid area in contact with the solid and f_2 is the fraction of liquid area in contact with the trapped air.

In the study by Wenzel, these two phases were differentiated using the contact angle hysteresis, the Wenzel wetting mode was found in systems with larger values of contact angle hysteresis. Whenever a process involved the wetting of a solid by a liquid, three different interfacial boundary surfaces; solid-liquid, solid-air, and liquid-air interfaces are involved. A wetting liquid droplet replaces an area of the solid-air interface by an equal area of solid-liquid interface and is generally also accompanied by an extension of the liquid-air interface. These surface relations varied with the conditions of wetting kinetics and changed progressively as wetting proceeded. Given that each interface had its own specific surface energy content, the interfacial changes due to wetting lead to a change total surface energy (an increase or decrease of surface energy). Wetting can therefore be described as a thermodynamic process and the magnitude of the free energy change determines the spontaneity of wetting, the rate and propagation against the external forces.

Considering a drop of water resting on a horizontal solid surface the specific energy content of the solid interface will be different for the wetted area under the sessile droplet than for the dry area around the droplet, assuming the wetted area has a lower specific energy the drop tends to spread spontaneously until it reaches it maximum wetting area, droplet spreading was characterized by energy dissipation increasing the wetted area under the drop and the free liquid surface over around the droplet will also be increased, the former involves a release of energy while the latter represents consumption of energy.

This dynamics was consistent with experimental data and thus the conclusion that for an identical increase in the free liquid area at the upper surface of the drop, a greater amount of actual surface is wetted under it if the surface of the solid is rougher than when it was smooth, [32, 52, 53]. In Figure 1.11, an illustration of the wetting dynamics on an ideally smooth surface is considered with an energy content equivalent to the specific energy of the interface. The force vectors S_1 and S_{12} acting along the periphery of the interface *ab*, their vector sum $S_1 - S_{12}$ defines the adhesion tension, its negative value indicates its resistance to wetting, the equilibrium relation between the surface tension S_2 of the liquid, the contact angle and adhesion tension.

Wenzel [32] further studied the significance of surface roughness to spreading and suggested that for rough surfaces there was a greater net decrease in energy to induce spreading and that the rough surface is wetted the more rapidly. The same reasoning was applied to a water-repellent surface, in which case the dry interface has the lower surface energy. The droplet will spontaneously assume a more spherical form for an identical change in the shape of the droplet area and total energy content of the free liquid surface. The interaction of the solid-liquid interface is greater for non-homogenous surfaces than for homogeneous surfaces because the rough surface provides a larger area of solid-liquid interaction. The net energy decrease will thus be greater for the rougher surface however in the reverse wetting; the rough solid is more strongly water-repellent. In conclusion the influence a rough surface is to magnify the wetting properties of the solid. A solid substance with a positive wetting tendency will wet the more readily, the rougher its surface. A schematic of the influence of surface roughness on advancing and receding contact angles is shown in Figure 1.12 below, where *n* is the surface roughness factor.

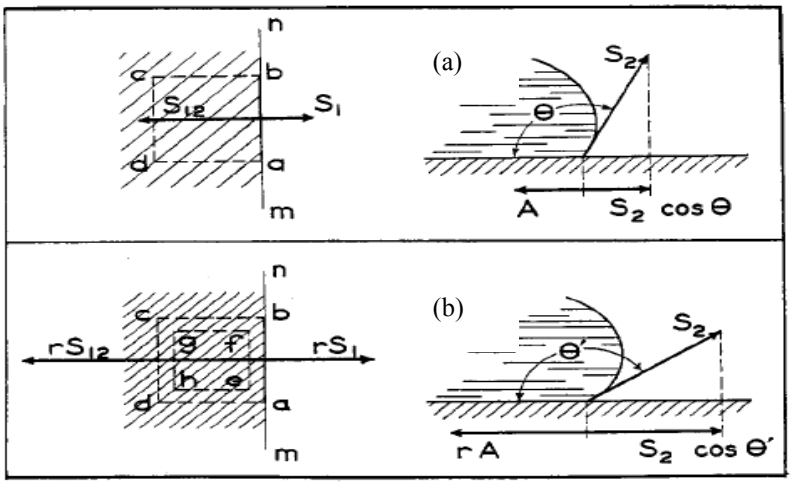

Figure 1.11: Vector relations of surface forces for solid smooth surface (a) and solid rough surfaces (b), redrawn from [32].

The roughness factor n, is given by

$$n = \frac{actual\ surface}{geometric\ surface} \qquad 1.10$$

Cassie and Baxter extended the analysis of apparent contact angles for rough surfaces to porous surfaces, particularly those encountered in natural and artificial clothing. They verified their analysis by direct measurement of θ' (apparent contact angle) and θ'_r (apparent receding angle) for a wire grating and θ_a (advancing contact angle) and θ_r (receding contact angle) were measured on a flat plate whose surface was identical with the surfaces of the wires. They immersed the wires in a solution of paraffin wax in benzene and heated to melt the crystals formed, on cooling they observed the wires were uniformly coated with a wax film whose thickness was comparable with, [49].

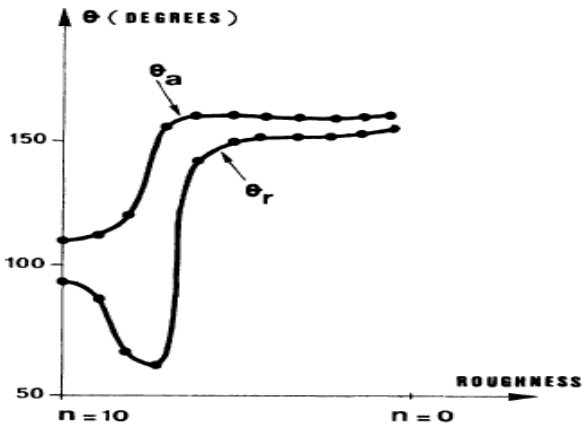

Figure 1.12: Advancing and receding contact angles evolution on a wax substrate as a function of surface roughness redrawn from [31].

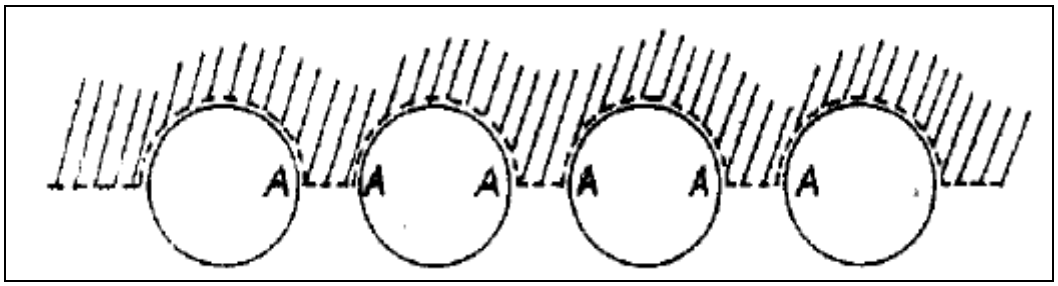

Figure 1.13: Water on cylinders to describe wetting on porous surfaces, redrawn from [49].

Assuming the total area of the solid-liquid interface in Figure 1.13 is f_1 and f_2 the total area of the liquid-air interface in geographical area equal to unity and parallel to the rough surface, γ_{SV} and γ_{LV} are the surface tensions in the solid-liquid and liquid-vapor interface. When water spreads over the unit area the solid-vapor interface becomes unstable and energy is transferred along the solid-liquid and solid-vapor interface. The total energy expended at the geometrical area of the interface is given as

$$E_D = f_1(\gamma_{LS} - \gamma_{SV}) + f_2\,\gamma_{LV} \qquad 1.11$$

From Young's Eq. the contact angle (in this case the advancing contact angle) is given as;

$$cos\theta_A = \frac{\gamma_{sv}-\gamma_{sl}}{\gamma_{lv}} \qquad 1.12$$

and Eq. 1.11 can then be rewritten as

$$E_D = \gamma_{LV}\,(f_2 - f_1 cos\theta_A) \qquad 1.13$$

substituting Eq. 1.13 into Eq. 1.12;

$$cos\theta_A = -E/\gamma_{LV} \qquad 1.14$$

From numerical and experimental analysis the apparent contact angle was derived by Cassie and Baxter, from which they were able to conclude that water-repellent clothing structures and for ducks is due to the structure of its feathers rather than to any exceptional proofing agent.

Petrov and Petrov computer models that showed the presence of an insoluble monolayer of surfactant that significantly affected the spreading dynamics, [54]. The presence of the insoluble monolayer enhanced the overall spreading rate through two major mechanisms; the development of positive surface curvature near the moving contact line which produced a favorable radial pressure gradient within the drop, and the reduction in the equilibrium contact angle. Both of these mechanisms were driven by the accumulation of surfactant at the three phase contact line due to surface convection.

1.1.5 Pinning and De-pinning Droplets

A pinned droplet can be described as the droplet in contact with a solid substrate and maintains a constant drop radius, this phenomenon can be observed in evaporating droplets (water on Teflon) and non-evaporating droplets (silicon oil on Teflon). de Ruijter et al.[5], Ivanova et al.[6] and Sefiane et al.[13], studied the pinning and de-pinning of a sessile droplet, and they found that these phenomena were influenced by surfactant concentration,given that surfactant solutions increase the wetting potential of their solutions until the CWC is reached. For evaporating liquids there was possibility that the molecules of the droplet rearranged due to changes in the volume of the droplet and thus the concentration of surfactant within the droplet, evaporation can lead to a temperature gradient which could result in a stick-slip motion of the pinned droplet on the substrate, however this stick-slip movement will also depend on the homogeneity of the substrate.

Yeomans et al, analyzed the pinning of the contact line on super-hydrophobic substrates [25], and they ascribed the pinning of the contact line at the edges of the droplet to a threshold force below which the drop will not move, however after this threshold they do start to move, they do so much more easily which can transcend to a flow.

In the work by Koopal [27], it was concluded that a droplet in contact with a real surface can remain pinned to the solid surface while evaporation progressed, the evaporation rate was directly dependent on the dynamics of the contact droplet radius, a de-pinned droplet will deviate significantly from these dependencies.

Tang et al [49], carried out spreading experiments on hydrophobic lotus leaf surfaces, and they concluded that the surface structure and surface tension gradient influenced the transition from pinning to depinning of surfactant solutions on hydrophobic surfaces.

Nguyen and Nguyen studied evaporating water droplets on hydrophobic substrates [55], and they concluded that pinning or depinning of a droplet determines the progression of

the evaporation rate and that the pinning or depinning of a droplet in contact with a solid surface is as a result of a balance (pinning) or imbalance (depinning) of hydrostatic and capillary forces acting along the solid-liquid interface. They compared a theoretical model which they developed by predicting the evaporative flux and experimental data from literature, they obtained a good fit. They concluded that the evaporation rate in sessile droplets was stronger when the droplet is pinned more than when it is de-pinned.
Shi et al studied the pinning and depinning of molten Mg during its evaporation from a single aluminium crystal surface, [56]. This behavior was controlled by the competition between surface free energy and energy barrier, when the surface energy was greater than the energy barrier the droplet was pinned and in the reverse arrangement depinning was observed.
Kajiya et al [43], studied the dynamics of water sessile droplets advancing on visco-elastic SBS–paraffin gel substrates, and they observed that the droplet contact line exhibited three different regimes of motions, and their transition is characterized by a frequency of the surface deformation which was determined by the apparent contact line velocity and droplet. They concluded that the transitions of the contact line motions (continuous–stick-slip–continuous) were the consequence of the rheological property of the gel affecting the dynamics of the contact line, and this depended on the frequency, the behavior of the liquid contact line on gels shows both aspects of wetting on elastic solids and on viscous liquid sheets. At an intermediate frequency where the gel behaves neither as a solid nor as a liquid, the stick-slip motion appeared. In addition they studied the spreading behavior of liquid droplets on gels, which were under the influence of swelling equilibrium, and they observed a strong coupling between the volume exchange and contact line dynamics.

1.1.6 Theoretical Models for Spreading

There has immense interest on the subject of wetting because of its importance as outlined earlier and its numerous technological applications. To understand the spreading behaviour of liquids in contact with solid surfaces experimental and theoretical analysis of the problem has been carried out by different researchers for different spreading conditions ranging from spreading on hydrophobic surfaces, heated surfaces, patterned surfaces, vibrating surfaces etc. We will consider the following theories:

1.1.6.1 The theory of Blake

The analysis of spreading of droplets was berth from an interpretation of Kramer's postulation [57]; in his paper in 1940 he proposed that „a particle which is caught in a potential hole and through the shuttling action of Brownian motion can escape a potential barrier yields a suitable model for elucidating the applicability of the transition state method for calculating the rate of chemical reactions'. Many years passed before this postulation was applied to the moving contact line problem i.e. the wetting or dewetting of a solid surface, the theory developed is referred to as the molecular-kinetic theory of wetting. Another hydrodynamic model was developed and both models were used simultaneously mainly because experimental results agreed with either model. The molecular-kinetic theory has been modified by Blake and Haynes to include the effects of viscosity and solid-liquid interactions, [58].

More recently de Ruijter et al [56], applied the molecular dynamic simulations to the study wetting processes, irrespective of the importance of hydrodynamics the peculiarity of the moving contact line has made it imperative to consider molecular dynamics of the three phase contact line. The molecular dynamic theory for wetting dynamics was first developed by Blake and Haynes to account for contact line dissipation, [58]. The basic ideas of the molecular-kinetic theory are that liquid molecules are in constant thermal motion with a characteristic velocity, *v* which can measured as a function of the characteristic length, λ and frequency, κ (of displacements) at a given temperature i.e. (*v*) = λκ, these functions constitute a three phase contact line at molecular level, the frequency of displacements parallel to the solid wall was denoted by κ^+ for outward displacements from the liquid and κ^- for inward displacements, the velocity of the contact line *(V)* is given by and a schematic is shown in Figure 1.14

$$V = \kappa^+ + \kappa^- \qquad 1.15$$

at equilibrium where V

$$\kappa^+ = \kappa^- = \kappa^0 \qquad 1.16$$

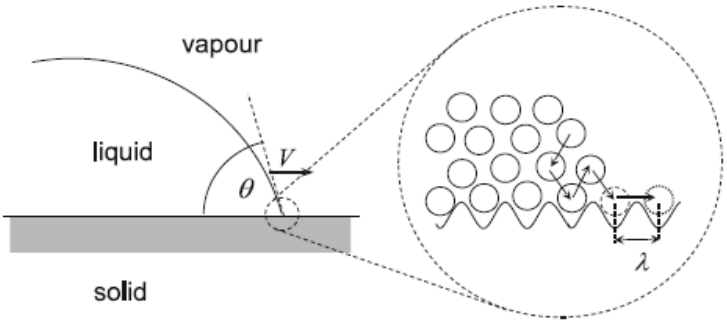

Figure 1.14: Schematic representation of molecular displacements within an advancing three-phase zone, *V* is the velocity, θ, the contact angle and λ, the distance between molecules, redrawn from [58].

Blake and Haynes described the velocity contact line in terms of molecular length and frequency which allowed them apply Erying's theory of absolute reaction rates to obtain the velocity, *V*. the theory relates the equilibrium frequency to the molar activation energy, they obtained the equation, [58].

$$\kappa^0 = \left(\frac{T\kappa_B}{h}\right) exp\left(\frac{-\Delta G_w^*}{N_A \kappa_B T}\right) \qquad 1.17$$

where κ_B and h are the Boltzmann and Planck's constants respectively and N_A is the Avogadro number. They proposed that if κ^+ was larger in magnitude than κ^{-0} the imbalance will create motion in the direction of the larger frequency making it difficult for inward flow. They incorporated the parameters ω and *n* which represented the work done per unit area by the driving force and the number of sites per unit area of the solid surface where work was dissipated. The total frequency of molar displacement was given as

$$\kappa = \kappa^+ - \kappa^- = 2\kappa^0 sinh\left(\frac{\omega}{2n\kappa_B T}\right) \qquad 1.18$$

The driving force is due to an imbalance of surface tension acting on the contact line which is as a result of disturbance of adsorption equilibrium at the various interfaces as the contact line moves over the solid surface, the solid-liquid interface is created or destroyed, when the expression for the work done in incorporated into the velocity equation they obtained

$$v = 2\kappa^0 \lambda \sinh\left(\frac{\gamma_{LV}(cos\theta^e - cos\theta}{2n\kappa_B T}\right) \qquad 1.19$$

For an evenly balanced system the wetting velocity was related to four equilibrium material dependent quantitiesκ^0, λ, γ_{LV} and θ^e, for a near equilibrium system they obtained the expression

$$v = \gamma_{LV}(cos\,\theta^e - cos\theta)/\varepsilon \qquad 1.20$$

where $\varepsilon = \kappa_B T/\kappa^0\lambda^3$ and it relates the velocity of the contact line to the driving force, they referred to this parameter εas the contact line friction. The next step was to incorporate the activation free energy with the equilibrium frequency κ^0 and contact line friction, where v_L and η_L were given as the liquid viscosity and molecular flow volume respectively they recognized that there was work done related to the equilibrium work of adhesion between the liquid and solid interface. They solved the contact line friction equation and obtained the expression

$$\varepsilon = \left(\frac{\eta_L v_L}{\lambda^3}\right) exp\left(\frac{Wa^0}{n\kappa_B T}\right) \qquad 1.21$$

Eq.s 1.14 and 1.15 have been used to determine the dynamics of wetting and the variation of the dynamic contact angle for a wide range of systems; these equations were valid for experimental data molecular dynamics simulation reported in literature [59, 60].

Svitova et al.[38], Heine et al.[60], and Ivanova et al.[61], used this theory to analyze wetting experiments and they concluded that changing the magnitude of the solid-liquid interaction would affect the wettability which leads to a change of the dynamic contact angle, they defined two regimes of wetting for a given solid–liquid system; a low velocity regime and a high velocity regime.

Fitting the low and high velocity regime separately resulted in quite different values for the molecular parameters λ and κ^0. Svitova et al. concluded that the molecular kinetic theory has an advantage over the hydrodynamic model because the MKT approach concentrates on processes occurring in the vicinity of the advancing contact line, which stem from the attachment of fluid particles to a solid, and it ignored the dissipation due to viscous flows in the core of the liquid droplet, [38].

1.1.6.2 Rate theory of Wetting

The wetting rate law is an important analytical model to describe the process occurring at the triple phase contact line. Slavchov et al. developed a model based on equilibrium, a linear dependence rate *dr/dt* and the driving force can be expected, represented by the expression, [62];

$$\frac{dr}{dt} = m(\bar{x}_y - x) \qquad 1.22$$

Where m is the phenomenological mobility coefficient, a characteristic property of kinetic wetting, $\bar{x}_y$ is the cosine from Young's equilibrium contact angle ($\bar{x}_y = cos\theta_y$) and x is the cosine from the current contact angle ($x = cos\theta$).

This linear dependence has limited applications but more precise non-linear rate laws were proposed to describe the wetting kinetics for experimental data. Slavchov et al. considered the triple phase contact line (solid-liquid-gas) propagating over a heterogeneous surface. The heterogeneity was modeled by a certain number of surface tension fluctuations referred to herein as "spots" of surface concentration given by $c_s = 1/\Lambda^2$, these spots are normally due to chemical heterogeneity or surface roughness, Λ is the characteristic distance between spots and λ is the mean linear size, normally $\lambda < \Lambda$, [62].

The medium was characterized with average surface energies for γ_{SG} and γ_{SL} for the dry and wet media respectively, given that γ'_{SG} and γ'_{SL}, the average surface energies of the dry and wetted spot areas. Given that the relation $\gamma'_{SG} - \gamma'_{SL} < \gamma_{SG} - \gamma_{SL}$ was satisfied, then the spot areas were more difficult to wet than the medium surface, and there referred to them as "hygrophobic spots in hygrophilic medium", they observed that, spots served as a barrier to the triple phase contact line propagation. In an opposite case, observed "hygrophilic spots in hygrophobic medium". From the analysis by Changera et al. the terms "hygrophobic" or "hygrophilic" are only valid in comparison with the average value of the surface energy, the average macroscopic values of the surface energies i.e. medium and spots, [42].

$$\bar{\gamma}_{SL} = \frac{\gamma_{SL}(\Lambda^2 - \lambda^2) + \gamma'_{SL}\lambda^2}{\Lambda^2} \quad \text{and,} \quad \bar{\gamma}_{SG} = \frac{\gamma_{SG}(\Lambda^2 - \lambda^2) + \gamma'_{SG}\lambda^2}{\Lambda^2} \qquad 1.23$$

The hypothetical mechanism of the line propagation is shown on Figure 1.15, it is important to note that the triple phase contact line is rough i.e. it is a broken curve even at equilibrium.

Slavchov et al proposed that the roughness was determined mainly by the heterogeneity of the solid substrate from a thermodynamic point of view the triple phase contact line was in a macro-state consisting of large number of "microstates" (i.e. different configurations of triple phase contact line giving the same average position). The triple phase contact line was constantly passing from one microstate to another due to thermal fluctuations. Regions of the triple phase contact line at distance larger than $\Lambda$from each other are considered non-interacting, i.e. independently moving. This is equivalent to line movement occurring in small steps forward and backward, [62].

The schematic for interacting molecules is shown in Figure 1.15, it was observed that any movement in either direction involves only the triple phase contact line region for a molecule of size $\sim\Lambda$. In Figure 1.15a and Figure 1.15c, two local minima (two microstates) of the triple phase contact line are shown, having free energies F_1 and F_2. There is an intermediate "activated" state between them, corresponding to a free energy maximum F^* as shown in Figure 1.15b. We now proceed to estimate the average differences between these free energies, [62].

Surface roughness and chemical heterogeneity can lead to surface energy fluctuations which would act as energy barriers for the three phase contact line motion. Based on this assumption made by Slavchov et al., the three phase contact line propagation rate was obtained as a function of the three phase contact angle in terms of either nucleation rate theory or Erying's absolute rate theory. To execute this model a general bi-exponential rate law was deduced and wetting kinetic characteristics were related to surface properties (roughness and heterogeneity) using available data from imagine analysis. The main assumption for this model is that the three phase contact line is rough and its propagation occurs in shifts of small regions of the three phase contact line backwards and forwards i.e. steps, and these steps occurred independently, a schematic of the rate analysis and the interaction with the solid-liquid–gas interface is shown in Figure 1.16.

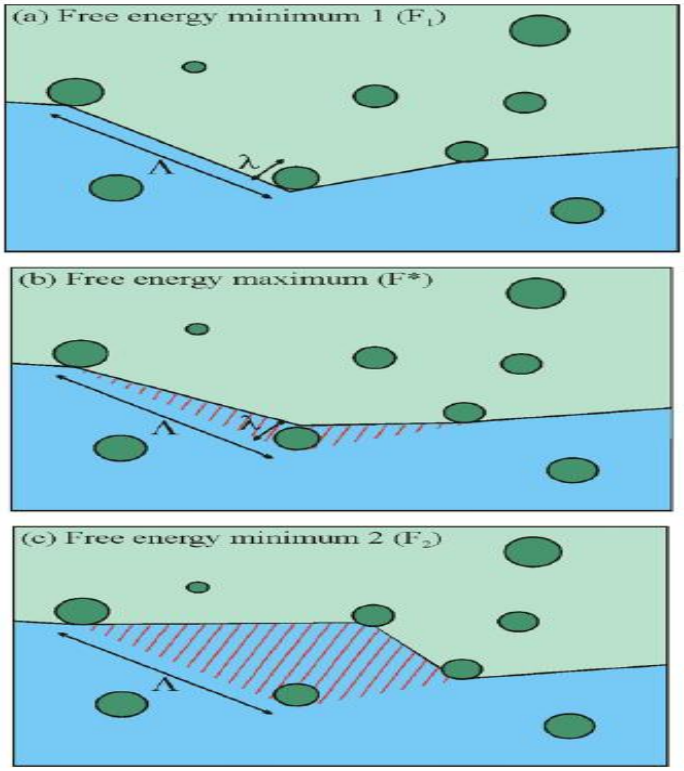

Figure 1.15: Mechanism of three phase contact line propagation over a heterogeneous surface, redrawn from [62].

The triple phase contact line passes through spot a number of spot sites given by $R_L 2\pi r/\Lambda$ where R_L is the roughness factor for the contact line roughness analogous to the Wenzel factor [32]. The rate of area change is then given in Eq. 1.24 where v_A and v_R are the advancing and receding frequencies of site movements and *r* droplet radius.

$$\frac{d\pi r^2}{dt} = (v_A - v_R)\Lambda^2 R_L \frac{2\pi r}{\Lambda} \qquad 1.24$$

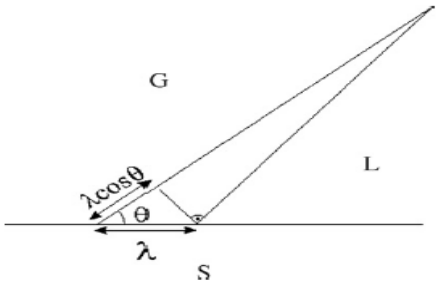

Figure 1.16: Scheme of solid-liquid-gas triple phase contact line for liquid-gas area when a region of the triple phase contact line of length Λ shifts an infinitesimal length λ forwards or backwards. Redrawn from [62].

The absolute frequency ν is a measure of how often the triple phase contact line attempts to overcome the barriers due to the advancing and receding angles and the magnitude is same regardless of the direction. De Gennes [64], estimated the absolute frequency using the capillary wave frequency with the resulting equation, where ρ is the density:

$$v^{cap} = \sqrt{\frac{\pi}{4}\frac{\gamma}{\rho\Lambda^3}} \qquad 1.25$$

Another method is the extrapolation of the absolute frequency to the molecular theory applying Erying's theory for rate processes where the frequency was determined by the loss of transitional degree of freedom of the activated state, therefore

$$v^E = \frac{kT}{h} \qquad 1.26$$

where b_A and b_R are dimensionless parameters (activation areas) and the characteristic velocity v_0 which is related to the barrier F_0, the rate law can then be rewritten as;

$$\frac{dr}{dt} = v_0\left[e^{-b_A\left(x-\bar{x}_y\right)} - e^{-b_R\left(x-\bar{x}_y\right)}\right] \qquad 1.27$$

The rate law was compared to experimental data from experiments performed by Petrov et al. [54] using alcohols, oils and aqueous trisiloxane solutions, they found the rate law correctly reflected the observed advancing/receding symmetry and compared satisfactorily with experimental data but in the cases of high and low spreading velocities, they observed discrepancies with experimental data which they proposed was due to the exclusion of hydrodynamic flow dissipation in the formation of the model.
Petrov and Petrov [54] and Wasan et al [42] concluded that for the three phase contact line propagation the wetted area grew at the expense of the molecules in the drop and the speed of propagation was determined by the barrier of a moving contact line as described by the rate law or by the movement of molecules from the bulk of the drop by three phase contact line as in the case of hydrodynamics. Slavchov et al [62] also highlighted an important consequence from the triple phase contact line as the ability of the fluid to induce roughness due to surface corrugations.

1.1.6.3 Autophilic Spreading Theory

Another theoretical model was proposed by Starov et al. [63], to predict the evolution of the contact line radius L and contact angle θ for the spreading process for a droplet of surfactant solution. In the absence of surfactants the droplet formed an equilibrium contact angle $\theta > \pi/2$. If the water contains surfactants three transfer processes were observed between the liquid and all three interfaces: surfactant adsorption at both (i) liquid–solid interface and (ii) liquid–vapor interface, and (iii) solid–vapor interface just in front of the drop, the adsorption interaction at the interfaces (i) and (ii) results in the decrease of corresponding interfacial tensionsγ_{SV} and γ.They proposed that the transfer of surfactant molecules onto the solid–vapor interface in front of the drop results in an increase of a local free energy; however, the total free energy of the system also decreased, a schematic of this surfactant molecule transfer is shown in Figure 1.17 below.

Therefore the surfactant molecule transfer in (iii) proceeded via a relatively high potential barrier and, thus is considerably slower than adsorption processes (i) and (ii), they concluded they were "fast" processes compared with (iii). The adsorption of surfactant molecules in front of the moving contact line resulted in a partial hydrophilization of the substrate surface which allows spreading over the hydrophobic substrate. Thus it goes without saying that the slowest process will be the rate determining step for this process, the initial contact angle is defined as [49];

$$cos\theta^0 = \frac{\gamma_{sv}-\gamma_{sl}}{\gamma_{lv}} \geq \frac{\pi}{2} \qquad 1.28$$

Where γ_{sv}, γ_{sl} and γ_{lv} represent the surface tensions at the solid-vapor, solid-liquid and liquid-vapor interfaces. Lamb [64] and Ivanova et al. [61], concluded that at the initial time the instantaneous adsorption of surfactant unto the solid surface at the three phase contact line is represented as $\Gamma_s(t)$ and Γ_e the equilibrium surface density of adsorbed surfactant molecules, and proposed that the driving force of the process was proportional to the difference of adsorptions i.e. $\Gamma_s(t)$-Γ_e. The time evolution of surfactant adsorption was given by:

$$\frac{d\Gamma_s(t)}{dt} = \alpha[\Gamma_e - \Gamma_s(t)] \qquad 1.29$$

Given the condition that $\Gamma_s(0)$ at $t = 0$ and where $\tau_s = 1/\alpha$, the time scale of surfactant transfer from the droplet to the solid-liquid interphase at the three phase contact line.

$$\alpha = \alpha_T \Xi \exp\left(\frac{-\Delta E}{\kappa T}\right) \qquad 1.30$$

Where Ξ is a fraction of the liquid-vapour interface covered by surfactant molecules, α_T is a prefactor determined only by thermal fluctuations, ΔE the energy barrier for surfactant transfer from liquid droplet to solid-liquid interface, κ and T are the Boltzmann constant and absolute temperature respectively, [19].

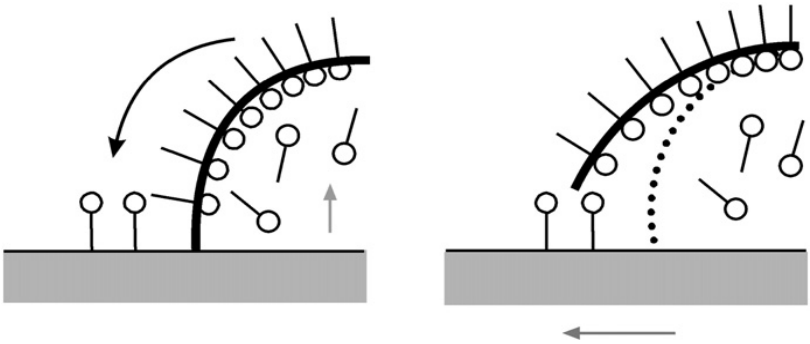

Figure 1.17: Spreading mechanism of aqueous surfactants solutions on hydrophobic surfaces according to Starov et al. redrawn from [19].

Starov et al.[52] assumed that transfer of surfactant molecules onto the hydrophobic solid interface occurred at the liquid-vapor interface, it was difficult to assess the contribution of surfactant molecule transfer along the solid surface from beneath the liquid, and they showed experimental data to support this assumption. The drop surface coverage Ξ was an increasing function of the bulk surfactant concentration inside the drop that reached a maximum at the critical micelle concentration (CMC). It can be inferred from Eq.1.30 that at low surfactant concentration inside the drop, τ_s will decrease as concentration increases until it surpasses the CMC where it levels off at its lowest value. According to Antonov's rule [65] the surface tension at the solid-vapor interface is given by

$$\gamma_{sv}(t) = \gamma_{sv}^{\infty} \frac{\Gamma_s(t)}{\Gamma^{\infty}} + \gamma_{sv}\left(1 - \frac{\Gamma_s(t)}{\Gamma^{\infty}}\right) \qquad 1.31$$

Given that γ_{sv}^{∞} is the interfacial tension at the solid-vapor interface for the area covered with surfactant and $\Gamma^{\infty}$the number of sites available for adsorption, the final contact angle $\theta^{\infty}$is given as;

$$cos\theta^{\infty} = \frac{\gamma_{sv}^{\infty} - \gamma_{si}}{\gamma_{lv}} \quad 1.32$$

The instantaneous contact angle was obtained by substituting Eq.1.28 into Eq. 1.31, and the same boundary conditions as Eq. 1.29 are valid. The resulting expression for the instantaneous contact angle becomes:

$$cos\theta(t) = \cos\theta^{0} + \lambda\frac{\Gamma_{s}}{\Gamma^{\infty}}[1 - \exp(-\alpha t)] \quad 1.33$$

This model has is consistent with experimental data from Venzmer and Wilkowski [11], Weiss [36], Chong et al. [37] and Tang et al [49]. on the spreading of an aqueous surfactant solution (sodium dodecyl sulfate) on different hydrophobic substrates and they found that the time scale dependence for surfactant transfer from the droplet to the solid substrate qualitatively agreed with their theoretical prediction as shown in the plots below supporting the idea of transfer of surfactant molecules at the three phase contact line being responsible for spreading of droplets, this theoretical model has also been validated in other systems.

1.1.7 Current Research Progress on the subject of Spreading

In the recent times there has been a lot of interest in spreading of droplets (pure fluids and mixtures). Several experimental, theoretical and computer simulated research on the droplet spreading. Ivanova et al. [61], described super-spreaders as trisiloxanes that possess the ability to promote fast spreading of aqueous solutions on hydrophobic surfaces. In this section, an up to date review of investigation of spreading will be discussed with respect to several parameters that can influence or inhibit the spreading of droplets on substrates such as heat, substrate roughness, droplet size and composition.

Rowan et al. carried out experiments using water on PMMA and they found that while the rate of mass loss is proportional to the height and not to the base radius when the triple line is pinned, [66]. Birdi et al. they studied the evolution of water drops on PTFE by measuring the mass evolution with time, they found the triple line was pinned with no spreading and the evaporation rate was constant, [67].

Barthwal et al. carried out experiments using water droplets onto glass and polycarbonate substrates of known surface roughness, the droplets profiles were measured by an optical technique while the evaporation was measured by a micro-balance, and they found that during the evaporation process the contact base radius remained constant while a linear decrease in drop mass was observed, as shown in Figure 1.19, [68].

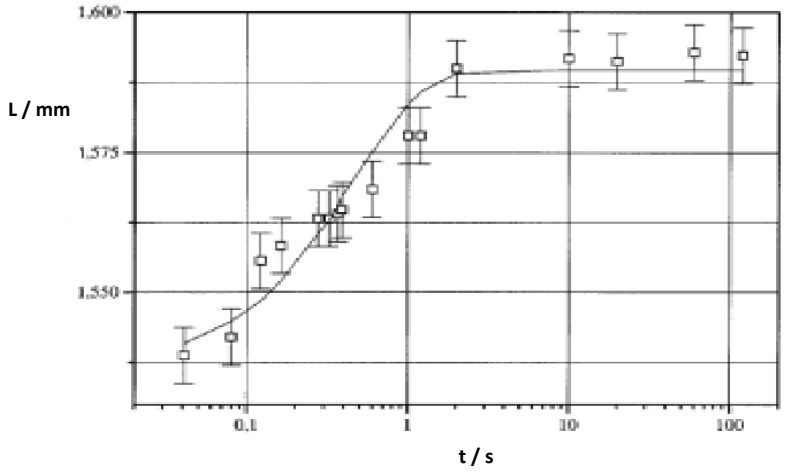

Figure 1.18: Time evolution of the spreading of 1% SDS over (a) PTFE and (b) polyethylene substrate, concentration above CMC, redrawn from [49].

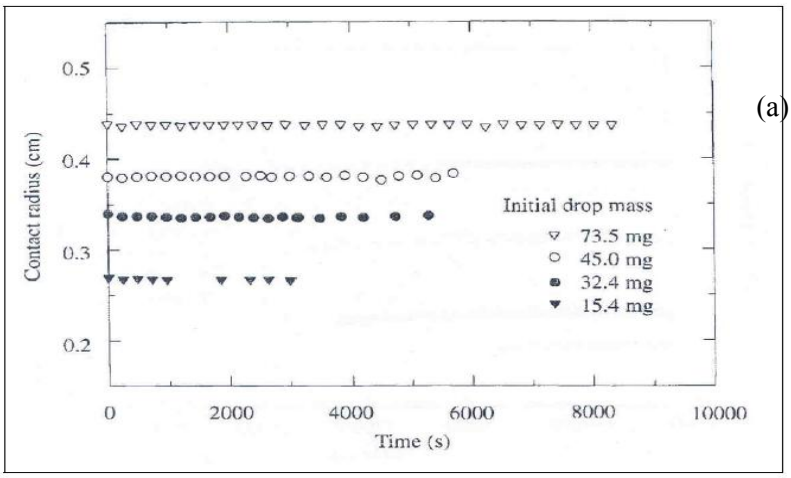

(a)

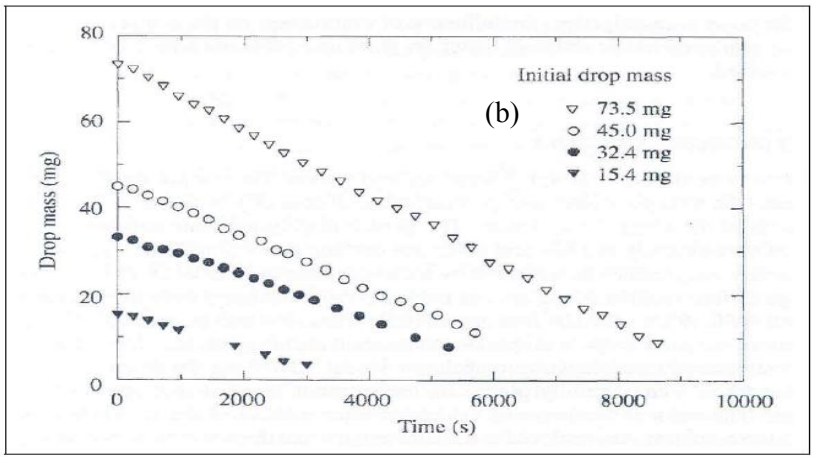

Figure 1.19: (a) Contact radius against time for water drops deposited on glass (b) mass against time for water drops deposited on glass, redrawn from [68].

Ivanova et al. [6] and Doganci et al. [69] found the surface tension in conventional surfactants reached a minimum with increasing concentration until it formed somewhat of a plateau as shown in the plot of surface tension as a function of concentration. It has been shown that after a particular concentration there is no observable difference in the spreading potential of the fluid, this point was referred to as the critical wetting concentration (CWC). This existence of this concentration was also measured with respect to the initial contact angle Figure shown in 1.20b, it can be observed that the advancing contact angle reaches a constant value after a concentration of the surfactant and further increase does not change the contact angle.

Rafai and Bonn [2] and von Bahr et al [17] measured the evolution of the radius of the moving front for a solution of superspreaders, and they found that the evolution of the contact droplet radius proceeded in two stages: a rapid first stage and slower second stage. In the first stage they observed that the solubility of the surfactant increased as well as the spreading exponents while in the second stage the spreading exponent seem independent of surfactant solubility.

1.1.1

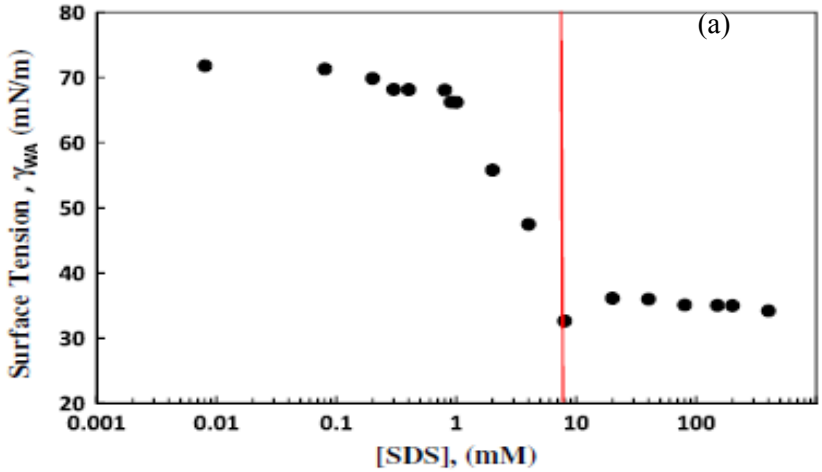

1.1.2

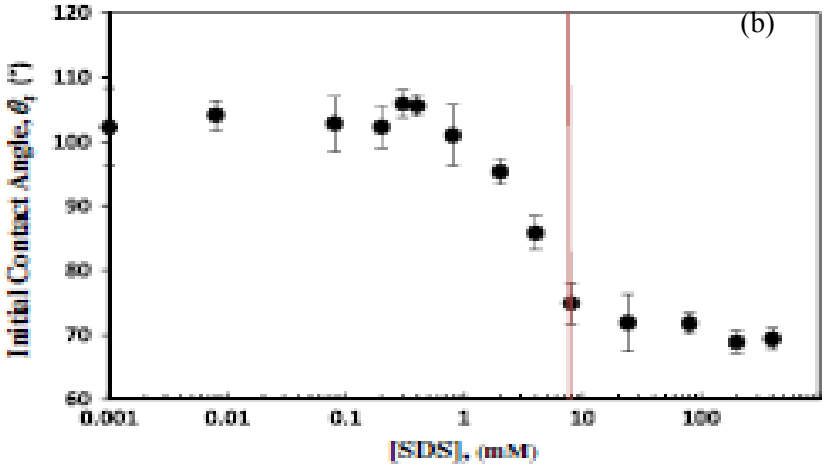

Fig 1.20: (a) Surface tension isotherms at 25ºC for SDS (b) the CWC in terms of the initial contact angle, redrawn from [70].

In addition von Bahr et al. [17] studied the spreading kinetics of aqueous ethanol and surfactant solutions. They found rapid spreading for aqueous solutions in the range of 30 microseconds due to imbalanced interfacial forces while in surfactant solutions, they found another slower spreading regime driven by adsorption and diffusion at longer time scales at the three phase contact line.

Chong et al. measured the wetting kinetics of trisiloxane surfactants with 6 and 8 oxyethylene groups at concentrations close to the critical aggregation concentration and the critical wetting concentration and three hydrophobic substrates with different surface properties, [37]. They found the spreading behavior depended on the hydrophobic/roughness properties of substrates, rapid spreading and complete wetting

were observed for both trisiloxane surfactant solutions at the critical wetting concentration on a substrate with a moderate hydrophobicity. For both highly hydrophobic Teflon AF and Parafilm substrates only partial wetting was found, their experiments also showed that the spreading behaviour over all substrates proceeded in two stages. At the critical aggregation concentration for both trisiloxanes on all substrates the time lag of the spreading was detected. The existence of large aggregates at low concentrations and relatively large spreading as during the initial stages of spreading were helpful for generating the Marangoni effect, but the Gemini structure did not show good spreading characteristics.

Lee et al.studied the spreading of surfactants over a thin aqueous layer in order to investigate the Marangoni force on spreading, [4]. They compared the behaviour of a series of trisiloxane surfactants and three different poly (ethylene glycol) mono-dodecyl ethers ($C_{12}E_4$, $C_{12}E_5$ and $C_{12}E_6$). They found a moving circular spreading front after depositing a small droplet of surfactant solution onto a thin water layer. The time evolution of the moving front could be subdivided into a rapid first stage and a slower second stage. They concluded that the surface tension gradient depended upon the existence of different types of surfactant aggregates influencing the transfer of surfactant molecules to the leading edge of the contact line. However, they found no link between these experiments and the superspreading process on hydrophobic substrates, since typically spreading is drastically reduced by using more hydrophilic, micelle-forming surfactants.

Zhang and Han carried out experiments using glucosamide based trisiloxanes on polystyrene surfaces to determine the influence of concentration over time, [10]. They used Dynamic Light Scattering (DLS) to study the role of surfactant aggregates on the spreading dynamics, and they found these surfactants showed super-spreading behaviour on hydrophobic surfaces however the spreading mechanism differed from that of ethylene oxide trisiloxanes. The existence of large aggregates at low concentrations and relatively large spreading areas during the initial stages of wetting is helpful for generating the Marangoni effect, but the Gemini structure does not show good spreading characteristics. In further work by Zhang and Han [154], they found the spreading area of glucosamide based trisiloxanes on polystyrene to be approximately 25 times the spreading area of water on the same substrate.

Radulovic et al. investigated the spreading behavior of two commercial superspreaders, [71]. They found that a non-ideal behaviour which was proven to be largely dependent

on the total concentration of the binary surfactant mixture and the hydrophobicity of the substrate on which it was spreading. They argued that steric problems as a result of differences in geometry of the surfactant molecules were the key factors and impurities present in commercial surfactants could play a major role in the performance of binary surfactant mixtures and as a result certain applications mixtures of trisiloxanes with conventional surfactant can be more efficient than trisiloxanes alone.

Rafai et al. carried out experiments to validate the occurrence of superspreading exhibited by trisiloxanes and also explain the interfacial behaviour observed during spreading [72]. They compared the spreading kinetics of droplets of three different systems; i) an aqueous solution of a commonly used wetting agent diethylhexyl-sulfosuccinate, ii) an aqueous solution of a superspreading trisiloxane, and iii) silicone oil with the same equilibrium surface tension and viscosity as the trisiloxane solution, and they found that the organic surfactant slowed down the spreading kinetics, whereas the trisiloxane had the opposite effect: where the spreading was accelerated compared to the reference system. They concluded that there was a difference in affinity for the solid substrate or the transport efficiency of surfactant molecules to the substrate was different.

Mourougou-Candoni et al. [73], used high-speed photographic technique to observe the impact of single drops of surfactant solutions on low energy substrates, and they concluded that the dynamic surface tension was the driving force for spreading of surfactant solutions and not the equilibrium surface tension.

And in addition Rafai et al. [3] analyzed the spreading dynamics for non-Newtonian fluids and surfactant solutions, and they found there was competition between capillary driving forces and viscous dissipation, which resulted in the dependence for contact line radius and time given by the known power law relationship which bore similarity to tanners law that describes the combined effect of capillary and derjaguin pressure (disjoining pressure) in the vicinity of the three phase contact line as a driving force.

Tang et al. investigated the wetting kinetics on lotus leaves and they found that the substrate was influential to the spreading of surfactant solutions, [49]. The composite interface formed on the dry surface while it formed a wetted interface when moist this was due to the two peculiar levels roughness of lotus leaf.

Weiss [36], Changera et al. [42] and Nikolov et al. [74], carried out experiments using trisiloxanes on hydrophobic solid surfaces and they reported that spreading occurred in three stages, they also measured the spreading area and reduction in surface tension and

found a relation between the changes in surface tension and increased spreading area. This observation has given credence to the importance of surface tension gradients to the superspreading phenomenon.

Kumar et al. [75] used adsorption kinetics to measure the rate constants from liquid-solid to the liquid-air interface, the constants were obtained by measuring the reduction in dynamic tension as the trisiloxanes adsorb onto an initially clean air/water interface using the pendant bubble technique. They suggested that the rapid rate by which trisiloxane solutions spread over hydrophobic surfaces requires either that the surfactant concentration at the perimeter be large enough to maintain a low contact angle forcing rapid spreading or that the concentration at the apex be greater than at the perimeter so that the higher tension at the perimeter pulls the drop out as a Marangoni force.

Ananthapadmanabhan et al. [76] studied the spreading behavior of several siloxane surfactants on Parafilm®, and they also observed a relationship between turbidity and spreading, but no dependence of equilibrium surface tension and spreading. They concluded that the structure itself of Silwet molecule plays a governing role in determining its superior properties. The spread area is defined as the area of a droplet at some fixed length of time (not always specified). The spreading area, however, is used in two distinct ways either as an estimate of spreading rate or it may be a measure of the extent of spreading.

Zhu et al. [77], measured the spreading rates of six different silicon based surfactants solutions on a hydrophobic surface; they found that the two soluble surfactants did not superspread; however, the insoluble ones did, and that, in the case of the superspreading insoluble surfactants, the spreading rate passed through a maximum with increasing concentration. They concluded that the Marangoni effect was responsible for the observed superspreading of the insoluble surfactant solutions

Hill [78], studied the interdependence of the maxima in spreading rate versus concentration and substrate surface energy as competitive processes rather than viscous dissipation. Two fundamental differences were observed between surfactant solutions and pure liquids: the first is the time dependence of the surface and interfacial tensions and the possibility of molecular orientation influencing interactions between the liquid and the solid.

In further work Nikolov et al. [79] studied the spreading of trisiloxane ethoxylates on hydrophobic leaf surface. They concluded that the driving force for spreading was due

to the Marangoni effect, and that the superspreading behavior of trisiloxane ethoxylates was a consequence of the molecular configuration at the air-water interface.

Stoebe et al. [80], studied the spreading dynamics of trisiloxane on mineral oils, and they concluded that the spreading rate was driven by surfactant delivery to the vapor-liquid interface. Wagner et al. [81], studied the spreading dynamics of trisiloxanes as a function of temperature, and they found that the spreading rate increased with increasing temperature and the phase transition corresponded to the maximum spreading rate.

Rosen and Wu [82], studied the spreading kinetics of surfactant mixtures on hydrophobic substrates, and they concluded that the spreading dynamics was driven by the surfactant with the more dominant properties in the mixture.

Chengara et al. [14] showed that the spreading of drops in the presence of a surfactant was driven by surface tension gradient mechanism, and they demonstrated a maximum in spreading as a function of the surfactant concentration. They argued that at low surfactant concentrations due to air–liquid interface depletion and diffusional limitation from the bulk to the interface, a difference in the surface tension between the contact line and the apex of the drop would be the driving mechanism for spreading. This surface tension gradient was caused by a difference in the concentration of the surfactant at the interface between the contact line and the apex.

Halverson et al. [21] carried out molecular dynamic simulations for wetting on hydrophobic substrates they found the spreading of $C_{12}E_4$ consistent with Young´s Equation but an inconsistent behaviour for trisiloxanes, and they concluded that the deviation was a result of the size of droplet (small), the timescales (long time scales) and the assumptions to depict the strength of interactions used in modelling.

Samsonov [83] simulated the wetting kinetics for simple liquids and agreed with the opinion of de Gennes that for simple liquids (non polymers) spreading corresponds to rolling motion mechanism while polymer liquids spread due to short term slippage. Further work by Samsonov and Ratnikov [84] carried out a comparative molecular dynamic study on the spreading of simple fluids and polymer nano droplets to understand the spreading mechanism. They concluded that the spreading of simple fluids corresponds rather to the rolling motion mechanism whereas modeling polymer droplets spread according to the slippage mechanism.

Shen et al. [85] applied the molecular dynamic theory to study the influence of surfactants on droplet spreading over solid surfaces. The simulation was performed

when the droplet in question was surrounded by a monatomic solvent. However, it was not clear why the solvent in question looked more like vapor, they assumed that the surrounding liquid had a lower density than the droplet.

Alla et al [86] carried out computer simulation for spreading of glycerol-water mixtures with and without surfactants on hydrophilic glass surface using a computational fluid dynamic model for deposited droplets. The model initially developed for large volumes where gravity effects cannot be neglected was modified for droplets, they took into account the evolution of droplet base and contact angle with respect to time, and their results found a good agreement with experimental data as the model was able to incorporate surface tension, droplet volume and wall adhesion phenomenon, their results corresponded to the power law and the value of *n* on the spreading regime (where *n* is the spreading exponent).

Shen et al. [87] studied the dynamics of droplet spreading by molecular dynamics simulation for two immiscible fluids of equal density and viscosity. All the molecular interactions were modelled by truncated Lennard-Jones potentials and long-range van der Waals forces were introduced to act on the wetting fluid. They gradually increased the coupling constant for the van der Waals interaction between the wetting fluid and the substrate, and they found a transition in the initial stage of spreading and a critical value of the coupling constant, above which the spreading was pioneered by the precursor film. In the regime of complete wetting the observed that the radius of the spreading droplet varied with time as $R(t) \sim \sqrt{t}$, a behaviour also found in molecular dynamics simulations where the wetting dynamics was driven by the short-range Lennard-Jones interaction between liquid and solid.

Holdich et al. [1] and Alla et al. [86] studied theoretically and experimentally the kinetics of the spreading of liquid drops over solid substrates with a liquid source from the center of the droplet, and they found an overlapping of two processes: a spontaneous spreading and a forced flow caused by the liquid source at the center, both capillary and gravitational regimes of spreading were considered and their power laws were deduced.

Starov et al. [49] described the spreading mechanism of aqueous surfactant solutions over hydrophobic surfaces as a slow transfer of surfactant molecules on the bare hydrophobic surfaces in front of the moving liquid on the triple phase contact line. They predicted the dynamic droplet radius and contact angle for a system where surfactant solutions spread over hydrophobic substrates. In the theoretical treatment an assumption

was made that the transfer of surfactant molecules onto bare hydrophobic substrate in front is the rate determining step.

Ruckenstein [88], developed a theoretical model that suggested that when the macroscopic spreading condition was not satisfied (i.e. non- wetting), sufficiently strong attractive interactions between the hydrophobic portion of the surfactant and the hydrophobic surface could trigger the spreading of the surfactant over the substrate. This would lead to a bilayer of surfactant migrating along the surface, with the hydrophobic portion of the second surfactant exposed towards air and the hydrophilic head to the first layer. This was in line with the conclusion that only bilayer-forming surfactants are superspreaders, but the major challenge is how to explain the fast kinetics of the spreading process.

Kabalnov [89], proposed an explanation of the thermodynamics of superspreading based on the competition between van der Waals' forces and the spontaneous curvature of the adsorbed surfactant molecules. The model for calculation of the spreading coefficient involved two main components: a) van der Waals component, which is similar to the spreading coefficient of the hydrophobic tail all by itself, and b) monolayer frustration component, which depended on the bending modulus and the spontaneous curvature of the surfactant film. The frustration term was minimized at a negative spontaneous curvature, i.e. above the cloud point of the surfactant. This postulation was in line with the behaviour of conventional surfactants such as ethylhexyl sulfosuccinate used in industry, being balanced surfactants having rather short and branched hydrophobic tails.

Churaev et al. [90] suggested that the spreading behavior of aqueous trisiloxane dispersions was a result of a disjoining pressure gradient created by the surfactant aggregates, and they proposed that thick wetting films stabilized by vesicles and electrostatic forces were the equilibrium shapes formed by the spreading process. They found a good correlation between experimental data obtained on an inclined surface and hydrodynamic calculations when the disjoining pressure was included. However this postulation remains debatable for conflicts of results obtained by Changera et al [14], since according to their calculations, the disjoining pressure created by the surfactant vesicles cannot be strong enough to drive a film up a vertical plate at the rate observed experimentally.

Beacham et al. [91] have modeled the spreading process using hydrodynamics and surfactant transport equations, taking into account potential contributions to the

superspreading process, i.e. Marangoni stresses, diffusion in the bulk and along the interfaces, surfactant aggregate disintegration, adsorption kinetics and disjoining pressure. The results obtained were highly sensitive to the kinetic rates at both the vapor-liquid interface and the solid substrate. Efficient spreading correlated with the ability to maintain a sufficient surface tension gradient at the leading edge of the droplet. They concluded that the key to maintaining a balance between adsorption at the edge of the droplet and replenishment of surfactant at the gas-liquid interface are the relative magnitudes of the interfacial parameters. The compact nature of trisiloxane molecules was thought to be more advantageous than the structure of conventional surfactants, but may not be the most important feature, considering the existence of both superspreading non organo-silicone surfactant mixtures as well as non-superspreading trisiloxane surfactants.

Venzmer and Wilkowski [11] studied the influence of the substrate hydrophobicity, concentration of the surfactant in solution, and ionic/nonionic character of surfactant on drop spreading. Taking evaporation losses due to relatively low humidity during measurements into account, they found that spreading on highly hydrophobic and moderately hydrophobic substrate was time dependent. Moreover, the results obtained indicate that spreading in the long-time regime was controlled by the diffusive transport of surfactant to the expanding liquid–vapor interface.

Sefiane et al. [92], analysed the force spreading dynamics of nano-particle suspensions of poly-disperse alumina particles in ethanol on hydrophobic substrates. They induced spreading by reducing the volume of droplet at a constant volumetric flow rate, the advancing/receding contact line velocity increased with increased concentration until a concentration with no observable change. They suggested that surface forces describing interactions between nanoparticles as well as various interfaces in the confined wedge dominated the dynamics of the contact line and the wetting behaviour.

Changera et al. [93] carried out equilibrium analysis on the spreading behavior of partially wetting nano fluids using the augmented Laplace Equation which considers the contribution of the structural disjoining pressure, they found that the restructuring of the nanoparticles in the wedge film that lead to the distortion of the three phase contact line.

Kondiparty et al. [94], extended the study on the equilibrium analysis for the wedge film by predicting a suitable combination of properties of nano-fluids such as concentration (volume fraction), particle size, contact angle, and capillary and hydrostatic pressure, where the nano-fluids completely wet the surfaces. They

concluded that the displacement of the contact line was proportional to nanoparticle concentration (volume fraction) and that spontaneous wetting was driven by structural disjoining pressure gradient.

Matar et al. [95], studied the spreading of nano fluid droplets on hydrophobic substrates by solving the mass and momentum conservation equation i.e. Navier-Stokes, applying the lubrication approximation where viscosity was dependent on particle concentration. They concluded that nano particle dynamics was driven by convective diffusion however no experimental data to compare this results are available.

Kralchevsky et al. [96], studied the dynamics of hexadecane drops in aqueous surfactant solutions on a glass substrate, and they concluded that the contact line velocity of the droplet was a function of the contact line friction.

Wasan and Nikolov [97], studied the spreading mechanism of the spreading dynamics of polystyrene dispersion using reflected light digital video microscopy, and they found that these particles arranged themselves into two dimensional crystal-like patterns which were also responsible for the micellar film formed in oil-on glass systems.

1.2 Evaporation

Evaporation is a physical process that can be described in simple terms as the reduction in volume of a liquid (in this case a sessile droplet in contact with a solid surface). The evaporation of a liquid drop is basically a simultaneous heat and mass transfer operation in which the heat for evaporation is transferred by conduction and convection from warm air to the drop surface from which the liquid is transferred by diffusion and convection back into the air. Droplet evaporation is a complex phenomenon driven by the difference in liquid concentration gradient in the presence of gas and solid phases [65, 87, 98-100]. The process is accompanied by the shrinking of the droplet base. Evaporation may alter the dynamics of the droplet spreading as compared with non-evaporating case through the corresponding changes of the radius of the base and the contact angle, [101]. Important technological applications of evaporation processes are drying in evaporation chambers of air conditioning systems, fire extinguishing, fuel and spray auto-ignition, [52], coating and printing applications, self-cleaning materials and for agricultural applications such as spraying of pesticides and foliar fertilizer delivery [55,87, 98-100]. Other applications are fuel injection into combustion engines, rapid cooling by drop wise heat exchange and snow formation for making meteorological estimates, [102], controlling the deposition of particles on solid surfaces an example is

in paint manufacturing where a variety of additives are used to ensure the pigments remain evenly dispersed in drying [49, 65, 101]. In addition drop evaporation can be used in the manufacture of novel electronic materials such as polymeric thin film transistors [102] or the assessment of hazardous volatile chemicals, cosmetics and other species, [102]. Evaporation is also important in biological particle manipulation an example is in analysing blood and DNA samples in disease diagnosis, [101]. From the theoretical point of view the investigation of evaporating droplets can reveal the influence of Derjaguin pressure in a vicinity of the apparent three-phase contact line, [103].

1.2.1 Coupling of Spreading and Evaporation

The spreading and evaporation of a liquid droplet are two processes that occur either concurrently or simultaneously in the liquid droplet in contact with a solid surface. Understanding the coupling of these phenomena is important in the application processes above mentioned. Spreading of droplets was a result of the loss energy in the droplet due to increasing droplet radius whereas evaporation is due to viscous flows between the droplet and space, evaporation begins at the point of transition from spreading/wetting when evaporation becomes more dominant, [5]. The physical properties of solid substrate influence the transition from spreading/wetting to evaporation. Hydrophobic surfaces with low surface energy are not easily wetted and the transition occurs relatively quicker as the droplet remains pinned for longer periods, the surface roughness plays an important role in the evaporating mechanism of droplets right after deposition because for small droplets gravity effects during deposition can be neglected, [27]. The concentration of surfactant in an evaporating droplet will also influence the transition from spreading to evaporation, there is a critical wetting concentration (CWC) above which the droplet will spread at the same rate regardless of an increase in concentration, [6, 11, 12, 47]. In terms of the contact angle and droplet line radius the transition takes place at the point where the droplet reaches its maximum contact radius L_0 and contact remains constant; the angle at the maximum contact line radius is called the receding contact angle θ_r, where evaporation becomes more dominant, [63, 87, 98].

The presence of contact angle hysteresis has made it difficult to determine exactly the point of transition from spreading to evaporation in droplets the transition is most consistent with theoretical prediction when the contact angle hysteresis is negligible

during evaporation, [103-105]. For aqueous surfactant solutions Rowan et al. found that the drying rate for all concentrations began to decrease at the hydration level which can be inferred as the transition from spreading to evaporation [66]. However, Erbil [98] and Lui [106] reported that the stick-slip motion of evaporating droplets was observed in various polymers, and concluded that weak interaction between the polymer and solid substrate was responsible for the weak pinning triple line.

The surface tension of the liquid and the surface energy were identified as important driving forces in the transition from spreading to evaporation. On non-homogenous substrates the liquid is more likely to wet along the lines of the pattern, into the grooves of the substrate or possibly disintegrate into smaller droplets [107]. Other physiochemical properties of evaporating fluids such as volatility, viscosity and particle size and distribution could influence the overlapping of wetting and evaporation. A liquid that is highly volatile will experience a continous decrease of the droplet contact line eliminating completely or reducing considerably the lifetime of the droplet when it remains pinned, typical examples are hydrocarbons. On another hand the viscosity which determines droplet velocity of a fluid has to be considerably low for the droplet to remain pinned, highly viscous fluids their droplet completely wet the solid substrates in micro seconds and it becomes impossible to analyze the dynamics, the high viscosity does not allow the droplet to reach some form of equilibrium with its substrate e.g silicon oil on mica and glass. The presence of dispersed particles in a fluid can also influence the transition or overlapping of spreading/wetting to evaporation; for instance an unevenly dispersed suspension will create a concentration gradient that will influence the dynamics of an evaporating droplet in the direction of the gradient.

1.2.2 Review of Experimental Literature on Evaporation of Droplets Pure Fluids

The importance of evaporation cannot be overemphasized as we have identified its numerous applications in engineering, medicine, agriculture and biology. Many investigations have been carried out to analyze and understand the mechanism of evaporation in a sessile droplet, and different parameters have been identified as being the driving force of evaporation regardless of the system. The available literature demonstrates that Marangoni effects, diffusion, temperature gradients, humidity and substrate structure strongly influence drop evaporation.

1.2.2.1 *Pure Liquids from Substrates without Thermal Gradient*

In this section we shall review literature on evaporating droplets from surfaces with no thermal gradient.

Cioulachtjian et al. carried out experiments to determine the influence of vapor pressure on the evaporation of the droplet, [44]. They found that the droplet remained pinned for most of the evaporation process in the saturated vapor while in the unsaturated vapor they were simultaneous changes in the contact angle and droplet contact radius.

Erbil et al. studied the evaporation simple liquids (butanol, nonane, toluene and octane) onto Teflon ^{TM}, without any heating of the substrate, and found that the three phase contact line did not pin on the surface for the duration of the evaporation of the droplets, [108].

Morse et al. studied the study of evaporation of small spherical droplets of iodine. They found a key result; that the rate of evaporation rate was proportional to the radius of the three phase contact line and not to the surface area. The proportionality relationship derived by Morse et al was analyzed by Langmuir using the analogy between diffusion and conduction heat transfer, it was found that rate of evaporation was proportional to the radius of the droplet spherical cap, [98].

Cazabat et al. studied the evaporation rate of drops of pure and completely wetting liquids characterized by very low contact angles (< 60), they did not observe the pinning of the droplet and showed that the observed dynamics was controlled by the volatility of the liquid and the properties of the wetting film on the substrate, the receding angle was directly proportional to the volatility and inversely proportional to the thickness of the wetted film, [98]. In addition to their work, Cazabat et al. studied the evaporation dynamics for water on glass and n-octane on Teflon [84], and they observed that evaporation for these droplets occurred in constant contact angle mode while the rate of evaporation was dependent on the initial contact line radius assuming the droplet remained spherical.

Erbil et al. also studied the evaporation of relatively large drops of water and *n*-decane on polyethylene, epoxy resin and Teflon, for saturated vapor atmosphere and in open air, [105]. They measured the evolution of contact angle, height and contact droplet radius with respect to time and found three distinct stages in the evaporation process.: In the initial stage, which corresponded to a saturated vapor atmosphere, the droplet base contact radius L, remained constant while contact angle, θ, and droplet height, h, decreased, the same is observed for a second stage which corresponded to a non-

saturated atmosphere however the evaporation rate increased. In the third stage, typical for smooth surfaces, the height, *h* and contact line radius *L* reduced concurrently at a constant contact angle and in the final stage all measured parameters tending to zero, the triple interaction becomes increasing unbalanced.

Lui and Bonaccurso analyzed the evaporation of micro-droplets of pure liquids and simple organic liquids using non-image analysis, [106]. They used the micro-cantilever sensor to measure the bending and resonance frequency during drop evaporation from which the mass of the droplet was determined, the droplet radius and contact angle using the inclination and resonance frequency data of the cantilever, and found that the evaporation mechanism was the same for micro-droplets and macro-droplets for water and simple organic liquids.

Li et al. studied the evaporation dynamics of single and multiple water microdroplets on self-assembled monolayer disulfides of gold substrates, [107]. They found that the static contact angle decreased linearly with time and found and for gold monolayers, the droplets remained pinned for longer periods increasing the rate of evaporation.

Kulinich and Farzaneh, studied the mechanism of evaporation in terms of contact angle hysteresis, [108]. They observed that the evaporation of small water droplets on homogenous super-hydrophobic surfaces, i.e. $\theta > 150^{o}$, with similar surface chemistry were observed to follow different modes depending on pinning ability of surfaces. Surfaces with low contact angle hysteresis were found to follow the evaporation model of other hydrophobic surfaces (i.e. quasi-static contact angle and constantly decreasing contact diameter for most of the evaporation time). However for surfaces with a high contact angle hysteresis they found behaviour in accordance with the evaporation model normally associated with hydrophilic surfaces (constantly decreasing contact angle and quasi-static contact diameter). Water droplets were observed to evaporate faster on the surface with high contact angle hysteresis, due to high values of contact angle $\theta > 90^{o}$ that were sustained on the low-hysteresis surface for much longer periods of time and the evaporation rate of such droplets becomes low due to the pinning of the droplet contact line. They found the saturation vapor was generated near the contact line which hindered evaporation. In contrast, drops on the high-hysteresis surface reached contact angles $< 90^{o}$ faster, and afterwards evaporation occurred over the entire water–air interface. The experimental data obtained compared well with the previous theoretical analysis of spherical cap drops evaporating in different stages.

Yu et al. studied the evaporation of sessile water droplet onto PDMS and Teflon surfaces, with the assumption that the droplet remained spherical with uniform concentration gradient across the liquid-vapour interface, [109]. They found that all experiments began with a constant contact radius regime, followed with a constant contact area regime and a final regime which was a combination of the preceding regimes. They compared their findings with theoretical solutions and they found consistency with experimental data.

Chena et al. studied droplet evaporation of volatile liquid droplets in nano-liter wells, [110], they presented three stages of droplet evaporation: constant baseline regime, constant contact angle regime and finally a mixed regime i.e. both contact angle and baseline reduce concurrently until the droplet disappears, and they concluded that the evaporation dynamics was driven by the interfacial force balance and the diffusion force and the evaporation rate was proportional to the diameter of the well.

Sefiane et al. investigated the evaporation dynamics of methanol and water droplets on silicon wafers and they observed the evaporation of sessile water droplet followed the conventional evaporation profile over time, unlike methanol which showed a constant reduction in contact radius with no regime of pinning [110].

Dawaleswarapu et al. have studied the evaporation of sessile water droplets on hydrophobic substrates [111], and they found the contact angle decreased gradually until a constant value was reached at the early stage of evaporation where the liquid–solid contact area remained constant. Later, the liquid–solid contact area gradually decreased while the drop shape and contact angle became constant for the remainder of the evaporation process except for a short time interval near the end of evaporation.

Lee et al. analyzed the evaporation dynamics of water on three different hydrophobic and superhydrophobic modified copper surfaces (Contact angles up to 159º) with coating of the same self-assembled monolayer material were experimentally investigated, [112]. They found the behavior of droplet evaporation was divided into three stages: Stage I (constant contact area stage), Stage II (constant contact angle stage), and Stage III (mixed stage i.e. simultaneous reduction of contact angle and droplet contact radius). They concluded that the occurrence of these stages was dependent on the level of hydrophobicity of the substrate because the consistency of the evaporation stage process diminished as the substrates became increasingly hydrophobic.

Sefiane studied the evaporation dynamics of water on aluminum and PTFE [113], and found that the droplets evaporated faster on aluminum than on PTFE and concluded thus: that the higher thermal conductivity of aluminum suggested that a large amount of heat used in the evaporation process was drawn through the substrate and that the higher contact angles measured on PTFE compared to aluminum showed that greater wetting angles lead to lower evaporation rates.

Anantharaju et al. studied the evaporation dynamics was investigated experimentally for both smooth and rough surfaces [114], and they found a stage of constant volume and three distinct stages of evaporation, first stage with a pinned triple line, a second stage with moving triple line stage and a third stage with simultaneous reduction of the contact line and contact angle. They found the evaporation rate to be higher on the smooth surface compared to the rough surface, the rough surface amplified the hydrophobic property of the substrate which resulted in higher contact angles and the evaporation rate constant was found to be higher in the stage with moving triple phase line.

1.2.2.2 *Pure Liquids from Substrates with Thermal and Concentration Gradients*

Other experimental and theoretical models have been developed to understand in depth the influence of temperature, concentration and surface energy gradients on the evaporation of sessile droplets. In this section we will go through a comprehensive review of these parameters as mentioned in literature.

Mollaret et al. studied the wetting and evaporation of a sessile droplet of water over heated substrates of aluminum and PTFE with different thermal conductivities and surface energies which led to different wetting and evaporation dynamics, [115]. They found that increasing the temperature reduced the surface tension and in effect reducing the Young unbalanced force pulling on the triple line.

It has been reported that Bernardin et al. studied the temperature dependence of the quasi-static advancing contact angle of water on aluminum surface and found two distinct temperature dependent regimes for low contact angle and high temperature regimes and high contact angles for low temperature regimes, [115].

Hegsethet al. studied droplet evaporation of water droplets and postulated that the internal flow in the droplet is driven by surface tension gradients that arose from the

non-uniform temperature on the free surface resulting from variations in the local evaporation rates in proximity to solid surfaces, [115].

Kim et al. investigated the temperature dependence of the quasi-static advancing contact angle of water on heated aluminum surface, [116]. They found two temperature dependent regimes: at temperatures below 120ºC relatively constant contact angles were observed, while at higher temperatures the reduction of the contact angle was linear and the volume was found to decrease linearly with time. Further work carried out by Kim et al. showed that during droplet evaporation there is a flow which is driven by surface tension gradients due to temperature differences on the free surface which leads to temperature gradients in the long scale.

Hua and Larson studied the evaporation of water droplets with a concentration gradient on polymer surfaces, [118]. They observed three distinct regimes of evaporation: constant area, constant angle and a third regime with decrease in both the contact angle and area. They concluded that the transition between the three regimes was due to Marangoni instability from the concentration gradient of solute along the gas-liquid interface.

Moroi et al. used the gravimetric balance to measure the kinetics of an evaporating water droplet over three phase system, [119].They found no difference in the evaporation rate and the activation energy in the air-water and air-surfactant solution interface, and concluded that the molecular surface energy did not interfere with evaporation.

Lee et al [53], Starov and Sefiane [120] analyzed numerically the effects of marangoni stress along the liquid-solid interface for an evaporating droplet. They showed that the temperature gradients in an evaporating droplet resulted in Marangoni stress and convective flows inside the droplet, and observed a temperature gradient between the liquid-solid and the liquid-gas interfaces.

Girard et al studied the connection between the local evaporation flux along the drop surface and the interfacial temperature, [121]. They showed that, in case of spontaneous evaporation of sessile drops, the evaporation is concentrated in a narrow area adjacent to the three phase contact line. This result justified the linear dependency of the total evaporation rate on the drop base radius instead of area, which is well confirmed by a number of experimental results. The interfacial temperature of evaporating drop showed a substantial variation along the surface, being lower at the apex of the drop and most of the drop surface, and sharply rises near the three phase contact line. These temperature

gradients could lead to thermo-capillary convection within the bulk of the drop. Infrared thermography technique has been used to study the contact line dynamic for droplets on heated surfaces. Temperature differences between the apex of the droplet and the contact line were observed to decrease in time, while the rate of local temperature increase at the interface was found to depend linearly on time. The slope of this linear trend increased with the substrate temperature.

Dunn et al. [122] proposed a mathematical model for the quasi-steady diffusion limited evaporation of a thin axisymmetric sessile droplet of liquid with a pinned contact line, they studied the dependence of saturated vapour pressure on the temperature of the cooled dropletet surface, but they did not consider Marangoni convection. The predictions of their model were in good qualitative, and in some cases also quantitative agreement with their experimental results. In later work Dunn et al. [123] found a strong influence of thermal conductivity of the substrate on the evaporation of a pinned sessile droplet. In this model they considered the buoyancy of water vapour in the atmosphere, and they used Newtonwater vapour in the atmosphere, andthe substrate on the evapthis introduced an empirical coefficient to the system of equations By choosing the value of that empirical coefficient they managed to reach the quantitative agreement between their computer simulations and experimental data.

Ristenpart et al. [124] studied the influence of the substrate conductivity on a reversal of Marangoni convection within evaporating sessile droplets. They neglected the heat conductivity of the air and used predefined distribution of evaporation flux over the droplet surface. Irrespective of the assumptions made, their quantitative criterion for the circulation direction was confirmed experimentally.

Craster et al. [125] studied evaporation of sessile droplets to ambient vapour using the kinetic model of evaporation. In this model they have taken into account Derjaguin (disjoining pressure including structural forces due to presence of nanoparticles in the liquid. The main purpose of their study was the understanding of the influence of nanoparticles concentration on the processes of droplets spreading and evaporation, and they found that the evaporative flux was not diverging at the three phase contact line, but was still at a maximum.

Crafton et al. [126] studied the evaporation dynamics of water and n-heptane droplets on heated aluminium and copper surfaces, and their results showed that the trends in the wetted diameter, height and contact angle for water droplets were fundamentally different than heptane droplets, and that the evaporation rates of n-heptane droplets

were an order of magnitude greater than the water droplets, the heat fluxes for the n-heptane droplets are approximately an order of magnitude less than the water drops.

Wayner [45], analyzed experimental data for the wetting dynamics of evaporating droplets of water on copper surfaces, and concluded that a change in the film vapor pressure was important to the profile of evaporation for a decrease in contact angle as the droplet radius remained constant.

Xu et al. [127], studied the evaporation dynamics of water droplet on highly conductive substrates, and they concluded that the marangoni driven evaporation depended on the thermal conductivities and and the ratio of the substrate thickness to the contact radius of the droplet.

1.2.3 Evaporation of a Volatile Liquid

Four stages of evaporation have been described by Bourges-Monnier and Shanahan [103]:

1.2.3.1 *Spreading (Stage One)*

A liquid droplet in contact with a solid surface will spread, this stage being characterized by a reduction in the contact angle θ and a corresponding increase in the contact droplet radius, L, in the same regimethe volume of the droplet remains constant, as shown in Figure 1.19. Spreading depends on the surface tension gradient between the droplet and solid surface interface. For highly hydrophobic substrates this stage is usually very short and the reverse the case for hydrophilic substrates. Substrates can be modified to increase or reduce the spreading potential of a liquid droplet in contact.

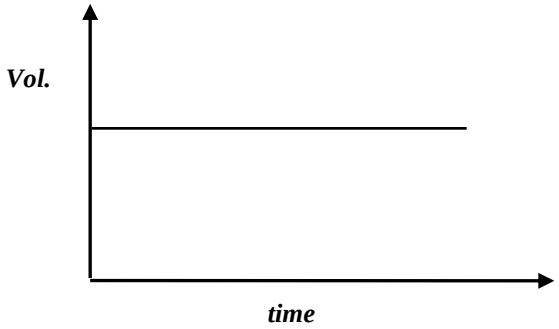

Figure 1.21: Spreading stage of an evaporation droplet with constant volume of an evaporating droplet.

1.2.3.2 *First Evaporation Stage (Stage Two)*

After the spreading stage, evaporation becomes the dominating mechanism, the contact angle decreases to the so-called advancing contact angle, θ_{ad}, and the droplet radius,L, remains constant (pinned droplet) while the droplet volume begins to decrease proportionally with time. The droplet remains pinned for as long as a balance of forces exist at the three phase contact line.

1.2.3.3 Second Evaporation Stage (Stage Three)

In this stage, the contact angle reduces until it reaches the so-called receding contact angle, θ_{red}, the contact droplet radius, L, begins to reduce as the droplet becomes de-pinned, and the volume continues to decrease. Depending on the surface energy of the substrate and thermal or concentration gradients within the droplet a stick-slip (alternate increase and decrease of contact line radius) movement of the contact line radius may be observed.

1.2.3.4 *Mixed Stage of Evaporation (Stage Four)*

In this final stage of droplet evaporation process, the droplet undergoes a simultaneous decrease in contact angle and droplet radius. The volume continues to decrease linearly throughout the evaporation and it is somewhat difficult to identify the controlling mechanism in this stage. These aforementioned stages of droplet evaporation are illustrated in Figure 1.20. The markers separate the stages 1, for spreading stage, stage 2 constant droplet base radius, stage 3 constant contact angle and stage for concurrent reduction in droplet base radius and contact angle.

1.2.4 Theoretical Description of the Evaporation Process

We will discuss briefly theoretical models that have been proposed in the literature to understand the phenomenon of evaporation of droplets from solid surfaces. Rowan et al. established that it would be inaccurate to make use of thermodynamic properties of a multi-component liquid for predicting the evaporation of a drop mixture on the basis of a pure liquid [128]. It is important to account for the interactions between the components to accurately predict the evaporation of mixtures. Doganci et al [129], described drop evaporation phenomenon as an extremely complex process occurring under natural conditions because the process is non-stationary, and occurs in a medium with unequal temperature and vapor concentration, and a convective circulation arises in the drop which prevents uniform temperature gradients. In addition, the heat transfer

between the medium and the drops takes place by three different mechanisms: conduction, convection and radiation. Thus, a number of simplifying assumptions have to be made by using a highly idealized model of the evaporation, process, and consequently the drop evaporation experiments should be made under conditions where the effect of some factors can be eliminated. "Quasi-stationary" drop evaporation and heat transfer were considered for the initial theoretical analysis, which means that the rate of the process at any given moment equals to the rate of the stationary process with the boundary conditions obtaining at that moment.

Borgues and Shanahan [105] proposed a model to describe the first stage of evaporation (where the droplet contact radius remains constant), and assumed that the diffusion of the vapor to the surrounding was radial. They defined the concentration gradient by

$$\frac{dC}{dt} = \frac{R_g C_{sat} cos\theta}{ln(1-cos\theta)} \frac{1}{R(R-Rcos\theta)} \quad 1.34$$

from which the evaporation rate is given by:

$$\frac{dV}{dt} = \frac{DA}{\rho L}\frac{dC}{dR}\Big|R_g = \frac{2\pi D R_g}{\rho L}\frac{cos\theta}{\ln(1-cos\theta)}\left(c_{sat} - c_{\infty}\right) \quad 1.35$$

Given that R is the radius of the sphere, R_g is the radius of the spherical cap, θ the contact angle, D the diffusion coefficient, A, is the liquid/vapor surface area, V is the volume of the droplet, ρ is the density of the fluid, c_{sat} the concentration in the liquid and c_{∞} the concentration of the bulk. They found a good agreement between experimental and theoretical results, and suggested using the model to estimate the diffusion coefficient.

Erbil et al. [100] used the analogy between diffusive flux and electrostatic potential to determine the evaporation rate of a sessile droplet which was approximately equal to the capacitance of an equiconvex lens of the same size. They obtained,

$$-\frac{dV}{dt} = \frac{2\pi D}{\rho L} C_x \left(c_{sat} - c_{\infty}\right) \quad 1.36$$

where C_x, is the capacitance, a variable derived from an analogy between the diffusive flux and electrostatic potential to determine the evaporation rate of a sessile droplet.

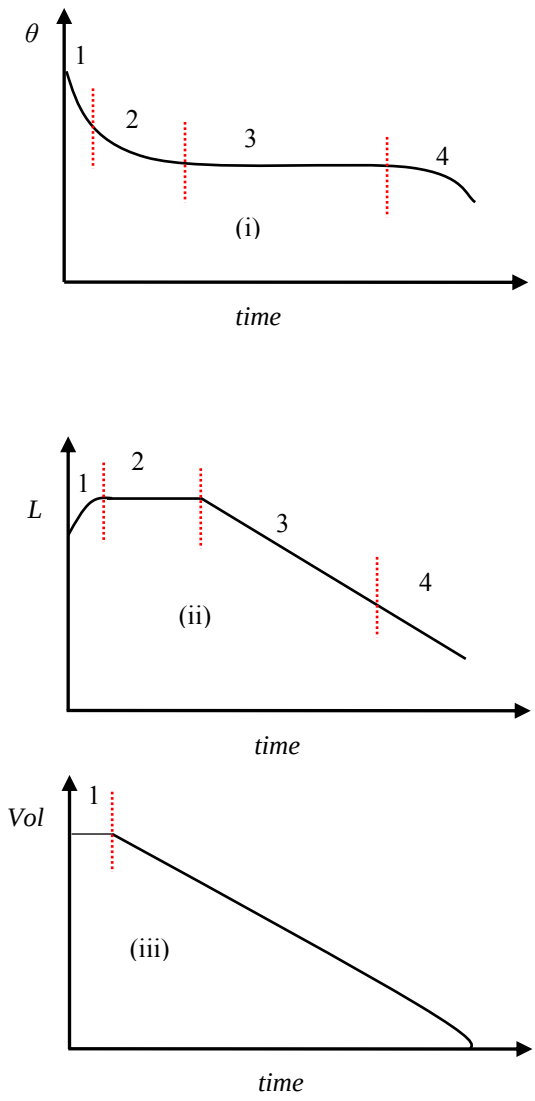

Figure 1.22: A schematic of the four stages of a sessile droplet evaporation for (i) contact angle, (ii) contact line radius (iii) and droplet volume as a function of time.

They formulated two polynomial expressions for large and small contact angles, taking the concentration gradient, *C(R),* of the vapor to be a function of *R*, they assumed that the atmosphere is saturated at *R*;

$$\frac{C}{R} = 0.63660 + 0.09591\theta^2 - 0.06144\theta^3 \quad \text{for} \quad 0 \leq \theta \geq 0.175 \qquad 1.36$$

and

$$\frac{C}{R} = 0.00008957 + 0.6333\theta + 0.1160\theta^2 - 0.08878\theta^3 + 0.01033\theta^4$$

f or $0.175 \leq \theta \leq \pi$ 1.37

In Figure 1.23 a schematic of this model is shown for two possible modes of evaporation, i.e. the constant base radius mode, and when the triple line is not pinned (constant contact angle), the evaporation rate is slow when the initial contact angle is high as shown in Figure 1.23 (a) , at slightly lower contact angles the evaporation rate increases with approximately the same magnitude in Figure 1.23(b), and at the lowest contact angle measured in these experiments the evaporate rate is fastest shown in Figure 1.23(c). The life time of the drop becomes shorter as the initial contact angle decreases.

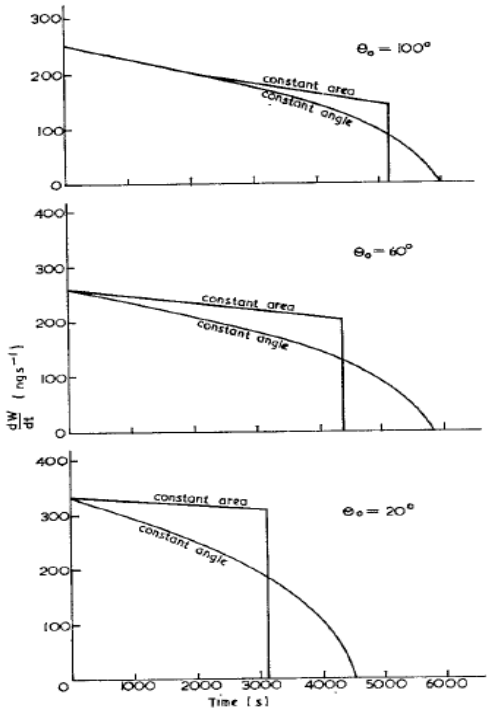

Figure 1.23: Theoretical evaporation rates for two modes of evaporation for methyl aceto-acetate drops onto goldsurface, redrawn from [83].

Hu and Larson [118] investigated the evaporation dynamics of a liquid droplet on a substrate, their droplets were small enough to have a spherical cap and a pinned contact line without heating and diffusion limited evaporation (quasi-steady state process). They developed a model for evaporation flux distribution along the liquid-gas interface using the finite element method (FEM) see Figure 1.24, to build the vapor concentration and evaporation flux. They observed that the evaporation flux was not uniform along the liquid-gas interface and became singular at the surface of the droplet. They show that

the expression for the evaporative flux developed by Deegan et al [104] fitted well the results. Given that

$$(\vec{J}.\vec{n}) = J_0\,(1 - \tilde{r}^2)^{-\lambda(\theta)} \qquad 1.38$$

J being the evaporation flux, $\vec{n}$ the flux vector along the surface ,J_0 the evaporation flux at the apex of the droplet, $-\lambda(\theta)$ a fitting parameter representing the non-uniformity of the evaporation flux along the interface, and $\tilde{r}$ the ratio of the radial position along the droplet to the contact line radius i.e *r/R*. For initial contact angles lower than 40º, the finite element method (FEM) analysis showed the evaporation rate was almost constant, represented by the expression below;

$$J(r,t) = \frac{Dc_v(1-H)}{R}\,(0.27\theta^2 + 1.30)(0.6381 - 0.2239(\theta - \tfrac{\pi}{4})^2(1-\tilde{r}^2))^{-\lambda(\theta)} \qquad 1.39$$

Where θ is the contact angle, D is the vapor diffusivity, c_v the saturated vapour concentration, H relative humidity, and t time.

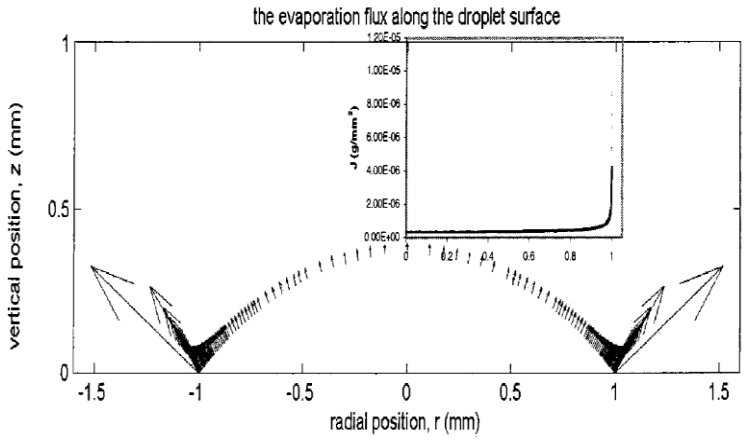

Figure 1.24: Distribution obtained by FEM analysis of the evaporation flux along the upper surface of the drop and the insert shows the magnitude of flux, redrawn from [117].

Guena et al [102] developed a hydrodynamic model to describe the advancing or receding dynamics of liquid edges on solid substrates based on the assumption of stationary diffusion driven evaporation proposed by Deegan et al [104]. The evaporation flux *J (r,(R(t))* at the free surface of an isothermal drop with a radius R, at a distance r from the droplet axis and for small contact angle, was given by

$$J(r,T) = \frac{J_0}{\sqrt{R(t)^2 - r^2}} \qquad 1.40$$

The evaporation parameter is known for a given liquid at a given temperature, the local evaporation flux diverges at the contact line but the evaporation rate for the total drop volume *V(t)* is given by

$$\frac{dV(t)}{dt} = 2\pi J_0 R(t) \qquad 1.41$$

Applying the conservation equation written at the distance *r* from the center of the drop, *h*(*r*, *t*) being the local thickness, *R*, the droplet base radius and U, the contact line velocity. Assuming *J*(*r*, *t*) is the evaporation flux per unit area of the substrate

$$\frac{\partial h}{\partial t} + \nabla(hU) = -J(r,t) \qquad 1.42$$

Averaging the velocity over thickness, and in the case of thin films the equation can be rewritten as

$$U(h,t) = \frac{h^2}{3\eta}\nabla\left(\lambda\triangle h - \rho g h + \prod(h)\right) + \frac{h}{2\eta}\nabla\gamma \qquad 1.43$$

where η is the viscosity of the liquid, γ the surface tension, ρ the density, g the acceleration of gravity and, $\Pi(h)$ is the disjoining pressure for the case of thin films. Neglecting gravity and surface tension gradients in the local velocity, the conservation equation. is rewritten as

$$\frac{\partial h}{\partial t} + \nabla\left[\frac{h^3}{3\eta}\nabla(\gamma\Delta h + \prod(h))\right] = -\frac{j_0}{\sqrt{R^2 - r^2}} \qquad 1.44$$

Equation 1.43 can be rescaled and using the maximum radius R_0 as the characteristic length, the corresponding angle θ_0, the characteristic thickness given by $R_0\ \theta_0$ and the characteristic time $\frac{R_0^2\theta_0}{j_0}$. Equation 1.44 is controlled by two dimensionless parameters:

a) the capillary number, C ,which is a variable that is a ratio of the liquid viscosity and evaporative flux with respect to the surface tension, maximum radius and corresponding contact angle, b) and van der Waals number, κ, which is a ratio of the Hamaker constant to the surface tension, maximum radius and corresponding contact angle.

$$C = \frac{3\eta j_0}{\gamma R_0 \theta_0^4} \qquad \text{and} \qquad \aleph = \frac{|A|}{6\pi\gamma\ R_0^2\theta_0^4} \qquad 1.45$$

Assuming there is no divergence of the evaporation flux for the profile described by Eq.

1.40, and the maximum value of the flux is reached at some distance l ($\approx a\theta^{-2}$) from the contact line, a being, the molecular length and that $\frac{dR}{dt} = 0$ for $R=R_0$, one obtains

$$\frac{dR}{dt}\theta - \frac{\gamma}{3\eta}\theta^4 \approx \frac{J_0}{\sqrt{2Rl}} \approx \frac{\theta J_0}{\sqrt{2Ra}} \qquad 1.46$$

The model is controlled by one non-adjustable parameter, the capillary number. It accounts for the power laws for droplet contact radius and contact angle, and also predicts accurate exponents for the size of droplets considered. The Wedge model captures the main characteristics of the physical processes, although an intermediate length scale is required for very small contact angles.

1.2.5 Review of Evaporation of Mixtures

Different wetting and evaporation mechanism have been observed in binary mixtures of volatile liquids and water, and it has been found that the mechanism is modified with respect to pure fluids due to the different volatilities of the fluids. The behavior of mixtures is unique in the sense that it is affected by the individual components and their inherent properties. In this section we present an overview of experimental analysis for evaporating liquid from solid surfaces.

Chandra et al. [130] and Marzo et al. [131] analyzed the dynamics of for aqueous surfactant solutions and found that the surfactants increased the heat transfer area and in the same process reducing the contact angle from 90º to 20º, which has important consequences for industrial processes. They also investigated the effect of sodium dodecylsulfate, (SDS), surfactant on the diffusion controlled evaporation rate of aqueous solutions on Teflon substrates, over a wide range of concentrations and found a reduction in the contact angle due to adsorption of SDS at the liquid-air and solid-liquid interfaces. The adsorption rate at the solid-liquid interface was much higher than that at the liquid-vapor interface, whereas the evaporation rate was not altered by the concentration however increasing the surfactant concentration of identical initial volumes resulted in a thinner droplet with a larger base diameter as seen in Figure 1.25. This lead to larger heat transfer areas and heat transfer distribution.

Doganci et al studied the evaporation of SDS solutions on to Teflon substrates over wide concentration range, [129]. They found that the adsorption of SDS at the solid-liquid interface was significantly larger than the liquid-air interface, and they concluded that the addition of surfactant did not alter the evaporation rate, although it influenced

that mode of drop evaporation with regard to the expected profile of droplet evaporation, i.e. constant droplet radius mode and constant contact angle mode.

It has been reported that Rafailovich et al. monitored the drop evaporation of methanol, ethanol, butanol, acetone and water on octadecyltrichlorosilane covered silicon surface, Teflon, parafilm and poly (di-methyl-siloxane) substrates, and concluded that the diffusion is mainly controlled by the diffusion of the liquid and is not sensitive to temperature and liquid composition, whereas the evaporation enthalpy, ΔH_{vap}, regulates the drop evaporation, [132].

Duursma et al. investigated the evaporation and sliding of water droplets on smooth and nano-scale rough fluoro-alkylsilane coatings having chemical heterogeneity [133]. The behavior of evaporating droplets on these two coatings were nearly identical for microliter scale water droplets; however the behavior was different when nano-liter scale droplets were used. The evaporation behavior of nanoliter scale droplets was affected by nano-scale surface heterogeneity.

They suggested that this effect was due to line tension effects at the three-phase contact line of these small droplets having larger Laplace pressure inside, and depended on both the period for the pinning of the three-phase contact line and the degree of droplet shape change.

Cheng et al. experimentally studied water-ethanol mixtures on gold substrates [134], and they found that the contact angle of the water-ethanol mixture decreased as the concentration of ethanol in the binary mixture was increased, the contact angle decreased from about 110º at low concentration to less than 40º for the highest concentration shown in Figure 1.26a. They also observed that the water-ethanol mixtures experienced an increase in contact angle after droplet deposition on the solid surface, the increase in contact angle is as a result of the rearrangement of molecules along the three phase contact line and the rapid evaporation of the more volatile methanol, this increase in contact angle is accompanied with a decrease in the solid-liquid contact area shown in Figure 1.26b. They suggested that this movement of the three phase contact line could also be due to surface tension. The contact evaporation area is also observed to increase as the concentration of the binary mixture moves from pure fluid to highly concentrated in Figure 1.26c which is consistent with the reduction of contact angle shown in Figure 1.26a.

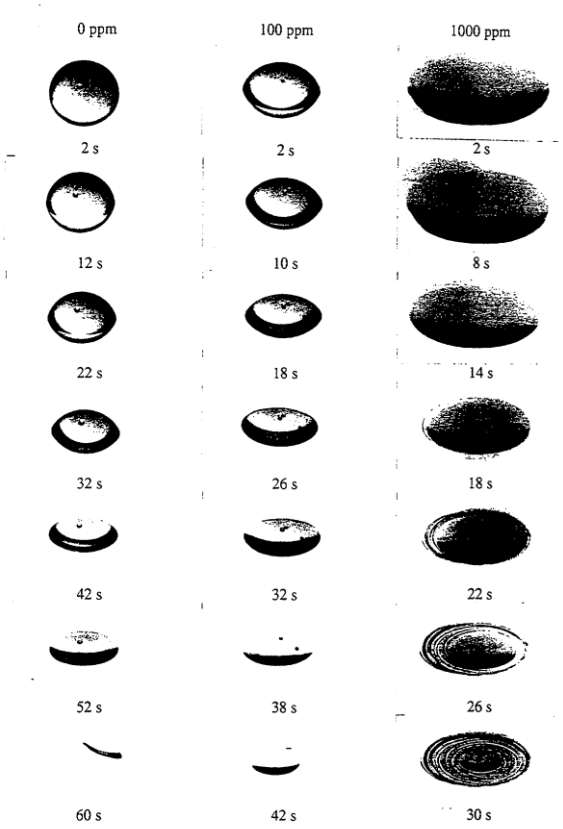

Figure 1.25: Evaporation of three water surfactant solutions SDS (0 ppm, 100 ppm and 1000 ppm) deposited on stainless steel surface at 80ºC, redrawn from [131].

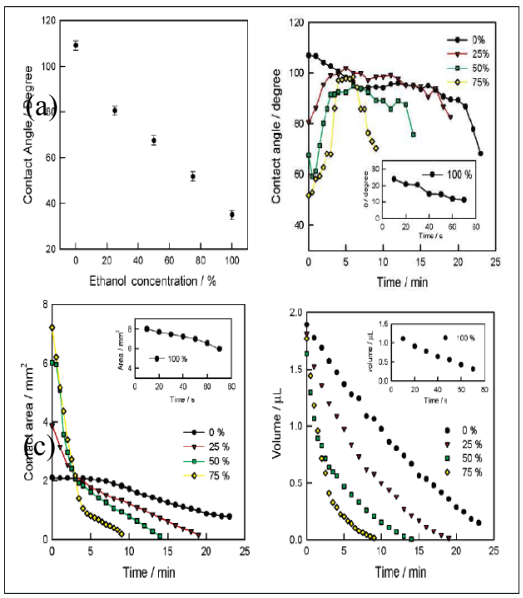

Fig 1.26: Evaporation of water-ethanol mixture from gold substrates, showing the dependence of (a) contact angle and concentration, (b) contact angle time,(c) contact area time, and (d) volume-time, redrawn from [134].

The reduction in volume is also consistent with the volatility of the mixture, in other words the more concentrated mixture has the highest evaporation rate as ethanol evaporates faster than water, shown in Figure 1.26d. The figures insert depict the behaviour of pure water to be able to compare and analyze the magnitude of deviation with respect to change in concentration of ethanol.

Sefiane et al. also studied binary mixtures of water-ethanol, [135]. They measured the contact angle, droplet base radius and droplet volume, and found that the evaporation process occurs in three stages; a first stage that corresponds to rapid evaporation of the more volatile component (A), a second regime in which there is intermediate regime is a competition of evaporation of between the components (B), and a third regime where the less volatile component clearly dominates (C). A schematic description is shown in Figure 1.27, the stages A, B and C correspond to the regions 1, 2 and 3 in Figure 1.27.

Birdi et al. studied the evaporation dynamics for an ethanol-water system for different concentrations onto polymer coated substrates and smooth silicon in saturated conditions, they measured the time evolution of the contact angle, contact line radius and droplet volume [67].They found that there was competition between evaporation and hydrodynamic flow. Their experiments showed a first regime with the evaporation of the more volatile ethanol in the droplet, the second regime was dominated by the less volatile water component. The presence the volatile ethanol was observed in the droplet after the first regime and it contributed to the wetting behaviour of the droplet mixture. They concluded that the mechanism that controlled the evaporation of such liquid mixtures were diffusion in the liquid phase and accumulation of the volatile component closer to the contact line.

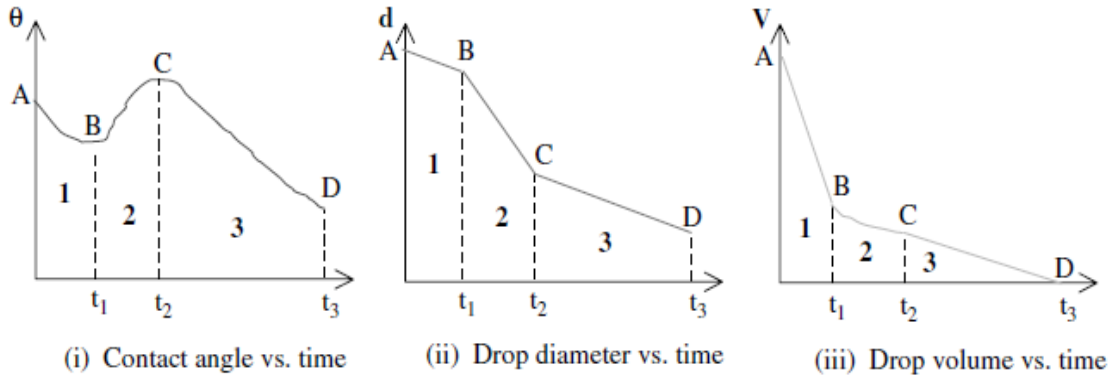

Fig 1.27: A schematic sowing the evaporation dynamics for a water ethanol mixture onto polymer surfaces, redrawn from [135].

Sefiane [113] carried out studies for the evaporation of surfactant solutions (Triton-X) onto PFTE and aluminium substrates, for various concentrations of the surfactant under different low vapor pressures. They found that the maximum overall evaporation rate occurred at constant surfactant concentration. They suggested that surfactant distribution on the liquid–vapor interface, and its accumulation near the triple line played major roles in the wetting and evaporation processes. The Marangoni effect caused by surfactant accumulation near the triple line was introduced to explain the depinning behavior of droplets at low surfactant concentrations. They also concluded that the higher thermal conductivity of aluminum shows that a large amount of is heat used in the evaporation process and is drawn from the substrate and the higher contact angle on PTFE indicates that larger wetting angles lead to lower evaporation rates.

Gokhale et al. [136], studied the advancing and receding contact angle for evaporating droplets of surfactant solutions (poly-alkyleneoxide- modified heptamethyltrisiloxane) on silica substrates under isothermal conditions. They observed that the surfactant formed a stable adsorbed film of reasonable thickness, and that during evaporative phase change, the adsorbed film broke into microdrops, which were surrounded by a different, stable, thin adsorbed film.

Zhu et al. [77] studied the spreading and evaporation dynamics of silicon based surfactant solutions on hydrophobic substrate and they found an overlapping of wetting and evaporation which resulted in an un even evaporation pattern.

The evaporation dynamics for azeotropic mixtures was studied by Rowan et al. [128]. For mixtures above the azeotropic point the contact angle decreased throughout the process of evaporation while the contact line radius remained pinned for approximately two-thirds of the process. For mixtures below the azeotropic point the drop became unstable with a distorted perimeter. The droplet dissociated into several droplets with even higher contact angles, and the contact angles subsequently reduced as evaporation progressed in the droplet.

Lui et al. [137] studied the evaporation of water-ethanol mixtures for droplets in a controlled environment at a fixed relative humidity, and found that the ethanol condensed onto pure water drops or drops of binary mixtures of different compositions, and this depended on the vapor pressure and the mixing ratio of the mixture and they also found a reduction in evaporation time.

Guena et al. studied different scenarios possible for evaporation of mixtures of binary alkanes onto silicon substrates, [138]. They concluded that the dynamics of evaporation was controlled by surface tension gradients and the influence of the volatility was dominant when unequal volume compositions were used.

The experimental results and theories previously discussed herein relate to evaporating volatile droplets for pure fluids and mixtures where neither the chemical composition nor volatility of one or both components of the mixtures has been the driving force for their evaporation. The evaporation dynamics follows a first stage of decreasing contact angle and constant contact radius and a second stage characterized by a decreasing contact radius and constant contact angle. The volume of the droplet decreases linearly with time indicating that the evaporation is diffusion controlled. For mixtures of surfactant solutions where the volatility of the solution is negligible with respect to the evaporation dynamics it becomes imperative to understand how parameters such as concentration of the surfactant, substrate surface and adsorption of surfactant molecules at the solid-liquid interface of the evaporating droplet influence the evaporation dynamics the of droplets. The influence of physical properties such as temperature and relative humidity can also determine the mode and rate of evaporation, and thus also require more understanding. The droplets considered are small enough to neglect the influence of gravity. In the preceding chapter we will propose a theoretical model to explain evaporation dynamics where there is an influence of the interaction at the solid-liquid interface and temperature gradients on evaporation.

1.2.6 Review of Evaporation profiles for Nano-particle Suspensions

When nano-particle dispersions or colloidal suspensions evaporate from a solid surface the pattern formation at the contact line is a result of the evaporation dynamics. Deegan et al. emphasized the importance of the study of the coffee ring formation which remained an intriguing subject over the years. Controlling the distribution of solute in the process of drying is important to numerous industrial and scientific processes. The coffee ring effect can be described as the rearrangement of solute particles usually from an evenly distributed solution to form a ring line structure of deposited particles, [104]. The understanding of pattern formation has wide applications in medicine for instance in DNA and blood analysis where the pattern formed after evaporation of blood samples is used to diagnose ailments. In paint manufacture several additives are used to ensure

the pigment is evenly dispersed and remains the same during drying; also in protien crystallography where evaporation driven convection is used to assemble two dimensional protien crystals, [101].A schematic of the coffee ring effect is shown in Figure 1.28.

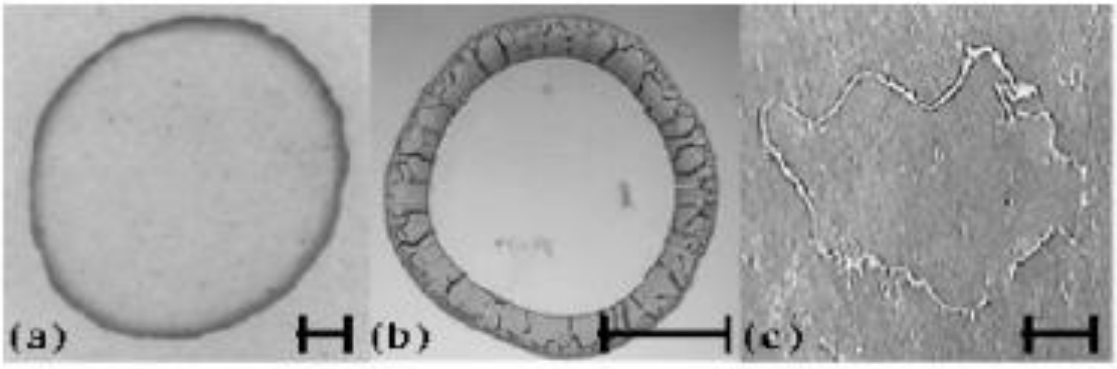

Figure 1.28:(a) Coffee stain, (b) Dried colloidal microsphere and (c) Salt deposit, the scale corresponds to 1cm, redrawn from [101].

Sefiane reported the pattern formation in blood samples and the changes in blood fluidity were determined by rheological factors such as the plasma viscosity, erythrocyte aggregation tendency, adhesion properties of platelets and leukocytes as well as composition and concentration of the plasma components. The structures formed at the liquid- solid interface structures are formed by the molecules and, mainly, by micro-aggregates of organic and mineral substances dissolved in the bio-liquid, [101]. The structure-specific peculiarities were defined by general physicochemical properties of the bio-liquid, quantitative and the qualitative composition of molecules of the given substances, and their ability to establish intra- and inter-molecular chemical bonds, see Figure 1.29. As a result, the bio-liquid structure carries integral information on the metabolism status of the organs washed by the bio-liquid and on the homeostasis of the body as a whole.

There are several complex patterns and their underlying mechanisms involve a number of interrelated processes such as precipitation, crystallization and gelation. Despite the preliminary application of the pattern-forming phenomena to practical medical diagnostics, fundamental understanding of the dehydration self-organization in biological and chemical fluids is still lacking.

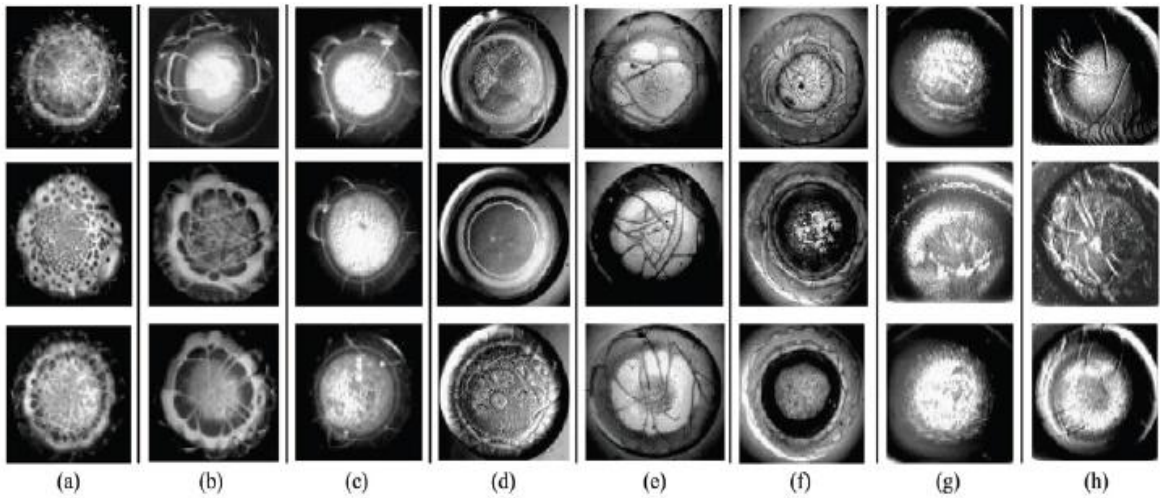

Figure 1.29: The morphological features of dried drops of serum in norm and different diseases or physiological states [101].

Deegan et al. [104] first showed that the ring was produced because the contact line remained pinned, and so the amount of solvent lost due to evaporation at the droplet's edge was replaced by solvent drawn from the center of the droplet. The driving force of flow that brought fluid from the center to the edge of the droplet also carried solute, which was deposited in a ring at the edge as the solvent evaporated. They also reported exploratory experiments using variety of liquids and dispersed particles, and observed ring like structure for partially wetting fluids. A broad range of surfaces (hydrophylic to hydrophobic) and solutes were used; they also varied the environmental conditions extensively and found no distortion to the ring structure. They developed a theory with the main idea that a pinned contact line induced an outward radial fluid flow when evaporation occurred at the droplet edge. They consider an axisymmetric drop where the conservation of fluid determines the relationship between the radial flow v, the position of the air liquid interface $h$and the rate of mass loss per unit surface area per unit time from the drop by evaporation J_s. The rate of change of amount of fluid at a radial distance r from the centre of the drop is the difference between the net flux of liquid into the column and the amount of mass evaporated from the surface element, where t and ρ are the time and density, respectively.

$$\rho \frac{\partial h}{\partial t} = \rho \frac{1}{r}\frac{\partial}{\partial r}(rhv) - J_s(r,t)\sqrt{1+\left(\frac{\partial h}{\partial r}\right)^2} \qquad 1.47$$

Solving for v by integrating the expression in 1.47, they obtained

$$v(r,t) = \frac{1}{\rho r h}\int_0^r dr\, r\left(J_s(r,t)\right)\sqrt{1+\left(\frac{\partial h}{\partial r}\right)^2} + \rho\frac{\partial h}{\partial t} \qquad 1.48$$

From this it is found that a non-zero v arises when there was a mismatch between the local evaporation rate and the rate of change of interface.

For the case where the limiting rate was the diffusion of the liquid vapour, they assumed that the evaporation of the drop rapidly attained a steady state so that the diffusion equation reduced to the Laplace Equation, given by

$$\nabla^2 u = D\partial_t u \approx 0 \qquad 1.49$$

where u represents the mass of vapour per unit volume of air and *D*, the diffusion constant for vapour in air. This assumption was valid for long times with the following boundary conditions: (1) along the surface of the drop the air is saturated with vapour and u_s is a constant, (2) the flux normal to the substrate ($J.n = -D\partial_n u$) is zero because the vapour does not penetrate the substrate and (3) u converges to the ambient vapour concentration u_∞ far from the drop. and this leads to;

$$J_s(r,t) \approx J_0 f(\lambda)[1-(r/R)^2]^2 \qquad 1.50$$

The velocity of the solute onto the solid surfaces were computed from the combination and manipulation of Eqs. 1.47-1.50 and they concluded that, the ring formation for an evenly distributed solute was dependent on the velocity of propagation of the particles, and the distance to the periphery of the droplet determine ring formation on solid surfaces.

Following this Hu and Larson [139] showed that particles of poly-methyl methacrylate had an affinity to deposit in the centre of an octane droplet, the same affinity was observed for mica flakes in octane, the difference in deposition patterns was as a result of flow fields in water and octane droplets ash shown in Figure 1.30.

To better understand this phenomenon they developed an evaporation model where they demonstrated that the momentum, mass, and heat transfer in the slowly evaporating droplet can be treated as quasi-steady processes in small, slowly drying droplets. Because of small Capillary and Bond numbers, the surface of the evaporating droplet with a pinned contact line can be regarded as a spherical cap and neglecting heat transfer in the radial direction they obtained an approximate analytical solution for the surface temperature as a function of radial position. This allowed them to conclude that

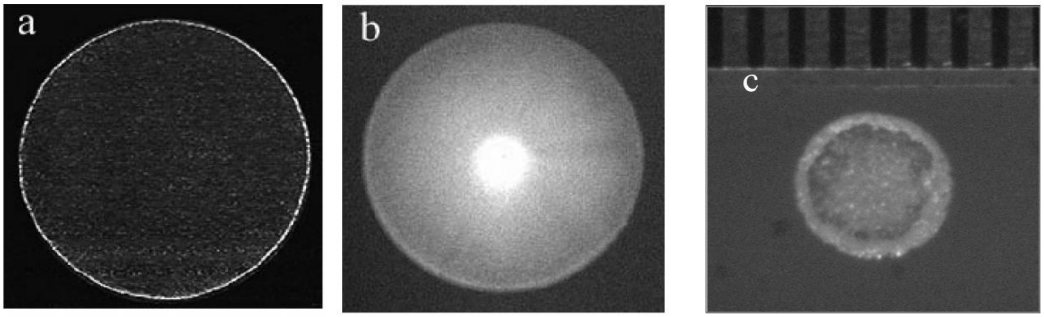

Figure 1.30: (a) Ring deposition pattern of fluorescent polystyrene particles on glass (b) octane droplet containing PMMA particles deposited on a glass coverslip coated with PFLA. (c) The same as part b except the particles are mica flakes on cover glass, redrawn from [139].

the coffee-ring phenomenon required not only a pinned contact line, particles that adhere to the substrate, and high evaporation rate near the droplet's edge, but also that the Marangoni effect resulting from the latent heat of evaporation had to be suppressed.

For a suspension droplet dried on a glass surface the particles collected near the edge of the droplet boundary (contact line), and often left a striped pattern as the droplet evaporated. During drying, the motion of the droplet contact line resembled the stick-slip motion and it shrunk toward the center in an oscillatory motion. To explain the oscillatory motion and the mechanism of the stripe formation, Adachi et al. formulated a mathematical model that included a force of friction at the contact line observed when particles flowed from inside the droplet to the boundary of the droplet, [140]. As a result of competition between the frictional force and surface tensions at the contact line, the droplet oscillates as it dried and a striped film composed of particles was generated.

In further work Deegan [141] studied the evaporation of sessile drops and the resulting ring stain formation from a drying suspension and water droplets onto mica substrate under ambient conditions. They found that the ring formation was due to capillary flow driven by the fact that most of the evaporation occurred at the contact line

The behavior of mono disperse nanoparticle suspension in low pressure environment was studied by Askounis et al, [141]. They found that lowering the vapor pressure resulted in a variety of patterns (i) an aggregation of particles in one direction which confirmed the presence of the stick-slip regime, (ii) the formation of unique rings that represent a constantly pinned triple phase line and (iii) irregularly shaped deposit with higher particle accumulation at the edge of the droplet and is characteristic of rapid evaporation.

Shmuylovich et al. studied microliter droplets of water containing latex particles [142], and they found a succession of pinning and depinning of the contact line that was responsible for multiple ring formation and the pinning of the contact line depended on the concentration of particles at the droplet edge.

Bhadwaj et al. resolved the axisymmetric, two-dimensional flow field in the drop via numerical solution of the Navier–Stokes Equations coupled to the energy equations in the drop and in the underlying solid substrate, [143]. The diffusion of vapour in the atmosphere was also solved numerically which provided an exact boundary condition for the evaporative flux at the free surface, while the particle concentration was tracked by solving a continuum advection–diffusion equation. The interaction of the liquid–air interface with the peripheral deposit of colloidal particles, depinning and receding of the contact line were simulated by the authors. The formation of different deposit patterns obtained experimentally was explained well by their simulations.

Brunett [144], studied the drying of colloidal suspensions on micro-pillar water repellent surfaces and found a complex structure similar to the classical „„coffee-ring'', showing tiny deposits on outwards of the main ring. The drop was impaled onto the texture and was strongly pinned at the contact-line; tiny deposits occurred while the drop still remained on top of pillars in a Cassie-Baxter state. These experiments were carried out using non-volatile and UV-curable liquid, the presence of these deposits was the direct consequence of the weak but finite pinning force on the surface, which lead to the retention of small liquid droplets and after drying of these droplets to the deposition of the inside colloidal particles. Therefore, the volume distribution of these deposits is ruled by complex hydrodynamics processes: local pinning of contact-line, stretching, pinch-off of a liquid bridge and detachment of liquid. In addition to these effects, the presence of particles at relatively high concentration influenced the pinning force on each post.

Thiele et al. [145], developed a hydrodynamic model to describe the pattern formation of film of a liquid suspension of nanoparticles or a polymer solution deposited on a surface. They proposed that the dispersion may dewet on the surface and as the solvent evaporates the solute particles/polymer can be deposited on the surface in regular line patterns. The hydrodynamic was based on a long-wave approximation that predicts the deposition of irregular and regular line patterns due to a self-organized pinning–depinning cycle that resembles a stick–slip motion of the contact line. They concluded that the line pattern properties depended on quantities such as the evaporation rate, the

solute concentration, the Peclet number, the chemical potential of the ambient vapour, the disjoining pressure, and the intrinsic viscosity.

Chen and Evans [146] studied the drying of a colloidal dispersion on super-hydrophobic substrates (copper modified with perfluorooctyl-triethoxysilane), and they concluded that the „œoffee ring' effect was modified if the contact angle was high enough to restrict the rate of evaporation adjacent to the three phase line of a sessile drop, as occurs on a super-hydrophobic surface.

Yanan Gan and Li Qiao [147] studied the the effect of added aluminum nanoparticles on the evaporation characteristics of fuel droplets were investigated under both natural and forced convections and they measured the evaporation rate by considering various base fuels, at varying particle concentrations and at convective flow temperatures. They concluded that the continuous decrease in droplet evaporation rate was a result of particle aggregation inside a vaporizing droplet, a rather slow process under natural or weak convection when the droplet lifetime was longer or comparable to the characteristic aggregation time, larger aggregates are formed during the droplet evaporation process, which could inhibit diffusion and thus reduce the evaporation rate.

Nanda et al. [148] studied the size-dependent evaporation of free-spherical PbS nanoparticles by in-flight sintering of size-classified aerosols. The temperature at which the particle size decreased due to evaporation was found to be size dependent and decreased with decreasing particle size. A linear relationship between the evaporation temperature and the inverse of the particle size was obtained as seen with size-dependent melting of nanoparticles and shows the presence of the Kelvin effect and allows one to estimate the surface energy of nanoparticles.

Kajiya et al. [149], studied the concentration field of an evaporating droplet of florescent polystyrene anisole dispersion by fluorescence and lateral profile measurement, and they found that a strong region of concentration was created in the vicinity of the of the contact line in an early stage and the concentration of polymers in the central region remained constant for the duration of evaporation. They concluded that particle deposition was a result of outward flow of fluid from the centre of the droplet.

1.3 Objectives of this Thesis

The evaporation of surfactant solutions and nano particle dispersions is a subject that has gained importance in recent years because of the wide range of their applications in technology, agriculture, medicine and the likes. A droplet in contact with a solid surface creates a sessile droplet which proceeds through processes of spreading and evaporation and the understanding of the individual stages and the transition from one to the other will serve in the formulation of products for diverse applications. There is sufficient understanding of the spreading of surfactant solutions on hydrophilic and hydrophobic surfaces in literature, the evaporation dynamics of pure fluids in which case there was no influence from neither concentration gradients nor adsorption at the liquid-solid or liquid-air interfaces is also understood. The results established at the moment for evaporating droplets onto smooth solid surfaces under partial wetting conditions are that:

i. Evaporation process begins right after the drop has spread over the solid substrate, and that the drop remains a spherical cap shape during evaporation and the evaporation rate is proportional to the radius of the drop onto the substrate, L.

ii. The spreading and evaporation process is composed of four stages: 1) L increases while the contact angle, θ, decreases down to the advancing contact angle value, θ_a. 2) The contact angle decreases from θ_a down to receding contact angle value, θ_r, at constant L. 3) Contact angle remains constant and equal its receding value θ_r, while the radius of the base droplet, L, decreases.

iii. The contact angle, θ, and L both concurrently decrease until the drop completely evaporates.

With regard to the aforementioned already existing results for spreading and evaporation dynamics of pure fluids from hydrophobic substrates a handful of problems remain unsolved which will form the basis of the results and discussion of the research presented herein.

a. To develop a theory for the evaporation of surfactant mixtures with respect to the change in concentration.
b. To develop a theory for drops of multi-component fluids that takes into consideration the influence adsorption at the solid-liquid interface on evaporation.

c. To develop a hydrodynamic model able to describe the four stages of the simultaneous spreading and evaporation process.
d. To compare the hydrodynamic description of the drop evaporation with the molecular thick layer beyond the three-phase contact line. Such matching must take into consideration the DLVO forces acting at a mesoscopic scale near the contact line.
e. To describe the evaporation process of complex fluids: polymer and protein solutions and nanoparticle suspensions.
f. Analyze pattern formation onto substrate and the influence of other parameters such as volume fraction and temperature.
g. To build a theory able to describe the evaporation of drops onto patterned surfaces.

Chapter Two

2.0 Experimental Section

2.1 The Materials

For the purpose of experiments to analyse spreading and evaporation in this work, aqueous solutions of Silwet L-77 and nano particles of different sizes but the same chemical composition were used. Silwet L-77 was purchased from Sigma-Aldrich (Germany) and nano-particles from Life Technologies (Germany) and all were used as received. The particles hold sulfate groups at their surface thus the water suspensions are estabilized by Coulombic repulsions. Particles with three diameters were used: 20, 200, and 1000 nm, respectively. Poly (4, 5-difluoro-2, 2-bis(trifluorimethyl)-1,3-dioxole-co-tetrafluoroethylene), hereinafter referred to as TEFLON-AF, was purchased from Sigma-Aldrich (Germany) as powder, Flourinet F-77 was bought from 3M (USA), and the non-conductive silicon wafers were obtained from Siltronix (France). Ultrapure deionized water (Younglin Ultra 370 Series, Korea) with a resistivity higher than 18 MΩ and TOC lower than 4 ppm was used for preparing all the surfactant solutions. To coat the silicon wafer surface with Teflon AF, the TEFLON-AF powder was suspended in the Flourinet F-77 as described by Ivanova et al. (0.5g of Teflon AF in 200ml of Flourinet) and stirred until all the particles were dispersed [61]. The silicon wafers were cleaned in iso-propanol in an ultrasonic bath for thirty minutes, and then in piranha solution for twenty minutes, the substrates were dried using jet air to prevent pattern formation on drying. The Teflon suspension was applied to the silicon wafers and the solution left to evaporate for approximately 24 hours. The average roughness of the 10μm x 10μm surface was measured by AFM (tapping mode), approximately 1nm, the macroscopic contact angle of pure water was (105±2°) on those substrates.

2.1.1 Silwet Solutions

All the surfactant solutions were prepared by volume using a calibrated micro-syringe precise to ±0.1μl. A pH ≈ 7.0 buffer was used as solvent to prevent hydrolysis of the Silwet L77, and the solutions were used within 5 hours of their preparations. Before the experiments were started the solutions were thoroughly shaken and then ultrasonicated for 5 minutes. Surfactant concentrations that will be reported referred to the critical

aggregation concentration described by Ivanova et al. [6] and Ping et al. [37] and cover a broad range.

2.1.2 Nano-particle Suspensions

The suspensions of nanoparticles were used as received and they were always stored in a refrigerator at temperatures below 4ºC (without freezing). The nanoparticles used in these experiments were sulphate modified latex beads with sizes 0.02µm, 0.1µm and 0.2µm respectively. The suspensions were always ultrasonicated for at least 5 minutes before use to disperse any aggregates. Colloidal suspensions in water were prepared by diluting the original suspension in terms of the volume fraction. The volume fraction Φ is given by;

$$\Phi = \frac{V_p}{V_p + V_w} \qquad 2.1$$

where V_p is the volume of particles and V_w is the volume of water. The following volume fractions: 0.001, 0.01, 0.1, 0.2 and 0.3 have been studied.

2.2 Droplet Shape Analyzer for spreading and evaporation

The Droplet shape analyzer was fabricated and constructed for measuring contact angle, droplet base radius and height evolution with time. It is composed of both the hardware part; camera, dosing system, stage, substrate support, and lighting and the software part (image analysis). It is possible to control and measure the relative humidity and the temperature within the measuring cell.

2.2.1 Hardware description:

Figure 2.1 shows the overall scheme of the equipment and Figure 2.2 a photograph of the actual system.

The details of the system are given below following the labels in Figure 2.1.

(1) Video system composed of a CCD camera.

Image device	Type 1/3 (diag. 5.92 mm) type progressive scan KODAK IT CCD KAI340
Effective picture elements	648 (H) x 488 (V)
Lens mount	Adjustable C-Mount: 17.526 mm (in air); Ø 25.4 mm (32 tpi)
Picture sizes	640 x 480 pixels (Format_0 Mode_2 to Mode-5)

ADC	14 bit
Color modes	Mono8
Frame rates	30 frames per second and 60 frames per seconds
Gain control	Manually adjusted
Shutter speed	Manually adjusted
External trigger shutter	Programmable, trigger level control, single trigger, bulk trigger, programmable trigger delay
Internal FIFO memory	Up to 105 frames
Transfer rate	100 Mbit/s, 200 Mbit/s, 400 Mbit/s, 800 Mbit/s
Smart functions	AGC (auto gain control), AEC (auto exposure control), AWB (autowhite balance), color correction, hue, saturation, real-time shading correction, LUT, 64 MByte image memory, mirror, sub-sampling. High SNR, storable user sets. Two configurable inputs, four configurable outputs

(2) Light source;

(3) Manual dosing system; Hamilton microliter syringes (SN 701, 10 µl), was used to deposit droplets of approximately 4 microliter (≤ 4µl).

(4) Hygrometer/thermometer: The hygrometer was used to measure the humidity and temperature in the cell throughout the duration of the experiments. It has a precision of ± 2% and ± 2ºC, respectively

(5) Temperature controller i.e. thermostat; a thermostat was attached to the measuring cell as shown in Figure 2.4b, making it possible to maintain constant temperature.

(6) Humidity controllers supersaturated salt solutions within the measuring cell.

(7) Measuring Chamber: The chamber is fabricated from steel and glass windows, the glass specifications are given as

(i) LGW-1006 (Lead glass window) 100mm diameter x 6mm Thickness; was used for the cover of the chamber.

(ii) TSG-8208 (Toughened Glass) 82mm diameter x 8mm Thickness; was used for the bottom of the chamber.

(iii) BPW-5052 (Borosilicate plate Window) 50 mm x 50mm x2.2mm Thickness; was used for the window of the chamber shown in Figure 2.3. The chamber is cylindrically shaped with dimensions of 13cm by 10cm height (including the cover).

(8) Computing System.

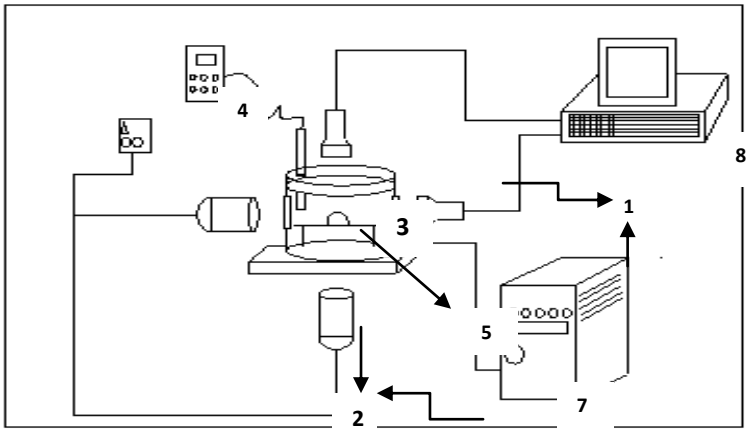

Figure 2.1: Schematic of the experimental Set-up, the numbers 1-8, identify components listed.

Figure 2.2: Complete measuring apparatus

2.2.2 The Measuring Chamber

A schematic of the chamber is shown in Figure 2.3a and a photograph in Figure 2.3b, the chamber was insulated to prevent the influence of external temperature or humidity,

the cylindrical component was made of steel coated and double glazed glass. The design allowed light to stream from the side and beneath the chamber thus the droplet evolution could be followed both from the side and the top view. The position of the light source was such that it eliminated reflection or blurred vision. The chamber was connected to a thermostat to control the temperature within desired ranges. Supersaturated salt solutions were used to control the humidity within desired ranges [150]: $MgCl_2.xH_2O$, $CaCl_2.xH_2O$ for relative humidity ≈ 30%, Sodium Bromide (NaBr) and/or Potassium Bromide (KBr) ≈ 50% and Potassium Bromide (KBr) and/or Potassium Chloride (KCl) ≈ 90%. The chamber was designed such that a cooling or heating liquid could be passed into the walls around the chamber by the thermostat. It has a trench like support for the substrate and salt solution for humidity control. On the top lid there was an opening only wide enough for the probe of the hygrometer/thermometer to monitor the temperature and humidity for the duration of the experiment. The side glasses, bottom glass and top lid were all double glazed to prevent loss of heat from the chamber or condensation in the chamber, the substrate support is located at the same level as the glass windows for the camera and the light source.

The chamber has a hole on the front side where the syringe for droplet deposition, the position of the syringe allows one to place the droplet in the mid-point of the camera view in line with the calibration, as shown in Figure 2.4.

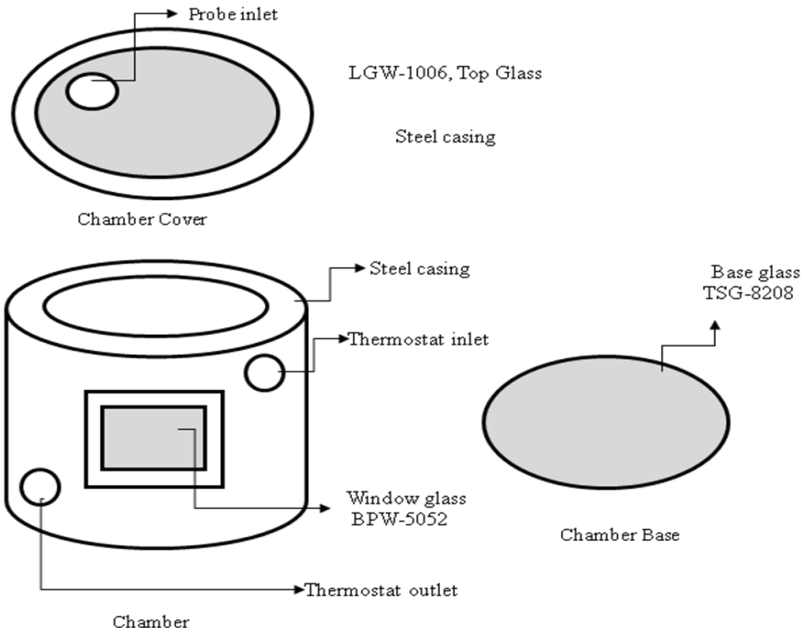

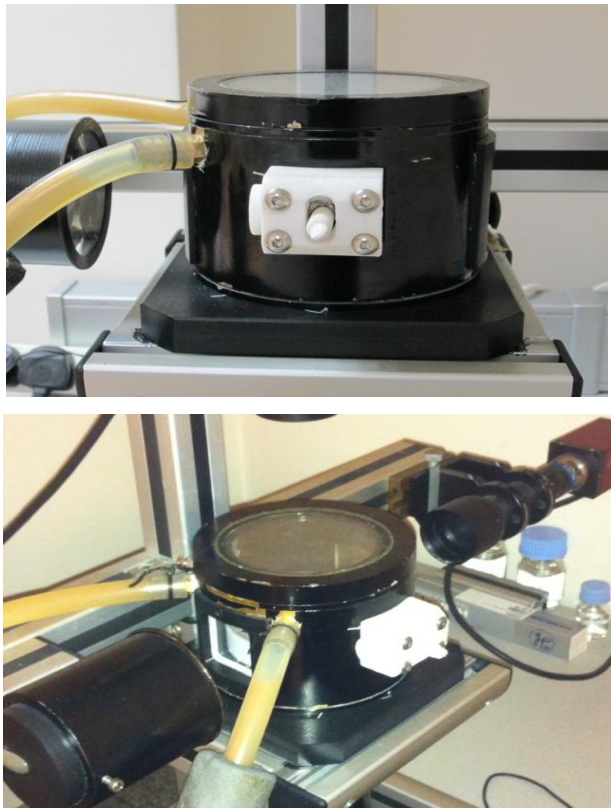

Figure 2.3: Top: scheme of the measuring Chamber; botom: picture of the measuring chamber.

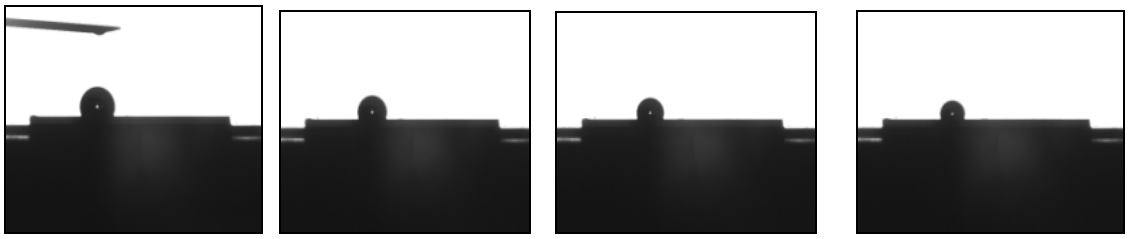

(a) (b) (c) (d)

Figure 2.4: Droplet profiles on solid surfaces at (a) 0 seconds, (b) 30 minutes, (c) 60 minutes, and (d) 90 minutes at 90% relative humidity and 18ºC.

The apparatus measured the drop profile by the analysis and evaluation of the digitized droplet image. Before each experiment, three settings: image sharpness, brightness and camera tilt were adjusted. The position of the light source enabled the deflection of light reflection of the droplet on the substrate surface, prevented blurred images and to make easier the baseline determination. The camera was calibrated by using a high precision microliter ruler.

2.2.3 Software description

The software includes the following components:

1. Image controller that includes sharpness, brightness and contrast adjust settings.
2. Movie recorder, with a maximum of frequency of 30 fps. There is the possibility to program a video sequence in several steps with different single frame frequencies and recording times.
3. Contact angle measurement software measures the droplet shape by fitting the profile of a complete circle, measuring the height of the droplet (the distance from the substrate to the top of the droplet). The droplet radius of the fitted circle was also measured. The measurement technique is valid for contact angles above 15º.

The steps for performing experiments of spreading and evaporation are:

- The cameras were calibrated imaging micro-ruler with a precision of ±0.1μm. The thermostat is switched on and set at a temperature, another time lag to obtain equilibrium
- The salt solution was deposited in the trench in the chamber until equilibrium was reached (normally over 24hrs).The camera was switched on from the computer to record the first dynamics of the droplet interaction with the substrate.
- The substrate was placed on the support at a central point to the focus of the camera.
- The syringe with approximately 4μl of aqueous solution was inserted into the chamber and the droplet deposited on the substrate.
- The spreading and evaporation dynamics were monitored until the droplet was no longer visible.
- The experiments were repeated a minimum of five times.
- Image analysis using computer software.
- Exporting the data to calculate parameters contact angle, droplet base radius and the volume and their applications.

2.2.4 Measurement of Contact Angle

The measurement of the contact angle θ and droplet radius *R*, were obtained from the fitting of a complete circle, the contact line radius is given by *L* and is obtained thus. The height, *h* of the droplet was also measured, and it was ensured that the measurement dynamics always started from a flat homogenous surface, see Figure 2.5. To calculate the contact angle, contact base radius and volume the following measurements were interpolated.

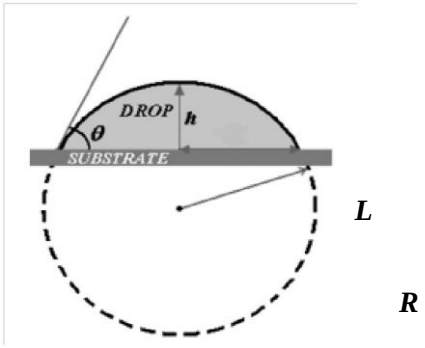

Figure 2.5: A schematic of a sessile drop on a substrate and measured parameters, the drop height (*h*), the contact radius *L*,, the radius of the sphere forming the spherical cap (*R*), and the contact angle (θ).

The following geometrical relations are easily established:

$$L = Rsin\theta \qquad 2.2$$

with θ given in radians

$$\theta = Asin((R-h)/R), \qquad 2.3$$

The volume is obtained as function of *r* and *h* and is given as

$$V = \frac{1}{6} * \pi h[3(L/4) + h^2] \qquad 2.4$$

After calibration, the error in the measurement of contact angle was ± 2º and ±1% for the droplet base radius.

2.3 Tensiometer

Interactions occur between the molecules of a liquid and those of any liquid or gaseous substance which is not soluble in the liquid; these result in the formation of an interface. Energy is required to change the form of this interface or surface. The work required to

change the shape of a given surface is known as the interfacial or surface tension. The Kruss-K10 Tensiometer shown in Figure 2.6 was used in the work reported herein.

The Tensiometer determines the surface tension with the help of a probe susceptible to wetting suspended from a precision weight balance; this is either a ring or a plate; in this work a plate probe has been used. A height adjustable sample carrier is used to bring the liquid to be measured into contact with the probe. A force acts on the balance as soon as the probe touches the surface. The length of the probe is known (circumference of ring or length of plate) thus the force measured can be used to calculate the interfacial or surface tension. The probe usually a material with very high surface energy, for this reason a plate made of roughened platinum is used for the measurements.

Figure 2.6: Image of the tensiometer Kruus K-10 used in this work.

The Plate Method; In the plate method described in Figure 2.7, the liquid was raised until the contact between the liquid film surface and the plate (metal probe) was made. The maximum tension acts on the balance at this instant; this means that the sample does not need to be moved again during the measurement. The tension is calculated using the following equation;

$$\gamma = \frac{F}{\pounds cos\theta} \qquad 2.5$$

where γ is the surface or interfacial tension; F is the force acting on the balance, $\mathcal{L}$ is the wetted length and θ is the contact angle. Since the plate is made of roughened platinum and is optimally wetted, the contact angle is virtually 0°. This means that the term *cos* θ has a value approximately 1, thus only the measured force and the length of the plate need to be taken into consideration.

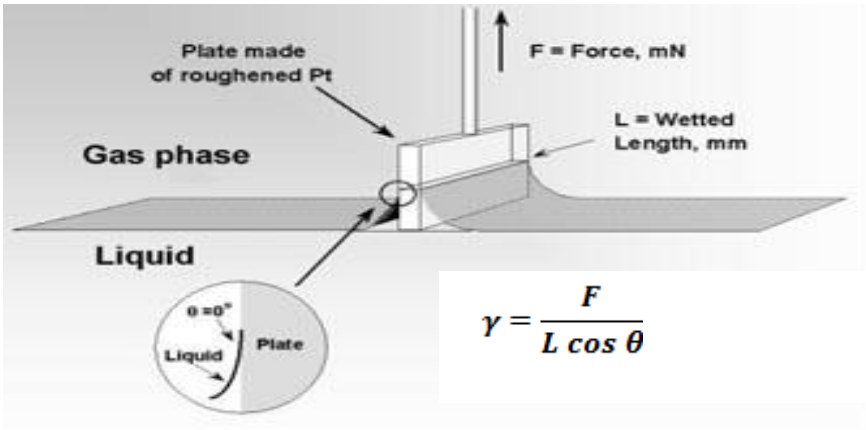

Figure 2.7: Scheme of the plate measuring method

Steps for performing experiments to measure Surface tension

1. Turn on the equipment and set the Tensiometer at the desired temperature.
2. Clean the probe using a Bunsen burner, allow the heat turn the probe just red and then allow the probe return to room temperature.
3. Transfer the solution or the suspension to be measured into a clean measuring cell.
4. Gently place the probe on the weight hinge and ensure the probe rests gently inside the beaker, and secure the system to prevent influence of the surrounding.
5. Adjust the scales to the zero point, and then elevate the liquid casing till it reaches the tip of the probe and allow some time to eliminate any vibration effects.
6. Initiate measurement using the plate mode and record the value for surface tension when the value is stable.
7. The measurements were repeated a minimum of three times.
8. The first measurement was always done with water to determine the accuracy since the surface tension of water is a known measurement.

9. The probe and beaker were cleaned after each experiment.

2.4 Quartz Crystal Micro-Balance

The impedance based quartz crystal microbalance (QCM) has for a long time been routinely used to provide information about a wide range of interfacial processes both at air-solid and liquid-solid interfaces. The quartz crystal microbalance (QCM) is a well-known tool to measure film thicknesses in the nanometre range [151, 152]. In the simplest case is when the quartz resonator surface is covered with a rigidly coupled mass (purely elastic) the QCM functions as a purely gravimetric probe giving the mass of the finite deposited layer. On the other extreme i.e. in the case when one side of the quartz resonator is immersed in a purely viscous media (Newtonian liquid) the QCM functions as a probe for the liquid properties like density or viscosity.

Buttry and Ward outlined the main advantages of using impedance analysis for QCM applications compared to oscillator and other QCM measuring methods, [153]:

The oscillator method only measured the series frequency (one frequency), which is only a part of its properties. Whereas the impedance analysis fully characterizes the quartz crystal and enables the measurements of several overtones which gives multidimensional information to describe a much more complete behaviour of the quartz crystal and its adlayers.

In the oscillator method the quartz resonant frequency depends on the components of the oscillator circuit, which also can induce errors in the measured frequency changes. Whereas, in the impedance analysis the frequency of the applied voltages are independent of the quartz crystal resonance and are not determined by the quartz crystal. Therefore, the resonance frequency determined for the quartz crystal is more close to its natural resonance and hence the measured changes in the quartz crystal properties resembles to true changes without any interference from measuring electronics.

The oscillator method and other QCM methods do not function in certain situations, such as heavy mass loading or highly viscous damping. Whereas, impedance analysis have been shown to tolerate highly viscous damping to a higher extent than other QCM methods used.

According to Hook and Kasemo [154], the classical application of quartz crystal resonators is micro-gravimetry, and for thin films the resonance frequency is approximately inversely proportional to the thickness of the plate. When the damping in the deposited film becomes sufficiently large, the simple linear relation between Δf

(frequency) and Δm (mass) is no longer valid. This leads to two new requirements to maintain the technique as a useful sensor technique, namely (i) technical solutions that provide information not only about changes in resonance frequency, but also changes in energy dissipation, D, of the oscillating system, and (ii) suitable theories to make full use of this new information.

The original setup and measurement chamber briefly shown in Figure 2.8, has in also used in all of our measurements (Q-Sense, Göteborg, Sweden).

(a)

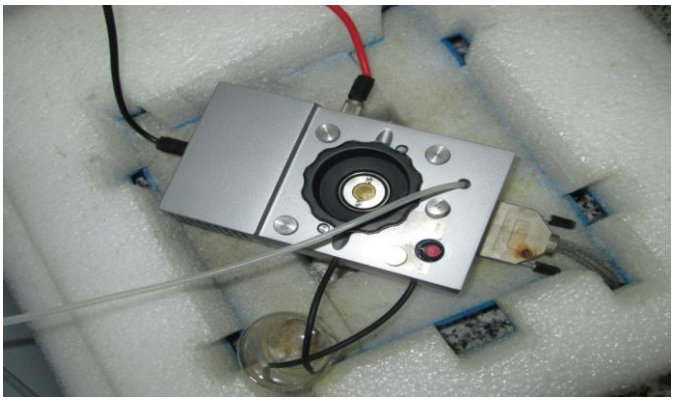

(b)

Figure 2.8; Experimental set up of (a) The Quartz Crystal Microbalance, and (b) The Measuring Cell.

2.4.1 Measurement Methodology

The principle of the measurement was based on the switching on and off periodically the driving power for the sensor and recording the output voltage from the freely decaying oscillator, a schematic shown in Figure 2.9. To a very good approximation, the amplitude of oscillation decayed exponentially in time, while the driver circuit was disconnected.

The QCM oscillation decay was recorded by a digitized oscilloscope using a low- or high-resistance probe, which ensured that the crystal decayed close to the series or parallel mode [151]. The decaying voltage output from the crystal, has a frequency given by the resonance frequency (f_0) of the crystal (in our system approx. ~5MHz), was mixed prior to reading with a constant reference frequency (f_r) (which is about 100 kHz lower than f_0) and filtered in a low-pass filter with a cut off frequency of ~500 kHz. The output signal is thus the frequency difference f, between f_r and the QCM oscillator (sensor) frequency, f_0. The recorded signal, $A(t)$, is then transferred to a computer, where a numerical fit to an exponentially damped sinusoidal is performed. Given that

$$A = A_0 e^{-t/\tau} \sin(2\pi f t + \alpha) \qquad 2.6$$

and

$$D = \frac{1}{\pi f t} = \frac{1}{Q} = \frac{E_{dis}}{2\pi E_{st}} \qquad 2.7$$

Where Q is the quality factor, E_{dis} the energy dissipated and E_{st} is the energy stored during one period of oscillation.

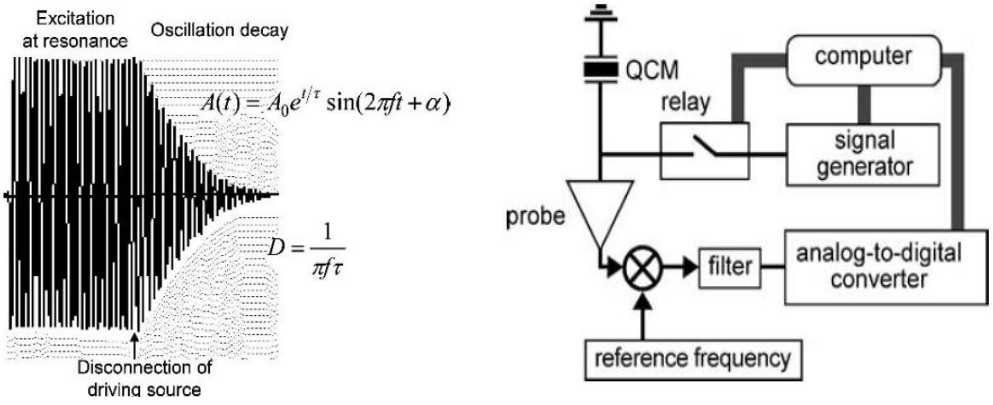

Figure 2.9: Scheme of the measurement profile for a QCM, redrawn from [154].

The simultaneous measurements for f and D are performed with a repetition rate of approximately 1Hz, the measurement chamber for liquid phase measurements was constructed with special attention primarily to temperature stability and mechanical stress induced on the crystal when mounted to avoid temperature- and pressure-induced transients in f and D e.g., one liquid is replaced with another. In order to obtain reliable data in conducting salt solutions it is important to pay attention also to capacitive leakage

over the crystal. This is taken care of by measuring in the series mode, see Figure 2.9 and/or by having the side of the crystal facing the liquid completely covered with the electrode material.

In this passive method the quartz crystal is connected to an impedance analyser, which applies an alternating voltage at various frequencies across the crystal, measuring the current as a function of the applied voltage. The magnitude and phase of the impedance can be determined in form of am impedance spectrum as shown in Figure 2.10 in the impedance- frequency and phase-frequency curve, the impedance is given numerically by Eq. 2.8, where $U(\omega)$ is the voltage and $I(\omega)$ the current passing through the circuit.

$$\text{Impedance: } Z(\omega) = \frac{U(\omega)}{I(\omega)} \qquad 2.8$$

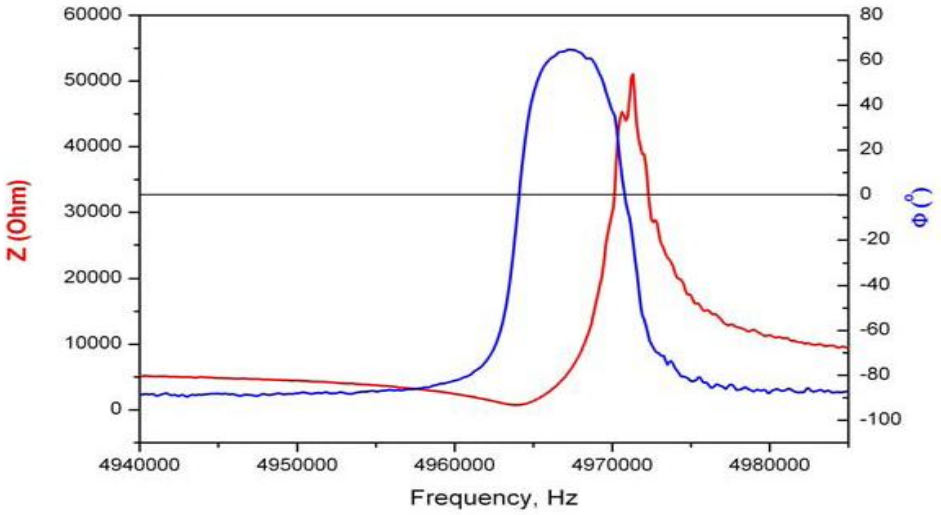

Figure 2.10: Example of the characteristic impedance-frequency and phase-frequency curves of a quartz crystal obtained by impedance analysis.

In the case where the quartz crystal is loaded with a finite viscoelastic layer contacting a liquid the surface mechanical impedance is given by Eq. 2.9

$$Z_s = Z_s^{liquid}\left[\frac{Z_s^{liquid}\cosh(\gamma h_f)+Z_s^{film}(\sinh(\gamma h_f)}{Z_s^{film}\cosh(\gamma h_f)+Z_s^{liquid}\sinh(\gamma h_f)}\right] \qquad 2.9$$

where $Z_s^{film} = (\rho_f G)^{1/2}$ is the characteristic impedance of a visco-elastic film, Z_s^{liquid} is the characteristic mechanical impedance of a Newtonian liquid,$\gamma = j\omega(\rho_f/G)^{1/2}$, the complex wave propagation constant, h_f is the visco-elastic film thickness, $\rho_f$is the

viscoelastic film density, and $G = G' + jG'' = \mu + j\omega\eta$ is the film complex elastic modulus.

An example of modeling a viscoelastic layer formed from solution adsorbing onto a hydrophobic quartz crystal was measured with the KSV QCM-Z500 instrument, where Synperonic, a water-soluble short polymer was adsorbed onto a hydrophobic quartz crystal in pure water. The quartz crystal was made hydrophobic by immersing a clean gold coated quartz crystal into an ethanol solution of octadecylmercaptan. The recorded frequency changes of different overtones for the adsorption of Synperonic onto the hydrophobic quartz crystal surface. The baseline before injection of Synperonic is taken in pure water. The change in frequency after injecting Synperonic for the different overtones does not match the overtone number i.e. the normalized frequencies do not superimpose on one curve see Figure 2.11. This is a clear indication that the adsorbed Synperonic layer forms a viscoelastic layer when it adsorbs onto the hydrophobic quartz crystal.

There are several viscoelastic models to analyze the measurements of deposited mass during adsorption, but the most promising one was based on the transmission line model. Basically, the transmission line model relied on the possibility to convert the electrical characteristics of the quartz crystal and its adlayers to their mechanical or viscoelastic properties. Hook and Kasemo obtained electrical properties of the quartz crystal and its adlayers by impedance analysis of the quartz crystal [154].

In the limit of thin rigid films the full analysis reduces to the Sauerbrey Equation, which is described by the shift of the quartz crystal resonance frequency is linearly proportional to the mass of the deposited film as long as the film is uniform, thin compared to the thickness of the crystal and rigid/elastic such that it can be treated as an extension of the quartz crystal, [152].

$$m_f = -C\frac{\Delta f}{v} = -Z_q\frac{\Delta f}{2vf_f^2} \qquad 2.10$$

Given that m_f is the mass deposited on the sensor, $C = Z_q/2f_0^2$ is a sensitivity factor and is dependent on the crystal used, in this experiments it had the value of 17.8ng·s^{-1}, Δf is the change in frequency due to adsorbed material, v the number of harmonics, f_f is the fundamental frequency of the quart crystal (approximately 5MHz for the crystals

used herein) and Z_q ($8.8 \cdot 10^{-6} kg \cdot m^{-2} \cdot s^{-1}$) is the impedance of the quartz crystal, described by the expression.

$$Z_q = \rho_q \mu_q \quad 2.11$$

where ρ_q, is the density of the quartz crystal ($2.65 g.cm^{-3}$) and μ_q is the modulus shear of the quartz crystal ($2.95 \cdot 10^6$ N·cm^{-2}).

The steps for performing adsorption experiments with the quartz crystal balance are:

-The electrodes are cleaned in piranha solution and dried with jet air.

-Dispersed Teflon suspension is deposited on the electrode and the solvent left to evaporate for 24 hours.

-Calibrate the QCM using measuring the capacitance and impedance of a known electrode.

-Place the electrode in the QCM adsorption chamber and passed water into the adsorption chamber, and ensured they were no bubbles in the chamber, and water was used to obtain a base line from which to reference adsorption of the sample solution.

-Run the software and monitor the recorded frequencies until stability was achieved.

-Introduce the sample solution or dispersion to be analysed into the chamber gradually and the monitored the harmonics/frequency until stability is reached.

-Introduce water again as a cleaning agent, repeated as many times as required.

-Analyze the adsorption profile using the software, according to the equations described above.

2.5 Scanning Electron Microscope

The JEOL-6400 is a new-generation, fully computer-controlled scanning electron microscope, the extremely fine electron source of the field emission system enables the attainment of much higher resolution images than a conventional SEM. Useful magnifications in excess of 200,000 times are obtainable, which translates to a resolution of 1.5nm at an accelerating voltage of 30kV. Insulating samples may also be examined without a conventional conductive coating of gold or carbon, Figure 2.12 shows a photographic representation of the SEM.

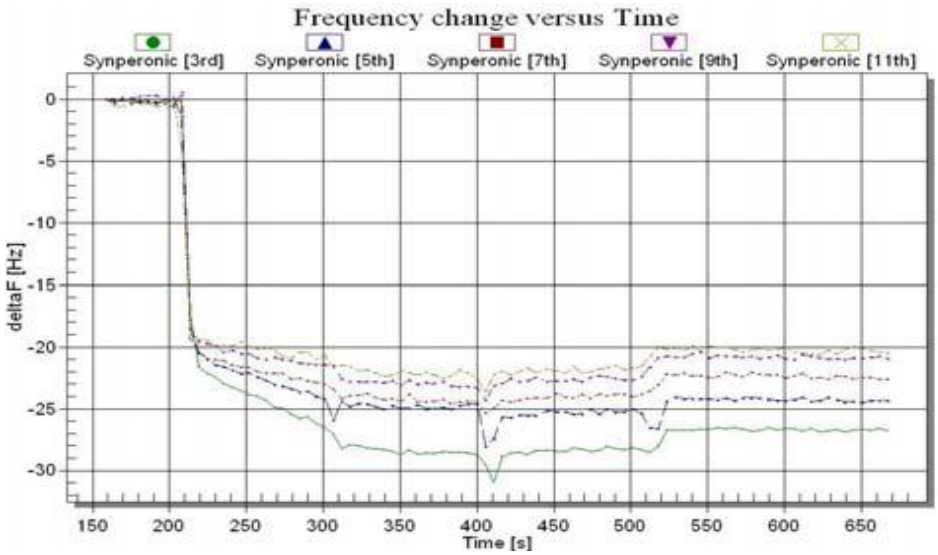

Figure 2.11: Frequency change of Synperonic adsorption onto a hydrophobic quartz crystal in water measured at several overtones with the KSV QCM-Z500 instrument, normalized with the number of the overtones, redrawn from [129].

The sample stage can handle specimens up to 20 cm in diameter making it ideal for inspection of items such as compact discs and wafers.

Operating/Measuring procedure of SEM;

The substrates were arranged in an orderly manner on the scanning electron microscope support.

The support with the substrates attached was inserted into the vacuum chamber.

The chamber was shut and the chamber is pumped down to vacuum, the process normally takes a few minutes.

The images were recorded and sections of particular interest magnified (30µm- 500µm) and saved.

Recorded the magnification of each specimen measured.

The chamber was decompressed and the substrates extracted.

Figure 2.12: Scanning electron microscope JEOL-6400 used to study the morphology of the deposits left by the nanosuspensions after evaporation.

Chapter Three

Experimental Results

3.1 Spreading

3.1.1 Spreading of Surfactant Solutions

The results for the spreading and evaporation of sessile drops are presented in this chapter, a sessile droplet in contact with a solid surface will wet the surface, the rate of spreading/wetting and the mode of spreading, and the contact angle will depend on the type of substrate (hydrophobic or hydrophilic). When surfactant solutions are deposited on solid surfaces the spreading dynamics is affected by factors not present in pure fluids; surfactant solutions are known to reduce the surface tension of pure water andthe surface energy of hydrophobic substrates, the magnitude of both reductions depend on the surfactant concentration for diluted solutions. There are results in literature to show that spreading and evaporation of a sessile droplet on a solid surface proceeds in four stages. Ivanova et al [6], studied the spreading dynamics over hydrophobic substrates and concluded that the spreading depended on the concentration of surfactant and was characterized by the following steps:

i. A relaxation of a droplet immediately after a deposition, the duration of this stage is in the range of milliseconds. In the end of a relaxation a contact angle is formed, which is referred to as an initial contact angle.
ii. During the next stage the droplet does not spread out at all. We refer to that stage as “a lag time”, the lag time is very short and almost not detectable;
iii. A stage of fast stage spreading for surfactant concentrations above CAC/CMC but not visible at low concentrations, below CAC/CMC;
iv. A slower stage of spreading, which corresponds to the second stage of spreading in the case of high concentration of surfactants, above CAC/CMC, and the only stage of spreading at concentrations below CAC/CMC.

For the purpose of this work we have restricted ourselves to the stages (iii) and (iv) due to the limitations of the experimental technique described in this Thesis. According to the theory proposed by Starov et al. [155], the spreading of surfactant solutions onto

hydrophobic substrates is due to the transfer of surfactant molecules from the liquid bulk to the three phase contact line, the rate of this transfer is dependent on the concentration of surfactant in the liquid bulk. It has also been established that there is a concentration of surfactant at which an increase to the concentration does not influence the spreading velocity, [6]. In this work the spreading dynamics for Silwet L-77 solutions for concentrations below and above CAC and for nanoparticle dispersions will be studied experimentally as a function of concentration, temperature and relative humidity.

Figure 3.1 shows representative spreading results for Silwet L-77 solutions onto PTFE AF surface at 18ºC and 30% relative humidity, and qualitatively similar results were obtained at other temperatures and relative humidities, recall that Silwet L-77 does not form micelles but vesicles. As expected the droplet contact radius, L, increases during the spreading process until it reaches a plateau whose value increases with concentration. This behaviour is observed for all the temperatures and relative humidities studied. The fact that the droplet contact radius L, is different at $t=0$ for different concentrations is because the initial volume of the droplets is slightly different, see Figure 3.1c. The droplets are deposited manually and we observe that as the concentration of the surfactant is increased the surface tension between the liquid and the syringe reduces and this leads to residual volumes of the surfactant solution on the syringe after droplet depositon, the spreading stage is completed within 30 to 60 seconds. During spreading the contact angle reduces from the initial (or equilibrium) contact angle θ^e to the advancing contact angle, θ_{ad}, and as expected the advancing contact angle reduces with increasing the surfactant concentration. It is found that the volume, V, remains constant indicating that the spreading of the droplet is the more dominant process, and is not affected by evaporation. The results for spreading of surfactant solutions for concentration below and above the CAC, and at 30% relative humidity and 18ºC are shown in Figure 3.1.

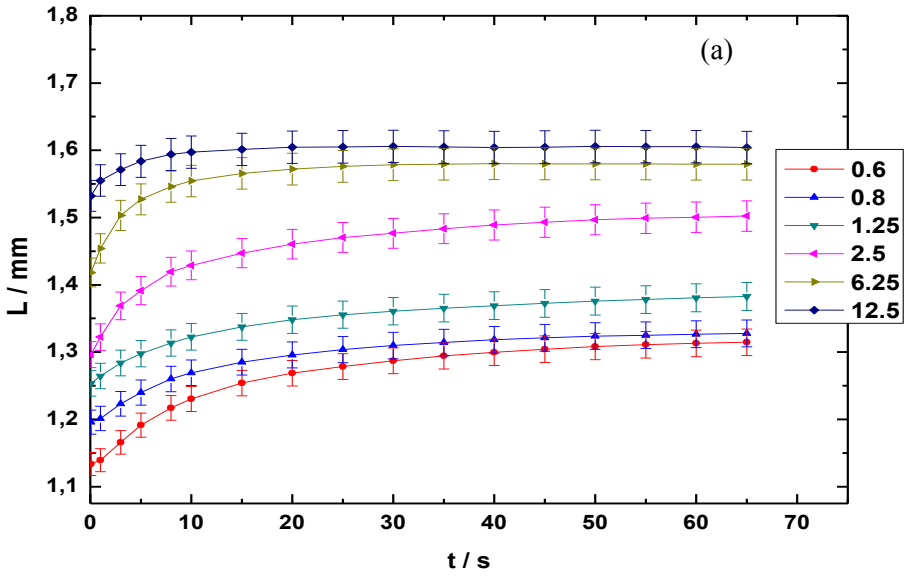
(a)
L / mm
t / s
0.6
0.8
1.25
2.5
6.25
12.5

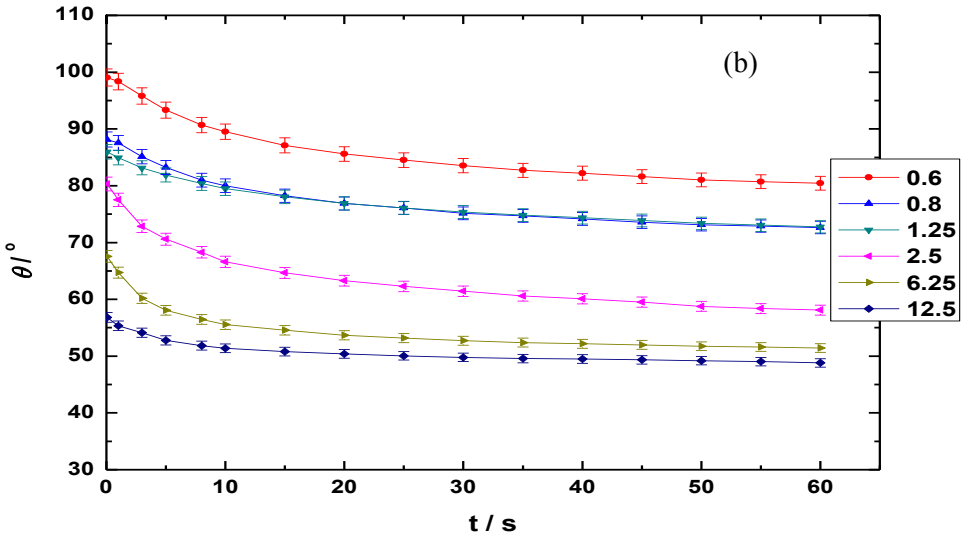
(b)
θ / °
t / s
0.6
0.8
1.25
2.5
6.25
12.5

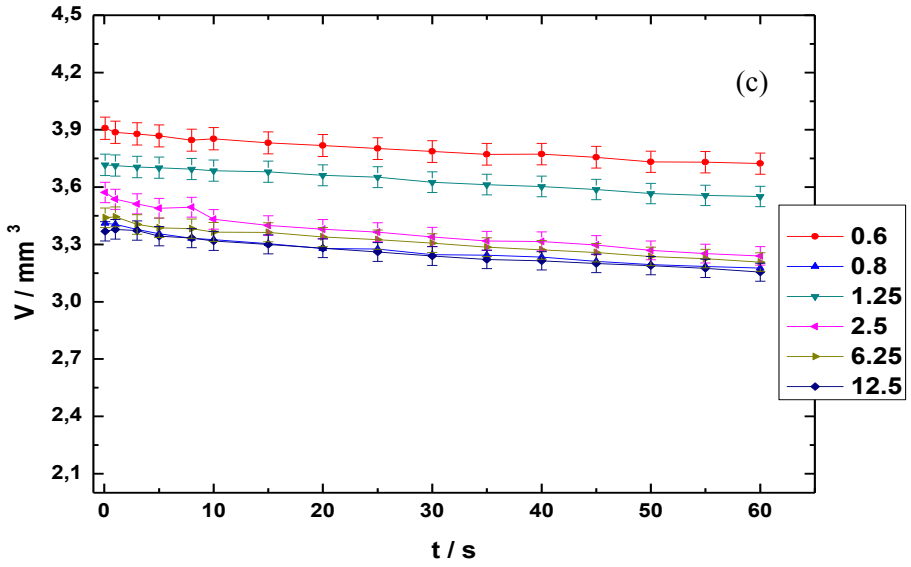

Figure 3.1: Spreading dynamics of sessile droplets of Silwet L-77 solutions at different concentrations and at constant temperature 18ºC and relative Humidity, 30% (a) Contact angle, (b) Droplet base radius, and (c) Volume of the droplet. The concentrations are expressed in units of critical aggregation concentration, CAC).

For higher relative humidities and temperatures i.e. 90% and 30ºC, the behavior is qualitatively similar to the dynamics described in Figure 3.1, although the increase of the droplet contact radius L, is relatively faster because it reaches the maximum L_0, in very short times as shown in Figure 3.2a. The saturated ambient conditions lead to an increase in the energy barriers for the molecules to overcome and initiate spreading, thus the spreading stage is brief. At low temperatures the molecules of the surfactant solutions lack the activation energy created by high temperatures and hence their ability to over come energy barriers is greatly diminished and as a result the droplet contact radius reaches a maximum in shorter time, the dynamics of spreading is fundamentally the same as seen in Figure 3.2.

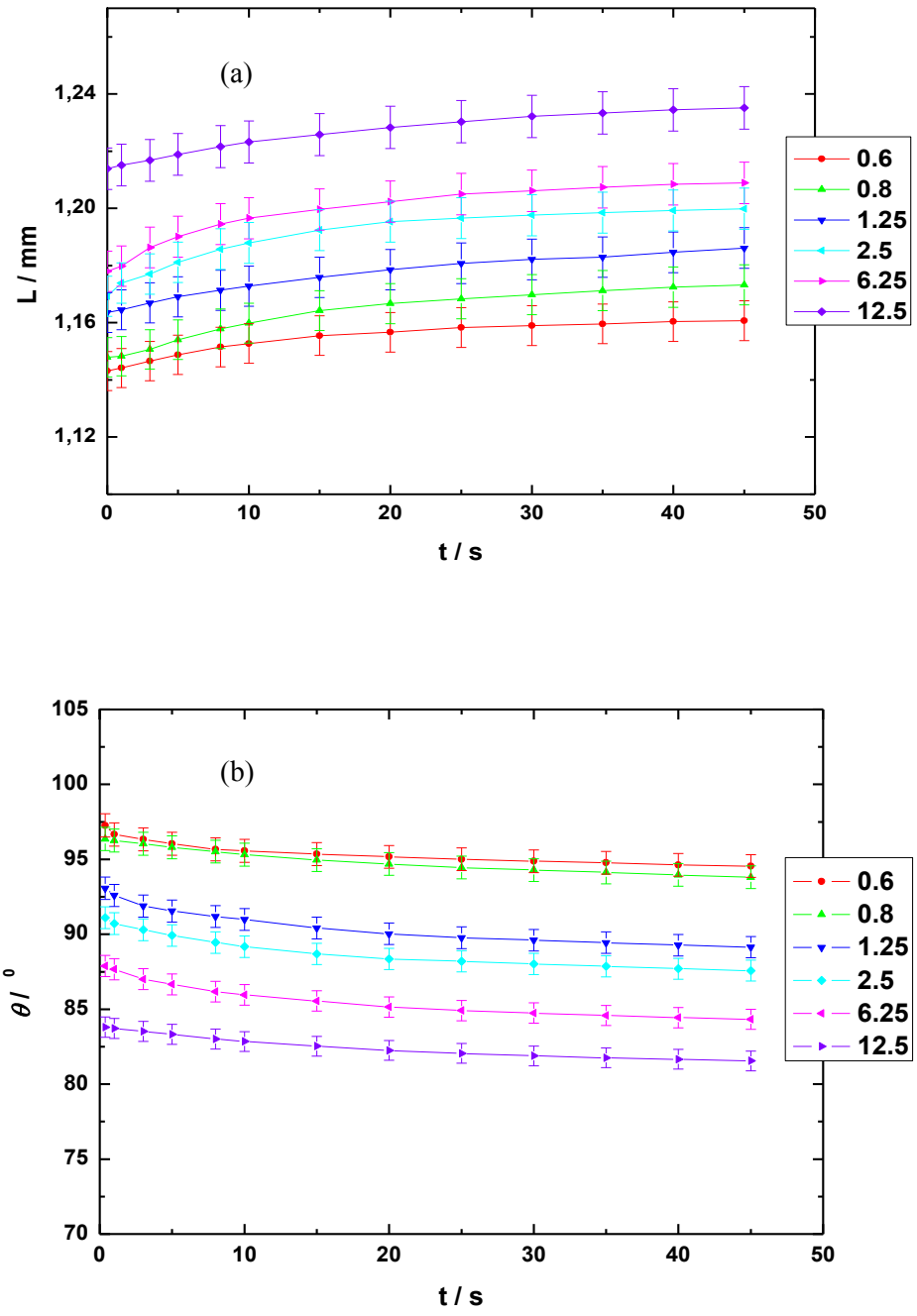

Figure 3.2: Spreading dynamics of sessile droplets of Silwet L-77 solutions at different concentrations and at constant temperature 18ºC and relative Humidity, 90% (a) *θ,* (b) *L*, and (c) *V*. The concentrations are expressed in units of critical aggregation concentration, CAC.

The results presented in Figure 3.1 and Figure 3.2 are from the spreading of trisiloxane surfactant (Silwet L-77) for concentrations below and above the CAC at a given temperature and varied relative humidities respectively. The increase of the droplet base radius as the concentration is increased has been demonstrated in Figure 3.1a and Figure 3.2a. The simultaneous decrease of the initial contact angle the droplet forms on deposition until it reaches the value of the advancing contact angle is observed, and the advancing contact angle has been described as the angle at which evaporation becomes dominant.

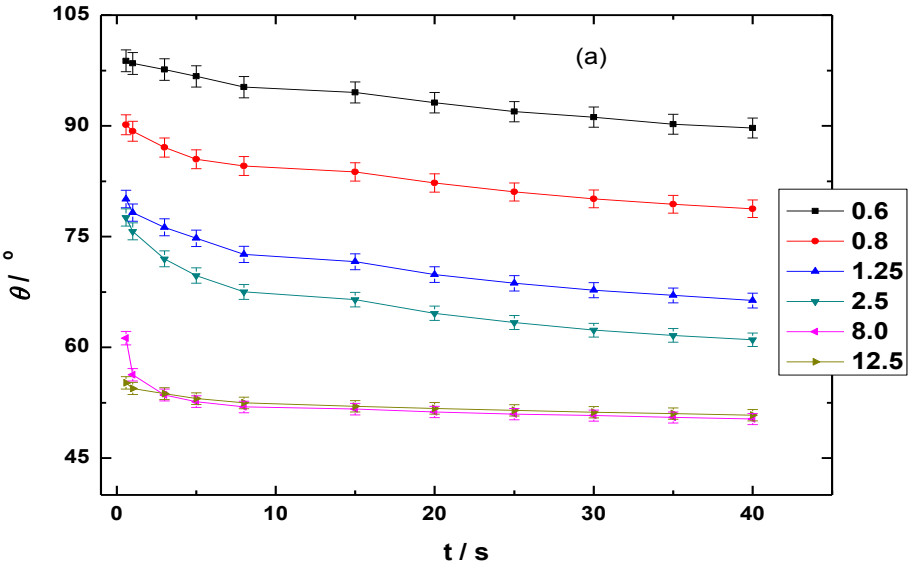

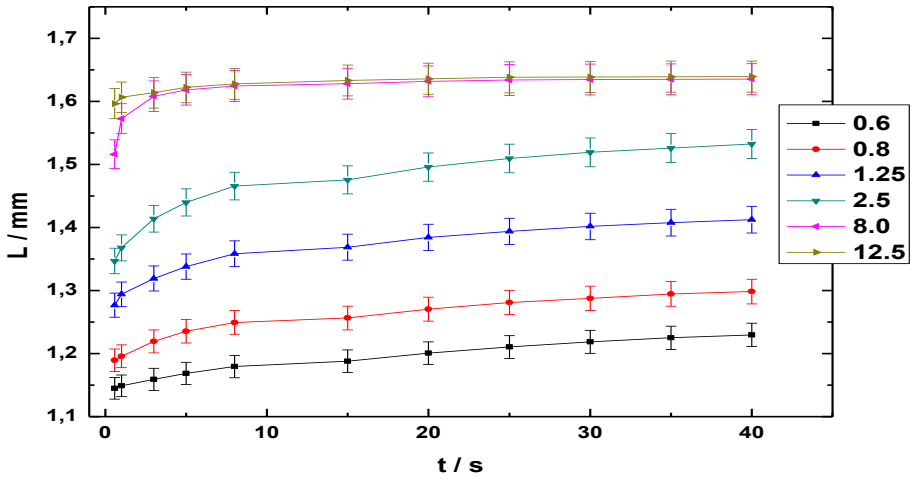

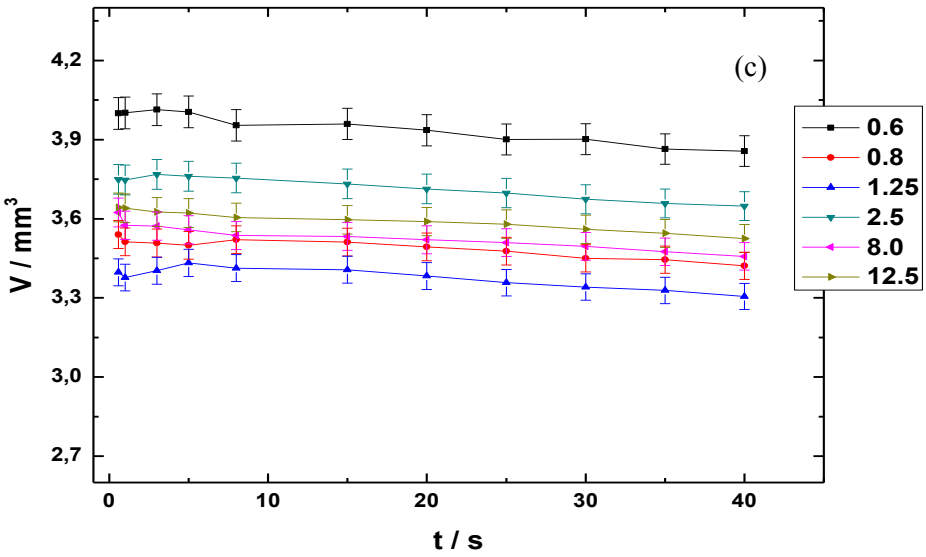

Figure 3.3: Spreading dynamics of sessile droplets of Silwet L-77 solutions at different concentrations and at constant temperature, 30ºC and relative Humidity, 30% (a) θ, (b) L, and (c) V. The concentrations are expressed in units of critical aggregation concentration, CAC.

Figure 3.3 shows the trend for spreading at 30ºC temperature and 30% relative humidity and they are qualitatively consistent with the spreading dynamics shown in Figure 3.1 and Figure 3.2. however, it is important to note that the duration of spreading stage in Figure 3.3a is significantly shorter in this case, as a result of high temperatures and low relative humidity. The molecules of surfactant become highly mobile and there is an increase in interaction of molecules and the solid substrate which possesses high thermal conductive properties contributes to driving the evaporation process, thus reducing the duration of the spreading stage.

3.1.2 Critical Aggregation Concentration and Critical Wetting Concentration

The critical aggregation concentration (CAC) and critical wetting concentration (CWC) are important parameters used to determine the spreading potential of a surfactant solution with respect to the concentration of the solution. From the advancing contact angle, θ_{ad}, obtained at the end of the spreading process it is possible to obtain the critical aggregation concentration (CAC), and from the receding contact angle we can obtain the critical wetting concentration (CWC) of the Silwet L-77 solutions. The critical aggregation concentration (CAC) and crtitcal wetting concetration (CWC) for

trisiloxanes have been investigated by Ivanova et al. [6], and they found that the CAC and CWC of Silwet L-77 to be approximately 1.0g/mol and 2.5g/mol respectively. Figure 3.4 shows the results of the CAC and CWC obtained from experimental data presented here.

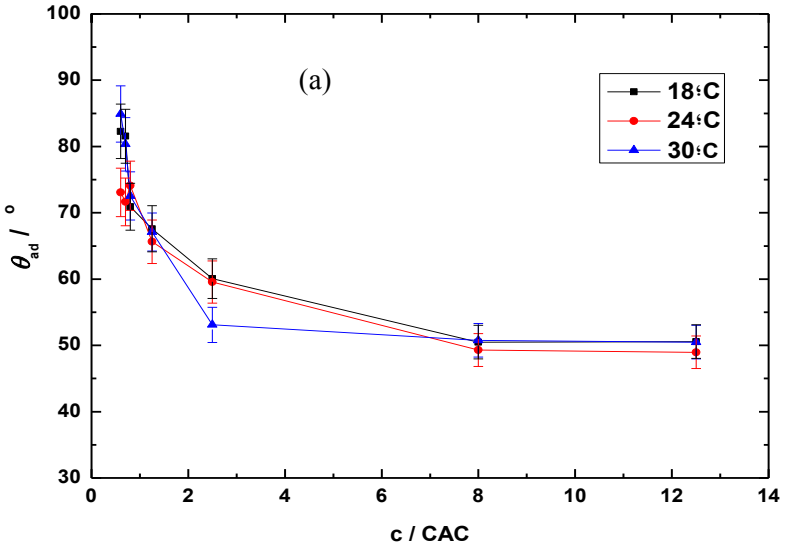

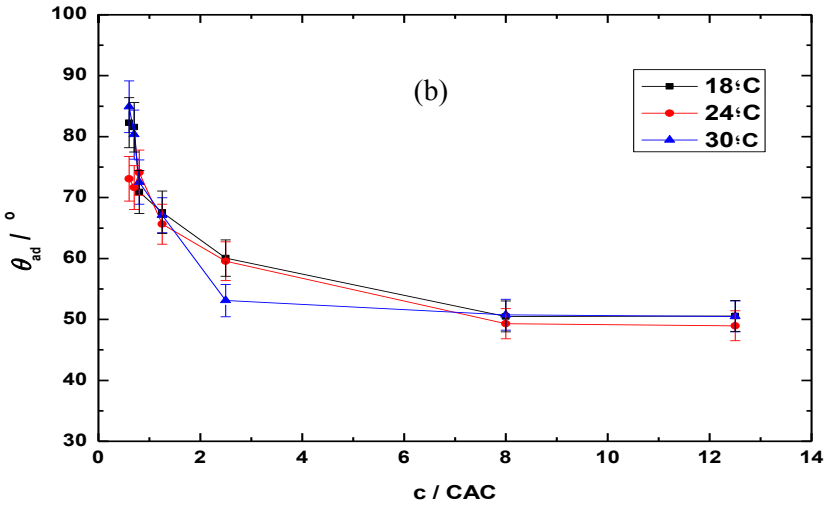

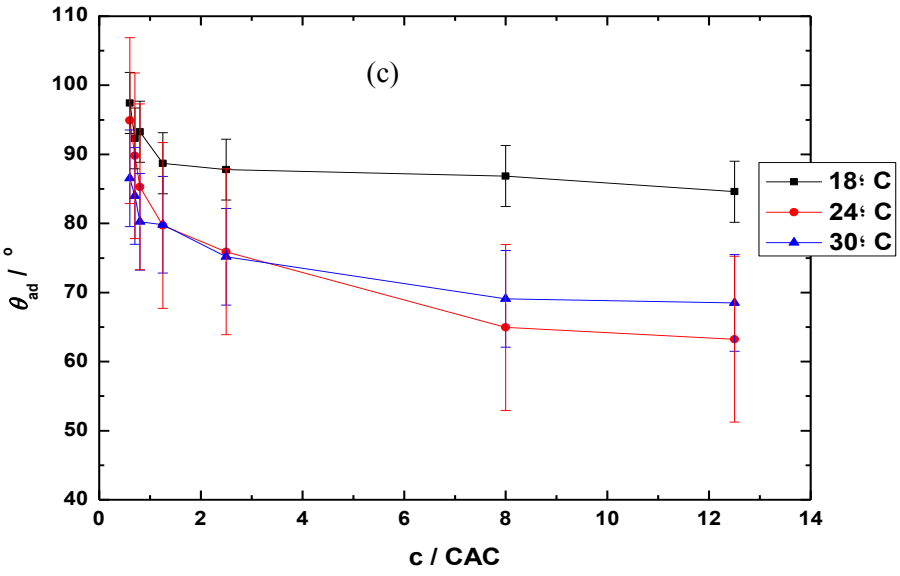

Figure 3.4: The advancing contact angle with respect to the CAC at constant relative humidities of, (a) 30%, (b) 55%, and (c) 90% over three measure temperatures, 18ºC, 24ºC and 30ºC.

In Figure 3.5 we show the relationship between the advancing contact angle and the concentration for constant temperature, and varied relative humidity, we observed that the critical aggregation concentrations is constant, the aggregations begin to form and it reaches a concentration where the concentration no longer influences the advancing contact angle.

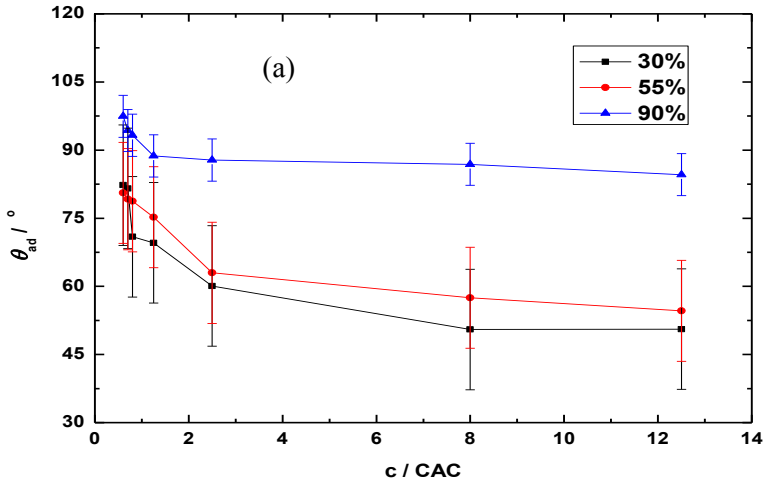

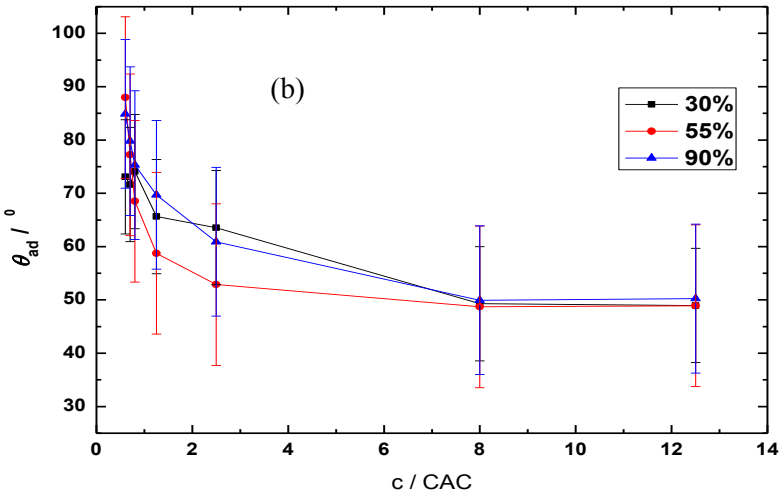

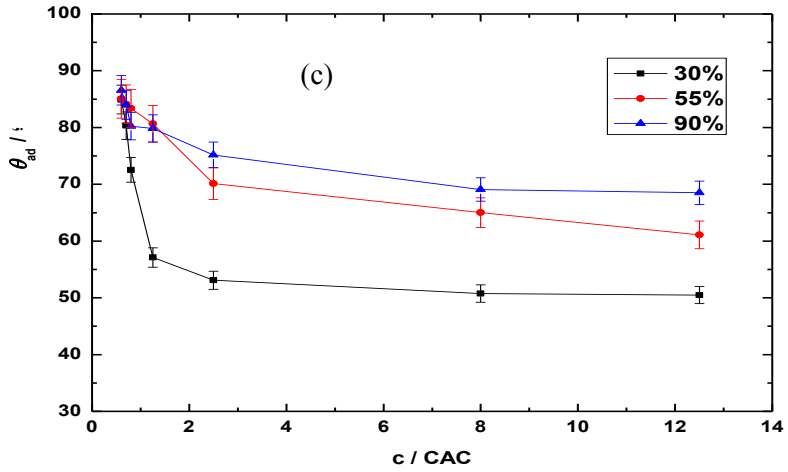

Figure 3.5: The advancing contact angle with respect to the CAC at constant temperatures of, (a) 18ºC, (b) 24ºC, and (c) 30ºC over three measured relative humidities 30%, 55%, and 90%.

Figures 3.4 and 3.5 show the dependence of the advancing contact angle, θ_{ad}, on concentration. It is observed that the advancing contact angle reduces as the concentration of the surfactant solution increases until a concentration at which the advancing constact angle remains constant regardless of an increase in the concentration of surfactant, at that concentration micelles have formed in the solution that result in no change in the interaction and behavior of the surfactant solution. In figure 3.6 we present the dependence of the critical wetting concentration on relative humidity and temperature.

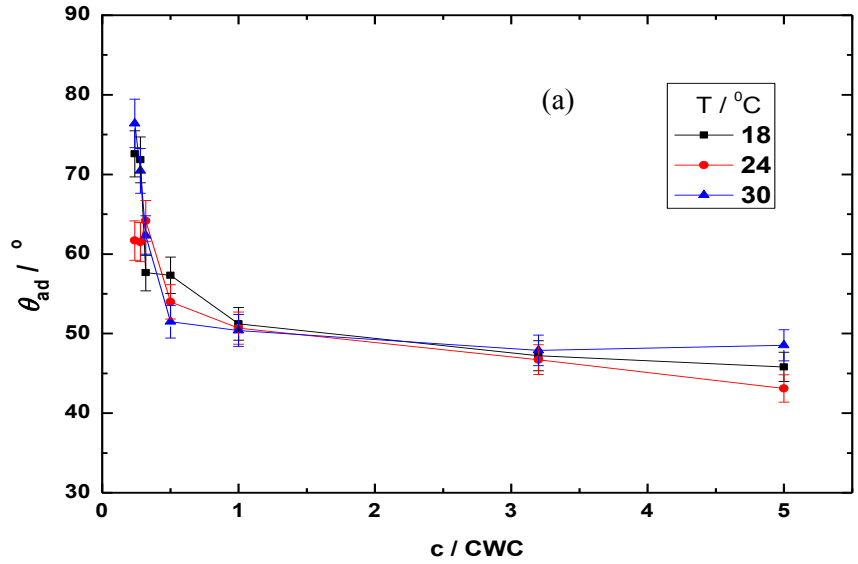
(a)
T / °C
18
24
30
θad / °
c / CWC
90
80
70
60
50
40
30
0
1
2
3
4
5

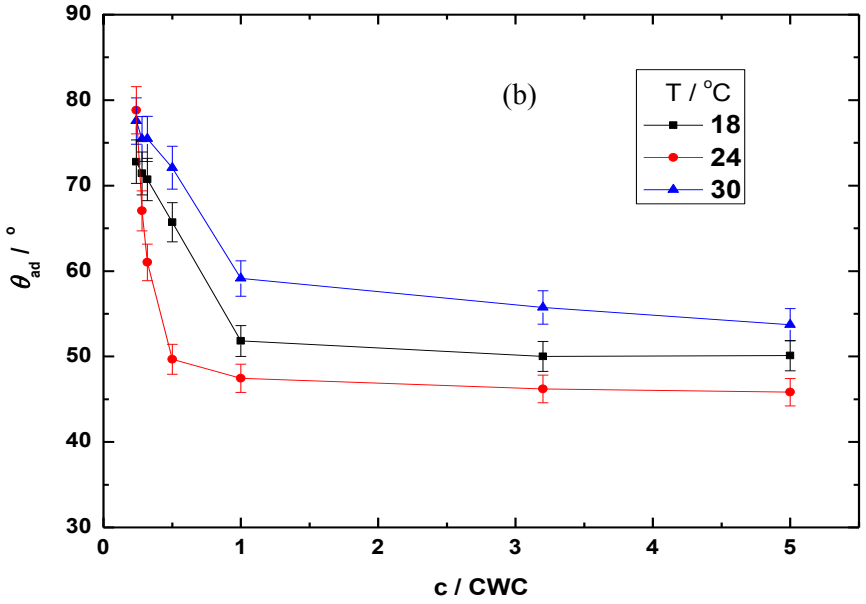
(b)
T / °C
18
24
30
θad / °
c / CWC
90
80
70
60
50
40
30
0
1
2
3
4
5

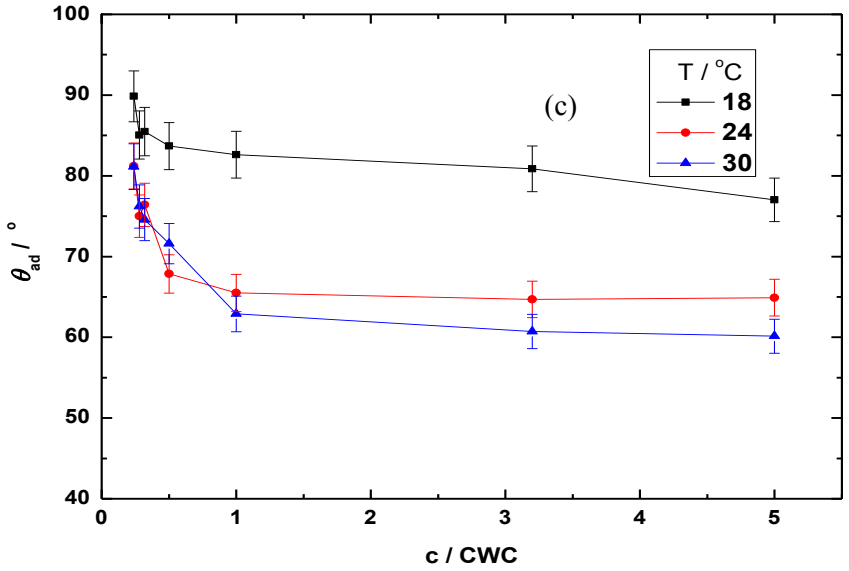

Figure 3.6: The advancing contact angle with respect to the critical wetting concentration (CWC) at constant relative humidities of, (a) 30%, (b) 55%, and (c) 90% over three measure temperatures, 18ºC, 24ºC, and 30ºC.

The concentration at which the advancing contact angle remains constant irrespective of an increase in the surfactant concentration is called the critical wetting concentration. We can observe that the critical wetting concentration is independent of the relative humidity and temperature, because the advancing angle of the droplet becomes constant at the same concentration in the measurements made, from Figure 3.4 and Figure 3.5. The results obtained in Figure 3.6 are qualitatively consistent with experimental data from literature for the analysis of the spreading dynamics of trisiloxane surfactants on hydrophobic substrates by Ivanova et al. [6] and Lee et al [19], where the critical wetting concentration, (CWC) of Silwet L-77 surfactant was determined as 2.5g/mol, (2.5CAC).

3.1.3 Spreading of Nanoparticle Dispersions

We have carried out the study of suspensions of nanoparticles 0.02μm, 0.2μm, and 1μm diameters unto PTFE-AF surfaces at different particle concentration, at two temperatures 22ºC and 35ºC and 30% constant relative humidity. Figure 3.7a shows that *L* remains constant within experimental uncertainty for the three particles particles measured, at the two temperatures and for all the volume fractions studied. This

behaviour is completely different from what has previously been described for Silwet L-77 solutions and sodium dodecyl sulphonate (SDS), [6] or pure fluids [106], it appears to infer that these suspensions do not spread after deposition. Eventhough the error bars of θ and V are large, see Figure 3.7 to allow one to reach a definative conclusion, it seems that both quantities decrease as time increases. The volume, V should remain constant during spreading but that is not the case in the data shown in Figure 3.7b and Figure 3.7c seem to correspond to the early part of the first stage of evaporation. From literature it has been proven that the pinning of the contact line drives evaporation, therefore the conclusion that the compared time regime for the spreading nanoparticle dispersions corresponds to the early stage of the first evaporation stage is valid.

We have presented the results for the non-spreading of nano-particles on hydrophobic substrate for 0.02μm and 1.0μm particle sizes in Figure 3.7 and Figure 3.8 respectively, the results are qualitatively correct for interaction between hydrophobic dispersed suspension and hydrophobic substrate. These experiments were carried out for two other temperatures and at constant relative humidity, the change in volume along with decreasing contact angle indicates the first stage of evaporation, no spreading was observed irrespective of the particle size and volume fraction. In the subsequent sections we will present results for the adsorption of these nanoparticle dispersions onto hydrophobic PTFE-AF substrates to study and understand the dynamics at the solid-liquid interaction.

In Figure 3.8 we show the experimental results for the non-spreading of 0.1μm sized particles,at 24ºC, 30% relative humidity. The dynamics is consistent with what is observed for smaller particle sizes as shown in Figure 3.7.

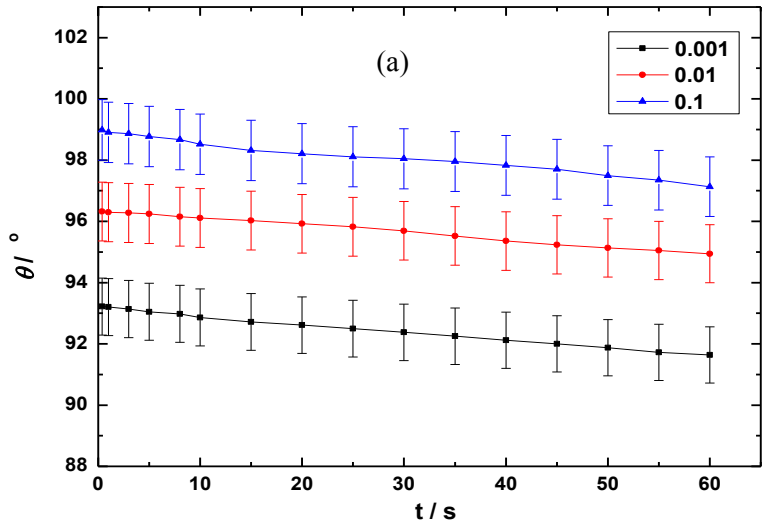
(a)
0.001
0.01
0.1
θ / °
t / s
102
100
98
96
94
92
90
88
0
10
20
30
40
50
60

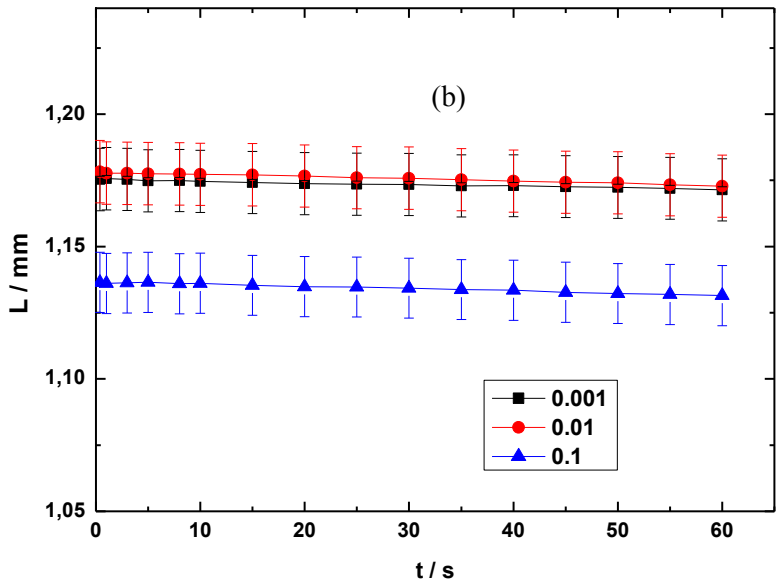
(b)
0.001
0.01
0.1
L / mm
t / s
1,20
1,15
1,10
1,05
0
10
20
30
40
50
60

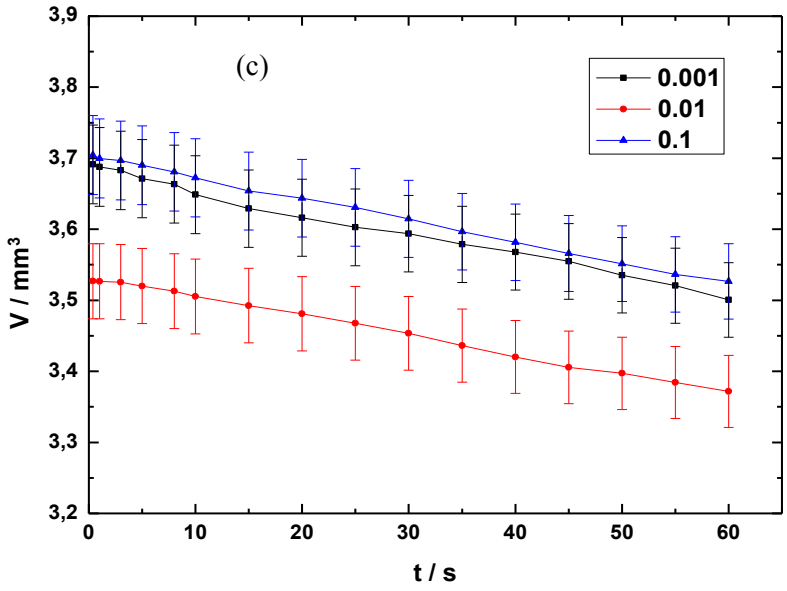

Figure 3.7: Time dependence of (a L, (b) θ , and (c) V for the dispersions of latex nanoparticles (0.02µm) at 22ºC and 30% relative humidity. The labels indicate the particle volume fraction and the experiments were done using a PTFE-AF substrate.

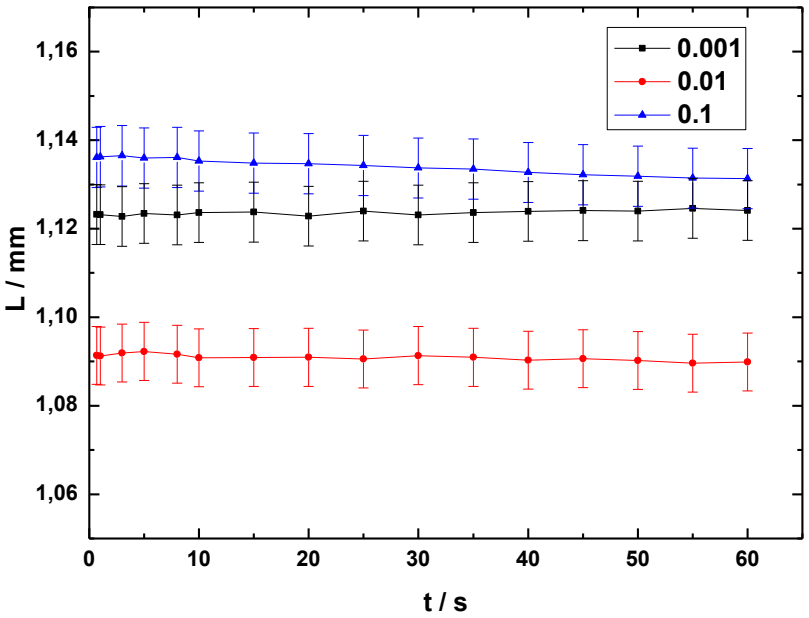

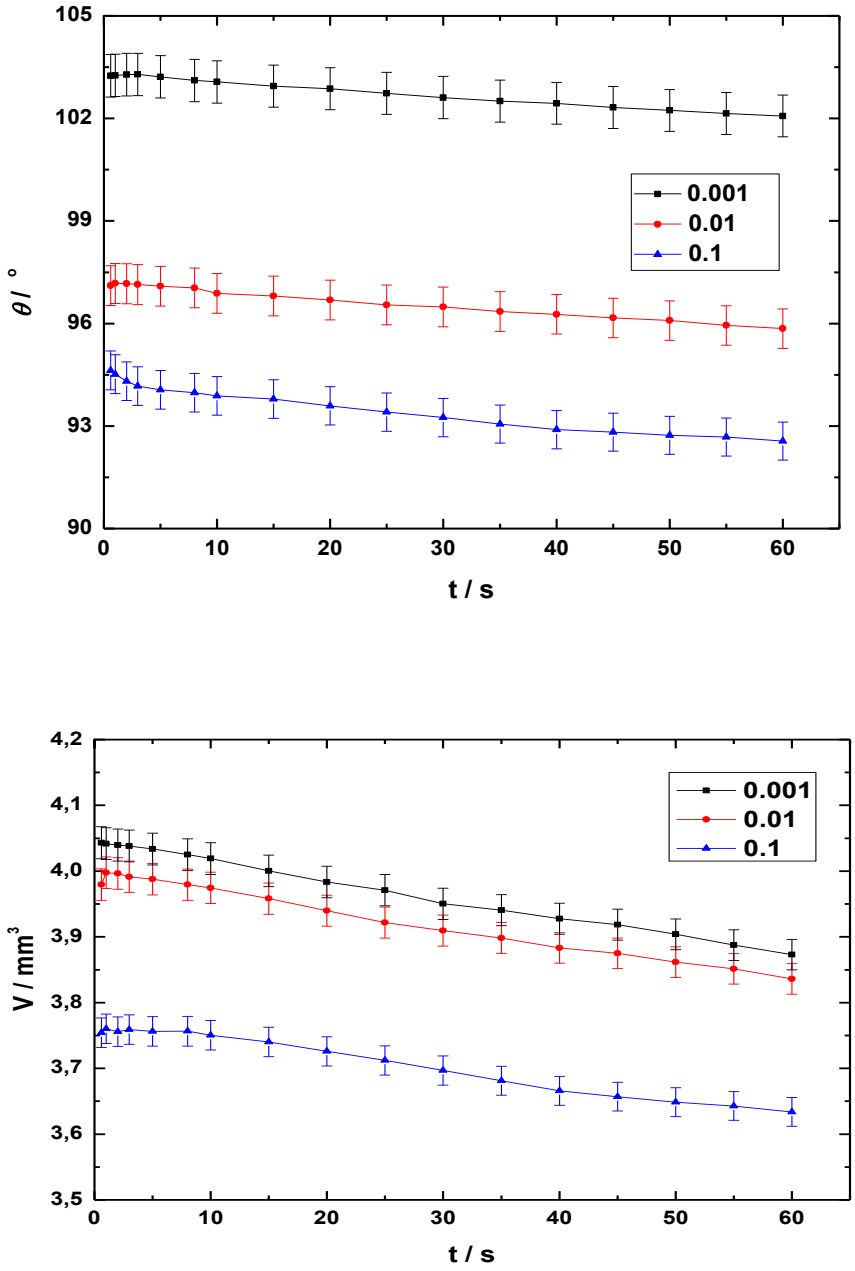

Figure 3.8: Time dependence of (a) L, (b) θ , and (c) V for the dispersions of 1.0µm paticle size latex nanoparticles at 22ºC and 30% relative humidity, the labels indicate the particle volume fraction and the experiments were done using a PTFE-AF substrate.

3.2 Evaporation

3.2.1 Evaporation of Droplets of Surfactant Solutions.

The first evaporation stage begins at the end of the spreading regime when the droplet radius has reached its maximum value, L_0 and the contact angle has reached the value of the advancing contact angle, θ_a. Evaporation has been described as a physical process that is influenced by physical parameters such as vapor pressure, temperature and humidity as we show in the results presented herein. The whole spreading and evaporation process for Silwet L-77 solutions are shown in Figure 3.8 and Figure 3.9 for constant temperature 18ºC, and 30% and 90% relative humidity respectively. The relative humidity and temperature affect the duration of evaporation and the dynamics of the evaporation process, a subject we will discuss further in this work.

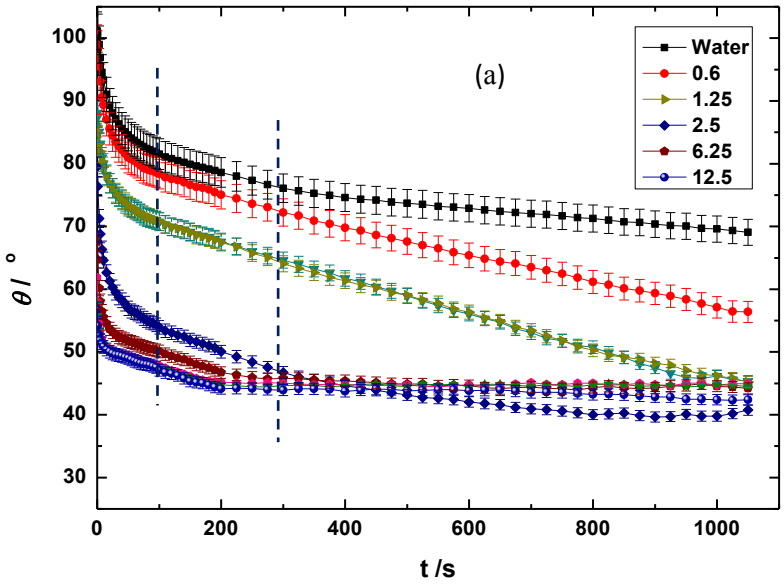

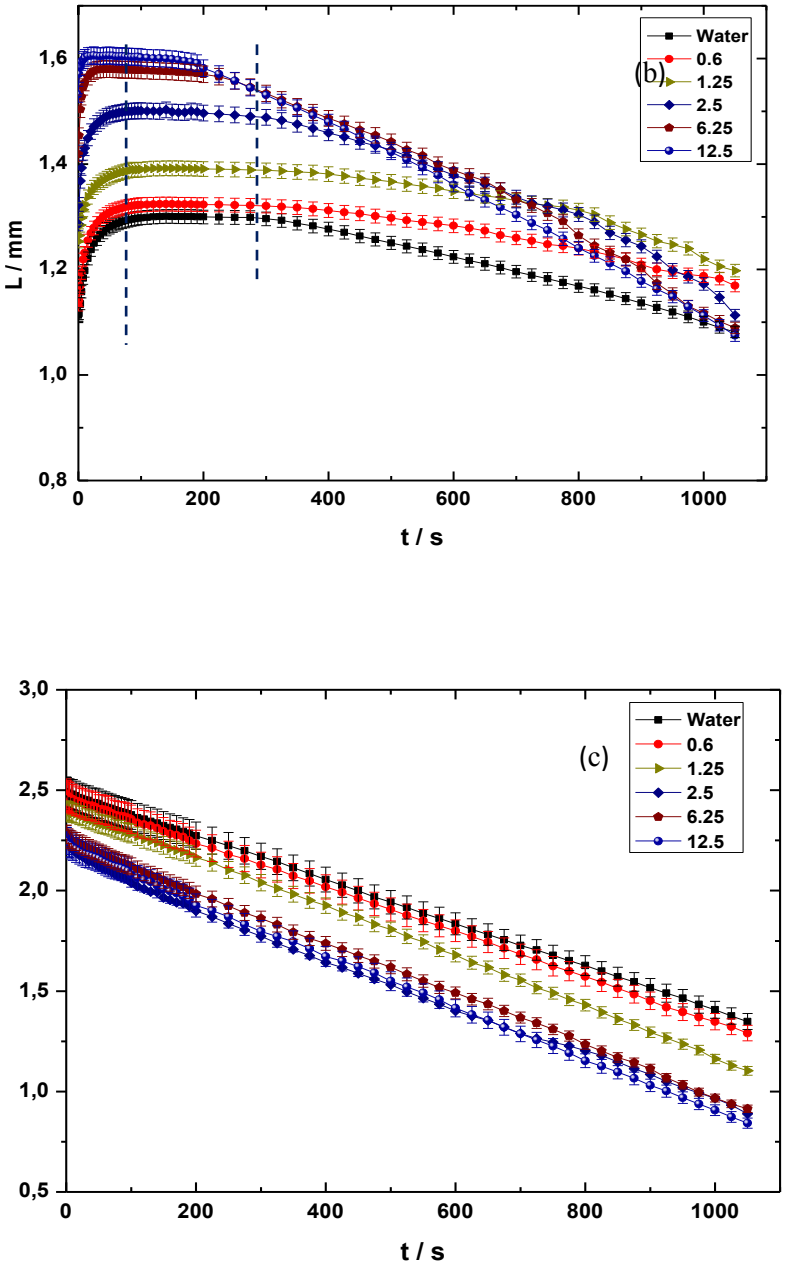

Figure 3.9: Time dependence of (a) *θ, (b) L,* and (c) *V* for Silwet L-77 solutions at different concentrations for the whole spreading –evaporation process at 18ºC and 30% relative humidity. The broken lines in figures (a) and (b) indicate the limit between the different evaporation stages.

One can observe that the contact angle of the droplet goes through its advancing contact angle and receding contact angle as predicted in the first evaporation stage, and the droplet radius reached a maximum before evaporation begins to dominate. The first

evaporation stage is represented by the parallel lines in Figure 3.9a and Figure 3.9b, the first line corresponds to the value of the advancing contact angle and corresponding maximum droplet contact area which is the beginning of evaporation, and the second line represents the end of the first stage and the beginning of the second stage corresponding to the receding contact angle. The crossing of experimental data for the droplet contact radius in Figure 3.9b, is largely due to the difference in the initial volume of droplet on which the contact radius is dependent. Doganci et al. studied the evaporation dynamics of a droplet of sodium dodecylsulfate, SDS, solutions over Teflon substrates [129]. They found that $V^{2/3}$ of the volume decreased linearly with time which meant that the evaporation of Sodium dodecylsulfate, SDS, doplets was a diffusion conrolled process because the droplet remained spherical for the duration of the evaporation. The evaporation was predominant at the three phase contact line, given that the evaporation rate of a sessile droplet is proportional to the contact radius, the linear reduction of the contract droplet radius can be applied to the volume, and thus a linear reduction of $V^{2/3}$ can be used to confirm diffusion controlled evaporation. From Figure 3.9 (c) we can conclude that the same mechanism holds for Silwet L-77 solutons. The duration of evaporation in these experiments is however affected by the relative humidity when compared with the duration of the experiments in Figure 3.10, for the same concentrations, and using the same PTFE-AF substrates.

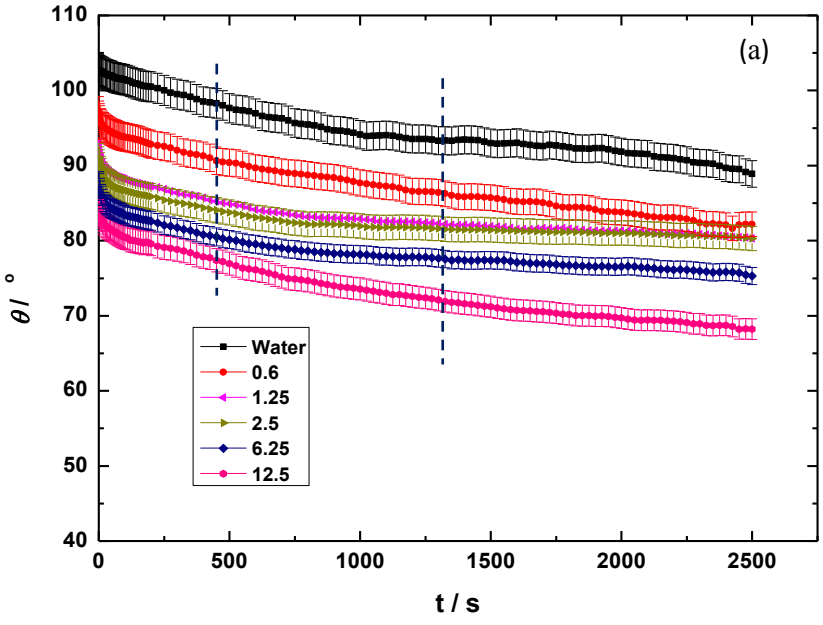

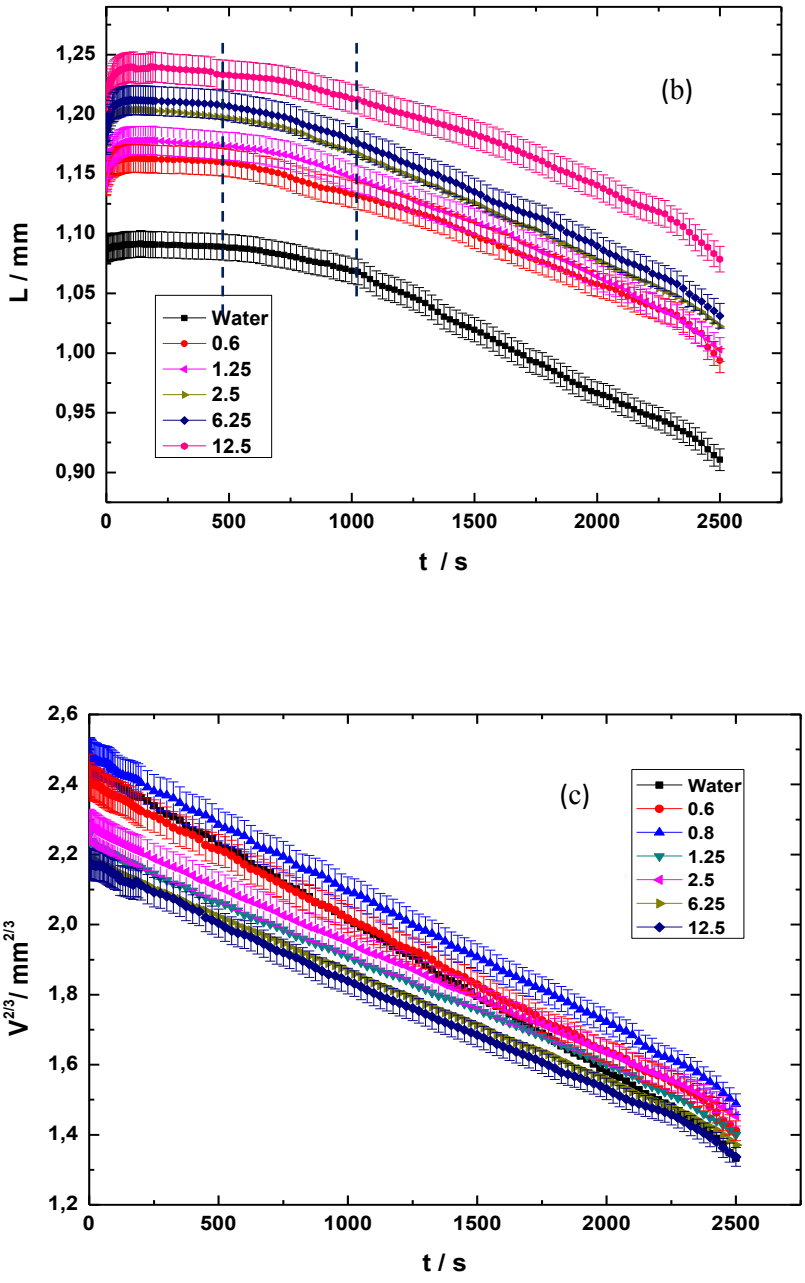

Figure 3.10: Time dependence of (a) *θ, (b) L,* and (c) *V* for Silwet L-77 solutions at different concentrations for the whole spreading –evaporation process at 18ºC and 90% relative humidity. The broken lines in figures (a) and (b) indicate the limit between the different evaporation stages.

As expected, it is observed in Figure 3.10 that at high relative humidities the evaporation dynamics is slower, the molecules have a higher energy barrier to overcome

for molecules to move from the solid-liquid interface to the solid-vapor interface. Another interesting observation is that during the second evaporation stage for concentrations below the CAC, no constant contact angle stage is observed, for all the temperatures and relative humidities measured, see Figure 3.9a and 3.10a. We propose that this deviation from the expected dynamics is due to to the change in the concentration of the droplet as evaporation progresses which leads to a change in the adsorption at the liquid-solid and liquid-vapor interfaces. Above the CAC, the second stage of evaporation is consistent with the behaviour found in pure fluids, this is due to an over saturation of surfactant solution in the droplet and regardless of an increase in concentration of surfactant due to evaporation the contact angle remains constant for the duration of evaporation, an idea we will develop and discuss further in this work. In Appendix I the first and second stages of evaporation are presented for other temperatures and relative humidities studied.

The time scales for the stages of evaporation for surfactant solutions for concentrations where there is an influence from the solid-liquid interface and the constant contact angle mode is not observed uring evaporation below the CAC is shown in Tables 3.1 to 3.3. The Tables show that in real experiments the second stage of evaporation in Silwet L-77 for low surfactant concentrations does not proceed with the constant contact angle.

3.2.2 Evaporation of Nanoparticle Dispersions

The study of the evaporation of latex nanoparticles has been carried out, and the results are shown in Figure 3.11 and Figure 3.12 for 0.02μm and 1.0μm sized particles respectively, where it is observed that the dynamics of evaporation dynamics followed the predicted two stages of evaporation; the first stage of evaporation where the contact angle decreases while the contact radius remains constant, followed by a stage characterized by a decrease in the contact radius and constant contact angle, the stages are seperated by the broken lines. For nanoparticles in addition to particle concentration, one might guess that particle could play a vital role in the evaporation dynamics. As we mentioned in Section 3.1.3, nanoparticles do not show a spreading process withing the time window measureable with the experimental setup described herein. The evaporation of nanoparticle dispersion shown by the reduction of the volume, see Figure 3.11c, is linear. $V^{2/3}$ decreases linearly over the duration of evaporation, the droplet evaporation follows a similar dynamics described in the experimental results of Doganci et al. [129], where the decrease of of the volume ($V^{2/3}$)

was also linear. It can be concluded that the evaporation dynamics of nanoparticle dispersions is driven by diffusion, the constant contact radius also drives evaporation.

Table 3.1: Evaporation stages at 30% Relative Humidity

	C/CAC	0.6	0.7	0.8	1.25	2.5
Temperature						
18	**1st Stage**	50s-5,15mins	60s-,15mins	45s-7,30mins	60s-6,40mins	60 sec-6mins
	2nd Stage	6,15 -30mins	5,30 -30mins	7,30 -30mins	7 -30mins	6,15 -30mins
24	**1st Stage**	60s-6mins	50s-6mins	15s-5mins	40s-8,20mins	15s-5mins
	2nd Stage	6,15 -30mins	6,15 -30mins	5- 30mins	8,20- 30mins	5- 30mins
30	**1st Stage**	1,05-5mins	45s-5mins	50s-5mins	45s-5mins	40s-5,25mins
	2nd Stage	5,25-24mins	5,25-24mins	5,25-24mins	5,25-24mins	5,50-24mins

Table 3.2: Evaporation Stages at 55% Relative Humidity

	C/CAC	0.6	0.7	0.8	1.25	2.5
Temperature						
	1st Stage	60sec-8mins	1,20-8mins	50sec -8mins	50sec -8mins	1,10 -8mins
18	**2nd Stage**	8,15sec-40mins	8,15sec-40mins	8,15sec-40mins	8,15sec-40mins	8,15sec-40mins
	1st Stage	1,50- 10mins	1,25- 14mins	50s- 8,50mins	60s- 12mins	40s- 10mins
24	**2nd Stage**	10,15-40mins	14,15-40mins	9-40mins	12,15-40mins	10,15-40mins
	1st Stage	55s- 10mins	1,10- 7mins	1,10- 7mins	45s- 5,30mins	1,50- 11,30mins
30	**2nd Stage**	8,45-40mins	7,15-40mins	7,15-40mins	7,15-40mins	11,45-40mins

Table 3.3: Evaporation Stages at 90% Relative Humidity

	C/CAC	0.6	0.7	0.8	1.25	2.5
Temperature						
18	**1st Stage**	30sec-11mins	45sec-15mins	15sec-14mins	15sec-11mins	15sec-12mins
	2nd Stage	11- 40mins	15,15- 40mins	14,15- 40mins	11,15- 40mins	12,15- 40mins
24	**1st Stage**	1-11mins	1,30-15,30mins	20sec-14mins	75sec-18mins	20sec-16mins
	2nd Stage	11- 40mins	15,45- 40mins	11,15- 40mins	18,25- 40mins	16,15- 40mins
30	**1st Stage**	1,10-9,40mins	1-10,25mins	20sec-7,30mins	30s-10,40mins	30s-10,20mins
	2nd Stage	10- 40mins	10,50- 40mins	7,45- 40mins	11- 40mins	10.40- 40mins

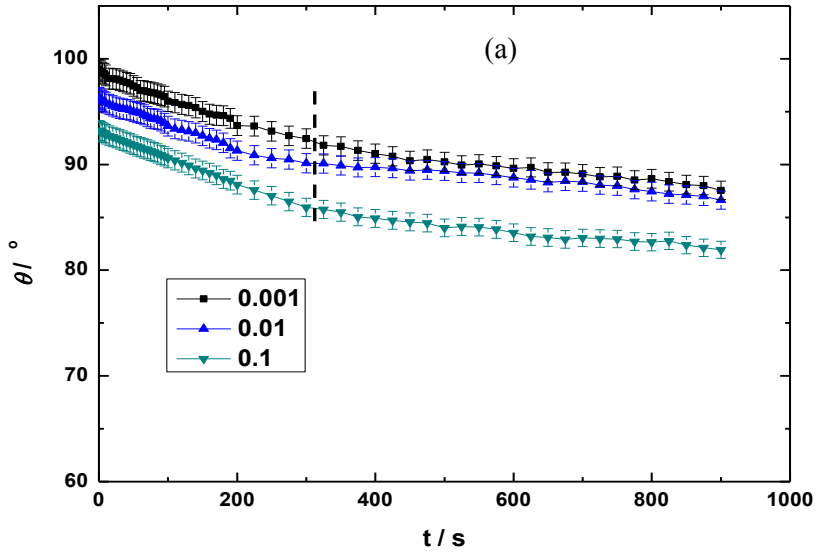
(a)
θ / °
t / s
0.001
0.01
0.1
100
90
80
70
60
0
200
400
600
800
1000

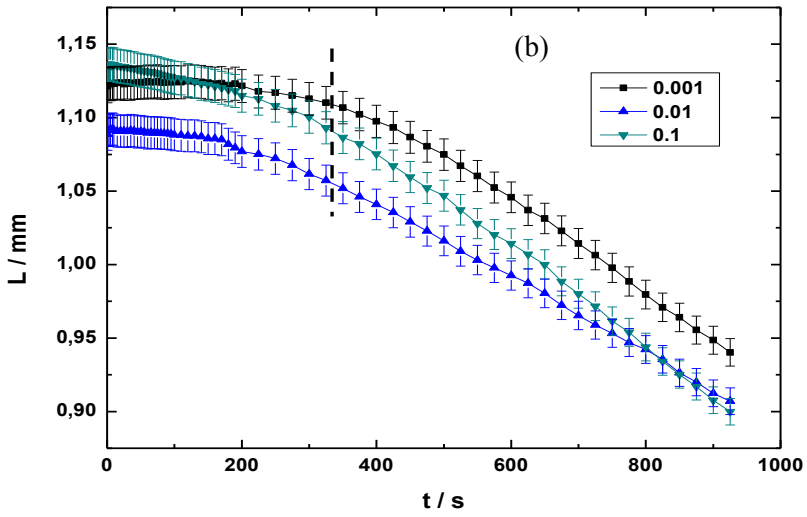
(b)
L / mm
t / s
0.001
0.01
0.1
1,15
1,10
1,05
1,00
0,95
0,90
0
200
400
600
800
1000

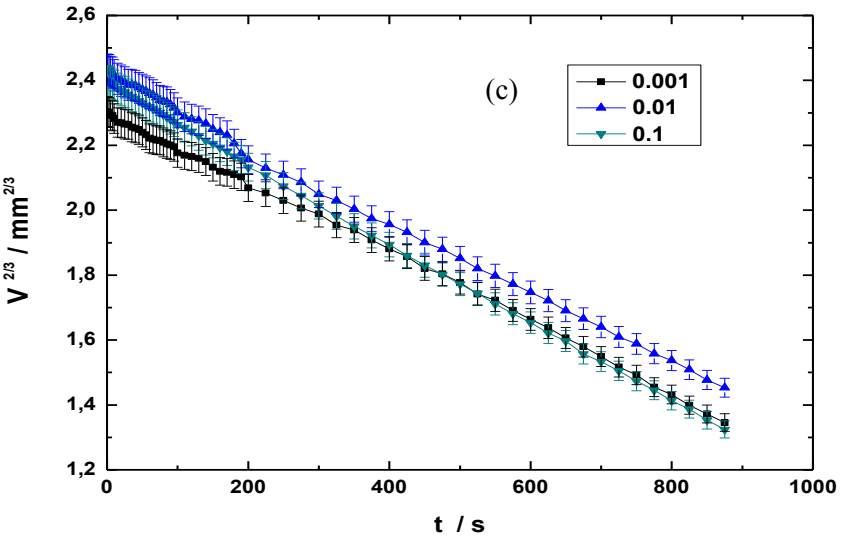

Figure 3.11: Time dependence of (a) θ, (b) L, and (c) V for nanoparticle dispersions (particle size 0.02μm) in terms of volume fractions for the whole evaporation process at 22ºC and 30% relative humidity.

We observe that physical properties such as temperature and relative humidity also influence the evaporation rate of nanoparticle dispersions, and that neither the particle size nor the volume fraction of the dispersion seems to play any role in the dynamics of evaporation nor change the rate of evaporation. In Figure 3.12 we show the evaporation dynamics of the same particles and at higher temperatures.

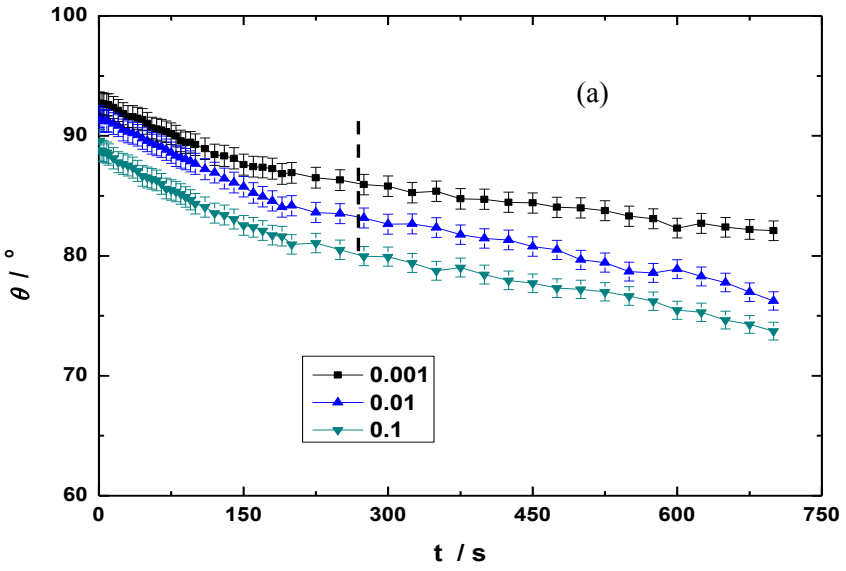

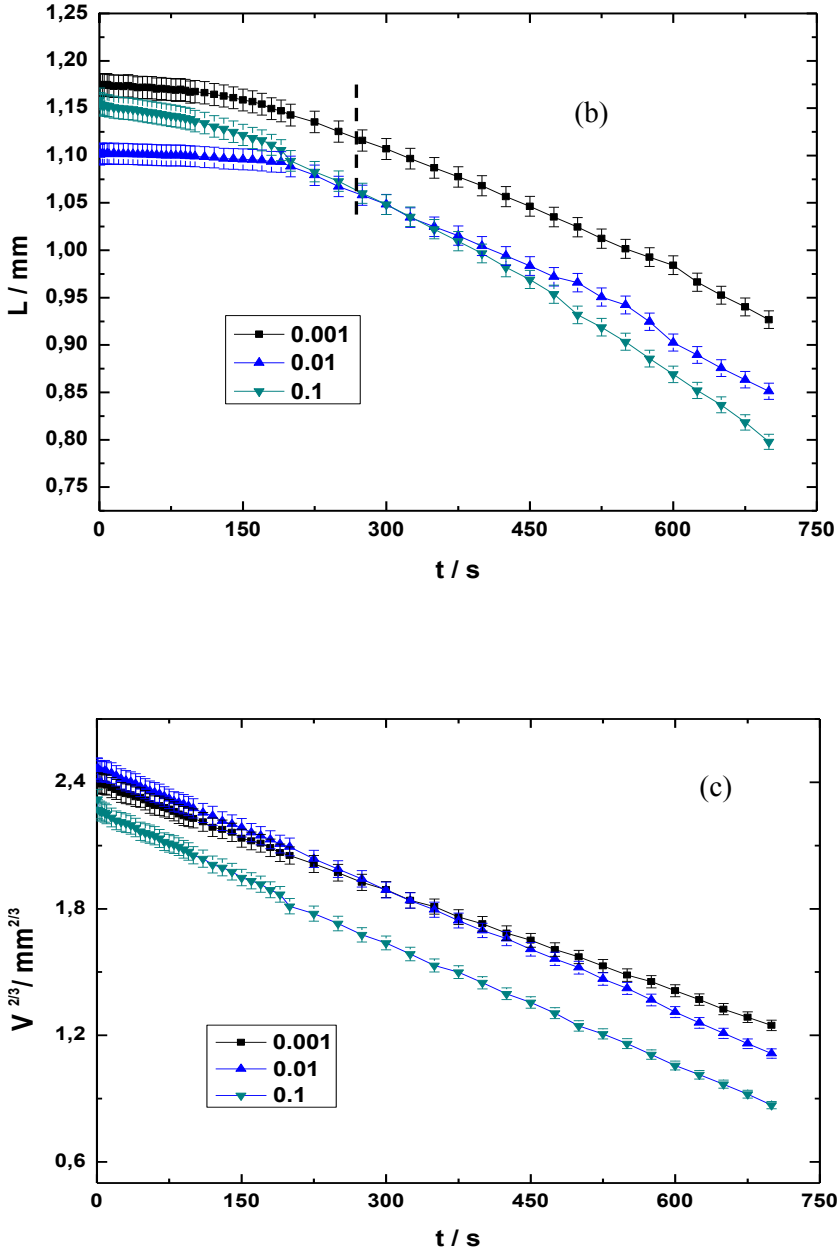

Figure 3.12: Time dependence of (a) θ, (b) L, and (c) V for nanoparticle dispersions (particle size 0.02µm) in terms of volume fractions for the whole evaporation process at 35ºC and 30% relative humidity.

The evaporation dynamics at higher temperatures remains consistent with the two stage evaporation process, however we observed that the rate of evaporation is faster due the increase in temperature,. The decrease of the contact angle as the particle concentration is increased is also observed, we can thus conclude that the particle distribution

influences the contact angle of the evaporating droplet but not necessarily the evaporation dynamics of nanoparticle dispersions used in this work.

The pinning-depinning mechnism (also referred to as stick-slip motion) has not been observed in in these experiments within the volume fraction and particle size of the nanoparticle dispersions used. Sefiane [101], carried out experiments on the evaporation of blood serum on glass surfaces was studied, and he found that the blood droplets were pinned and formed patterns which have been used in disease diagnosis. Deegan and co-workers [87], found the a stick-slip motion during evaporation of suspensions of coffee droplets, but not salt solutions onto mica surfaces, and they concluded that the stick-slip mechanism was dependent on surface roughness or chemical heterogeneities of the suspensions. The behavior and mechanism of this phenomenon in the experiments carried out herein can have been influenced by the non-interaction of the dispersion and the solid at the interface, and the chemical structure of the nanoparticle dispersion may be similar (hydrophobic) and as such will lead to a repulsion between the dispersion and substrate while the droplet remained pinned.

3.2.3 Coffee Ring Effect

Besides understanding the dynamics of evaporating sessile droplets of nanoparticle dispersions, the formation of patterns on the substrate after evaporation is also an interesting phenomena, it has frequently been referred to as the coffee ring effect. Sefiane [86], studied the pattern formation made from blood serum droplets onto glass, they found that the evaporation at the contact line induced an internal flow of fluid towards the edge of the droplet, this flow lead to an accumulation of concentrated dispersed particles that formed rings. The patterns formed have been used to diagnose ailments that change the mophorlogy of blood droplet, a comparison was made between the pattern formed from a healthy blood droplet and they studied the deviations from the patterns made by the dried droplet of a healthy person. Deegan et al. [104] studied the the pattern formation of coffee stains and salt solutions onto mica surface, and found the droplet self-pinned regularly in the case or coffee droplets and irregularly in salt solutions, and they concluded that pattern formation was as a result of competition between pinning and dewetting as a result of the solid-liquid interaction at the interface.

Some photographic images of the patterns found in this work are shown in Figure 3.13 and Figure 3.14. for particle diameter 1.0μm in evaporating conditions of 22ºC and 35ºC respectively, at constant relative humidity of 30%. From Figure 3.13, we observe that

the droplet remains spherical throughout the evaporation given the circular shape of the residue, the influence of temperature and volume fraction on pattern formation is observed when we compare the images for patterns formed from evaporation at 22ºC and 35ºC. From Figure 3.13 and Figure 3.14, we observe that the particle deposition increases as the volume fraction is increased, and when we compare these images in Figure 3.13 with the images in Figure 3.14 for higher temperatures, the same spherical shape is maintained but the pattern of deposition changes, for instance a distinct ring shape observed in Figure 3.13(ii) for 0.01 volume fraction 22ºC, is observed in 0.001volume fraction at 35ºC.

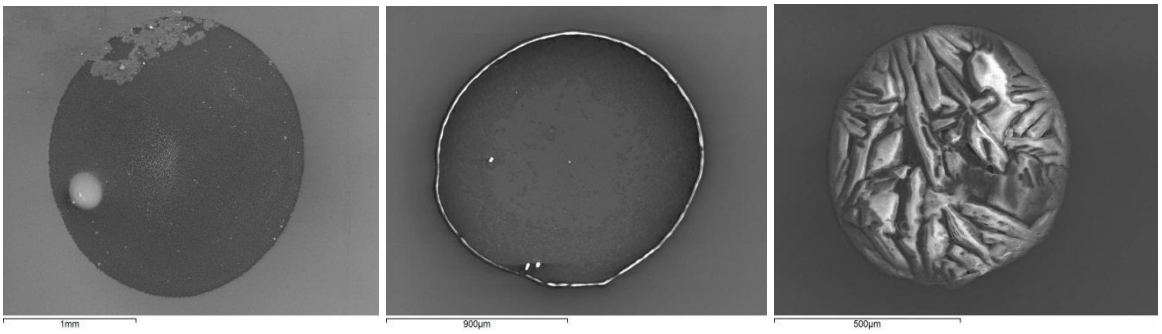

(i) (ii) (iii)

Figure 3.13: Morphology of dried droplets of nanoparticle dispersions for volume fractions of (i) 0.001, (ii) 0.01 and (iii) 0.1 at 22ºC, 30% relative humidity, for particles of 1.0µm of diameter.

The appearance of the distinct ring in lower volume fractions in Figure 3.14(i) for higher temperature can be as a result of increased energy level of dispersed particles, and the particles move at a faster rate to the triple phase contact line.

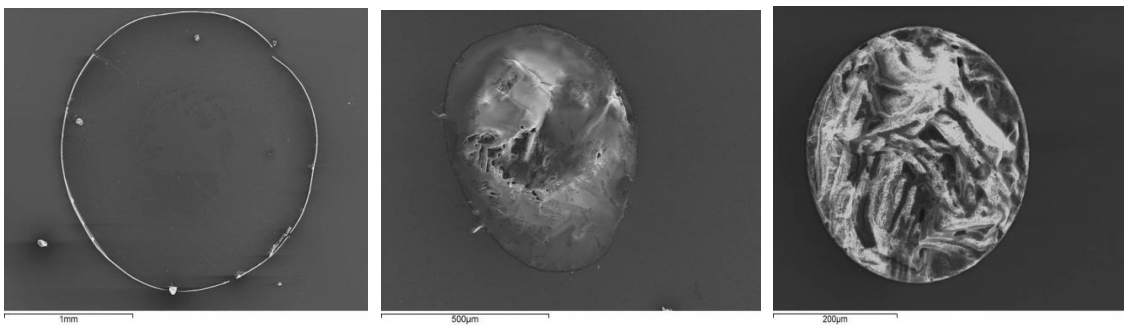

(i) (ii) (iii)

Figure 3.14: Morphology of dried droplets of nanoparticle dispersions for volume fractions of (a) 0.001, (ii) 0.01 and (iii) 0.1 at 35ºC, 30% relative humidity, and particles of 1.0µm of diameter.

The ring shape observed is because during evaporation of the droplet of the nanoparticle dispersion remains spherical through the evaporation process from which we can infer that the evaporation is diffusion controlled, following the same mechanism as the evaporation of surfactant solutions, a fluid flow is induced inside the droplet as a result of evaporation and this transports the particles towards the three phase contact line. This flow is due to the fact that evaporation is faster at the contact line [101], a behavior that has been observed in Figure 3.13.and Figure 3.14. We can see again that the temperature of the evaporating conditions is also an important factor that influences pattern formation as it speeds the evaporation process, by speeding up the flow inside the droplets. For the highest volume fraction of particles measured, we found the particle are also deposited close to the centre, and show cracks due to stress induced during the drying of the droplet, Figure 3.14(iii), this pattern formation is consistent with results obtained from drying droplets of serum, reported by Sefiane [101].

High temperatures create a temperature gradient between the droplet and the substrate and molecules in the droplet become increasingly activated to move to the three phase contact line where evaporation is rapid, Figures 3.15-3.18 show the pattern formation in nanoparitcle dispersions for a range of particle diameter and evaporation conditions at constant relative humidity. 30% and temperatures of 22ºC and 35ºC respectively.

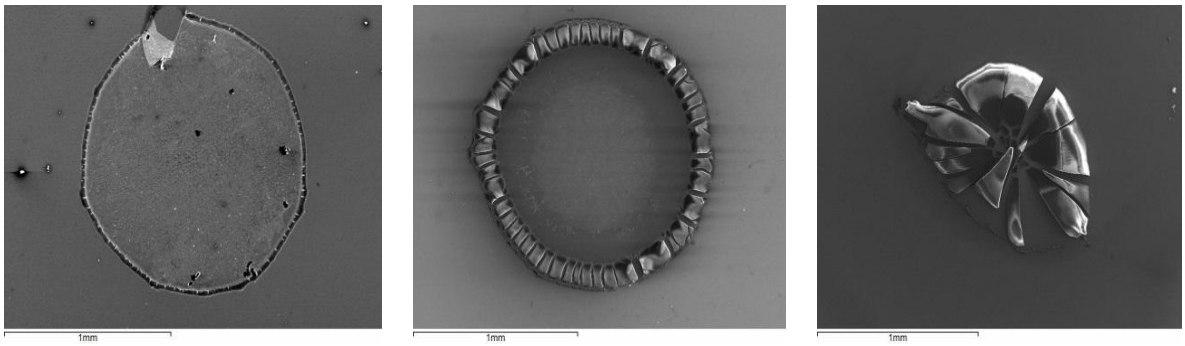

(i) (ii) (iii)

Figure 3.15 : Morphology of dried droplets of nanoparticle dispersions for volume fractions of (i) 0.001, (ii) 0.01 and (iii) 0.1 at 22ºC, 30% relative humidity, and particles of 0.02μm of diameter

(i) (ii) (iii)

Figure 3.16: Morphology of dried droplets of nanoparticle dispersions for volume fractions of (i) 0.001, (ii) 0.01 and (iii) 0.1 at 35ºC, 30% relative humidity, and particles of 0.02µm of diameter

Again the evaporation rate is faster at higher temperatures at constant relative humidity, thus the dispersed particles are transported faster to and deposited at the egde of the droplet, the ring shape formation is however not affected by temperature in this case. From the images shown in Figure 3.13 until Figure 3.18, from the nanoparticle dispersions studied in this work we may conclude qualitatively that the particles in dispersion align according to the more dominant effect of the evaporation process, either particle size or temperature gradient. The results dicussed here quaitatively corresponds with those obtained from experiments by Sefiane, [101], where blood serum was allowed to evaporate and the patterns obtained on the evaporating glass surface were as a result of concentration gradients in the blood sample as a result of different deficiencies or infections in the blood and Deegan et al. [104], where coffee droplets were used. The fact that the droplet remains spherical throughout the evaporation process is also confirmed by the coffee ring.

3.3 Surface Tension of Nanoparticle Dispersions

The surface tension for nanodispersions of 0.02µm, 0.2µm, and 1.0µm sized particles were measured and the relationship between the volume fraction, surface tension, and temperature were measured. Figure 3.19 shows the relationship between the surface tension and temperature with respect to the volume fraction, for a nanoparticle dispersion of 0.02µm particle size, results we have compared with the surface tension of water.

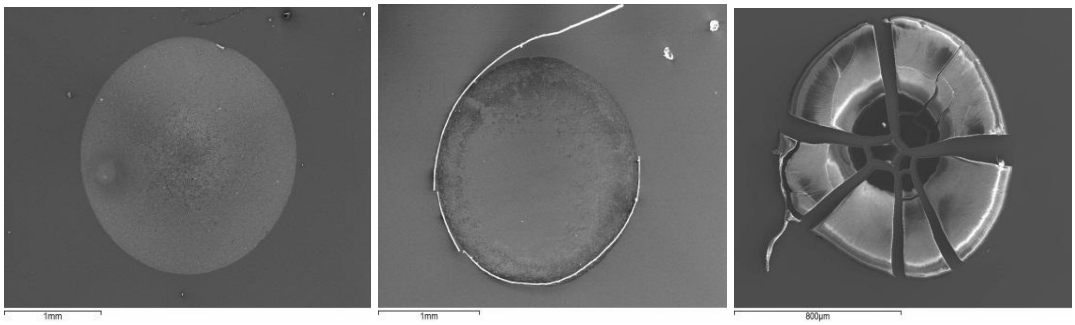

(i) (ii) (iii)

Figure 3.17: Morphology of dried droplets of nanoparticle dispersions for volume fractions of (i) 0.001, (ii) 0.01 and (iii) 0.1 at 22ºC, 30% relative humidity, and particles of 0.2µm of diameter

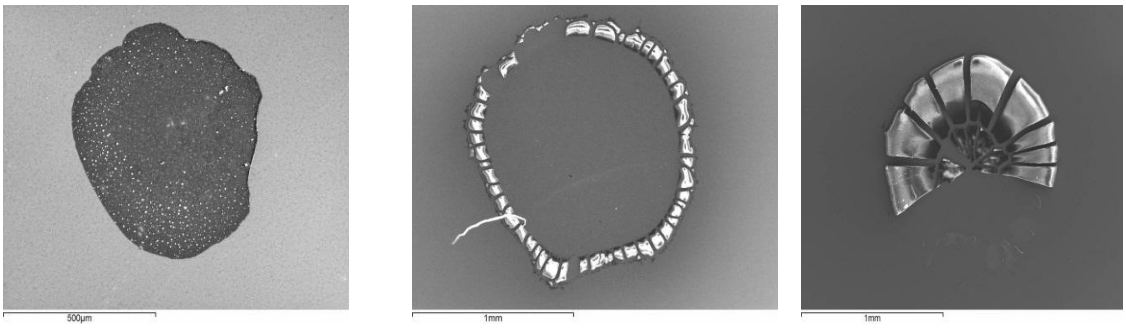

(i) (ii) (iii)

Figure 3.18: Morphology of dried droplets of nanoparticle dispersions for volume fractions of (i) 0.001, (ii) 0.01 and (iii) 0.1 at 35ºC, 30% relative humidity, and particles of 0.2µm of diameter

From the qualitative relationship between surface tension and volume fraction with respect to temperature shown in Figure 3.19, we may infer that for 0.02µm sized particles the surface tension reduces as the temperature and volume fraction are both incresed, eventhough the decrease in surface tension is small the results still indicate that the particles adsorb at the liquid-vapor interface and therefore in the case of evaporation the surface concentration (volume fraction) of nanoparticles is expected to increase as the droplet evaporates. The surface tensions for larger particle sizes at varying volume fraction were also measured and are shown in Figure 3.20 below.

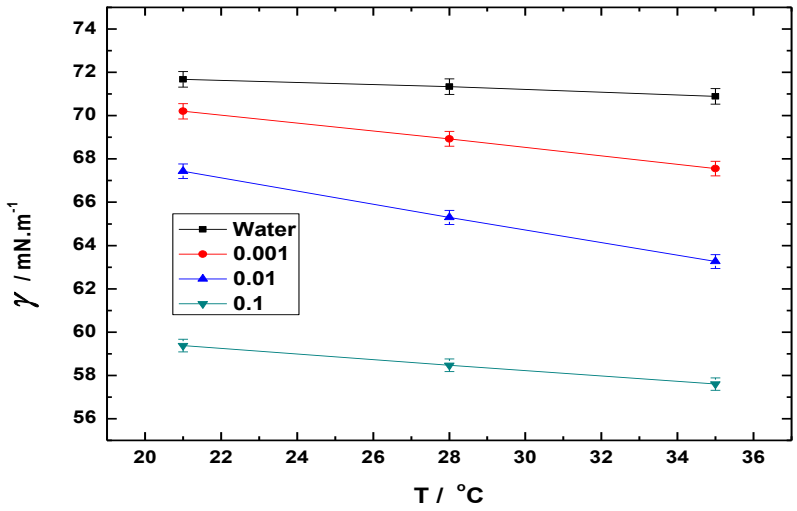

Figure 3.19: Surface tension as a function of temperature and three different volume fractions for latex nanoparticle suspensions of 0.02μm diameter

From Figure 3.20 we observe that the surface tension is more dependent on the temperature and not so much on the particle size, however an interesting find is the similarity in the behavior of low volume fractions and high volume fractions, we can explain the behaviour with the argument of a constant interaction at the solid-liquid interface for mixtures of high concentrations, then we can assume that the low and high volume fractions behave as pure liquid and the intermediate volume fraction presents an influence of the solid-liquid interaction on the surface tension. We may conclude that the surface tension is dependent on the temperature and the volume fraction of nanoparticle dispersions for all the particle sizes studied in this work.

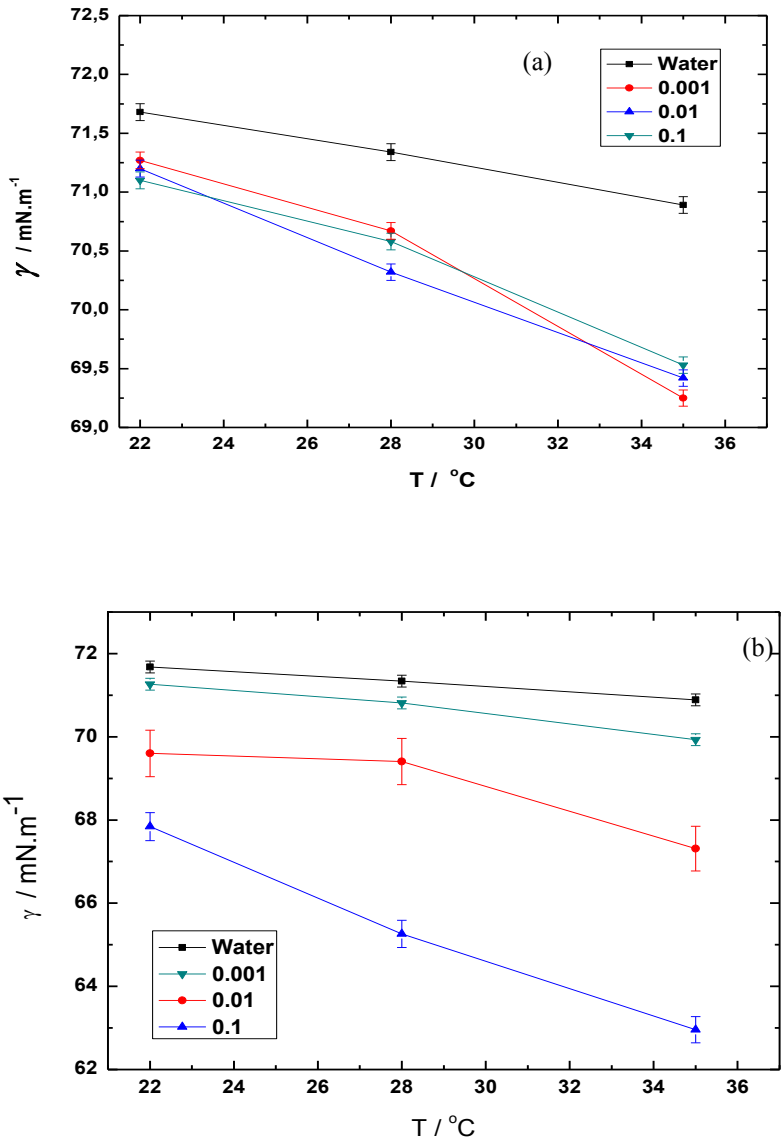

Figure 3.20: Surface tension as a function of temperature and volume fraction for latex nanoparticle suspensions of (a) 0.2µm, and (b) 1.0µm diameter

3.4 Adsorption

3.4.1 Adsorption of Surfactant Solutions

The behaviour of the contact angle depends on the adsorption of surfactant at the solid-liquid interface because it changes γ_{SL}. Therefore the spreading-evaporation kinetics is linked to both the kinetics of adsorption at the solid-liquid interface. Also one must expect that the adsorption at the liquid-vapor interface to be important for spreading and evaporation because it changes γ_{LV}, and in addition the monolayer formed acts as a

barrier for matter transfer between the liquid and the vapour. Notice that the adsorption kinetics at both the liquid/solid and at the liquid/air interfaces is coupled to that of the spreading-evaporation. Ritacco et al. [169] studied the adsorption kinetics of trisiloxanes of different chain lengths at the air/liquid interface. Those results are relevant for the present study because Silwet L77 is a mixture of three trisiloxanes with 6, 7 and 8 methoxy groups in their hydrophilic tails. The results of Ref.[169] will be used later on in this work.

The adsorption process of Silwet L-77 surfactant solution on gold electrodes covered with Teflon was studied using the quartz crystal micro-balance. Figure 3.21, shows the results for the adsorption of Silwet L-77 solution at 24ºC and 30%, which are close to the conditions used for the evaporation experiments. One can observe that the adsorption rate of surfactant solutions increases as the concentration is increased. As expected the adsorbed amount of surfactant molecules at each concentration increased gradually until it reaches a plateau, whose value increases with concentration.

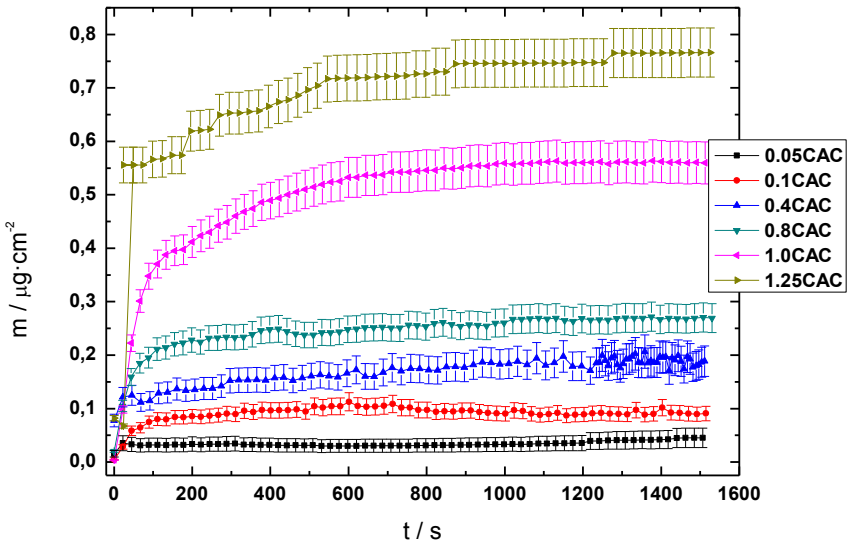

Figure 3.21: Adsorption of Silwet L-77 solutions onto Teflon AF at 24ºC and 30% relative humidity.

A comparison of the experimental results with those of Ritacco et al [156] points out that the adsorption at the solid/liquid interface is quite faster than at the liquid/air interface. However, one must not consider that after aprox. 500 s the solid liquid interface has reached equilibrium when the drop is evaporating because the bulk concentration continuously increases, and therefore the adsorbed mass moves from one

of the curves of Figure 3.21 to the upper one as time increases. A comparison of the plateau value for c = C.A.C. in Figure 3.21 with the corresponding value of adsorption at the liquid/air interface (Figure 2.b of Ref. [156]) points out that the adsorption at the solid/liquid interface is about 15 times higher than at the liquid/air one. Hence, it is necessary to calculate the adsorption curves as evaporation proceeds starting from a given concentration c_0.

The following protocol can be used to obtain the time dependence of the mass adsorbed onto the solid during evaporation, m_{dro}, from the results shown in Figure 1. For the sake of example we will focus on the drop with initial concentration c/CAC = 0.05, the same has been followed for the drops with other initial concentrations.

a) During evaporation the bulk concentration of the drop at time t is given by

$$c_t = \frac{c_0 V_0}{V_t} \qquad 3.1$$

where V_t is the volume of the drop at time t of evaporation, which is obtained from the image analysis of the experimental data.

b) Using the values of c_t we have obtained the times for which c_{dro}/CAC of the drop with c_0/CAC 0.05 are equal to 0.1, 0.4, 0.8, 1.0, which we call $t_{0.1}$, $t_{0.4}$, $t_{0.8}$, $t_{1.0}$, respectively.

c) Using the curves of Figure 3.21 we calculate the adsorbed amounts for $t_{0.1}$ (from the curve corresponding to c/CAC=0.1), $t_{0.4}$ (from the curve corresponding to c/CAC=0.4), $t_{0.8}$ (from the curve corresponding to c/CAC=0.8), $t_{1.0}$ (from the curve corresponding to c/CAC=1.0). These adsorbed amounts are called m_{ev}, and are plotted in Figure 3.22 for the drops of the different initial concentrations. Notice that for c_0/CAC = 0.1 we will have the same value of m_{ev} at t = 0 than for c_0/C = 0.05 at $t_{0.1}$, and so on. The results show that m_{ev} increases quite fast with evaporation time, and eventually it should reach a plateau for high values of t. In order to obtain m_{ev} for higher t's, it would be necessary to measure the adsorption kinetics for values of c well above the CAC. However, this is not the range of concentrations for which discrepancies between experimental data of the second evaporation stage and the pure fluid theory are found.

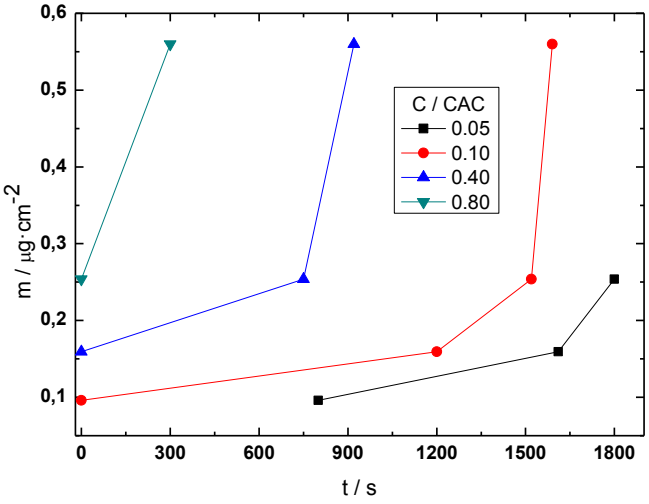

Figure 3.22.- Time dependence of the mass adsorbed onto Teflon AF during the evaporation time for different initial bulk concentrations of the drops.

Guzman et al. [157] found that the adsorption kinetics of polymers is a bimodal process, and that during the adsorption process there is a fast adsorption regime, which could be related to rapid transportation of polymer chains deposited at the interface. They found that this process was not diffusion controlled because its time-dependence was not consistent with the $t^{1/2}$. The second, slower, regime could be related to the intenal reorganization of the polymer chains. The adsorption kinetics of surfactant molecules has been described using the model proposed by Raposo et al. [158]:

$$m = A_1\left(1 - e^{-\frac{t}{\tau_1}}\right) + A_2\left(1 - e^{-\frac{t}{\tau_2}}\right) \qquad 3.2$$

where m is the mass adsorbed per unit area, A_1 and A_2 are amplitudes, and τ_1 and τ_2 are the characteristic times of the fast and slow adsorption processes respectively. The second term in Eq. 3.2 accounts for the reorganization of the solution after the adsorption at the interface. Therefore Eq. 3.2 can then be rewritten for maximum surface adsorption, as Eq. 3.3.

$$m = m_\infty - A_1 e^{-\frac{t}{\tau_1}} - A_2 e^{-\frac{t}{\tau_2}} \;;\; m_\infty = A_1 + A_2 \qquad 3.3$$

m_∞ being obtained from the experimental plateau of the m vs. t plot at high adsorption times (see Figure 3.21. In order to overcome the high correlation of the parameters A_i and τ_i when a set of data is fitted to the sum of two exponentials, we have used the

following procedure: If $\tau_1 << \tau_2$, it is possible to fit the long-time data to Eq. 3.4. A typical example of the quality of the fit of experimental data to Eq. 3.4.a is shown in Figure 3.23. Once A_2 and τ_2 have been obtained, one can use Eq. 3.4.b to obtain A_1 and τ_1.

$$\ln(m_\infty - m) = \ln A_2 - \frac{t}{\tau_2} \qquad 3.4.a$$

$$\ln(m_\infty - m - A_2 e^{-\frac{t}{\tau_2}}) = \ln A_1 - \frac{t}{\tau_1} \qquad 3.4.b$$

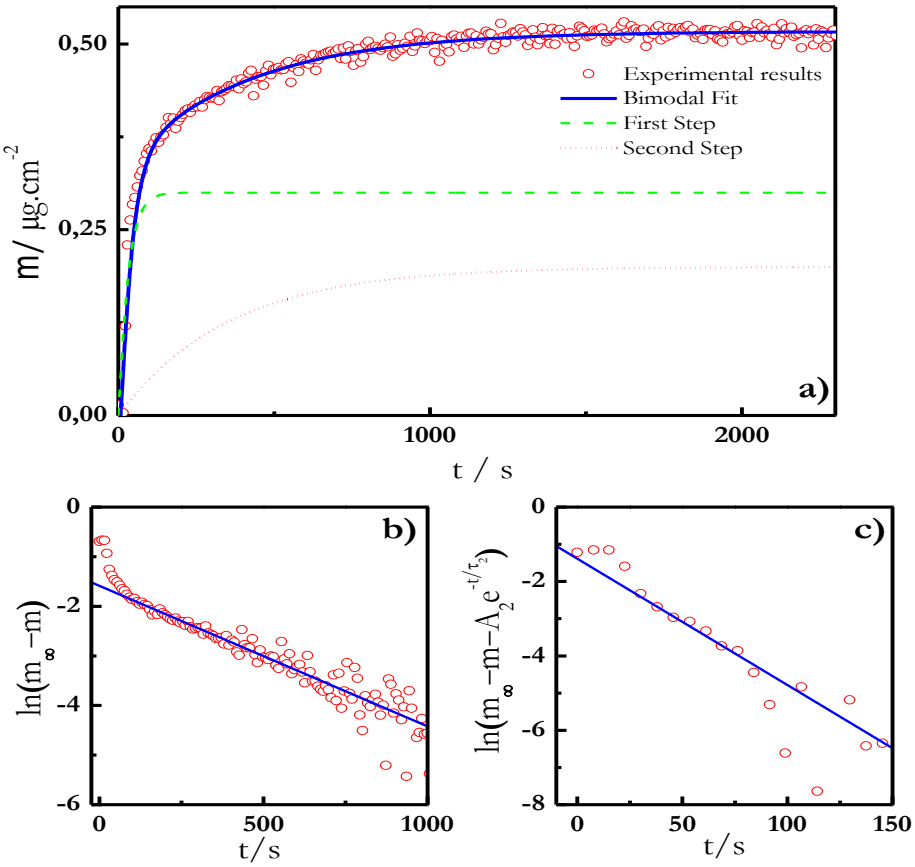

Figure 3.23.- Typical plot of an adsorption kinetics experiment of Silwet L77 onto Teflon AF surface, and its fit to Eq. 3.2 (a), Eq. 3.4.a (b) and Eq. 3.4.b (c). The data correspond to concentration of surfactant c = C.A.C.

The parameters leading to the best fit of the adsorption kinetics are given in Table 3.2. It is observed that the characteristic time for the first process is rather similar for all the

concentrations, and within the uncertainty of the fit except for the lowest surfactant concentration where the quality of the data and of the fit are worse. The values of τ_2 decrease as c increases being again the lowest concentration the exception. As expected, $m_\infty = A_1 + A_2$ increases with concentration. The quality of the fit shown in Figure 3.213.a is representative of all the experiments performed for concentrations close to and above the C.A.C., as it can be observed in Figure 3.24. Figure 3.24 shows the comparison between all the experimental data and the best fit to Eq. 3.2. It must be noticed that at low surfactant concentrations and short times the adsorption is low, and close to the experimental sensitivity.

Table 3.4.- Parameters obtained from the fits of the adsorption kinetics data to Eq. 3.4. The uncertainty of $\boldsymbol{\tau_1}$ is ± 10 s, and that of $\boldsymbol{\tau_2}$ is close to ± 10%. The uncertainties of A_1 is close to ± 8%, and that of A_2 is close to ± 10%.

C / C.A.C.	**A_1** / μg·cm^{-2}	**A_2** / μg·cm^{-2}	**τ_1 / s**	**τ_2 / s**
0.05	0.09	0.06	10	1500
0.1	0.09	0.04	30	2500
0.4	0.14	0.06	30	750
0.8	0.20	0.08	30	700
1.0	0.26	0.30	30	320
1.25	0.50	0.21	25	200

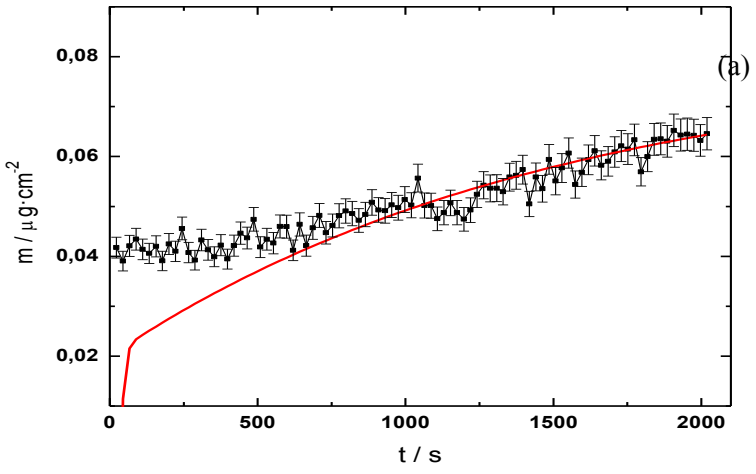

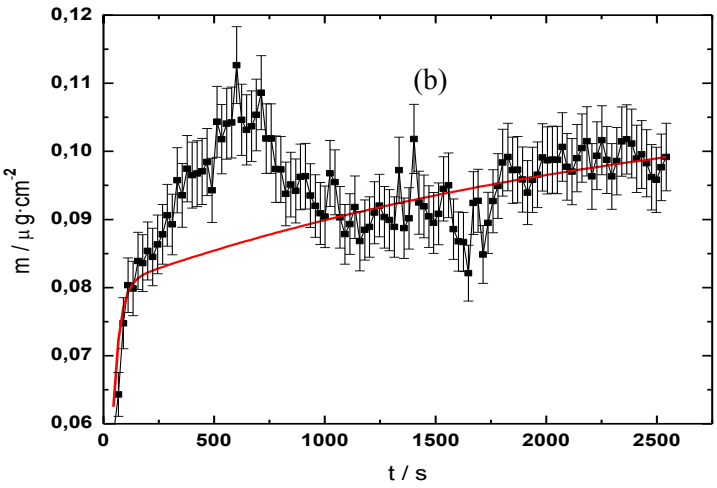
(b)
m / µg·cm-2
t / s
0,12
0,11
0,10
0,09
0,08
0,07
0,06
0
500
1000
1500
2000
2500

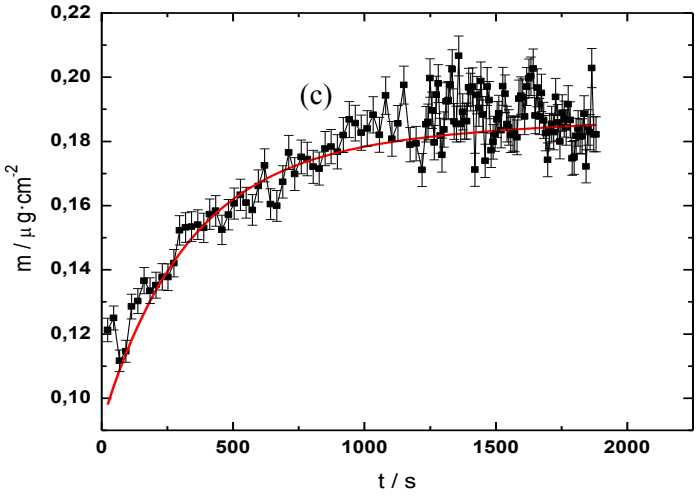
(c)
m / µg·cm-2
t / s
0,22
0,20
0,18
0,16
0,14
0,12
0,10
0
500
1000
1500
2000

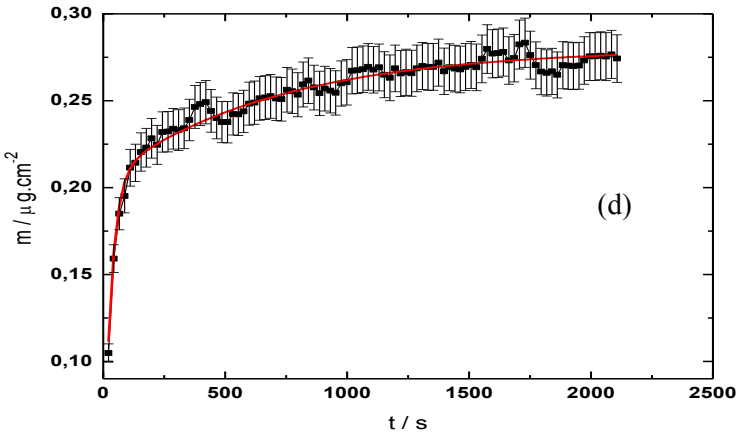
(d)
m / µg.cm-2
t / s
0,30
0,25
0,20
0,15
0,10
0
500
1000
1500
2000
2500

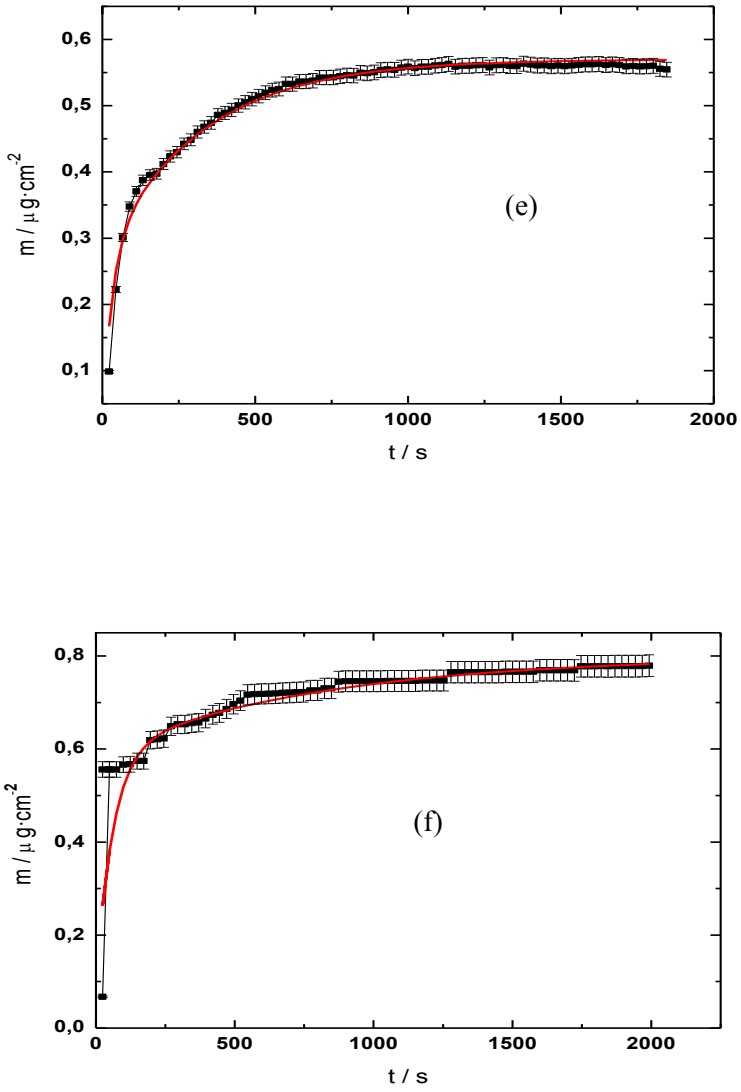

Figure 3.24: Comparison of the experimental data, symbols, for Silwet L-77 and the fits, continuous lines, to Eq. 3.2. Concentrations given as c/C.A.C. are:(a) 0.05, (b) 0.1, (c) 0.4, (d) 0.8, (e) 1.0, and (f) 1.25.

3.4.2 Adsorption of Nanoparticle Dispersions

The adsorption has been measured using the quartz crystal micro-balance at a constant temperature. The adsorption kinetics of nanoparticle suspensions onto PTFE-AF surface was studied for different particle sizes and for different volume fractions at 24ºC, and 30% relative humidity. The results obtained for nanoparticle dispersions of particle size 1.0µm are shown in Figure 3.25, indicates that the nanoparticles adsorbed minimally onto PTFE-AF substrates at low volume fractions and as the volume fraction is

increased the interaction at the solid liquid interface remains unchanged with no adsorption observed, the implication of this behavior will be discussed in depth in the next chapter.

The adsorption dynamics for 0.02µm particle size nanoparticle dispersion is also studied, see Figure 3.26, where it can be observed that the adsorption of nanoparticles generally of very small magnitude increases as the volume fraction is increased. The lack of adsorption of the nanoparticle dispersions used here can be ascribed to the chemical properties of the particle and the solid-liquid interface. The hydrophobic nature of the nanoparticles makes it increasingly difficult to adsorb onto hydrophobic PTFE-AF coated gold substrates. To reach a definate conclution on the adsorption dynamics of these nanoparticles, it is important to carry out studies of nanoparticle dispersions of hydrophilic particles.

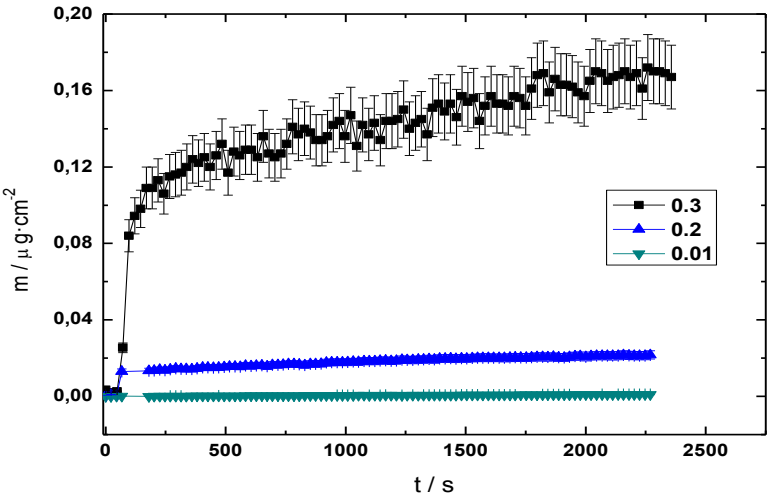

Figure 3.25: Adsorption kinetics for suspensions of particles of 1.0µm at constant 20 ºC and 30% relative humidity for the range of volume fractions shown in the inset.

It can be observed that both the particle size and volume fraction influence the adsorption kinetics of nanoparticle dispersions, even though the magnitude of adsorption is very low. As expected, the adsorption increases with the volume fraction. The implication of this behavior on the evaporation of nanoparticles will be discussed in the subsequent chapter.

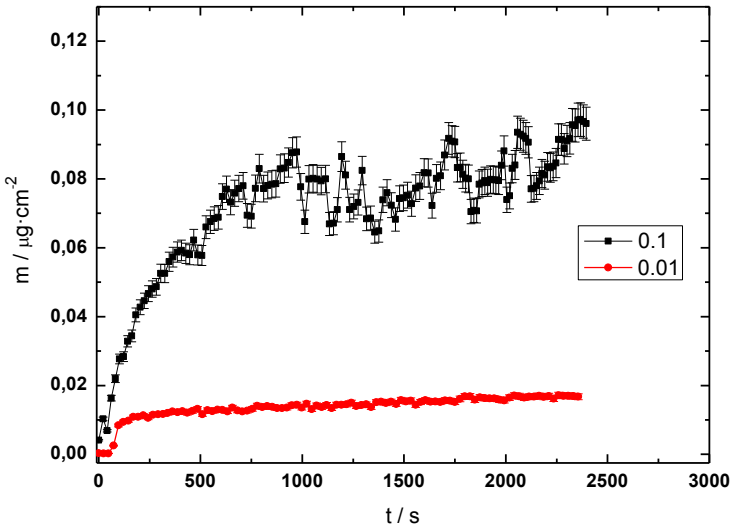

Figure 3.26: Adsorption kinetics for suspensions of particles of 20 nm at constant 20 ºC and 30% relative humidity for the range of volume fractions shown in the inset.

Chapter Four

4.1 Theoretical Description of Spreading and Evaporation.

In this section we will present a theoretical analysis on the spreading-evaporation kinetics of surfactant solutions and nanoparticle dispersions. Some recent theories for spreading and evaporation will be briefly described, and the experimental data presented in the previous chapter will be compared with the theoretical predictions. In the course of this analysis we will also propose explanations for the agreement or deviation of experimental data with theoretical predictions. In the next section we will compare experimental data with known spreading Theories for pure fluids and mixtures.

4.1.1. Autophilic Theory

Ivanova et al. [61] observed that the spreading process proceeded in two stages, as shown in Figure 4.1. They found that the contact angle decreased from an initial value, θ_0, down to the final value, θ_a (or the advancing contact angle), while the droplet contact radius increased from its initial value L_0 to the maximum contact radius, L. The evolutions of spreading, defined by the time dependence of the contact angle, $\theta(t)$, was described according to

$$\cos\theta(t) = cos\ \theta_0 + (\cos\theta_a - cos\theta_0)(1 - \exp(-\alpha t)) \qquad 4.1$$

and they showed that the dynamic contact angle over hydrophobic substrates was better described using a variable y, defined by:

$$\ln y = -\alpha t, \quad y = \frac{cos\theta_a - \cos\theta(t)}{cos\theta_a - cos\theta_0} \qquad 4.2$$

where $\cos\theta(t)$, $cos\theta_0$ and $cos\theta_a$ are the values of the contact angle corresponding to t, to $t=0$, , and at the end of the spreading process, $t = \infty$, respectively. $\alpha = \alpha_T \Gamma_{LV} \exp(\Delta E / k_B)$ and $\tau = \alpha^{-1}$ is the characteristic time scale of the process, it is determined by thermal fluctuations only, and defines the time scale for transferring a surfactant molecule from the droplet to the solid-vapor interface in front of the moving three-phase contact line [6]. ΔE is an energy barrier for surfactant transfer from liquid

droplet onto the solid-liquid interface, and Γ_{LV} is the surfactant concentration at the liquid-vapor interface in the vicinity of the three phase contact line.

In the case of the spreading of trisiloxane surfactant solutions on Teflon, Ivanova et al. [61] showed that for low concentrations, c < C.M.C. only one very slow regime of spreading was detected. They suggested that this regime was related to the adsorption of surfactant molecules in front of the moving three-phase contact line. The rate of the spreading was controlled by the diffusion of surfactant molecules from the bulk to the solid. For c > C.M.C. two stages of spreading were found: a fast stage followed by a slower stage similar to that at concentrations below the CMC. Both spreading stages are described by Eq. 4.3 and Eq. 4.4, assuming that the volume of the droplet remains constant.

$$\ln y = -t/\tau_1, \qquad y = \frac{cos\theta(t_1) - cos\theta(t)}{cos\theta(t_1) - cos\theta_0}; \qquad 0 < t < t_1 \qquad 4.3$$

$$\ln y = -t/\tau_2, \qquad y = \frac{cos\theta_1 - cos\theta(t)}{cos\theta_1 - cos\theta(t_1)}; \qquad t_1 < t \qquad 4.4$$

The straight lines in Figure 3.3 are the best fit of the experimental data to Eq. 4.3 and Eq. 4.4. From the slopes the values of τ_1 and τ_2 can be obtained. The linear behavior of the first stage of spreading can only be observed for very short times, time scales that are not possible to measure with the experimental setup described in this work.

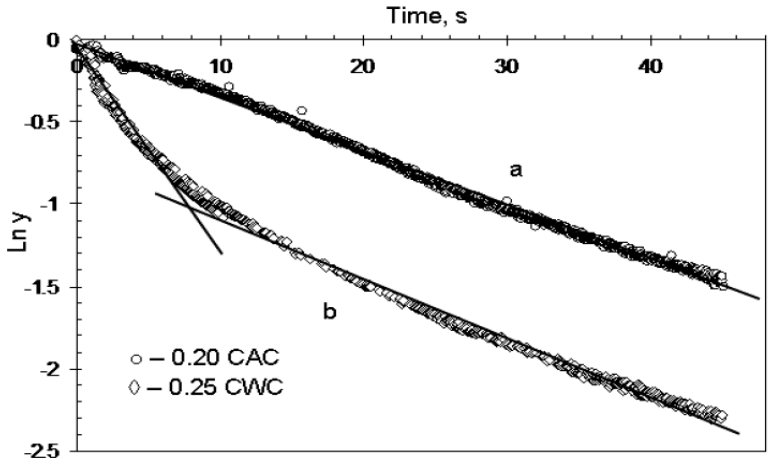

Figure 4.1: Dependency of ln *y* on spreading time fitted straight line according to Eq. 4.3 and 4.4 for ethoxylated trisiloxane surfactant onto hydrophobic Teflon substrate, redrawn from [6].

Figure 4.2 shows the plots for ln *y* vs. t for the data obtained in this work for two experimental conditions over the range of surfactant concentrations studied. It can be observed that the curvature at short times is only found at high temperatures and low relative humidity. For *c* >> C.A.C. the curvature is clearly observed which agrees with the results of Ivanova et al. [6, 61]. Even for high concentrations, the linear behavior of the first stage cannot be clearly defined, and a faster sampling rate should be used. In any case the scattering of the data, specially in the case of high relative humidity, does not allow to make a detailed dicussion of the dependence of τ_2 on the temperature, concentration and relative humidity.

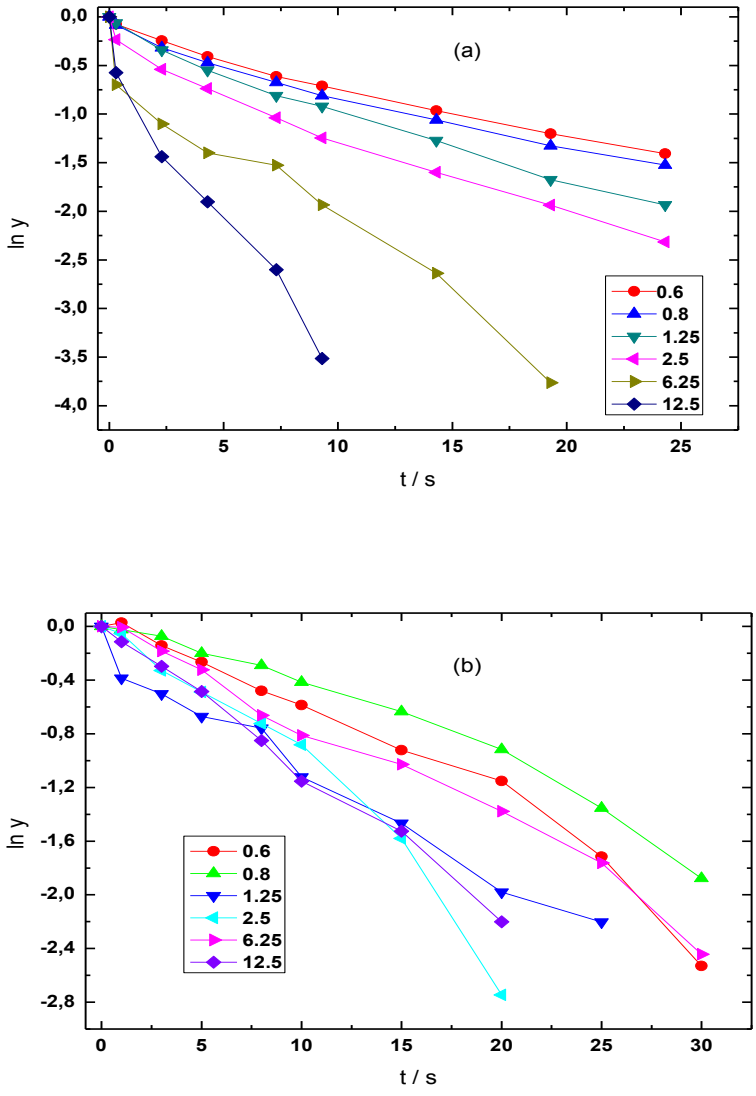

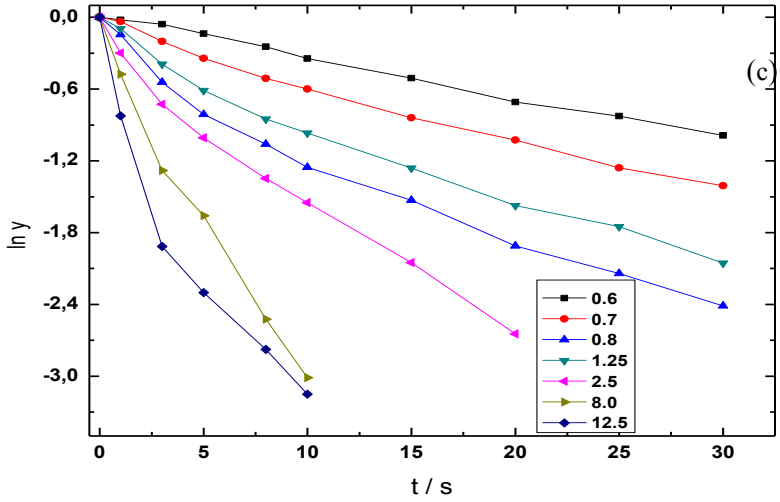

Figure 4.2 : Experimental data for spreading of Silwet L77 onto Teflon AF. The values of temperature and relative humidity are: (a) 30ºC, 30%, (b) 18ºC, 90%, and (c) 24ºC, 55%. The values of c / CAC are given in the insets.

Table 4.1: Values of de parameter α of Eq. 4.2 at 30% relative humidity

c / CAC / **T / ºC**	**0.6**	**0.8**	**1.25**	**2.5**	**8.0**	**12.5**
18	0.0735 ± 0.03	0.1736 ± 0.07	0.1913 + 0.09	0.3569 ± 0.2	0.5756 ± 0.4	0.6283 ± 0.55
24	0.0673 ± 0.4	0.0374 ± 0.07	0.3257 ± 0.2	0.363 ± 0.2	0.7776 ± 0.6	0.7001 ± 0.6
30	0.0287 ± 0.08	0.1789 ± 0.07	0.204 ± 0.1	0.0887 ± 0.03	0.1313 ± 0.03	0.3481 ± 0.2

Table 4.2: Values of α of Eq. 4.2 at 55% relative humidity

c / CAC / **T / ºC**	**0.6**	**0.8**	**1.25**	**2.5**	**8.0**	**12.5**
18	0.0014 ± 0.1	0.1972 ± 0.09	0.1157 ± 0.05	0.3716 ± 0.2	0.1152 ± 0.01	0.3511 ±0.2
24	0.0214 ± 0.085	0.3634 ± 0.2	0.2394 ± 0.1	0.3366 ± 0.2	0.3094 ± 0.2	0.3179 ± 0.2
30	0.0598 ± 0.05	0.0069 ± 0.1	0.1071 ± 0.06	0.346 ± 0.2	0.4931 ± 0.3	0.0221 ± 0.1

Table 4.3: Values of α of Eq. 4.2 at 90 % Relative Humidity

c / CAC / **T / ºC**	**0.6**	**0.8**	**1.25**	**2.5**	**8.0**	**12.5**
18	0.0347 ± 0.07	0.0515 ± 0.05	0.193 ± 0.09	0.1423 ± 0.04	0.0397 ± 0.07	0.0133 ±0.07
24	0.1574 ± 0.05	0.1177 ± 0.01	0.2319 ± 0.1	0.1363 ± 0.03	1.3142 ±1.0	0.1837 ±0.08
30	0.0882 ± 0.02	0.1848 ± 0.8	0.1669 ± 0.06	0.0343 ± 0.08	0.0882 ±0.02	0.0034 ± 0.1

The values of α for of the second spreading stage and for different experimental conditions is presented in Table 4.1 – Table 4.3. These values are consistent, within their experimental uncertainty, with those published by Lee et al. [19] and Sefiane et al.[92].

4.1.2 Molecular theory of Blake

This model arises from from large scale molecular dynamics simulations. According to these results, the movement of the contact line is as a result of the change in the solid-liquid interactions, which directly reduces the solid-liquid interfacial tension, and drives the movement of the contact line and reduces the contact angle simultaneously.

$$v = \gamma_{LV}\left(\cos\theta_a - \cos\theta\right)/\varepsilon \qquad 4.5$$

where v is the rate of spreading and ε is a constant that related the rate of spreading and with its driving force. In Figures 4.3 – 4.6 show the comparison of the experimental data the molecular kinetics theory for Silwet L77 under different experimental conditions. It can be observed that the agreement between theory and experiment is good within the experimental uncertainty.

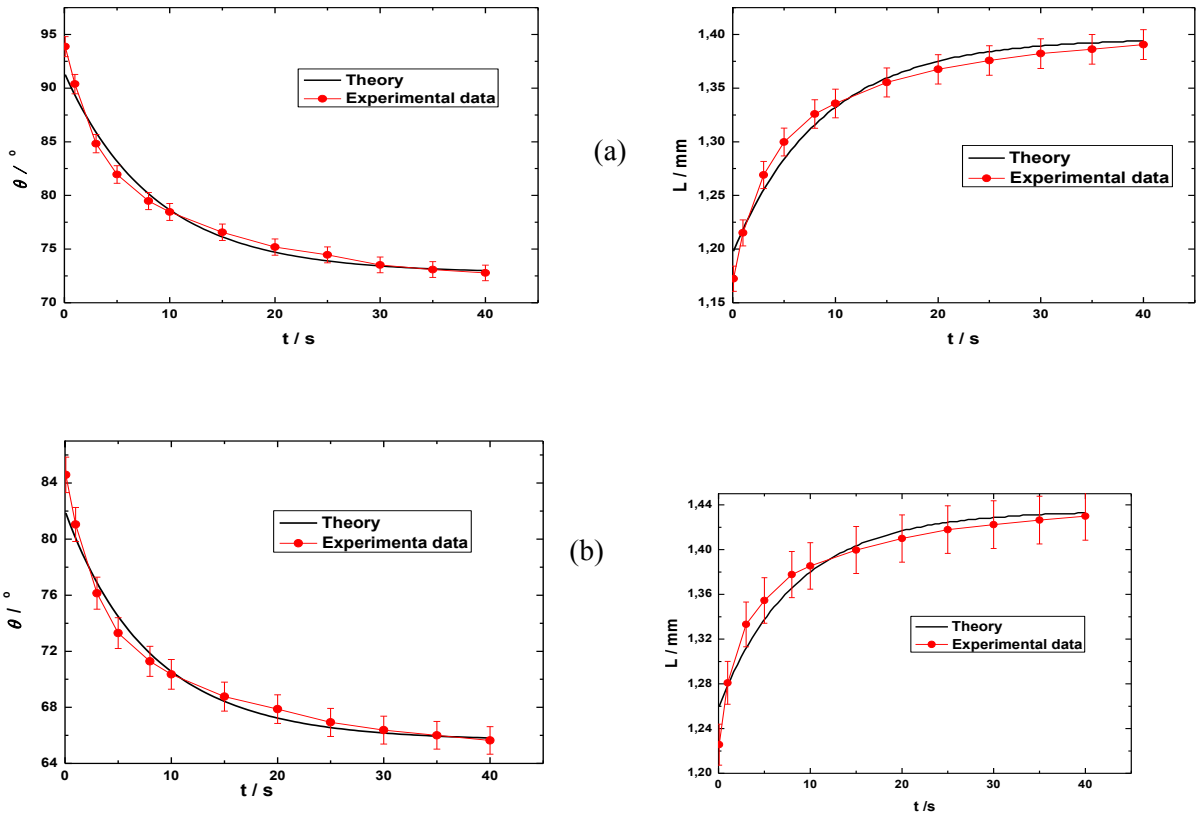

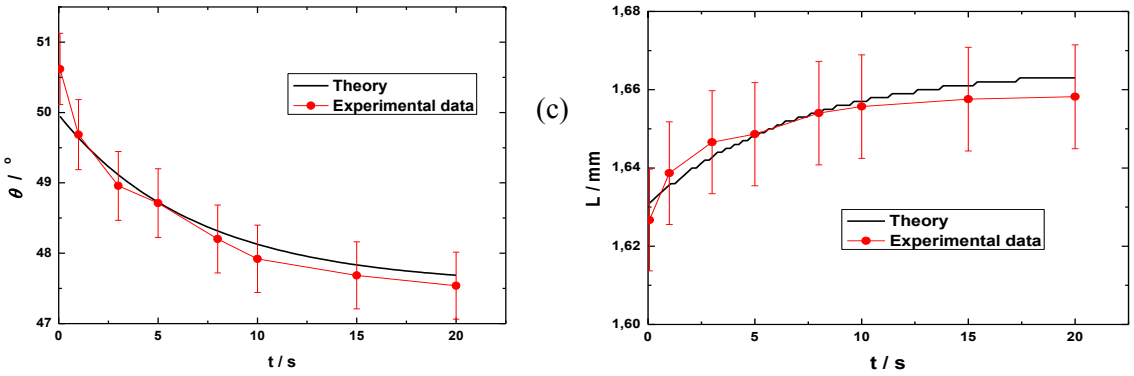

Figure 4.3.- Comparison of molecular kinetic theory with range of concentrations of surfactant solutions (a) 0.6CAC, (b) 1.25CAC and (c) 12.5CAC, at 24ºC and 30% relative humidity.

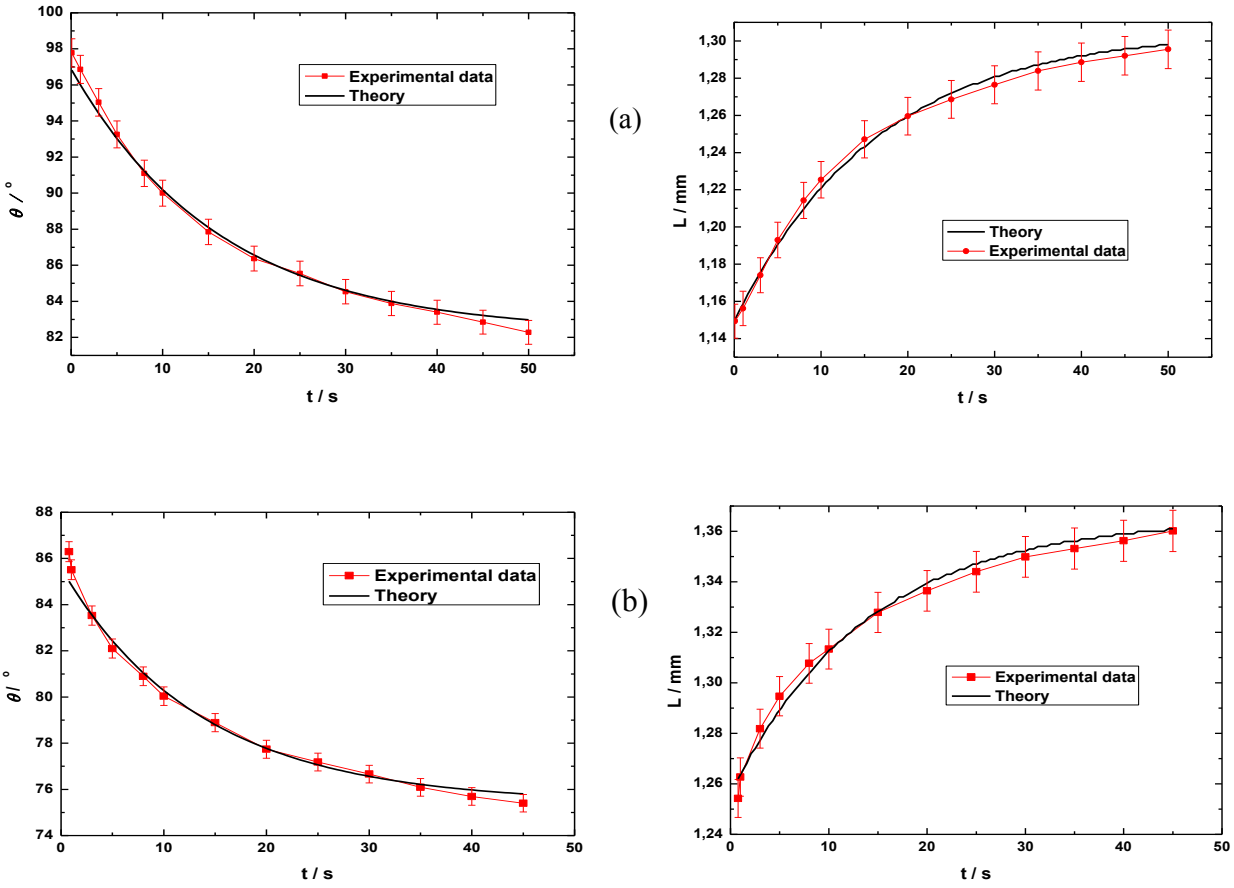

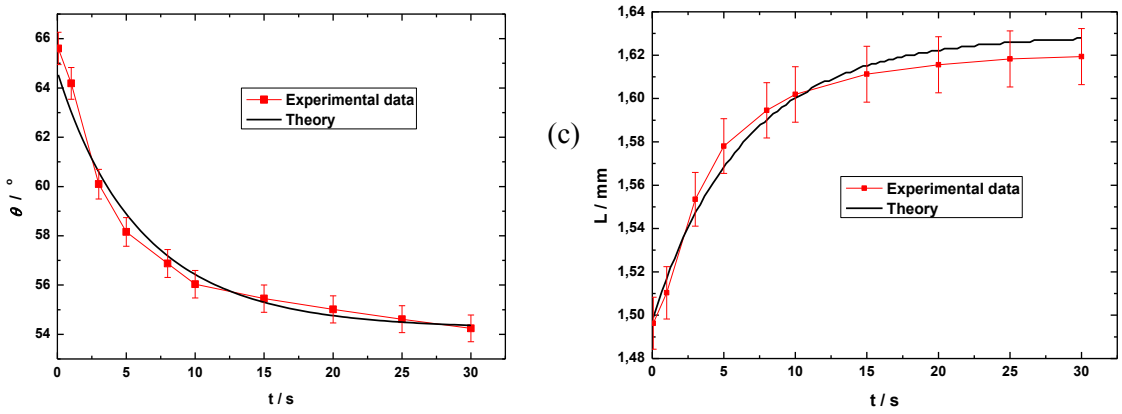

Figure 4.4.- Comparison of molecular kinetic theory with range of concentrations of surfactant solutions (a) 0.6CAC, (b) 1.25CAC and (c) 12.5CAC, at 24ºC and 55% relative humidity.

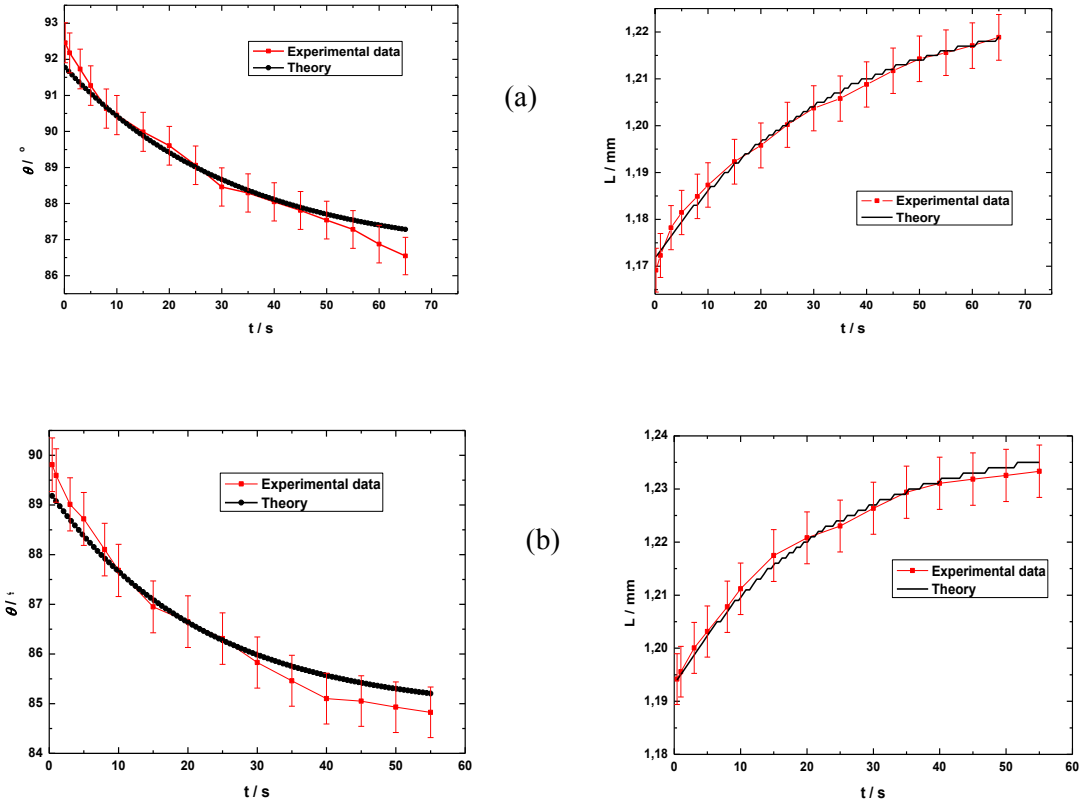

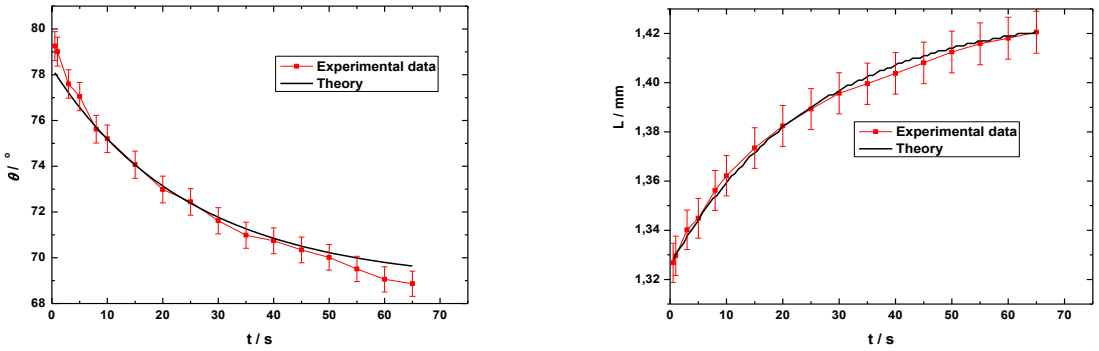

Figure 4.5.- Comparison of molecular kinetic theory with range of concentrations of surfactant solutions (a) 0.6CAC, (b) 1.25CAC and (c) 12.5CAC, at 30ºC and 90% relative humidity.

Table 4.4 shows the values of α at a constant temperature, 24 ºC, and three different relative humidities 30%, 55%, and 90%. Table 4.5 collects the values for 55% and three different temperatures.

Table 4.4.- Values of the α parameter for spreading at 24 ºC and different relative humidities.

c / CAC	**30%**	**55%**	**90%**
0.60	0.026 ± 0.005	0.040 ± 0.005	0.022 ± 0.005
0.80	0.037 ± 0.009	0.029 ± 0.005	0.027 ± 0.005
1.25	0.049 ± 0.007	0.041 ± 0.005	0.024 ± 0.005
2.50	0.064 ± 0.008	0.025 ± 0.006	0.031 ± 0.003
8.00	0.09 ± 0.09	0.028 ± 0.008	0.036 ± 0.005
12.50	0.14 ± 0.02	0.12 ± 0.04	0.027 ± 0.001

Table 4.5.- Values of the α parameter for spreading at 55% relative humidity and different temperatures.

c / CAC	**18ºC**	**24ºC**	**30ºC**
0.60	0.02 ± 0.02	0.040 ± 0.005	0.04 ± 0.05
0.80	0.06 ± 0.01	0.029 ± 0.005	0.03 ± 0.07
1.25	0.046 ± 0.01	0.041 ± 0.005	0.04 ± 0.05
2.50	0.04 ± 0.01	0.025 ± 0.006	0.03 ± 0.06
8.00	0.04 ± 0.02	0.028 ± 0.008	0.03 ± 0.08
12.50	0.07 ± 0.08	0.12 ± 0.04	0.088 ± 0.005

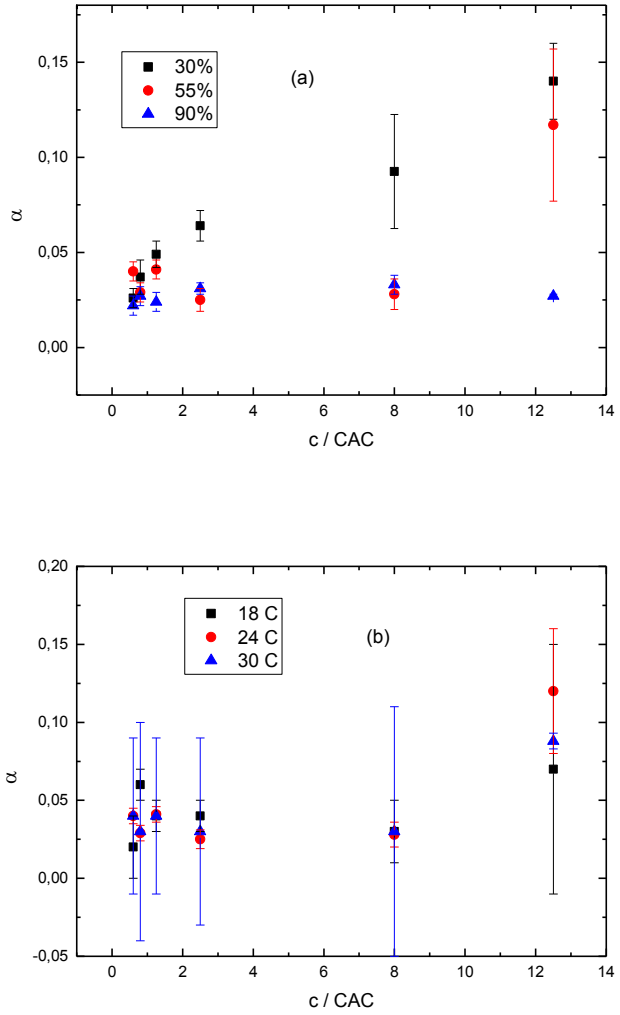

Figure 4.6.- Relative humidity, (a), and temperature, (b) dependences of the α parameter for the Silwet L77 solutions onto Teflon AF. The values of Figure 4.6.a correspond to 24 ºC, and those of Figure 4.6.b to 55% relative humidity.

Figure 4.6.a shows that except for the lowest relative humidity, the surfactant concentration has no clear influence on α. It can be clearly seen that the temperature does not have any effect on α at constante relative humidity.

4.1.3 Rate Theory of Wetting

The main concepts of the theory have been described in Chapter 1.

The concept of the rate theory is based on the propagation of the triple phase contact line for a situation where the contact line is rough and the propagation occurs as a result of an uneven surface substrate. The rate law is dependent on the freqency which thermal

capillary waves overcome the surface roughness induced by the free energy barriers. This hydrodynamic model has been successful in interpreting the case of complete wetting and contact line propagation for high capillary numbers. The experimental data shows a clear barrier assymetry, while the adsorption-desorption mechanism is generally associated with a symmetric barrier. The presence of the solid surface and the viscosity of the liquid due to the concentration influenced the propagation of the contact line. In Figure 4.7, Figure 4.8 and 4.9 respectively we show the comparison of the Rate Theory and experimental data for a range of concentrations for different temperatures and relative humidities. The relationship has been modelled according to the Eq. 4.6;

$$\frac{dL}{dt} = v_0[e^{-b_A(x-\bar{x}_y)} - e^{-b_R(x-\bar{x}_y)}] \qquad 4.6$$

where b_A and b_R are dimensionless activation areas, x and $\bar{x}_y$ are the contact angle at a given time and the final contact angle (advancing contact angle) respectively, L the droplet contact angle and v_0 is the characteristic velocity of the contact line.

Figure 4.7 show some representative results for the fits of the experimental results to Eq.4.6. A simple look to the data of the rate of change of the radius of the droplet basis points out clearly that the results cannot be fitted to a sum of two exponentials, and therefore no further analysis will be done.

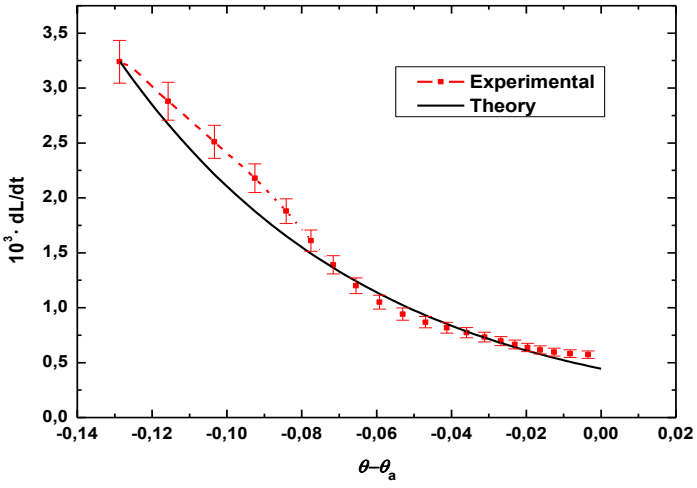

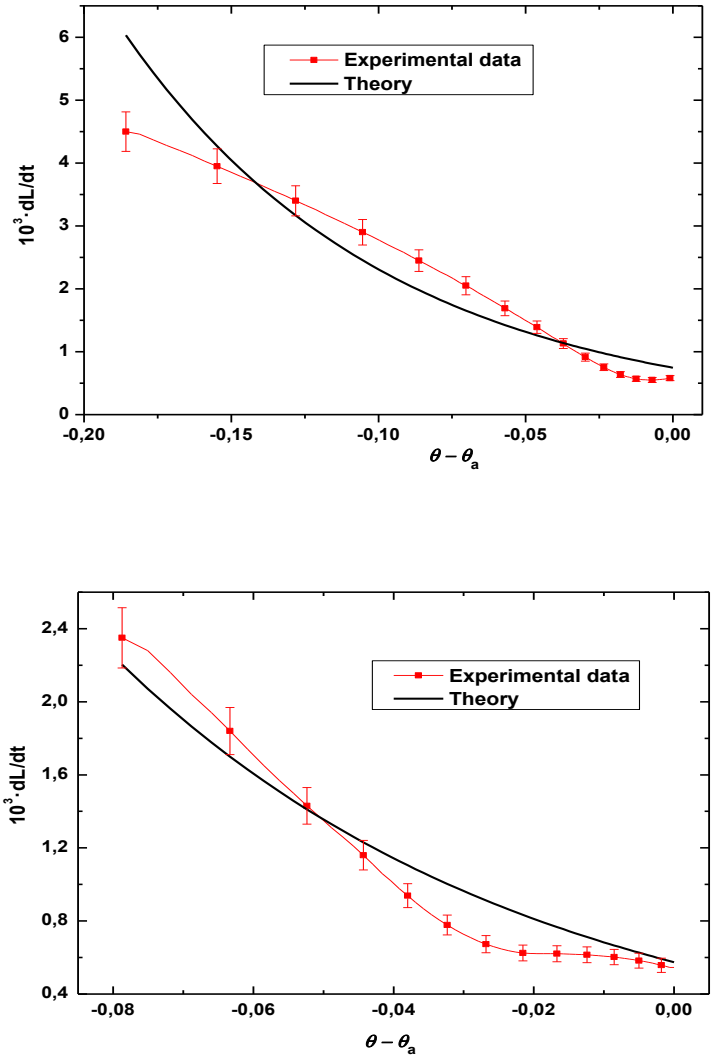

Figure 4.7: Comparison of the spreading Rate Theory with experimental data (a) 30% RH and 30ºC, (b) 55%, 24ºC, and (c) 90% RH and 18ºC, for 0.6 CAC Silwet solution. Symbols are calculated from the experimental data, and the black continuous line is the best fit to Eq. 4.

4.2 Theory of Evaporation

The evaporation of a sessile droplet is described as the reduction in volume of the droplet, and in this study we have assumed that the droplet remains spherical throughout the process of evaporation. The process of evaporation involves two distinct regimes; the pinning of the droplet on the surface while the droplet contact angle reduces and a second regime where the contact angle remains constant while the contact droplet radius reduces. It becomes important to understant the interaction at the three phase contact line:

i. A singularity of evaporation flux due to an incompatibility of boundary conditions at the liquid–gas interface and at the solid–liquid and solid-gas interface.

ii. The viscous stress singularity also appears at the three-phase contact line due to no-slip boundary condition at the solid surface which is usually used in continuum hydrodynamics.

The solution of those problems on a micro scale level and obtaining of corresponding macroscopic boundary conditions is one of the research goals in the field.

Some phenomenological results are well established for the evaporation of a drop of a fluid onto a perfectly smooth surface under partial wetting conditions:

a) Assuming the evaporation process right after the drop has spread over the solid substrate, and that the drop has a spherical cap shape, the evaporation rate is proportional to the radius of the drop onto the substrate, L.

b) The spreading and evaporation process is composed of four stages: 1) L increases while the contact angle, θ, decreases down to the advancing contact angle value, θ_a. 2) The contact angle decreases from θ_a down to receding contact angle value, θ_r, at constant L. 3) Contact angle remains constant and equal its receding value θ_r, while the radius of the base droplet, L, decreases.

c) Both the contact angle and L decreases until the drop completely evaporates.

Nevertheless many problems still remain to be solved:

i. To build a theory for drops of multi-component fluids that include all the physical processes abovementioned.

ii. To build a hydrodynamic model able to describe the four stages of the simultaneous spreading and evaporation process.

iii. To match the hydrodynamic description of the drop evaporation with the molecular thick layer beyond the three-phase contact line. Such matching must take into consideration the DLVO forces acting at a mesoscopic scale near the contact line.

iv. To describe the evaporation process of complex fluids: polymer and protein solutions and nanoparticle suspensions.

v. To build a theory able to describe the evaporation of drops onto patterned surfaces.

In what follows we will describe a theory aiming to describe the first two stages of evaporation. Let us consider an evaporating droplet with a spherical cap, and the droplet

contact radius is small enough to neglect the effect of gravity, see Figure 4.10. The evaporation takes place in the presence of a contact angle hysteresis, contact angle hysteresis is a property a liquid droplet exhibits as a result of a difference between the equilibrium, θ^e, and advancing, θ_a, contact angles due to an increase of contact line motion, we know that a concentration gradient exists between the proximity of the liquid-vapor interface and the bulk vapor phase, and this leads to a flow from the interface towards the less concentrated bulk gas region. Even when the substrate and the bulk liquid are initially at the same temperature, the evaporation process decreases the interface temperature due to the latent heat of evaporation. Deegan et al. [104] showed that the density of vapour flux, *j*, was not uniformly distributed over the surface of a sessile droplet, but is higher near the three phase contact line (see Figure 1.24). The latter non-uniformity generates flow inside the droplet, this justifies the results of Cazabat et al. [100] who showed that the vapour flux density, *j*, over the droplet is inversely proportional to the radius of the contact line. Girard et al. [159] resolved the non-dimensional Laplace, heat, and Navier- Stokes Equations with droplet boundary conditions that determine the outgoing heat flow for each interface element. This allowed the computation of the value of the dimensionless total outgoing heat flow that is defined as the integrated flux along the droplet free surface.

If we consider a spherical droplet, on a plane surface, the droplet forms a spherical cap with the substrate, and the contact droplet radius, *L*, is obtained as a function of contact angle from:

$$L = Rsin\theta \tag{4.7}$$

Where *R* is the radius of the spherical cap, and θ is the contact angle, the droplet height, *h*, is related to the contact angle by:

$$h = R(1 - cos\theta) \tag{4.8}$$

The reduction of the volume of the spherical cap can be can be characterized by the contact droplet radius and the height of the droplet as:

$$-\left(\frac{dV}{dt}\right) = \frac{4\pi RD}{\rho}(c_{sat} - c_{\infty})F(\theta) \tag{4.9}$$

The evaporation rate can be computed from the dimensionless normal temperature gradients in the gaseous phase and the heat flow, thus we obtain equation 4.9;

$$\frac{dV}{dt} = DR(c_{sat}(T_{av}) - Hc(T_{\infty})\Delta H_{vap}(T_{av})\emptyset \tag{4.10}$$

The heat flow Ø, depends on the contact angle which changes as evaporation proceeds, the evaporation rate of a sessile drop with respect to the heat flow as a function of the contact angle can be described by Eq. 4.11, [63]:

$$\frac{dV}{dt} = -2\pi \frac{DM}{\rho} [c_{sat}(T_{av}) - Hc_{sat}(T_{\infty})] F(\theta) L \qquad 4.11$$

where V represents the droplet volume, t the time, D, ρ, M represent the diffusivity in air, density and molar mass of the liquid respectively while H is the relative humidity of the ambient air, T_{av} is the temperature at the interface, T_{∞} is the temperature at an infinite distance, c_{sat} (T_{av}) and $c_{sat}(T_{\infty})$ are molar concentrations of saturated vapour at the corresponding temperature, θ, is the contact angle, L, the droplet contact radius and $F(\theta)$ is a function of the contact angle, and is 1 at $\theta = \pi/2$,this value is taken arbitrariy and results in negative values of the characteristic time for evaporation processes with contact angles $\theta > 90$, for hydrophobic substrates. Since the flux is not uniform through the surface neither is the surface temperature uniform.

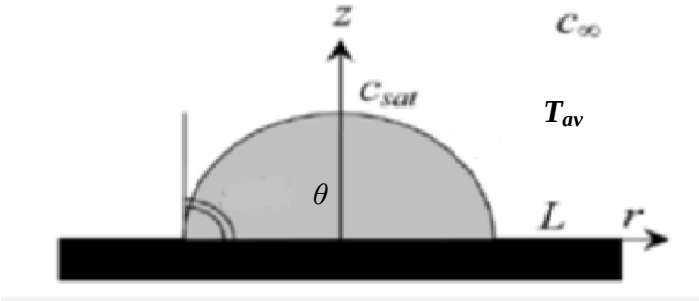

Figure 4.8: Geometry used for deriving the evaporation rate equation.

However Semenov et al. [63], in their postulation have not taken into account the temperature distribution over the liquid-vapor interface, but they have considered an average temperature value, T_{av}, obtained from simulation, which was defined as the equilibrium temperature between the temperature in the bulk, the temperature at the surface of the droplet and the solid substrate. They found that temperature in the bulk of a sessile evaporating droplet was dependent on the thermal properties of the substrates and the rate of evaporation, thus it is assumed that the average temperature of the droplet surface will remain constant for the duration of evaporation.

From computer simulations carried out by Semenov et al. [63], and they founf that the total evaporation flux of pure fluids could be described by the expression:

$$J = F(\theta) \cdot J_{\pi/2}(LT_{av}) \quad 4.12$$

where $J_{\pi/2}$ is the flux for $\theta = \pi/2$ and T_{av} the average surface temperature. For isothermal evaporation Picknett and Bexton [160] found that *F(θ)* could be parametrized by;

$$F(\theta) = \begin{cases} (0.6366 \cdot \theta + 0.09591 \cdot \theta^2 - 0.06144 \cdot \theta^3)/\sin\theta & \theta < 10^o \\ (0.00008957 + 0.6333 \cdot \theta + 0.116\theta^2 - 0.08878 \cdot \theta^3 + 0.01033 \cdot \theta^4)/\sin\theta & \theta > 10^o \end{cases} \quad 4.13$$

with θ given in radians.

$c_\infty = Hc_{sat}(T_\infty)$ from Eq. 4.10 is the concentration at an infinite distance and is dependent and on the relative humidity, the temperature at the bulk and the molar concentration, the evaporative flux over the droplet surface is given as:

$$J_{\pi/_2}(L, T_{av}) = 2\pi D[c_{sat}(T_{surf}) - c_\infty]L \quad 4.14$$

$J_{\pi/_2}(L, T_{av})$ is the analytical solution of the evaporative flux, from Eq. 4.10 - Eq, 4.13 it is possible to rewrite the evaporation rate as;

$$\frac{dV}{dt} = -\beta F(\theta)L \quad 4.15$$

given that

$$\beta = 2\pi \frac{DM}{\rho}[c_{sat}(T_{av}) - c_\infty] \quad 4.16$$

Eq. 4.15 clearly points out that for a pure liquid β depends T_{av}, and on the relative humidity through c_∞, and it also represents the mass conservation law for an evaporating droplet with the same conditions. The dependence of β on the average temperature and relative humidity is shown in Figure 4.9, according to computer simulations and is consistent with the influence temperature and relative humidity on evaporation.

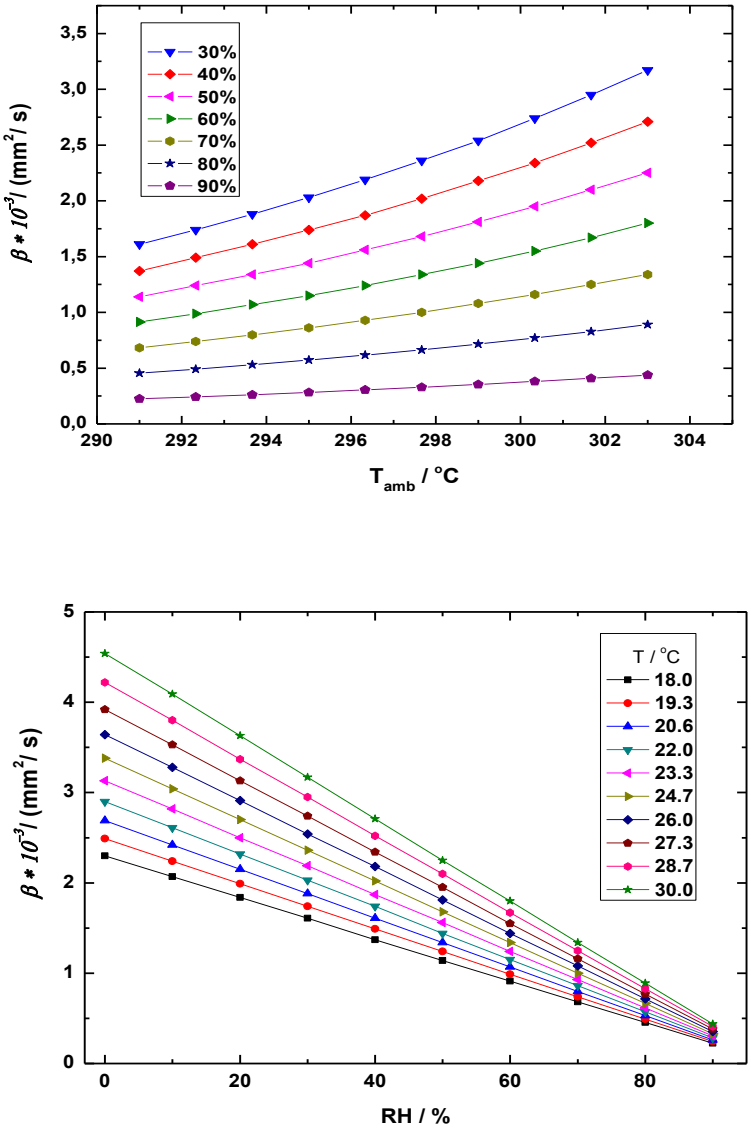

Figure 4.9: Dependence of β on (a)T_{av} and (b) Relative Humidity

4.2.1 First Stage of Evaporation

As it has been mentioned above during the first stage of evaporation the droplet contact line radius L, remains constant at the maximum value L_0, while the contact angle decreases from its initial value, θ_{ad} to the final value θ_r. The moment when L_0 is reached is taken as $t=0$, this process is illustrated in Figure 4.10.

Since we have assumed that the droplet remains spherical in shape during the first two stages of evaporation, the volume of the droplet can therefore be written as;

$$V = L^3 f(\theta), \quad f(\theta) = \frac{\pi}{3}\frac{(1-\cos\theta)^2(2+\cos\theta)}{\sin^3\theta} \qquad 4.17$$

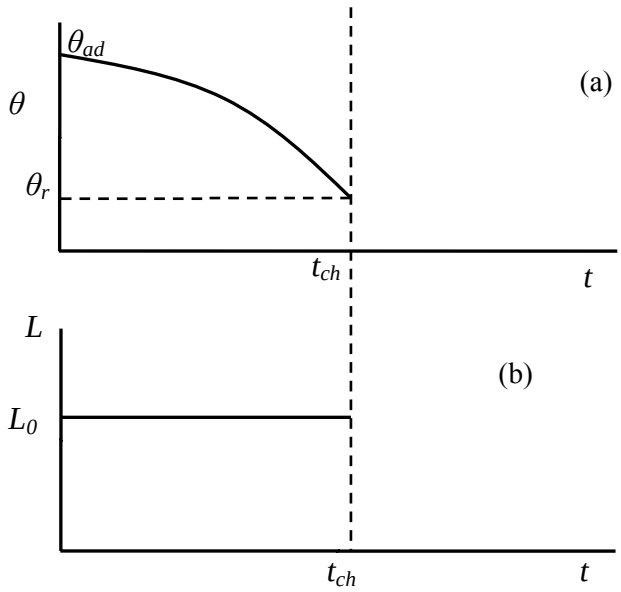

Figure 4.10: The dependencies of (a) θ and (b) L, during the first evaporation stage.

According to our previous consideration during both stages of evaporation the mass conservation law has the form given by Eq. 4.15 and a constant average surface temperature. Theoretical analysis for the first stage of evaporation can be derived using previously mentioned variables by, Semenov et al [63] and Hu and Larson [118]. Given that in the first stage of evaporation the droplet contact line remains constant at L_0, and using Eq. 4.17 we can rewrite Eq. 4.15 as;

$$L_0^3 f^{\cdot}(\theta)\frac{d\theta}{dt} = -\beta F(\theta) L_0 \qquad 4.18$$

where $f(\theta) = \frac{dF(\theta)}{d\theta}$ with the condition that $\theta|_{t=0} = \theta_a$

Introducing the following dimensionless time $\tau = (t/t_{ch})$, where $t_{ch} = (L_0^2/\beta)$ the characteristic time of the process, Eq. 4.13 takes the form:

$$f'(\theta)\frac{d\theta}{d\tau} = -F(\theta) \qquad 4.19$$

From a direct integration of Eq. 4.19 with the previous boundary conditions gives a characteristic time $A^{\cdot}(\theta, \theta_{ad}) = \tau$, being A given by;

.
$$A^{\cdot}(\theta, \theta_{ad}) = \frac{f^{\cdot}(\theta)}{F(\theta)} \qquad 4.20$$

Eq. 4.19 indicates that the time dependency $d\theta$ should be universal and independent of the nature of droplet and its volume but dependent on its advancing contact angle

(which can be measured independently). Semenov et al.[63] and Hu and Larson [118], proposed that the first stage of evaporation proceeds until the static advancing contact angle (θ_{ad}) reaches the receding contact angle (θ_r). Therefore at end of the first evaporation stage $\tau = (t/t_{ch})$, can be defined by:

$$A'(\theta, \theta_r) = \tau_r. \qquad 4.21$$

We now introduce the dimensionaless time based by rewritting Eq.4.21, by intergrating we have,

$$\int_{\theta}^{\pi/2} \frac{\bar{f}(\theta)}{F(\theta)} d\theta = \tau + \int_{\theta_{ad}}^{\pi/2} \frac{\bar{f}(\theta)}{F(\theta)} d\theta \qquad 4.22$$

assuming that, $B(\theta) = \int_{\theta}^{\pi/2} \left[\frac{\bar{f}(\theta)}{F(\theta)}\right] d\theta = \bar{A}(\theta, \pi/2)$, and $\tilde{\tau} = \tau + B(\theta)$, the resulting equation for dimensionless time becomes;

$$B(\theta) = \tilde{\tau} \qquad 4.23$$

When deriving the universal curve for the first evaporation stage $\tilde{\tau} = 0$ is arbitrarily associated with $\theta = \pi/2$. If the surface is hydrophobic i.e. $\theta > \pi/2$, then it will correspond to a negative value of time on the universal dependence curve. The universal behaviour predicted by Eq.4.19 has been checked using experimental data. Figure 4.11 makes such a comparison for water on different substrates with varying degrees of hydrophobicity. It is observed that the agreement with theory for the first stage is very good, the negative values of the reduced time correspond to contact angles $\theta > \pi/2$.

4.2.2 The Second Evaporation Stage

In the second evaporation stage the contact angle remains constant at θ_r and L decreases, as shown in Figure 4.12. and in this case Eq. 4.19 can then be rewritten as;

$$3L^2 f(\theta_r) \frac{dL}{dt} = -\beta F(\theta_r) L \qquad 4.24$$

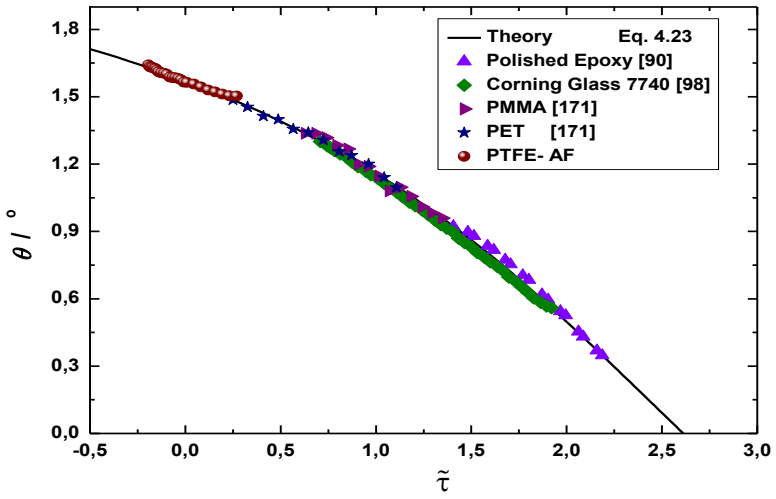

Figure 4.11: Comparison of experimental results for water droplets onto hydrophobic substrates with the universal curves predicted by the theory for the first stage of evaporation.

Introducing the same dimensionless time as in the first evaporation stage τ, and dimensionless contact line radius, $l=L/L_0$, Eq. 4.20 can be rewritten as:

$$\frac{dl^2}{d\tau} = -\frac{2}{3}\frac{F(\theta_r)}{f(\theta_r)}, \qquad \text{where } \tau > \tau_r \tag{4.25}$$

with the initial condition that $l(\tau_r)=1$, direct integration of 4.25 leads to

$$l^2(\tau) = 1 - \left(\frac{2F(\theta_r)}{3f(\theta_r)}\right)(\tau-\tau_r)^2 \quad \text{or} \quad l(\tau) = \sqrt{1+\frac{2F(\theta_r)}{3F(\theta_r)}(\tau-\tau_r)^2} \tag{4.26}$$

Again a universal dependence for a second stage of evaporation is derived from Eq. 4.26. Recall that this second stage ends before $l = 0$, because at somecharacteristic time, τ, both θ and L start to decrease (third stage), if we introduce the another dimensionless time;

$$\bar{\tau} = \frac{2F(\theta_r)}{3f(\theta_r)}(\tau-\tau_r) \tag{4.27}$$

when we apply that to Eq. 4.26, we have;

$$l(\bar{\tau}) = \sqrt{1-\bar{\tau}} \tag{4.28}$$

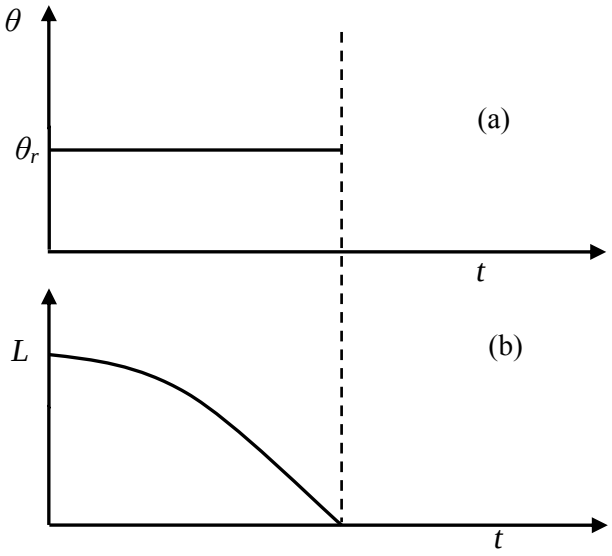

Figure 4.12: The dependencies of (a) θ and (b) L, during the second evaporation stage

In Figure 4.16 we show the comparison of the theoretical prediction of the second stage of evaporation for pure fluids over different substrates. Eventhough at short reduced times the experimental data collapse onto a single master curve, this is not so at higher values of $\bar{\tau}$. Moreover the theory slightly underestimates the experimental results. The theory developed does not include the third evaporation stage, in this regime the contact angle, contact line radius and volume all decrease simultaneously with time and the droplet no longer has a spherical cap shape.

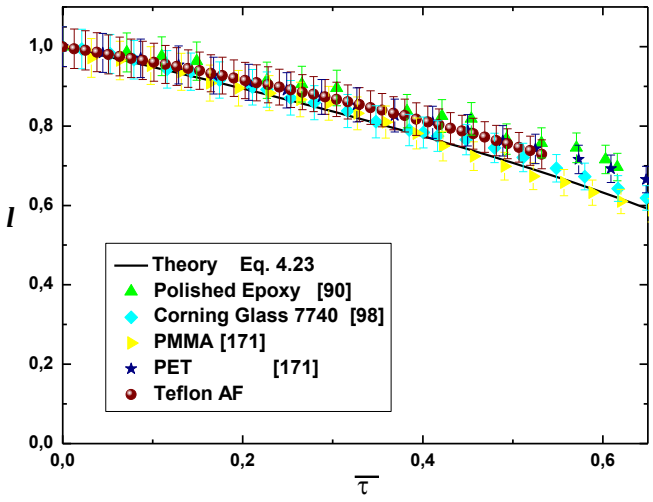

Figure 4.13: Comparison of experimental results for water onto hydrophobic substrates with the universal curve predicted by the theory for the second stage of evaporation.

1.3 Theoretical Description of the Evaporation of Surfactant Solutions

4.3.1 First Stage of Evaporation

The influence of surfactants on spreading has been experimentally described in section 4.1, in this section the predictions of the theory developed for the two stages of evaporation kinetics in the previous section for pure fluids will be compared with the evaporation of surfactant solutions, and afterwards with nanoparticle dispersions. The theoretical prediction will also be compared to the experimental data of Doganci et al. [129] for sodium dodecylsulfate, SDS, surfactant solutions above and below the CMC. A theoretical comparison of the first stage of evaporation is shown in Figure 4.14 and Figure 4.15 respectively, and good agreement between theory and experiments is observed over the whole concentration range.

The comparison of experimental data with theoretical prediction for the first evaporation stage is presented in Figure 4.14 for a wide range of concentrations of Silwet L-77, at varying environmental conditions of temperature and relative humidity. It is observed from Figure 4.14 that for Silwet L-77 solutions irrespective of the temperature and relative humidity of the system, the evaporation dynamics is consistent with the predicted theory for pure fluids for the first stage of evaporation, and the agreement is found for all concentration ranges measure for varied temperatures and relative humidities.

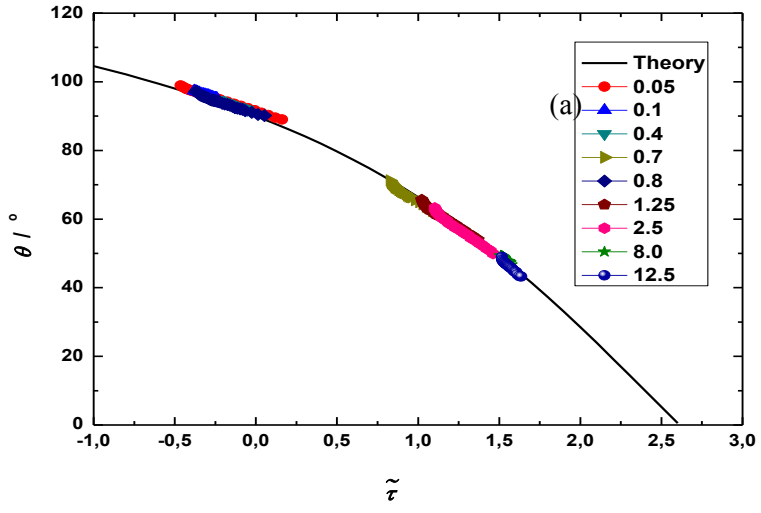

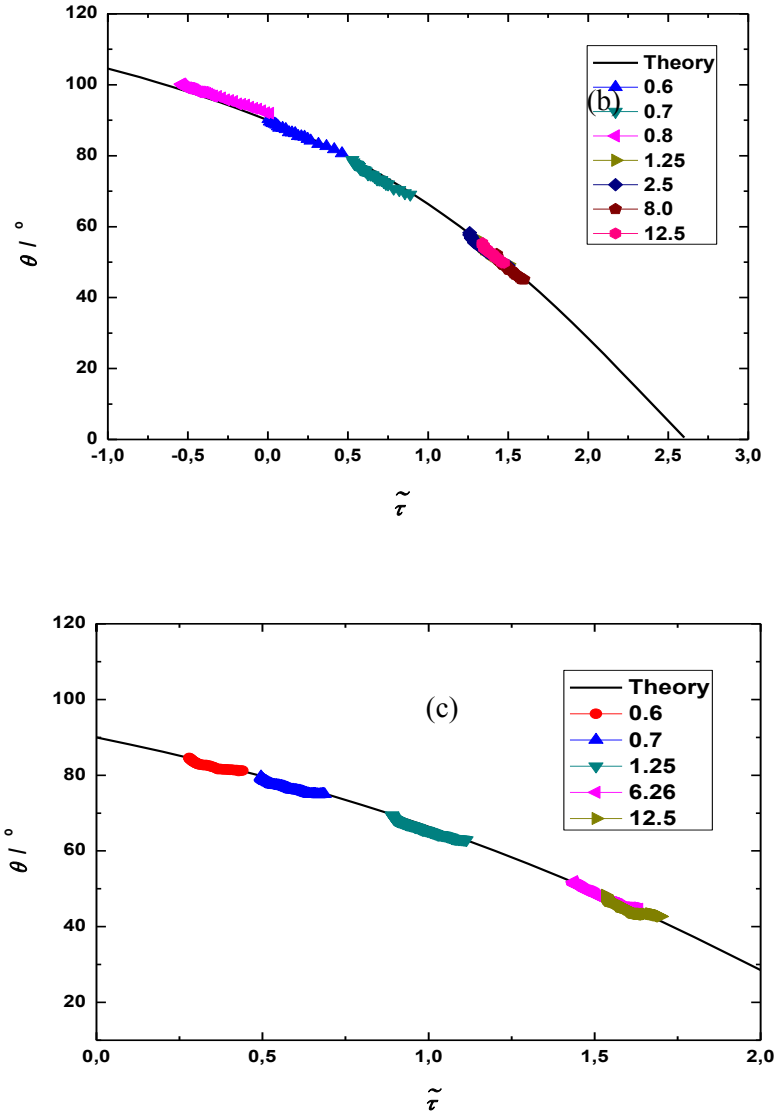

Figure 4.14: First evaporation stage for (a) 30%, (b) 55%, and (c) 90% and constant temperature 24ºC.

The results obtained in Figure 4.14 are somewhat suprising because one would expect that the presence of a surfactant monolayer at the liquid-vapor and solid-liquid interfaces would affect the evaporation dynamics with respect to the mass transfer through the liquid-vapor interface, as well as the contact angle, θ , and Young's Equation for contact angle, however this is not the case and will further be discussed in subsequent sections. The same behaviour is observed for SDS solutions over a wide range of concentrations, using experimental data from Doganci et al. [70], see Figure 4.15. The fact that Silwet L-77 does not form micelles as SDS but vesicles, means that

the nature of the aggregates does not seem to have any influence on the first evaporation stage, and the evaporation dynamics resembles that of a pure fluid.

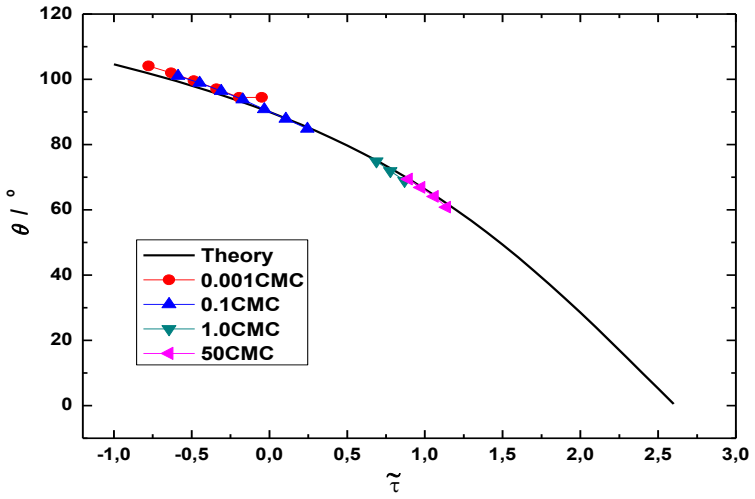

Figure 4.15: First stage of evaporation for SDS solutions, experimental data from Doganci et al. [129].

4.3.2 Second Stage of Evaporation

The second stage of evaporation for surfactant solutions presents new features compared with that of pure liquids. In real experiments we observed that the constant angle did not remain constant throughout the second stage of evaporation, but decreased as the time increased specifically for concentrations below the CAC in Silwet L-77 or the CMC in the case of SDS, there was a simultaneous decrease in the contact angle as well as the droplet contact radius. And in concentrations above the CAC in Silwet L-77 and CMC in the case of SDS, the constant contact angle mode predicted for evaporating droplets is restored. One can think of some physical reasons that may contribute to these findings in the low concentration range. In effect, this is the concentration range in which the adsorption at the liquid-vapor and solid-liquid interfaces changes during the evaporation process due to the increase of surfactant concentration within the droplet. This also affects the vapor pressure slightly and in effect c_{sat}, these effects have not been taken into consideration in the theory for evaporation described above. This suggests that the theory will not provide a good description of the experimental results, however it is important to make a comparison with the theory to get some insight on

which parameters have to be added or considered for the theory to accurately describe the behavior of mixtures.Figure 4.15 shows the representative results for Silwet L-77 solutions for dilute concentrations, deviations from the theoretical prediction are clearly observed.

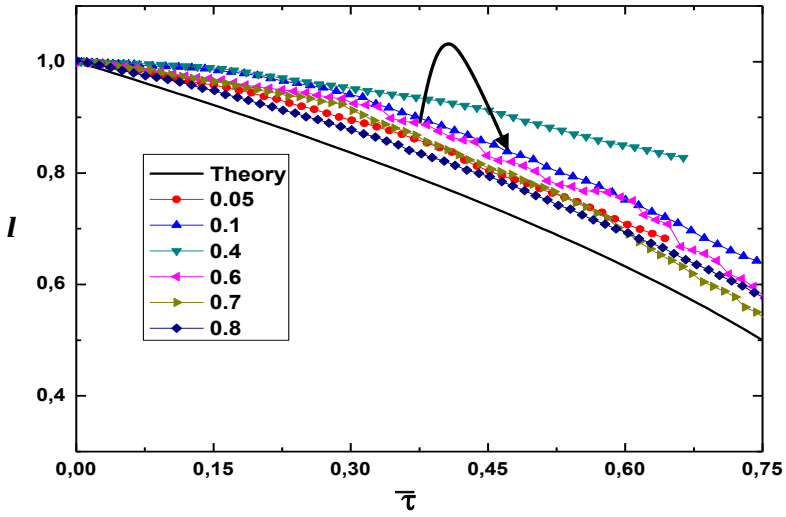

Figure 4.16: Second stage of evaporation for Silwet for concentrations below CAC at 24ºC and 30% relative humidity.

It has been observed that the deviation from the theoretical prediction goes through a minimum at very low concentrations (very dilute solutions) to a maximum at concentrations close to or at the CAC of silwet L-77 surfactant. This trend of deviation is observed in low concentrations of Silwet L-77 solutions at all the temperatures and relative humidities studied, see Figure 4.17. Even at high relative humidities, 90% and low temperatures 18ºC, the second stage of evaporation is still not consistent with the theoretical prediction irrespective of the slower evaproation rate, as seen in Figure 4.17.c. Similar results were obtained for low concentrations of SDS when compared with the theoretical prediction described above for the second stage of evaporation are shown in Figure 4.18, and in the same way the agreement of theoretical prediction with experimantal data return at very low concentrations. In section 4.5, we will try to modify the theory to for the evaporation of a mixture, and the influence of the adsorption at solid-liquid interface.

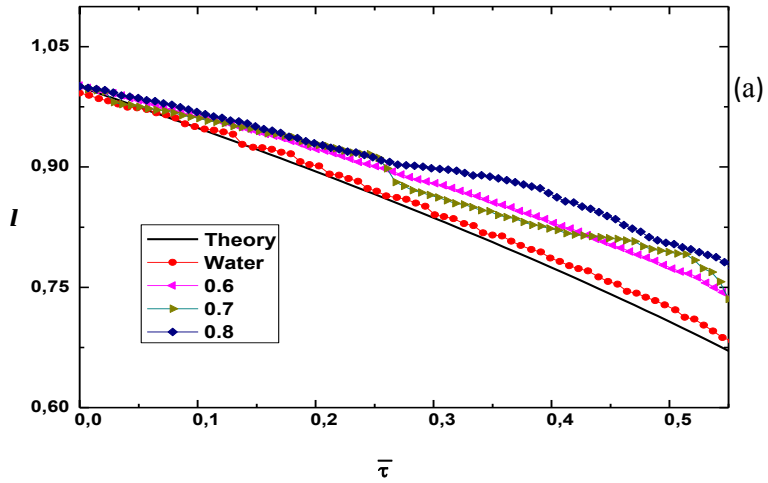
(a)
1,05
0,90
0,75
0,60
I
0,0
0,1
0,2
0,3
0,4
0,5
τ
Theory
Water
0.6
0.7
0.8

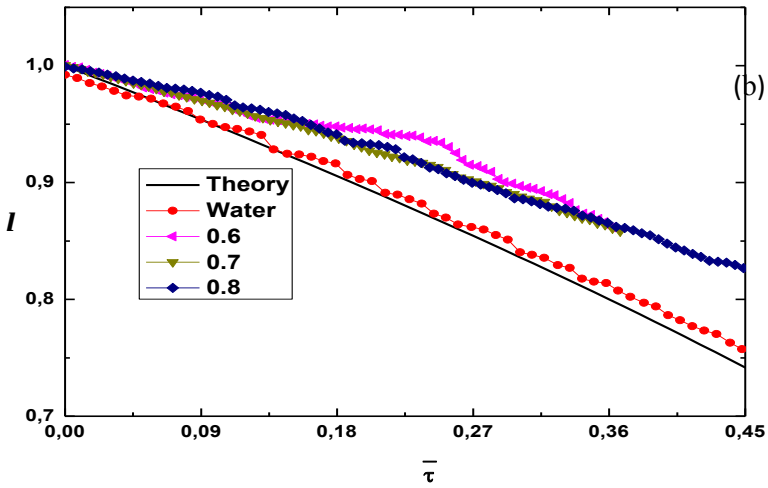
(b)
1,0
0,9
0,8
0,7
I
0,00
0,09
0,18
0,27
0,36
0,45
τ
Theory
Water
0.6
0.7
0.8

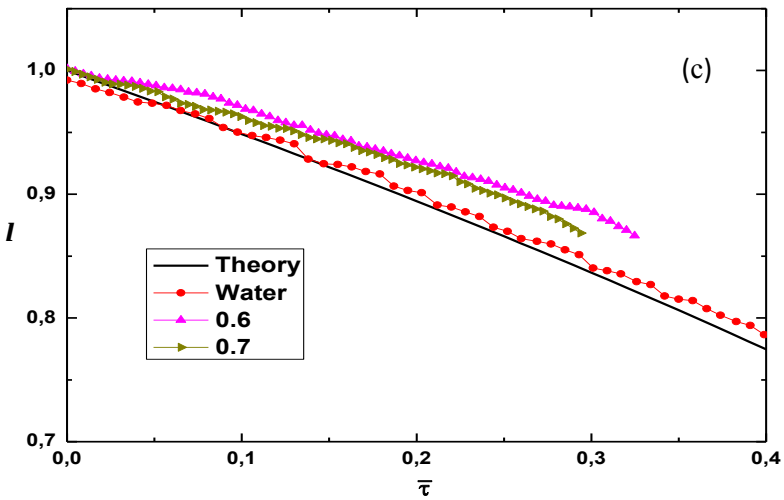
(c)
1,0
0,9
0,8
0,7
I
0,0
0,1
0,2
0,3
0,4
τ
Theory
Water
0.6
0.7

Figure 4.17: Second stage of evaporation for surfactant solutions below CAC; (a) 18ºC, 55% RH, (b) 30ºC, 90% RH, and (c) 18ºC, 90%.

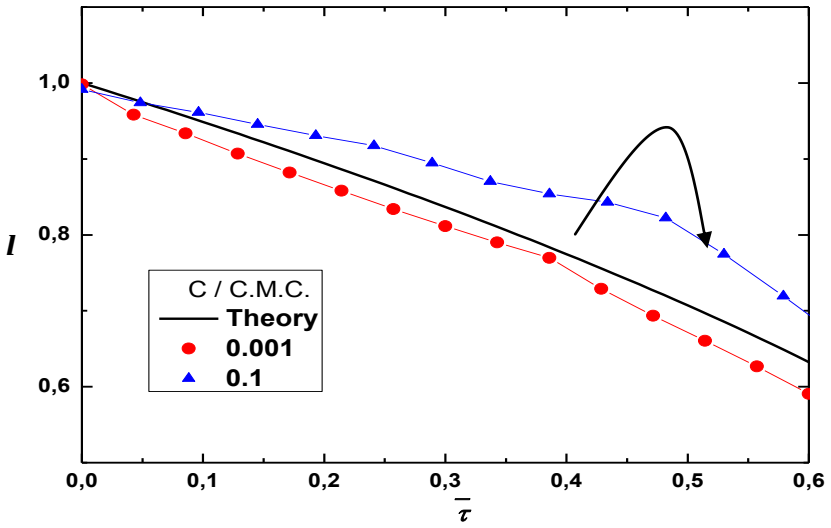

Figure 4.18: Second stage of evaporation for SDS solutions (below CMC), experimental data of Doganci et al. [129]

The results for concentrations above the CAC are shown in Figure 4.19, we observe a good agreement between the theoretical prediction and experimental data for Silwet L-77 solutions for the second stage of evaporation. This agreement observed between the theoretical prediction and experimental data can be explained thus: that for concentrations above the CAC in Silwet L-77, the liquid is already saturated with aggregates and any further increase in the surfactant concentration does not modify the adsorbed amount at neither the liquid-vapor nor the solid-liquid interfaces. Therefore neither the liquid-vapor nor the solid-liquid interfacial tensions are modified by the increase in concentration of surfactant in droplet as a result of evaporation, and according to Young´s law there is no effect on the contact angle. This postulation is consistent with the observation in this concentration range, where a constant contact angle (receding contact angle), θ_r, was observed during the second evaporation stage. In this sense we may conclude that the concentrated solutions behave as pure fluids, although θ depends on the concentration. Recall that Eq.4.28 predicts a universal behaviour irrespective of the nature of the fluid, in this case solutions of different concentrations could be regarded as fluids of different natutre for c >> CAC. In the case of dilute solutions where c < CAC, the modification of the of the solid-liquid and liquid-

vapor interfaces as evaporation progresses leads to an inconsistency with theoretical prediction.

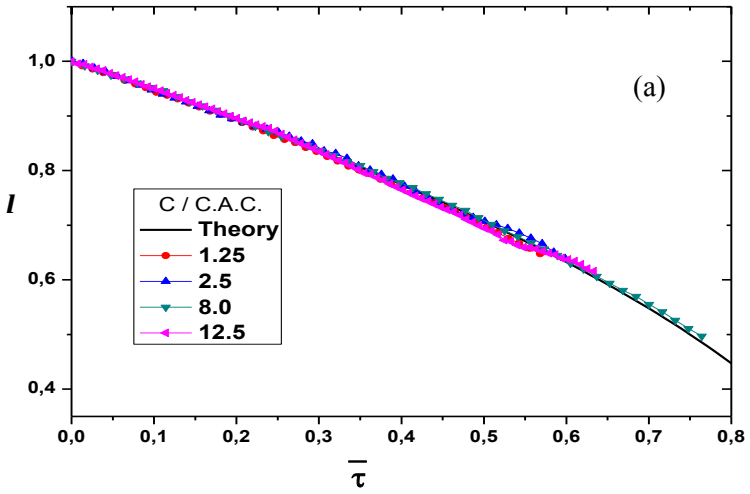

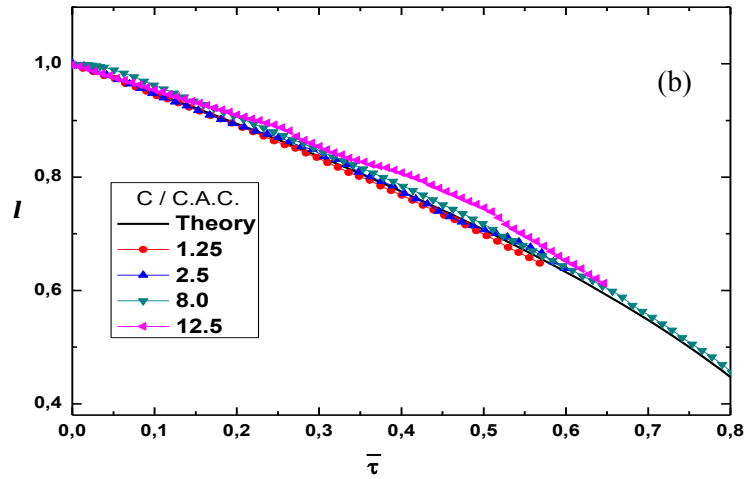

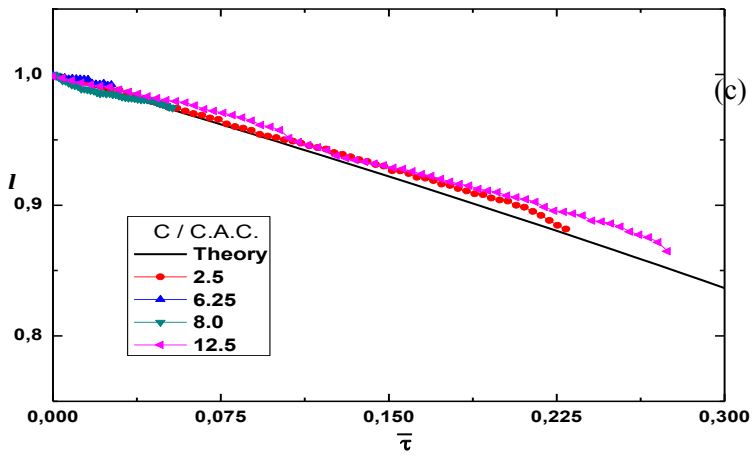

Figure 4.19: Second stage of evaporation for concentrations above the CAC threshold at constant temperature 24ºC and three relative humidities (a) 30%, (b) 55% and (c) 90%.

In Figure 4.20, we show the comparison of the theoretical prediction for the second evaporation stage and experiemental data for SDS solutions by Doganci et al. [129], for concentrations at the CMC and higher we can found a good agreement between the experimental data and theoretical prediction for the second stage of evaporation. It will be consistent to conclude that, the formation of micelles in the solution at higher concentrations does not change the interaction at solid-liquid interface, and the SDS solution may as well behave as a pure fluid.

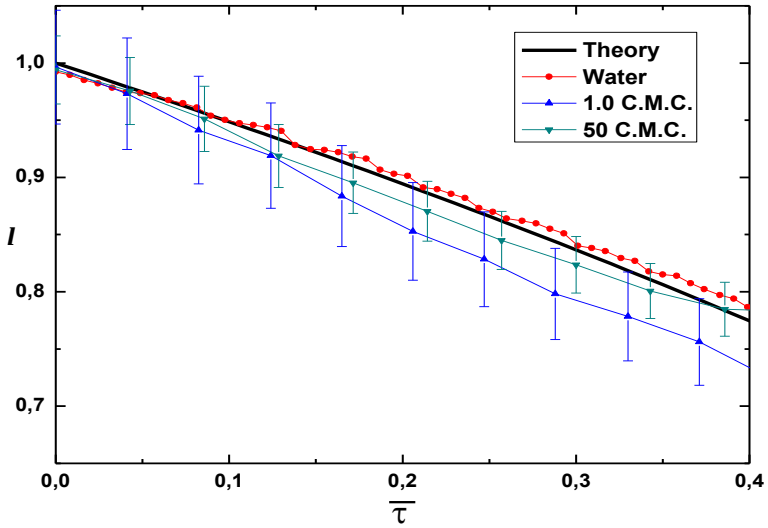

Figure 4.20.- Second stage of evaporation for SDS concentrations above the CMC threshold for SDS Solutions.

4.4 Theoretical Description of the Evaporation of Nanoparticle Dispersions.

4.4.1 First Stage of Evaporation

In Figure 4.21 we present the comparison of the experimental results obtained from the evaporation dynamics of nanoparticle suspensions of two different particle sizes 0.02µm and 1.0µm, at three different volume fractions of 0.001, 0.01, and 0.1, and for two different temperatures 22ºC, and 25ºC, and at constant relative humidity, 30%. As in the case of surfactant solutions, the agreement between the experimental results and the theoretical predictions is very good for the first stage of evaporation.

We find that there is no influence from neither the solid-liquid nor the liquid-vapor interfaces on the first evaporation stage. We can conclude that neither the particle size

nor the volume fraction of the suspensions has any influence on the first stage of evaporation, the temperature as well does not influence the dynamics of evaporation, the first stage of evaporation is a purely physical process, it does not require any driving force such as concentration for evaporation, relative humidity and temperature gradients a physical contributions to the evaporation process.

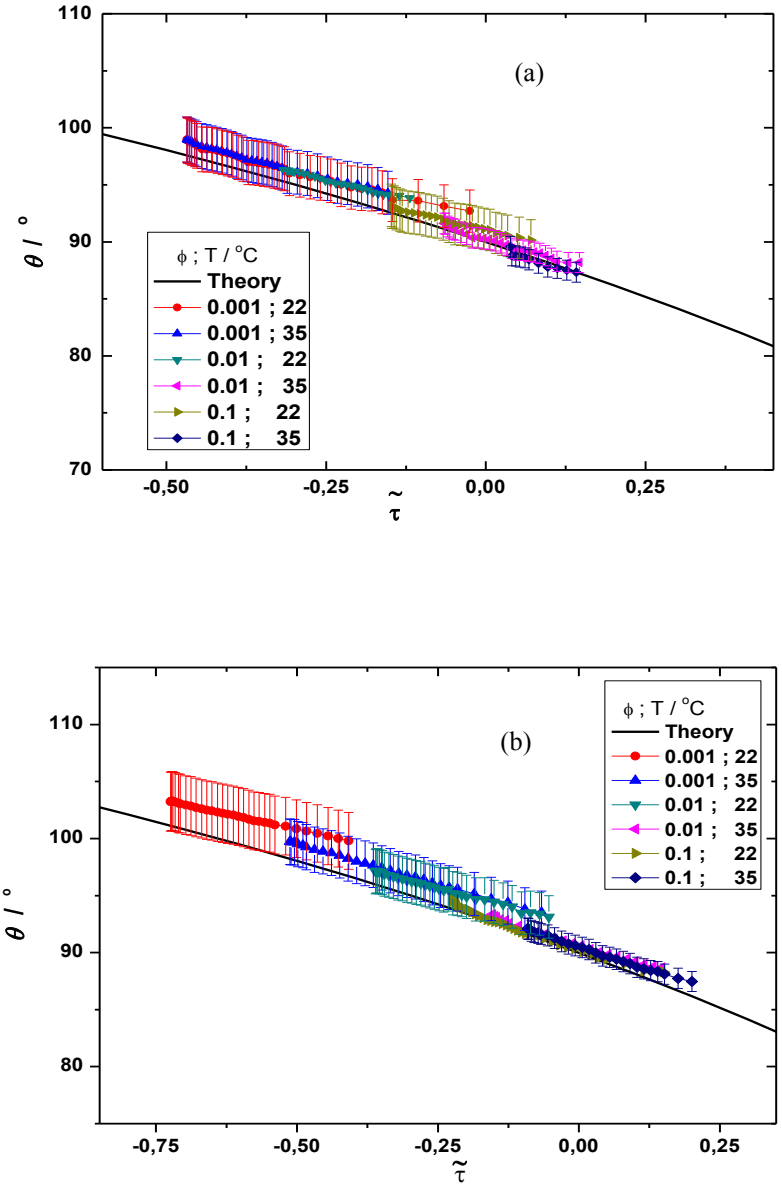

Figure 4.21: First stage of evaporation for nanoparticle dispersion for (a) 0.02µm, and (b) 1.0µm size particles for three different volume fractions 0.001, 0.01 and 0.1, two temperatures 22ºC and 25ºC, and 30% and relative humidity.The continous line is the theoretical prediction.

4.4.2 Second Stage of Evaporation

In Figure 4.22, we show the results for the comparison of the second evaporation stage of nanoparticle dispersions with the theoretical prediction. We can observe that the volume fraction and the particle size influences the dynamics of the second evaporation stage in a reverse behaviour compared to surfactant solutions. In the case of 0.02μm particle size, the deviation from the theoretical prediction increases as the volume fraction increases, see Figure 4.22.a, recall that the adsorption of nanoparticles decreased as the volume fraction increased, it is logical to infer that the increase in the volume fraction creates an interfacial tension at the solid-liquid and liquid-vapor interface irrespective of the temperature during the second stage of evaporation and thus a deviation from the theoretical prediction for the second stage of evaporation.

The influence of particle size on the dynamics of the second stage of evaporation for nanoparticle dispersion of 1.0μm particle size. It can be observed that the agreement with theoretical prediction improves as the volume fraction increases, see Figure 4.22.b, it should be recalled that these 1.0μm sized nanoparticles adsorbed less onto PTFE-AF/Au substrates as the volume fraction was increased, which is consistent with the behaviour in the second stage of evaporation when compared to theoretical prediction. We may conclude that for small sized particles, 0.02μm, the increase in the volume fraction leads to a disequilibrium of the adsorption at the solid-liquid and liquid-vapor interfaces, which leads to a deviation from the theoretical prediction as the volume fraction is increased, and for larger particle sizes, 1.0μm, a reverse behavior sees an agreement with the theoretical prediction as the volume fraction is increased. However these nanoparticle dispersions adsorbed minimally onto PTFE-AF/Au surfaces which makes this conclusion of the influence of the interaction at the solid-liquid interface in nanoparticles subjective, however within this framework the volume fraction and particle size influenced the dynamics of the second stage of evaporation, as described above.

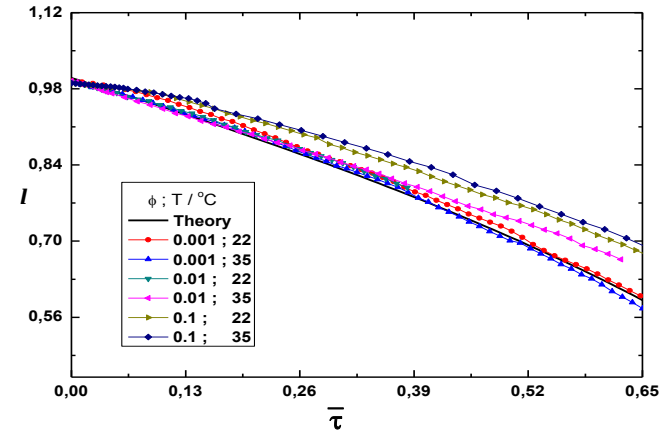

(a)

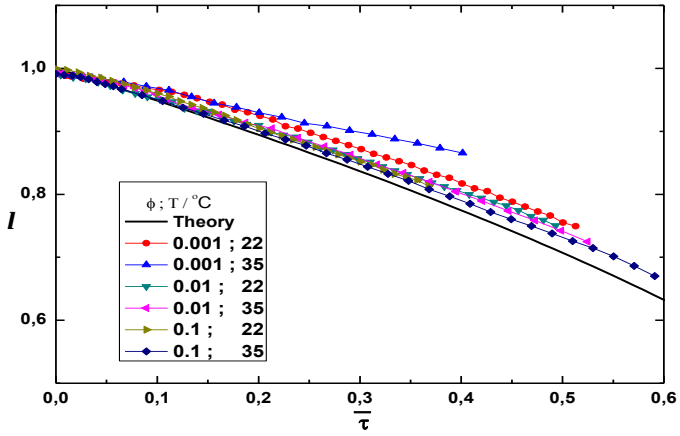

(b)

Figure 4.22: Second stage of evaporation for latex nanoparticle dispersions at constant relative humidity, 30% and two temperatures 22ºC and 35ºC, for three volume fractions, for particle size (a) 0.02µm, and (b) 1.0µm.

4.5 Influence of Adsorption on Evaporation of Surfactant Solutions

During the adsorption process we observed a fast adsorption step that is related to the transport of surfactant molecules through rapid mass deposition, the process is not diffusion controlled because mass deposited at the solid-liquid interface is not time dependent. The second slower process can be assumed to be as a result of the internal reorganization of the surtactant molecules at the solid-liquid interface.

We have proposed that the deviation from the theoretical prediction in the second stage of evaporation is influenced by the adsorption of surfactant molecules at the solid-liquid interface, the deviation was observed in surfactant solutions at concentrations below CAC for Silwet L-77, and CMC in SDS. The adsorption of surfactant molecules at the

solid-liquid interface has been measured for a range of Silwet L-77 surfactant solutions, see Figure 3.22, where it can be observed that the mass of surfactant adsorbed at the solid-liquid interface increased as the concentration of surfactant was increased. In what follows we will try to modify the theoretical prediction for the second stage of evaporation to account for the adsorption kinetics of surfactant solutions at the solid-liquid interface.

The first assumption that has been made without considering the adsorption kinetics during the evaporation surfactant solution is that;

$$\Gamma_{LV} = \Gamma_{SL} = \Gamma_{SV} \tag{4.29}$$

where Γ_{LG} is the adsorption at the liquid-gas interface, Γ_{SL} the adsorption at the solid-liquid interface, and Γ_{SG} is the adsorption at the solid-gas interface. For a droplet of an initial volume and concentration, the adsorption at the triple phase contact line is given by:

$$c_0 V = c_t V_t + \Gamma(c_t)(\gamma_{LV} + \gamma_{SL}) + \int_{t_r}^{t} \Gamma(c_t) d\gamma_{SV} \tag{4.30}$$

where c_0 is the initial concentration of surfactant in the droplet, V is the initial droplet volume, c_t and V_t are the concentration and volume at a given time, $\Gamma(c_t)$ is the mass of surfactant adsorbed at a given concentration, γ_{LV}, γ_{SL} and γ_{SV} are the surface tensions at the liquid-vapor, solid-liquid and solid-vapor interfaces respectively, and they can be described by the equations that follow;

$$\gamma_{LV} = 2\pi \frac{L^2}{\sin^2\theta}(1 - \cos\theta) \tag{4.31}$$

$$\gamma_{SL} = \pi L^2 \tag{4.32}$$

$$\gamma_{SV} = \pi L_r^2 - \pi L^2 \tag{4.33}$$

where L is the droplet contact radius, R is the radius of the droplet, h is the height of the droplet, L_r is the droplet contact radius corresponding to the receding contact angle, which is the beginning of the second stage of evaporation. Substituting Eq.4.31, Eq.4.32 and Eq. 4.33 into Eq. 4.30, we obtain the expression in Eq. 4.34

$$\bar{c_0}\bar{V} = c_t\bar{V} = +2\pi\left[\overline{\Gamma} l^2\left(\frac{1-\cos\theta}{\sin^2\theta} + \frac{1}{2}\right) - \int_{\tau_r}^{\tau} \overline{\Gamma}\, l dl\right] \tag{4.34}$$

where $\bar{c} = c/c_{CAC}$, $l = L/L_r$, $\bar{V} = V/L_r^3$, and $\overline{\Gamma} = \Gamma/c_{CAC}L_r$, thus Eq. 4.34 describes the amount surfactant adsorbed at the solid-liquid interface, or in other terms can be referred to as the rate of change of concentration at the solid-liquid interface as the droplet volume reduces due to evaporation.

The second assumption is based on the dependence of the adsorption of surfactant solution at the solid-liquid interface on the concentration of surfactant in the solution, which is;

$$\Gamma = \begin{cases} \Gamma_\infty \dfrac{c}{c_{CAC}} & c < c_{CAC} \\ \Gamma_\infty, & c \geq c_{CAC} \end{cases} \qquad 4.35$$

where Γ_∞ is the maximum surface adsorption.

Now Eqs. 4.34 and 4.35 have to be combined with the equations already discussed in Chapter 1 for the pure liquid theory. In summary, the imput data from the experiments are θ, V, h and L, which can be expressed as a function of the reduced time defined in the pure liquid theory, $\tau = t\dfrac{\beta}{L_r^2}$. The set of coupled equations to be solved now is

$$\begin{aligned} &\bar{V} = \ell^3 f(\theta) \\ &\bar{c}_0\bar{V}_0 = \bar{c}\bar{V} + 2\pi\left[\bar{\Gamma}\ell^2\left(\frac{1-\cos\theta}{\sin^2\theta}+\frac{1}{2}\right) - \int_{\tau_r}^{\tau}\bar{\Gamma}\ell\, d\ell\right] \qquad 4.36 \\ &\frac{d\bar{V}}{d\tau} = -\ell F(\theta) \end{aligned}$$

where f(θ) and F(θ) are the same functions used in the pure fluid theory. Notice that the only parameter that there is only one parameter to be fixed in the theory is Γ. Of course this is due to the assumption made in Eq. 4.29. The output of Eq. 4.36 are: $\bar{V}(\tau)$, $\ell(\tau)$ and c(τ), which after combination with θ(τ) allow one to calculate θ(c).

Figures 4.23 and 4.24 show that the agreement of the extended theory with the experimental data for the second stage is much better than the one obtained with the pure liquid theory. In effect, the tendency observed in the very low concentration regime is captured by the extended theory. In other words, the difference between both theories increases with c for very low c's, and then decreases again until coinciding near the C.A.C. (or the C.M.C. for SDS solutions). However, in order to obtain good quantitative agreement with the experiments, it has been necessary to use a value of Γ that is higher than the experimental values. For instance, for c = 0.9·C.A.C. a value

almost 40 times higher than the experimental Γ_{LV}, and more than twice the value of Γ_{SL} at the plateau have been used. Similar results were found for SDS.

The results are encouraging, and it can be expected that relaxing the strongly simplifying assumptions in Eq. 4.29, the theory will give reasonably good results using experimental adsorption data.

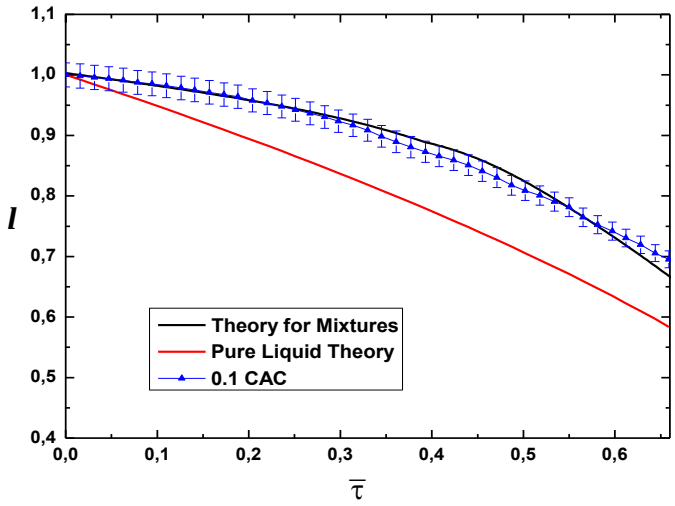

Figure 4.23.- Modified theory for the second stage evaporation for Silwet L-77 soultion at low concentrations, (0.1·CAC). 24ºC and 30% relative humidity.

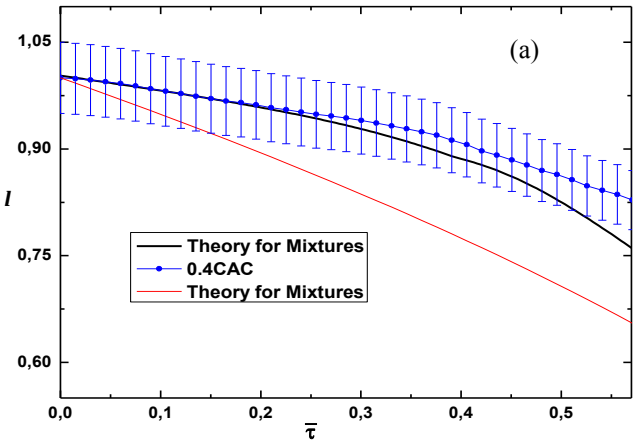

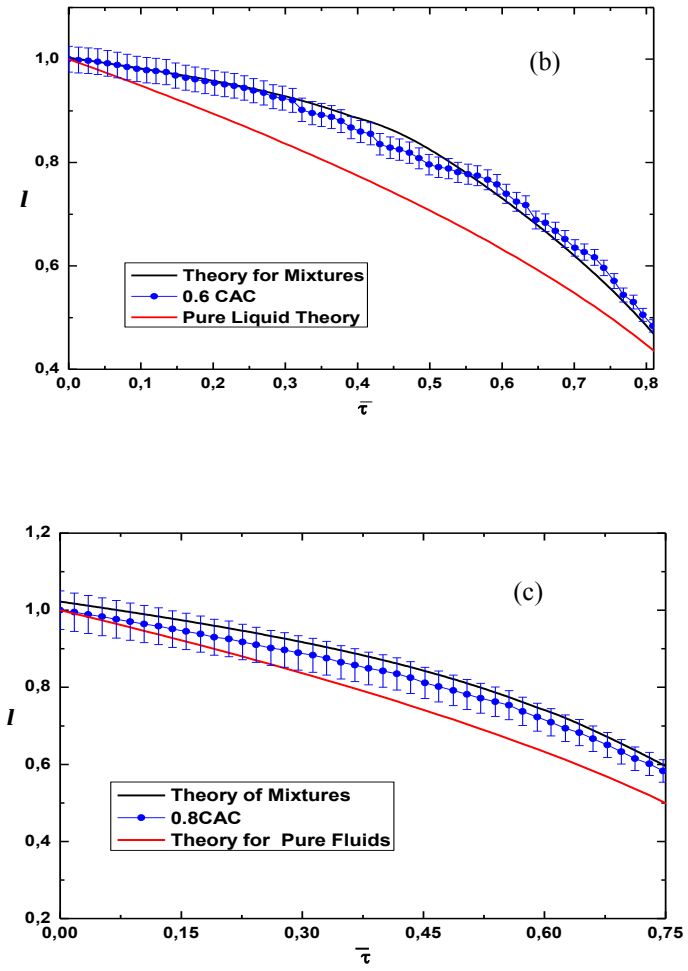

Figure 4.24.- Modified theory for the second stage evaporation for Silwet L-77 solution at (a) 0.4CAC, (b) 0.6CAC, and (c) 0.8CAC, at 24ºC and 30% relative humidity.

Chapter 5

5.1 Conclusions

We have carried an experimental and theoretical study of the spreading and evaporation process of droplets of aqueous surfactant solutions and nanosuspensions. The surfactant chosen has been a well known superspreader known as Silwet L77. Slightly hydrophobic charge estabilized latex nanoparticles of three different sizes have been used.

An experimental technique that includes two CCD cameras in a perpendicular configuration has been set up for measuring the contact angle, the drop volume, drop height and the radius of the drop base. The measuring cell operates under controlled temperature and relative humidity conditions.

In the spreading of surfactant solutions over hydrophobic substrate we have observed that the spreading proceeded in two regimes: a first fast stage and a second slower stage, the experimental setup described in this work has allowed us to monitor in detail only the second regime of spreading. Spreading of superspreaders is known to depend on surfactant concentration, and it is driven by the Marangoni stress between the apex of the droplet and the region close to the three phase contact line. The spreading ability of Silwet L-77, measured as the maximum value of the radius of the basis of the droplet, increases with the surfactant concentration over the whole concentration range studied. This trend was found for all the temperatures and the relative humidities measured. The spreading process was faster at high relative humidities, and slower at higher temperatures due to the high thermal conductivity of the substrate, the end of the spreading stage was the point where evaporation became more dominant. Nanoparticle dispersions did not spread on Teflon-AF substrates irrespective of the particle size and volume fraction for temperatures and relative humidities measured, the droplets remained pinned throughout and began to evaporate after deposition onto the substrate. It has been proposed that this is a result of the pinning of the three-phase line due to the deposition of particles on it. The spreading results have been analyzed using three different recent theories. It has been found that the theories proposed by Ivanova et al. accounts for the second slower spreading stage. On the other hand, the theory of Blake is able to explain reasonably well the experimental results, except those at very low

surfactant concentrations. Finally, the rate theory is not able to describe the qualitative behavior of the rate of increase of the radius of the contact line in terms of the time dependence of the contact angle.

It has been confirmed that the evaporation of surfactant solutions and nanosuspensions proceeds in three stages as in the case of pure liquids: a first stage in which the contact angle decreases at constant contact radius. During this stage the contact angle decreases from the advancing contact angle to the receding contact angle contact, while the contact radius remains constant at its maximum value after spreading. For pure liquids, the second stage of evaporation is characterized by a reduction in the droplet contact radius while the contact angle remains constant at the receding contact angle. In the third and final stage the contact angle and droplet contact radius decrease simultaneously until the droplet disappears. The evaporation dynamics we observed is driven by the diffusion of water molecules from the interface to the sorrounding vapor phase. This is confirmed because $V^{2/3}$ changes linearly with time. This is important because it is one of the assumptions made in the theory of evaporation of liquid droplets, to describe the flux of molecules from the droplet's surface to the vapor phase. This is the point through which the relative humidity effect enters in the theory.

The evaporation of dynamics of Silwet L-77 has been studied, experiments were carried out for a range of surfactant concentrations below and above the critical aggregation concentration, for three temperatures and three values of the relative humidity. The results obtained for the first evaporation stage are similar to those of a pure fluid: the contact angle decreases while the radius of the drop remains constant. qualitatively agree with the two stage evaporation kinetic model proposed for the evaporation of pure fluids. In surfactant solutions the first stage of evaporation is consistent with the theoretical model described for pure fluids, a result that is some what curious because it indicates that the presence of aggregates in the case of Silwet L-77 or micelles in SDS does not have any influence on the evaporation dynamics in this stage. Irrespective of the concentration of surfactant, temperature and, relative humidity the first evaporation stage is consistent with the theoretical description.

However it was found that during the second evaporation stage the contact angle does not always remains constant, specifically at concentrations below the CAC in the case of Silwet L-77, and below the CMC for SDS solutions. We have proposed that this is due to the increase of the surfactant concentration as evaporation increases, being accompanied by an increase of the surfactant concentration at both the solid/liquid and

liquid/air interfaces. The fact that this does not affect the first stage has been attributed to the different rates of the adsorption and evaporation processes. To test this effects the adsorption of Silwet L77 at the solid/liquid interface has been measured, while the adsorption at the liquid/air interface has been taken from previous results from the laboratory.

Similar behaviors were found for the nanosuspensions. The shapes of the deposits left after evaporation have been studied, and they have been found to be strongly dependent on the volume fraction of nanoparticles. Only for the lowest particle concentrations the deposits show the ring shape ("coffe ring effect"), whereas the deposits extend towards the center of the stain as concentration increases.

A theory to describe the first two evaporation dynamics for pure fluids has been proposed based on the assumption that the droplet remains spherical throughout the evaporation. Following previous computer simulations, the evaporation rate was assumed to be proportional to the droplet contact radius. To account for the cooling due to evaporation, an average surface temperature has been introduced for accounting for the differences in temperatures at the surface of the droplet and the substrate. The theory predicts a universal curve for the contact angle as a function of a reduced time during the first evaporation stage, and a second universal curve for a reduced radius of the droplet base as a function of a second reduced time. The theory has been found to describe quite well the evaporation of pure fluids on different hydrophobic substrates.

Even though the above theory also describes the first stage of evaporation of the surfactant solutions, the agreement with the experimental results is not satisfactory for the second stage for dilute solutions and nanosuspensions. The theory has been modified to take into account the effects of the increase of surfactant (or nanoparticle) concentration, as well as the adsorption at the interfaces as evaporation proceeds. The theory contains some strongly simplifying assumptions, thus too a large adsorption at the interfaces has to be used to reproduce quantitatively the experimental data in the low concentration region. However, the theory captures the qualitative different behavior of surfactant mixtures and nanosuspensions with respect to the one of pure liquids. It has to be remarked that in the case of nanosuspensions the adsorption at the solid/liquid interface is similar to that found for Silwet L77, whereas the adsorption at the liquid/air interface is much lower, so it seems that it is the first one that has a higher influence on the second stage, where the size of the droplet radius decreases.This clearly indicates

the directions in which the theory can be improved, using experimental adsorption data at the solid/liquid and liquid/vapor interfaces, and their corresponding kinetics.

5.2.- Perspectives

5.2.1.- Spreading

- To substitute the current CCD cameras by other with higher time resolution so that the first fast spreading stage can be studied. This has to be accompanied by a new design of the method for depositing the droplets on the substrates.
- To extend the spreading theory of Blake and the Rate Theory, that are the ones with a microscopic base, to establish a relationship between the structure of the surfactants and their spreading behavior.
- To extend the study performed to the spreading onto patterned surfaces and onto soft substrates (of interest in cosmetics).

5.2.2.- Evaporation

- To perform a systematic study of the relative importance of the adsorption at the solid/liquid and the liquid/air interface on the first and the second evaporation stages.
- To extend the theory presented for the evaporation of mixtures including the adsorption kinetics at the two interfaces.
- To study the evaporation of surfactant and polymer solutions, and of nanosuspensions on soft substrates.

References

1. R. Holdich, V.M. Starov, P. Prokopovich, D.O. Njobuenwua, R.G. Rubio S. Zhdanov, M.G.Velarde, Spreading of liquid drops from a source, Colloids Surf. A; Physiochemical Eng. Aspects, 2006, 282-283, 247-255

2. S. Rafai, D. Bonn, Spreading of Newtonian fluids and surfactant solutions on solid surfaces, Physica A, 2005, 358, 58-67.

3. S. Rafai, D. Bonn, E. Bertrand, J. Meunier, Long-range critical wetting: Observation of a critical end point, Phys. Rev. Lett., 2004, 92, 245701.

4. K.S. Lee, V.M. Starov, T.J.P. Muchatuta, S.I.R, Srikantha, Spreading of trisiloxanes over thin aqueous layers, Colloid J., 2009, 71, 365-369

5. M. J. de Ruijter, M. Charlot, M. Voue, J. De Coninck, Experimental evidence of several time scales in rop spreading, Langmuir 2000, 16, 2363-2368

6. N. Ivanova, V.M. Starov, R. Rubio, H. Ritacco, N. Hilal, D. Johnson, Critical wetting concentrations of trisiloxane surfactants, Colloids Surf. A: Physicochem. Eng. Aspects 2010, 354, 143–148

7. S. Sikalo, C. Tropea, E.N. Ganic, Dynamic wetting angle of a spreading droplet, Exp. Thermal Fluid Sci. 2005, 29, 795–802

8. M. Ghosh, K. J. Stebe, Spreading and retraction as a function of drop size, Adv. in Colloid Interf. Sci. 2010, 161, 61–76

9. K.Y. Chan, A. Borhan, Surfactant-assisted spreading of a liquid drop on a smooth solid surface, J. Colloid Interf. Sci. 2005, 287, 233–248

10. Y. Zhang, F. Han, The spreading behaviour and spreading mechanism of new glucosamide-based trisiloxane on polystyrene surfaces, J. Colloid Interf. Sci. 2009, 337, 211–217

11. J. Venzmer, S.P. Wilkowski, Trisiloxane surfactants-Mechanism of spreading and wetting, Amer. Soc. Testing and Mater., 1998, 18, 140-151

12. V. Slavchov, K.G. Sabbatovskiy, M. Stolz, K. Grundke, V.M. Rudoy, Unusual wetting dynamics of aqueous surfactant solutionson polymer surfaces, J. Colloid Interf. Sci. 2003, 267, 456–462

13. K. Sefiane, M. E.R. Shanahan, M. Antoni, Wetting and phase change: Opportunities and challenges, Cur. Opinion Colloid Interf. Sci. 2011, 16, 317–325

14. A. Changera, A. D. Nikolov, D.T. Wasan, Vertical spreading of aqueous trisiloxane solution driven by a spontaneously developing surface tension gradient, Ind. Eng. Chem. Res., 2008, 47, 3639-3644

15. S. David, K. Sefiane, L. Tadrist, Experimental investigation of the effect of thermal properties of the substrate in the wetting and evaporation of sessile drops, Colloids Surf. A: Physicochemical and Engineering Aspects 2007, 298, 108–114

16. M. Knoche, Organosilicone surfactant performance in agricultural spray applications: a review. Weed Research 1994, 34, 221–239

17. M. von Bahr, F. Tiberg, V. Yaminsky, Spreading dynamics of liquids and surfactant solutions onpartially wettable hydrophobic substrates, Colloids and SurfacesA: Physicochemical and Engineering Aspects 2001, 193, 85–96

18. M. Bienia, F. Mugele, C. Quilliet, P. Ballet, Droplets profiles and wetting transitions in electric fields, PhysicaA 2004, 339, 72 – 79

19. K.S. Lee , N. Ivanova, V.M. Starov, N. Hilal , V. Slavchov, Kinetics of wetting and spreading by aqueous surfactant solutions, Adv. Colloid Interf. Sci. 2008, 144, 54–65

20. E. Ruckenstein, G. O. Berim, Microscopic description of a drop on a solid surface, Adv. Colloid Interf. Sci. 2010, 157, 1–33

21. J. D. Halverson, Ch. Maldarelli, A. Couzisa, J. Koplik, Wetting of hydrophobic substrates by nano-droplets of aqueous trisiloxane and alkyl polyethoxylate surfactant solutions, Chem.Eng. Sci. 2009, 64, 4657-4667

22. M. Ferrari, F. Ravera, Surfactants and wetting at super-hydrophobic surfaces: Water solutions and non-aqueous liquids, Adv. Colloid Interf. Sci. 2010, 161, 22–28

23. K. Sefiane, L. Tadrist, Experimental investigation of the de-pinning phenomenon on roughsurfaces of volatile drops, Int. Commun. Heat Mass Transfer 2006, 33, 482–490

24. B. Evans, M. Chan, To wet or not to wet? Phys. World, 2006, 4, 48-52

25. B. M. Mognetti, H. Kusumaatmaja and J. M. Yeomans, Drop dynamics on hydrophobic and super-hydrophobic surfaces, Faraday Discus. 2010, 146, 195

26. R. S. Faibish, W. Yoshida, Y. Cohen, Contact angle atudy on polymer-grafted silicon wafers, J. Colloid Interf. Sci. 2002, 256**,** 341–350

27. K. Luuk, Wetting of solid surfaces: Fundamentals and charge effects, Adv. Colloid Interf. Sci. 2012, 179, 29-42

28. R. Andrade, O. Skurtys, F. Osorio, Experimental study of drop impacts and spreading on epicarps: Effect of fluid properties, J. Food Eng. 2012, 109, 430–437

29. M. Geoghegan, G. Krausch, Wetting at polymer surfaces and interfaces, Prog. Polymer. Sci. 2003, 28, 261–302

30. J. Radulovic, K. Sefiane, M. E.R. Shanahan, On the effect of pH on spreading of surfactant solutions on hydrophobic surfaces, J. Colloid Interf. Sci. 2009, 332, 497–504

31. S. David, An investigation of the wetting behaviour of evaporating drops, Ph.D. Thesis, The University of Edinburgh. August 2007

32. R. N. Wenzel, Resistance of Solid surface to wetting by water, Ind. Eng. Chem., 1936, 28, 988-994

33. G. Reiter and R. Khanna, Phys. Rev. Lett., 2000, 85, 2753

34. M. Sferrazza, L. Fraiture, W. Beziel, Department de Physique, Universite Libre de Bruxelle, Bruxelles, Belgium, submitted (2013)

35. P. G. de Gennes, Wetting: Statics and dynamics, Rev. Mod. Phys. 1985, 57, 827–863

36. V. C. Weiss, Theoretical description of the adsorption and wetting behaviour of alkanes on water, J.Chem. Phys., 2006, 125, 084718

37. C. Chong W. Ping, N. A. Ivanova, V. M. Starov, N. Hilal, and D. Johnson, Spreading behaviour of aqueous trisiloxanes solutions over hydrophobic polymer substrates, Colloid J. 2009, 71, 391–396

38. T. Svitova, R.M. Hill, C.J. Radke, Adsorption layer structures and spreading behavior of aqueous non-ionic surfactants on graphite, Colloids Surf. A: Physicochem. Eng. Aspects 2001, 183–185, 607–620

39. B.F. Macdonald, R.J. Cole, V. Koutsos, The formation of dewetting structures after evaporation of n-dodecane on graphite studied by atomic force microscopy, Surface Sci. 2004, 548, 41–50

40. D. Bonn, Wetting transitions, Cur. Opinion Colloid Interf. Sci. 2001, 6, 22-27

41. H. Matsubara, T. Shigeta, Y. Takata, N. Ikeda, H. Sakamoto, T. Takiue, M. Aratono, Effect of molecular structure of oil on wetting transition on surfactant solutions, Colloids Surf. A: Physicochem. Eng. Aspects 2007, 301, 141–146

42. A. Changera, A. D. Nikolov, D.T. Wasan, Surface tension gradient driven spreading of trisiloxane solution on hydrophobic solid, Colloid Surf. A: Physicochem. Eng. Aspects, 2002, 206, 31

43. T. Kajiya, A. Daerr, T. Narita, L. Royon, F. Lequeux, L. Limat, Advancing liquid contact line on visco-elastic gel substrates: stick-slip vs. continuous motions, DOI: 10.1039/c2sm26714d

44. S. Cioulachtjian, S. Launay, S. Boddaert, M. Lallemand, Experimental investigation of water drop evaporation under moist air or saturated vapour conditions, Int. J. Thermal Sci. 2010, 49, 859-866

45. H.Y. Erbil, A.L. Demiral, and Y. Avci, O. Mert, Transformation of a simple plastic into a super-hydrophobic surface. Science 2003, 299, 1377

46. Z. J. Cheng, L. Feng and L. Jiang, Tunable adhesive superhydrophobic surfaces for super paramagnetic microdroplets, Adv. Funct. Mater, 2008, 18, 3219–322

47. A. B. D. Cassie and Baxter, Wetttability of Porous Surfaces, Trans. Faraday Soc., 1944, 40, 546-55

48. T. Onda, S. Shibuichi, N. Satoh, and K. Tsujii, Super-water-repellent fractal surfaces, Langmuir, **1996**, *12*, 2125–2127

49. X. Tang, J. Dong, X. Li, A comparison of spreading behaviors of Silwet L-77 on dry and wet lotus leaves, J. Colloid Interf. Sci. 2008, 325, 223–227

50. L. Feng, S. H. Li, Y. S. Li, H. J. Li, L. J. Zhang, J. Zhai, Y. L. Song, B. Q. Liu, L. Jiang and D. B. Zhu, Super-hydrophobic surfaces: From natural to artificial, Adv. Mater. 2002, 14, 1857–1860

51. V. Starov, N. Ivanova, R.G. Rubio, Why do aqueous surfactant solutions spread over hydrophobic substrates?, Adv. Colloid Interf. Sci. 2010, 161, 153-162

52. S. Semenov, V.M. Starov, R.G. Rubio, M.G. Velarde, Instantaneous distribution of fluxes in the course of evaporation of sessile liquid droplets: Computer simulations, Colloids Surf. A: Physicochem. Eng. Aspects 2010, 372, 127–134

53. K.S. Lee, C.Y. Cheah, R.J. Copleston, V.M. Starov, K. Sefiane, Spreading and evaporation of sessile droplets: Universal behaviour in the case of complete wetting, Colloids Surf. A: Physicochem. Eng. Aspects 2008, 323, 63–72

54. G. Petrov, P. G. Petrov , Forced advancement and retraction of polar liquids on a low energy surface, Jordan, 1992, 64, 143–149

55. T. A. H. Nguyen, A.V. Nguyen, On the lifetime of sessile evaporating droplets, Langmuir 2012, 28, 1924-1930

56. L. Shi, P. Shen, D. Zhang, Q. Jiang, Pinning–depinning behavior in the wetting of (0001) α -Al2O3 single crystal by molten Mg , Appl. Surface Sci. 2011, 257, 10743–10747

57. H.A. Kramers, Physica 1940, 8, 284

58. T.D. Blake and J. De Coninck, Dynamics of wetting and Kramers' theory, Eur. Phys. J.. Special Topics, 2011, 197, 249-264

59. M. De Ruijter, J. De Coninck *and* G. Oshanin, Droplet spreading: partial wetting regime revisited, Langmuir *1999, 15*, *2209-2216*

60. D.R. Heine, G.S. Grest, E.B. Webb III, Spreading dynamics of polymer nano-droplets, Phys. Rev. E 2003, 68, 061603

61. N. Ivanova, V.M. Starov, D. Johnson, N. Hilal, R. Rubio, Spreading of aqueous solutions of trisiloxanes and conventional surfactants over PTFE AF coated silicone wafers, Langmuir 2009, 25, 3564-3570

62. R. Slavchov, V. Dutschk, G. Heinrich, B. Radoev, Justification of bi-exponential rate law of spreading over heterogeneous and rough surfaces, Colloids Surf. A: Physicochem. Eng. Aspects 2010, 354, 252–260

63. S. Semenov, V.M. Starov, R.G. Rubio, H. Agogo, M.G. Velarde, Evaporation of sessile water droplets: Universal behaviour in presence of contact angle hysteresis, Colloids and Surfaces A: Physicochem. Eng. Aspects 2011, 391, 135– 144

64. H. Lamb, Hydrodynamics, 6th ed., Cambridge, Cambridge University Press,1994

65. A. Robledo, C. Verea, J. O. Indeku, Wetting transition for the contact line and Antonov's rule for the tension, Phys. Rev. A, 1992, 45, 2423-2427

66. Handbook of Surface and Colloid Chemistry. Boca Raton, CRC Press, 1997. Rowan, S. M.; Newton, M. I.; McHale, G., Evaporation of micro-droplets and the wetting of solid surfaces J. Phys. Chem. 1995, 99, 13268

67. K.S. Birdi, D.T. Vu, , Wettability and the evaporation rates of fluids from solid surfaces, J. Adhesion Sci. and Tech., 1993, 7, 485-493

68. S. David, An investigation of the wetting behaviour of evaporating drops, Ph.D. Thesis, The University of Edinburgh, August, 2007

69. M.D. Doganci, B.U. Sesli, H.Y. Erbil, Diffusion-controlled evaporation of sodium dodecyl sulfate solution drops placed on a hydrophobic substrate, J. Colloid Interf. Sci. 2001, 362, 524-531

70. T. Svitova, R.M. Hill, C.J. Radke, Adsorption layer structures and spreading behavior of aqueous non-ionic surfactants on graphite, Colloids Surf. A: Physicochem. Eng. Aspects 2001, 183–185, 607–620

71. Y. Zhan, G. Zhang, F. Han, The spreading and superspreading behavior of new glucosamide-based trisiloxane surfactants on hydrophobic foliage. Colloids Surf A; Physchem. Eng. Aspects 2006, 276, 100–106

72. S. Rafaï, D. Sarker, V. Bergeron, J. Meunier, D. Bonn, Superspreading: aqueous surfactant drops spreading on hydrophobic surfaces, Langmuir 2002, 18, 10486–10488

73. N. Mourougou-Candoni, B. Prunet-Foch, F. Legay, M. Vignes-Adler,, and K. Wong, Influence of dynamic surface tension on the spreading of surfactant solution droplets impacting onto a low-surface-energy solid substrate, J. Colloid Interf. Sci. 1997, 192, 129–141

74. A.D. Nikolov, K. Koczo, G. Policello, T.D. Wasan, Mechanism for superspreading „role of surface tension gradient and surfactant adsorption, Proceedings: Adjuvant for Agro-chemicals, challenges and opportunities. Vol. II, Memphis, 1999, 125-130

75. N. Kumar, K. Varanasi, R.D. Tilton, S. Garoff, Surfactant self-assembly ahead of the contact line on a hydrophobic surface and its implications for wetting, *Langmuir*, 2003, 19, 5366–5373

76. K.P. Ananthapadmanabhan., E. D. Goddard, P. Chandar, Colloids Surf. A: Physicochem. Eng. Aspects, 1990, 44, 281

77. S. Zhu, W.G. Miller, L.E. Scriven, H.T. Davis, Superspreading of water-silicone surfactant on hydrophobic surfaces, Colloids and Sirfaces A; Physiochem. Eng. Aspects 1994, 90, 63-78

78. R. Hill, Superspreading, Cur. Opinion Colloid Interf. Sci. 1998, 3, 247-254

79. A.D. Nikolov, D. T. Wasan, A. Chengara, K. Koczo, G. A. Policello, I. Kolossvary, Superspreading driven by Marangoni flow, Adv. Colloid Interf. Sci., 2002, 96, 325-338

80. T. Stoebe, Z. Lin, R.M. Hill, M.D. Ward, H.T. Davis, Superspreading of aqueous films containing trisiloxane surfactant on mineral oil, Langmuir 1997, 13, 7282–7286

81. R. Wagner, Y. Wu, G. Czichocki, H.V. Berlepsch, F. Rexin, L. Perepelittchenkom, Silicon modified surfactants and wetting: II. Temperature-dependent spreading behaviourof oligoethylene glycol derivatives of heptamethyltrisiloxane. Appl. Organomet. Chem. 1999,13, 201–208

82. M.J. Rosen, Y. Wu, Superspreading of trisiloxane surfactant mixtures on hydrophobic surfaces. 1. Interfacial adsorption of aqueous trisiloxane surfactant-N-Alkyl pyrrolidinone mixtures on polyethylene. Langmuir 2001, 17, 7296–7305

83. V.M. Samsonov, On computer simulation of droplet spreading, Cur. Opinion Colloid Interf. Sci. 2011, 16, 303–309

84. V.M. Samsonov, A.S. Ratnikov, Comparative molecular dynamics study of simple and polymer nano-droplet spreading. Colloids Surf A: Physicochem. Eng. Aspects 2007, 298, 52–57

85. H. Alla, S. Freifer, T. Roques-Carmes, A computational fluid dynamics model using the volume of fluid method for describing the dynamics of spreading of Newtonian fluids, Colloids Surf. A: Physicochem. Eng. Aspects 2011, 386, 107– 115
86. Y. A. Shen, J. Koplik, Ch. Maldarelli, M.S. Tomassone, Molecular dynamics study of the influence of surfactant structure on surfactant-facilitated spreading of droplets on solid surfaces. Langmuir 2005, 21,12160–12170.
87. C. Wu, T. Qian, P. Sheng, Droplet spreading driven by van der Waals force: a molecular dynamics study. J Phys. Condens. Matter 2010, 22, 325101–325102
88. E. Ruckenstein, Effect of short-range interactions on spreading. J Colloid Interf Sci 1996, 179, 136–142
89. A. Kabalov, Monolayer frustration contributions to surface and interfacial tensions: explanation of surfactant superspreading. Langmuir 2000,16, 2595–2603
90. N.V. Churaev, N.E. Esipova, R.M. Hill, V.D Sobolev, V.M. Starov, Z.M. Zorin The superspreading effect of trisiloxane surfactant solutions. Langmuir 2001, 17, 1338–1348
91. D.R. Beacham, O.K. Matar, R.V. Craster, Surfactant-enhanced rapid spreading of drops on solid surfaces. Langmuir 2009, 25, 14174–14181
92. K. Sefiane, J. Skilling, J. Mac Gillivray, Contact line motion and dynamic wetting of nanofluid solutions, Adv. Colloid Interf. Sci. 2008, 138, 101–120
93. A. Chengera, A.D. Nikolov, A. Trokhymchuk., D. Henderson, Spreading of nano fluids driven by the structural disjoining pressure gradient, J. Colloid Interf. Sci. 2004, 280, 192-201
94. K. Kondiparty, A.D. Nikolov, W. Stanley, D.T. Wasan, The wetting and spreading of nanofluids on solid surfaces driven by structural disjoining pressure: statics analysis and experiments, *Langmuir*, 2011, 27, 3324–3335
95. O.K. Matar, R.V. Craster, K. Sefiane, Dynamic spreading of droplets containing nanoparticles, Phys. Rev E 2007, 76, 056315
96. P.A. Kralchevsky, K.D. Danov, V.L. Kolev, T.D. Gurkov, M.I. Temelska, G. Brenn, Detachment of oil drops from solid solid surfaces in the surfactant solution: molecular mechanisms at a moving contact line, Ind Eng. Chem. Res. 2005, 44, 1309-1321
97. D. T. Wasan, A.D. Nikolov, Spreading of nano fluids on solids, Nature 2003, 423, 156-159
98. H. Y. Erbil, Evaporation of pure liquid sessile and spherical suspended drops: A review, Adv. Colloid Interf. Sci. 2012, 170, 67–86

99. G. McHale, S. Aqil, N. J. Shirtcliffe, M. I. Newton and H. Y. Erbil, Analysis of droplet evaporation on a super-hydrophobic surface, Langmuir 2005, 21, 11053-11060. K. Sefiane, S. David and M. E. R. Shanahan, Wetting and evaporation of binary mixture drops, *J. Phys. Chem. B,* 2008, 112,11317–11323

100. H. Y. Erbil, Surface chemistry of solid and liquid interfaces, Blackwell Pub., Oxford, U.K., 2006

101. K. Sefiane, On the formation of regular patterns from drying droplets and their potential use for bio-medical applications, J. Bionic Eng. 2010, 7, S82–S93

102. G. Guéna, C. Poulard, M. Voué, J. De Coninck, A.M. Cazabat, Evaporation of sessile liquid droplets, Colloids Surf. A: Physicochem. Eng. Aspects 2006, 291, 191–196

103. F. Girard, M. Antoni, S. Faure, A. Steinchen, Evaporation and Marangoni driven convection in small heated water droplets, Langmuir 2006, 22, 11085-11091

104. R. D. Deegan, O. Bajakin, T. F. Dupont, G. Huber, S. R. Nagel, Th. A. Witten, Contact line deposits in an evaporating drop, Phys. Rev. E, 2000, 62, 756-765

105. C. Bourges-Monnier, M. E.R., Shanahan, Influence of evaporation on contact angle, Langmuir, 1995, 11, 2820

106. Ch. Liu, E. Bonaccurso, Micro-cantilever sensors for monitoring the evaporation of microdrops of pure liquids and mixtures, Rev. Sci. Instrum. 2010, **81**, 013702

107. G. Li, S. Moreno Flores, Ch. Vavilala, M. Schmittel, K. Graf, Evaporation dynamics of microdroplets on self assembled monolayers of dialkyl disulfides, Langmuir 2009, 25, 13438-13447

108. H.Y. Erbil, G. McHale and M.I. Newton, Drop evaporation on solid surface: Constant contact angle mode, Langmuir 2002, 18, 2636-2641. S.A. Kulinich , M. Farzaneh, Effect of contact angle hysteresis on water droplet evaporation from super-hydrophobic surfaces, Appl. Surface Sci. 2009, 255, 4056–4060

109. Y.-S. Yu, Z. Wang, Y.-P. Zhao, Experimental and theoretical investigations of evaporation of sessile water droplet on hydrophobic surfaces, J. Colloid Interf. Sci. 2012, 365, 254–259

110. Ch.-T. Chena, F.-G. Tseng, Ch.-Ch. Chieng, Evaporation evolution of volatile liquid droplets in nano-liter wells, Sensors & Actuators A 2006, 130–131, 12–19

111. H.K. Dhavaleswarapu,, Ch.P. Migliaccio, S.V. Garimella, J.Y. Murthy, Experimental investigation of evaporation from low-contact-angle sessile droplets, Langmuir 2010, 26, 880-888

112. Ch. Y. Lee, B. J. Zhang , J. Park, K. J. Kim, Water droplet evaporation on Cu-based hydrophobic surfaces with nano and micro-structures, Int. J. Heat Mass Trans. 2012, 55, 2151–2159
113. K. Sefiane, Effect of non-ionic surfactant on wetting behavior of an evaporating drop under a reduced pressure environment, J. Colloid Interf. Sci. 2004, 272, 411–419
114. N. Anantharaju, M. Panchagnula, S. Neti, Evaporating drops on patterned surfaces: Transition from pinned to moving triple line, J. Colloid Interf. Sci. 2009, 337, 176–182
115. R. Mollaret, K. Sefiane, J.R.E. Christy and D. Veyret, Experimental and numerical investigation of the evaporation a drop on a heated surface, Chem. Eng. Res. Des., 2004, 82, 471–480
116. J. H. Kim, S. I. Ahn, J. H. Kim, W.C. Zin, Evaporation of water droplets on polymer surfaces, Langmuir 2007, 23, 6163-6169
117. J. H. Kim, W.C. Zin, Polymer transport inside evaporating water droplets at various substrate temperatures, J. Phys. Chem. C, 2011, 115, 15375-15383
118. H. Hu, R.G. Larson , Evaporation of a sessile droplet on a substrate, J.Phys. Chem. B, 2002, 106, 1334-1344
119. Y. Moroi, M. Rusdi, I. Kubo, Difference in surface properties between insoluble monolayer and adsorbed film from kinetics of water evaporation and BAM images, J. Phys. Chem. B 2004, 108, 6351-6358
120. V. Starov, K. Sefiane, On evaporation rate and interfacial temperature of volatile sessile drops, Colloids Surf. A: Physicochem. Eng. Aspects 2009, 333, 170–174
121. F. Girard, M. Antoni, K. Sefiane, Infrared thermography investigation of an evaporating sessile water droplet on heated substrates, Langmuir 2010, 26, 4576–4580
122. G.J. Dunn, S. K. Wilson, B. R. Duffy, S. David, K. Sefiane, A mathematical model for the evaporation of a thin sessile liquid droplet: comparison between experiment and theory, Colloids Surf. A: Physicochem. Eng. Aspects 2008, 33, 503
123. G.J. Dunn, S.K. Wilson, B.R. Duffy, S. David, K. Sefiane, The strong influence of substrate conductivity on droplet evaporation, J. Fluid Mech. 2009, 623, 329
124. W.D. Ristenpart, P.G. Kim, C. Domingues, J. Wan, H.A. Stone, Influence of substrate conductivity on circulation reversal in evaporating drops, Phys. Rev. Lett. 2007, 99, 234502
125. R.V. Craster, O.K. Matar, and K. Sefiane, Pinning, retraction, and terracing of evaporating droplets containing nanoparticles, Langmuir 2009, 25, 3601

126. E. F. Crafton, W.Z. Black, Heat transfer and evaporation rates of small liquid droplets on heated horizontal surfaces, Int. J. Heat Mass Trans. 2004, 47, 1187
127. X. Xu, J. Luo, D. Guo, Criterion for reversal of thermal Marangoni flow in drying drops, Langmuir. 2010, 26, 1918-1922
128. S.M. Rowan, M.I. Newton, F.W. Dreiwer and G. McHale, Evaporation of micro-droplets of azeotropic liquids, J. Phys. Chem. B 2000, 104, 8217-8220
129. M.D. Doganci, B.U. Sesli, H. Y. Erbil, Diffusion-controlled evaporation of sodium dodecyl sulfate solution drops placed on a hydrophobic substrate, J. Colloid Interf. Sci. 2011, 362, 524–531
130. S. Chandra, M. di Marzo, Y. Liao and P. Tartarini, Effect of liquid-solid contact angle on droplet evaporation, Fire Safety Journal. 2005
131. M. Klassen, M. di Marzo, J. Sirkis, Infrared thermography of dropwise evaporative cooling, ASME HTD, 141
132. Rafailovich et al. private communication 2012
133. G.R. Duursma, K. Sefiane, S. David, Advancing and receding contact lines on patterned structured surfaces, Chem. Engn. Res. Design 2010, 88, 737-743
134. A. K .H. Cheng, D.M. Soolaman, and Yu, Evaporation or micro-droplets of water-ethanol mixtures on gold surfaces modified with self assembled monolayers, J. Phys. Chem. B, 2006, 11267–11271
135. K. Sefiane, L. Tadrist and M. Douglas Experimental study of evaporating water–ethanol mixture sessile drop: influence of concentration, Int. J. Heat Mass Trans. 2003, 46, 4527–4534
136. S. J. Gokhale, J. L. Plawsky, P. C. Wayner, Jr, Spreading, evaporation, and contact line dynamics of surfactant-laden microdrops, Langmuir 2005, 21, 8188-8197
137. Ch. Lui, E. Bonaccurso, H. J. Butt, Evaporation of sessile water-ethanol drops ina controlled environment, Phys. Chem. Chem. Phys., 2008, 10, 7150-7157
138. G. Guéna, C. Poulard, A.M. Cazabat, Evaporating drops of alkane mixtures, Colloids Surf. A: Physicochem. Eng. Aspects 2007,298, 2–11
139. H. Hu, R. G. Larson, Marangoni effect reverses coffee-ring depositions, J. Phys. Chem. B, 2006, 110, 7091
140. E. Adachi, A. S. Dimitrov, K. Nagayama, Stripe patterns formed on a glass surface during droplet evaporation, Langmuir 1995, 11**,** 1057-1060
141. A. Askounis, K. Sefiane, V. Koutsos, M. E.R. Shanahan, The effect of evaporation kinetics on nano-particle structuring within contact line deposits deposits volatile drops

Langmuir, in press. R.D. Deegan, Pattern formation in drying drops, Phys. Rev. E 2000, 1, 475

142. L. Shmuylovich, A. Q. Shen, H. A. Stone., Surface morphology of drying latex films: Multiple ring formation. Langmuir, 2002, 18, 3441–3445

143. R. Bhardwaj, X. H. Fang, D. Attinger, Pattern formation during the evaporation of a colloidal nanoliter drop: A numerical and experimental study. New J. Phys., 2009, 11, 075020

144. P. Brunet, Particle deposition after droplet evaporation on ultra-hydrophobic micro-textured surfaces, Soft Matter, 2012, 8, 11294

145. L. Frastia, A. J. Archer, U. Thiele, Modelling the formation of structured deposits at receding contact lines of evaporating solutions and suspensions, Soft Matter, 2012, 8, 11363

146. L. Chen, J.R.G. Evans, Drying of colloidal droplets on superhydrophobic surfaces, J. Colloid Interf. Sci. 2010, 351, 283–287

147. Y. Gan, L. Qiao, Evaporation characteristics of fuel droplets with the addition of nanoparticles under natural and forced convections, Int. J. Heat Mass Trans 2011, 54, 4913–4922

148. K. K. Nanda, F. E. Kruis, and H. Fissan, Evaporation of free PbS nanoparticles: Evidence of the Kelvin effect, Phys. Rev. Lett., 2002 89, 256103

149. T. Kajiya, D. Kaneko, M. Doi, Dynamical visualization of "Coffee Stain Phenomenon" in droplets of polymer solutions via fluorescent microscopy, *Langmuir*, 2008, 24, 12369–12374

150. F. E. M. O'Brien, The control of humidity by saturated salt solutions, British Electrical and Allied Industries Research Association, London

151. C. Lu, A.W. Czanderna Applications of piezoelectric quartz crystal microbalances. Amsterdam, Elsevier, 1984

152. D. Johannsmann, Studies of Viscoelasticity with the QCM, Springer Ser. Chem. Sens. Biosens 2007, 5, 49–109

153. D. A. Buttry , M. D. Ward, Measurement of interfacial processes at electrode surfaces with the electrochemical quartz crystal microbalance, *Chem. Rev.*, 1992, 92, 1355–1379

154. F. Höök, B. Kasemo, The QCM-D Technique for Probing Bio-macromolecular Recognition Reactions, Springer Ser. Chem. Sens. Biosens. 2007, 5, 425–447

155. V.M. Starov, S. R. Kosvintsev, M.G. Velarde, Spreading of Surfactant Solutions over Hydrophobic Substrates, J. Colloid Interf. Sci. 2000, 227**,** 185–190

156. H. A. Ritacco, F. Ortega, R.G. Rubio, N. Ivanova,V. Starov, Equilibrium and dynamic surface properties of trisiloxane aqueous solutions, Part 1: Experimental results, Colloids Surf. A. 2010, 365, 199-203

157. E. Guzman, V. San Miguel, C. Peinado, F. Ortega and R. G. Rubio, Polyelectrolyte multilayers containing triblock copolymers of different charge ratio, Langmuir, 2010, 26 (13), 11494-11502

158. M. Raposo, R. S. Pontes, L. H. C. Mattoso, and O. N. Oliveria, Kinetics of adsorption of poly(o-methoxyaniline) self-assembled films, Macromolecules, 1997, 30, 6095-6101

159. F. Girard, M. Antoni, S. Faure, A. Steinchen, Evaporation and Marangoni driven convection in small heated water droplets, Langmuir 2006, 22, 11085-11091

160. R. G. Picknett, R. Bexon, Evaporation of sessile or pendant drops in still air, J. Colloid Interf. Sci. 61, 1977, 336–*350*

Appendix I

Spreading and evaporation kinetics results for Silwet L77 solutions as a function of concentration, temperature and relative humidity.

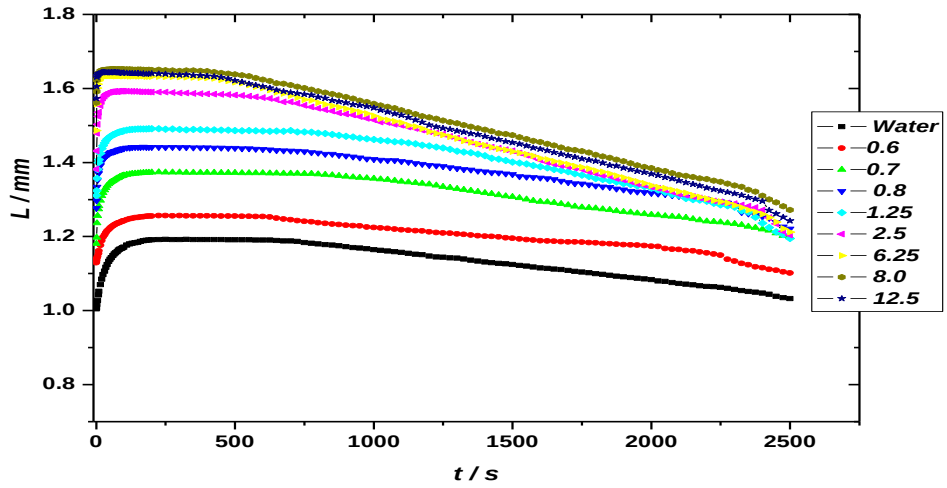

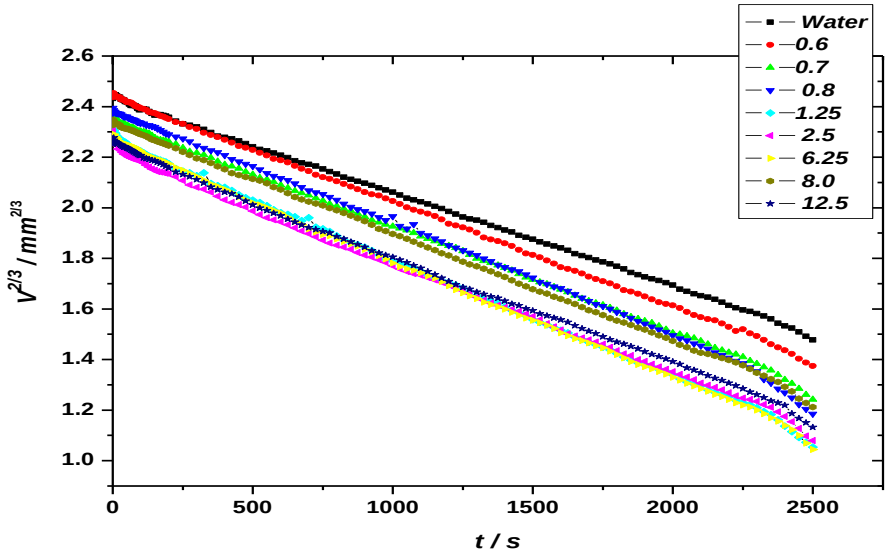

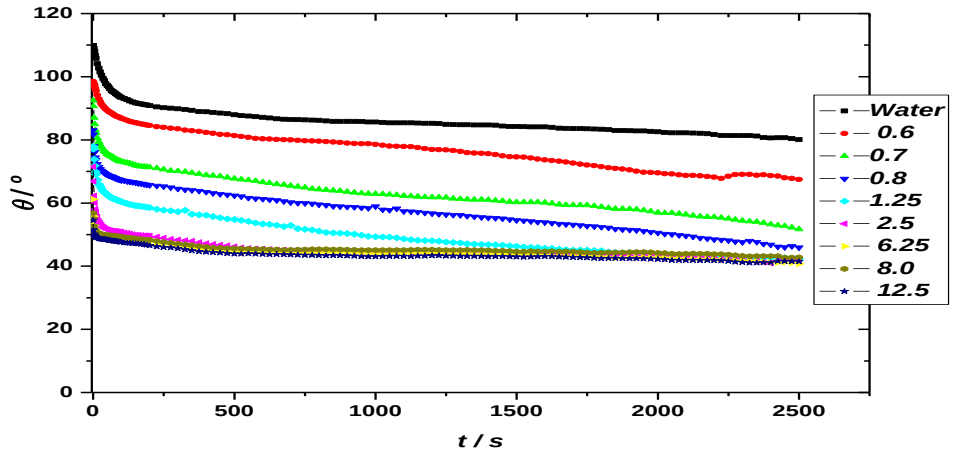

A.1: Measurements for (a) θ , (b) V and (c) L at 55% RH and 24ºC

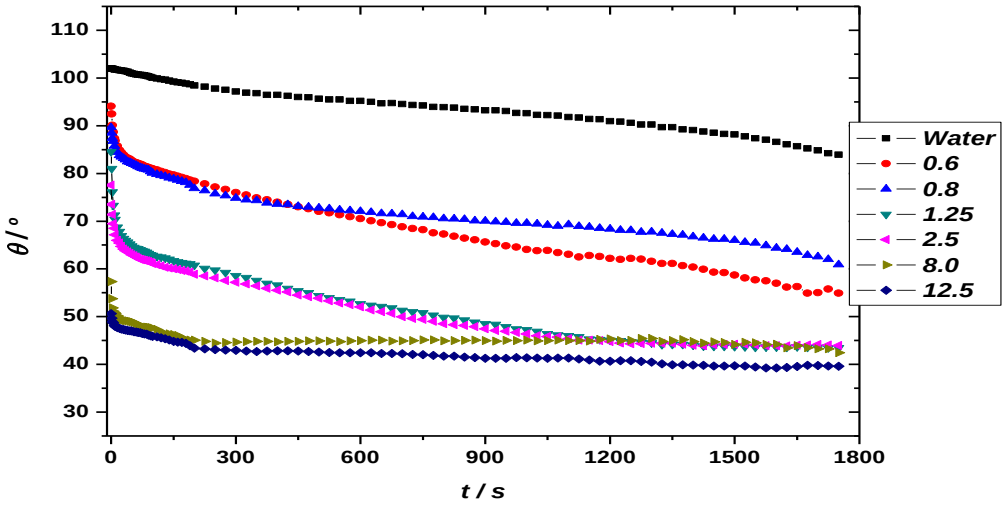

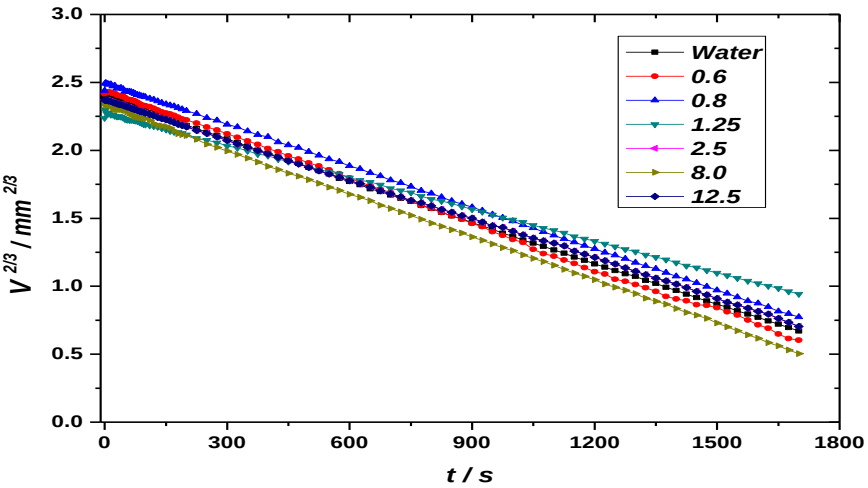

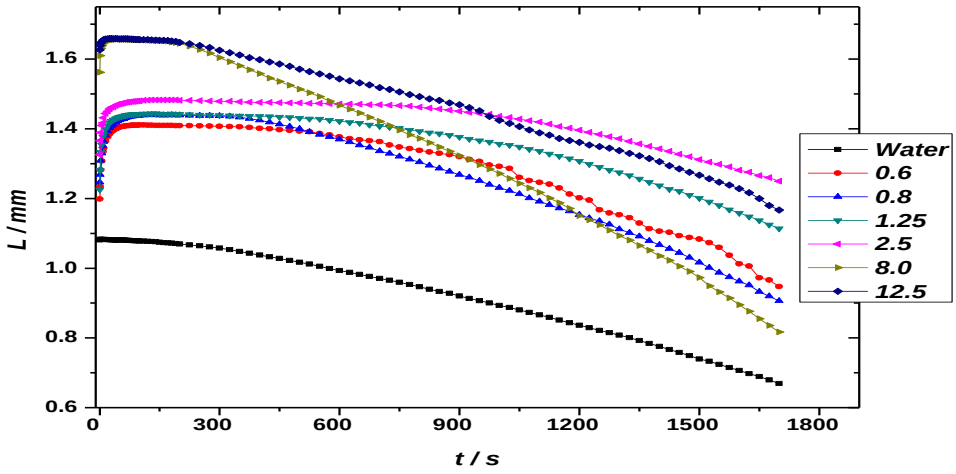

A.2: Measurements for (a) θ , (b) V and (c) L at 30% RH and 24ºC

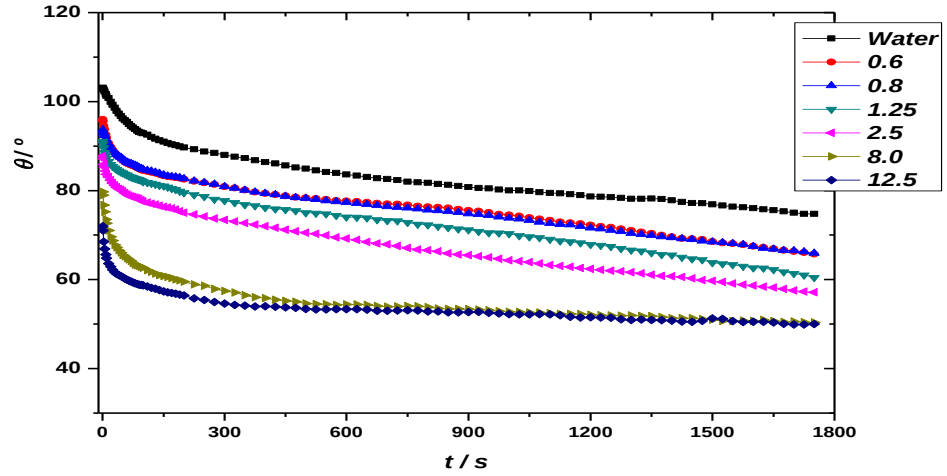

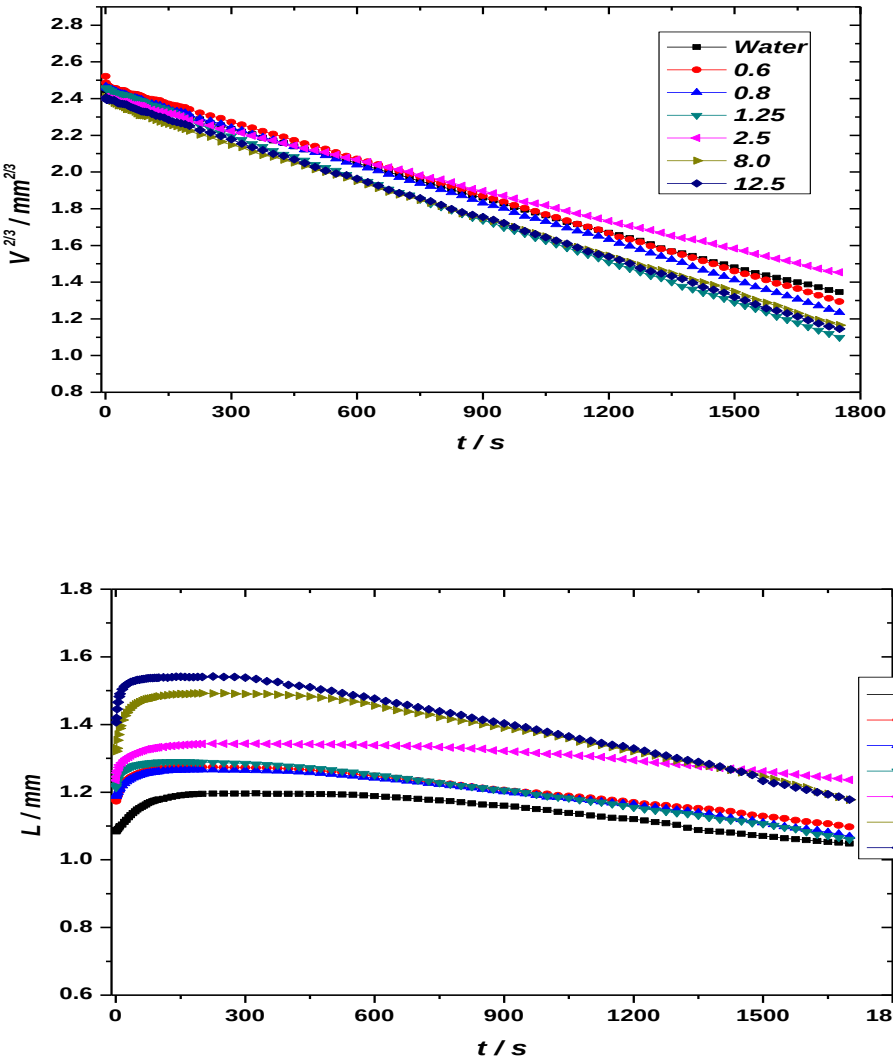

A.3: Measurements for (a) θ , (b) V and (c) L at 55% RH and 30ºC

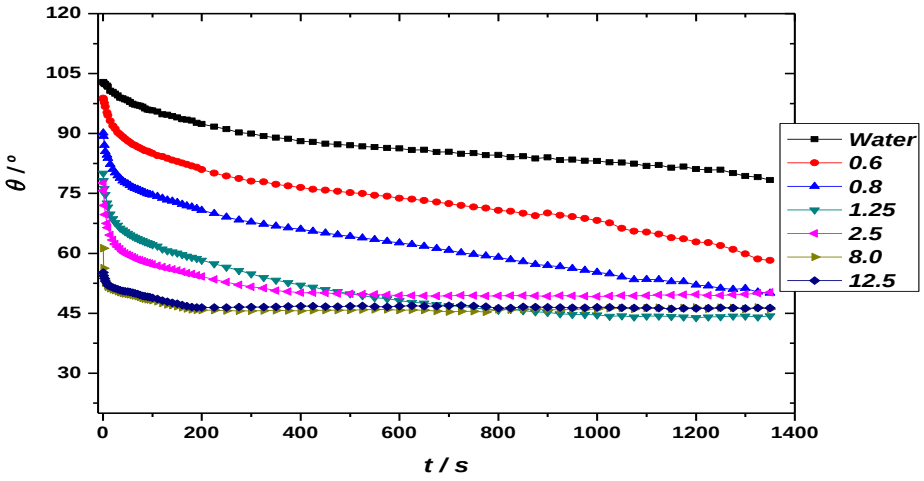
θ / °
t / s
Water
0.6
0.8
1.25
2.5
8.0
12.5

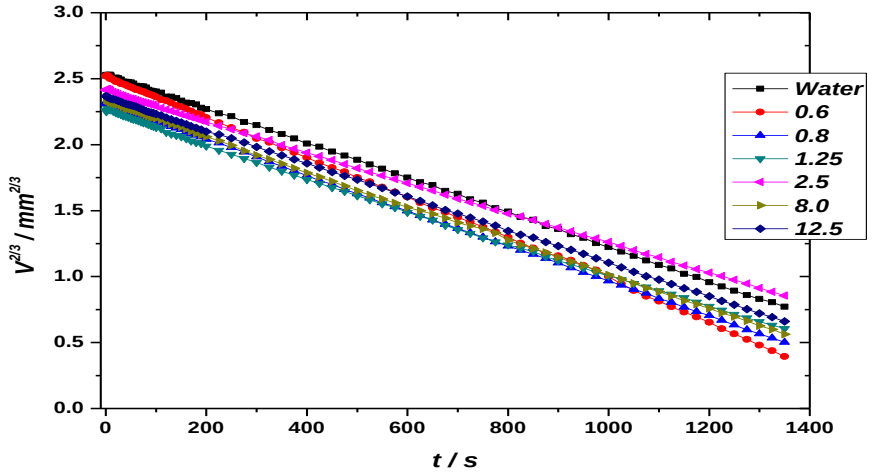
V^2/3 / mm^2/3
t / s
Water
0.6
0.8
1.25
2.5
8.0
12.5

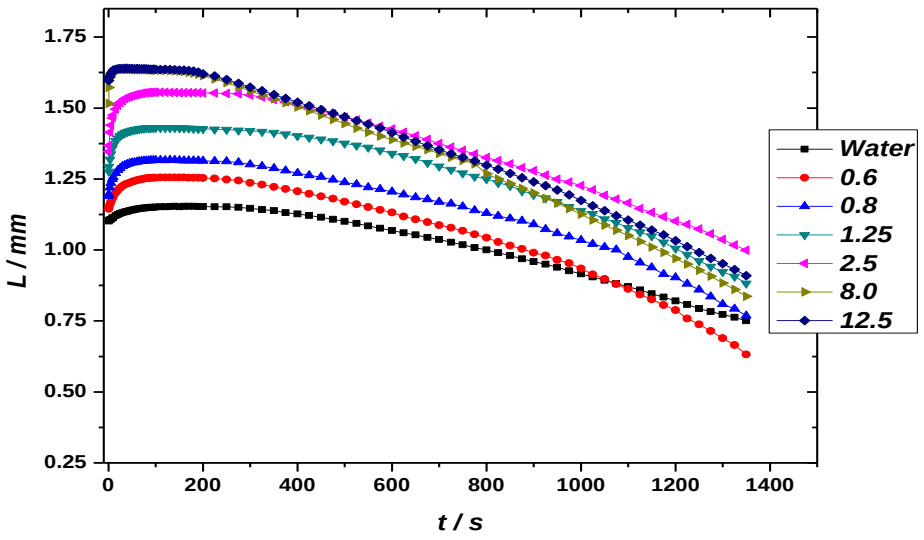
L / mm
t / s
Water
0.6
0.8
1.25
2.5
8.0
12.5

A.4: Measurements for (a) θ , (b) V and (c) L at 30% RH and 30ºC

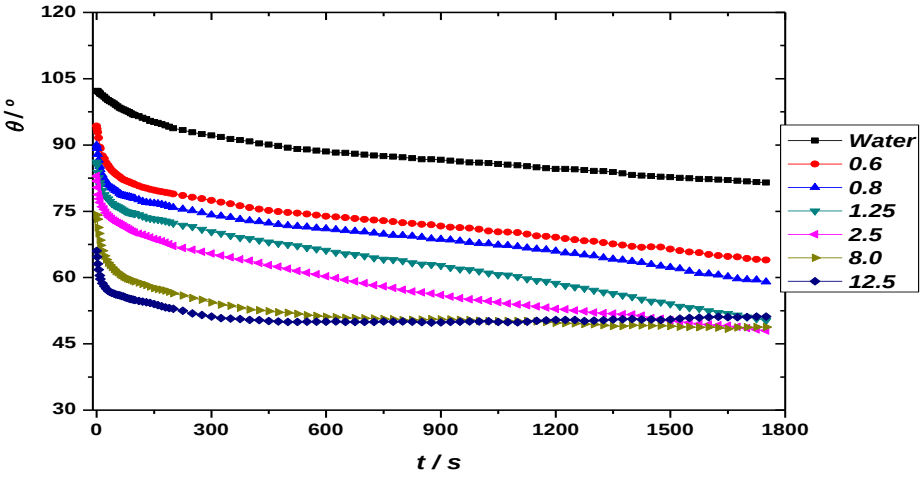

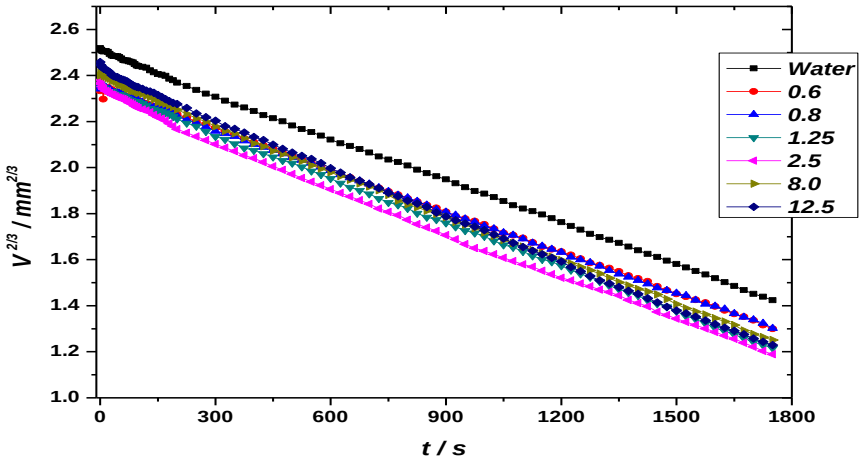

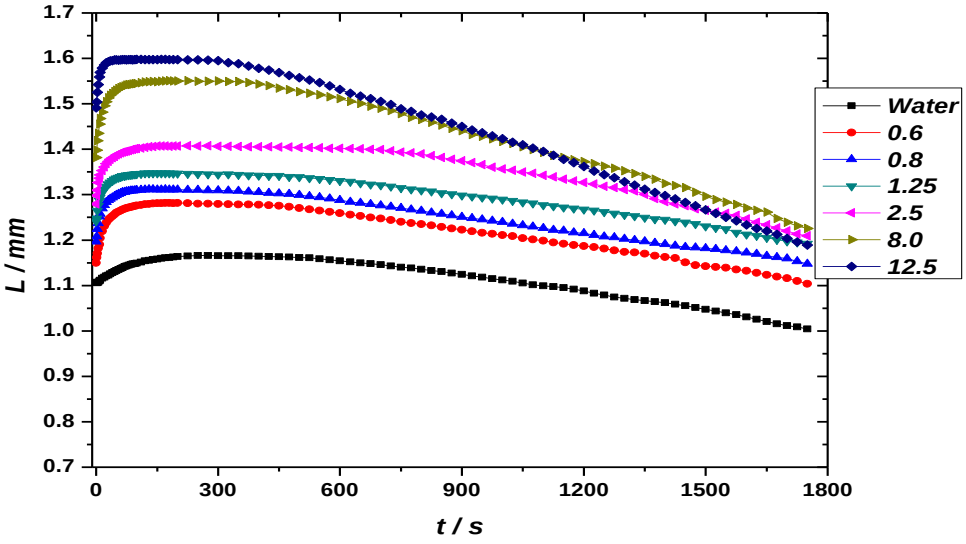

A.5: Measurements for (a) θ , (b) V and (c) L at 55% RH and 18ºC

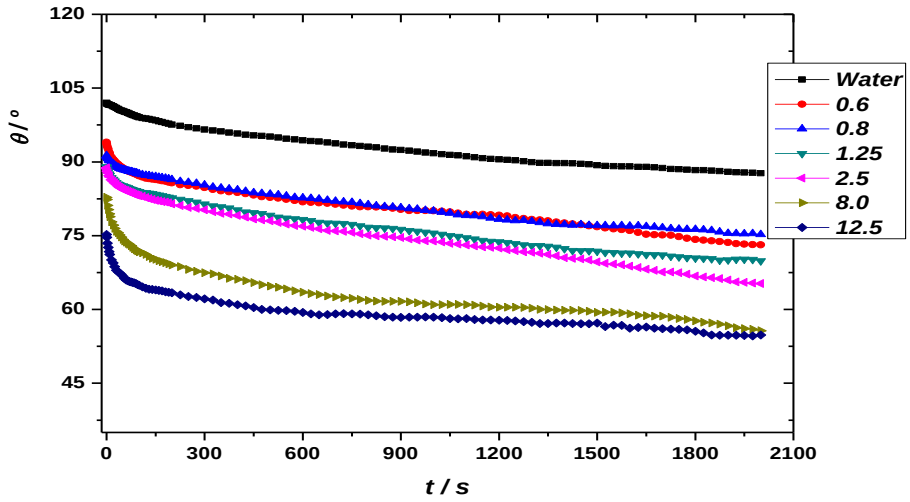

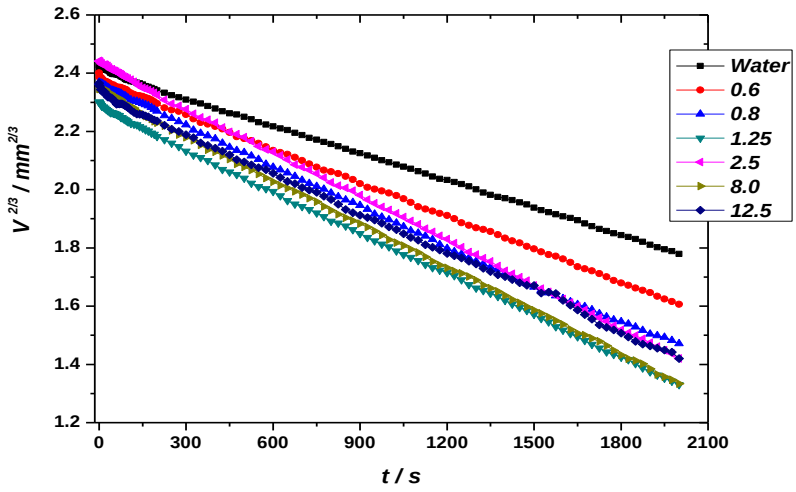

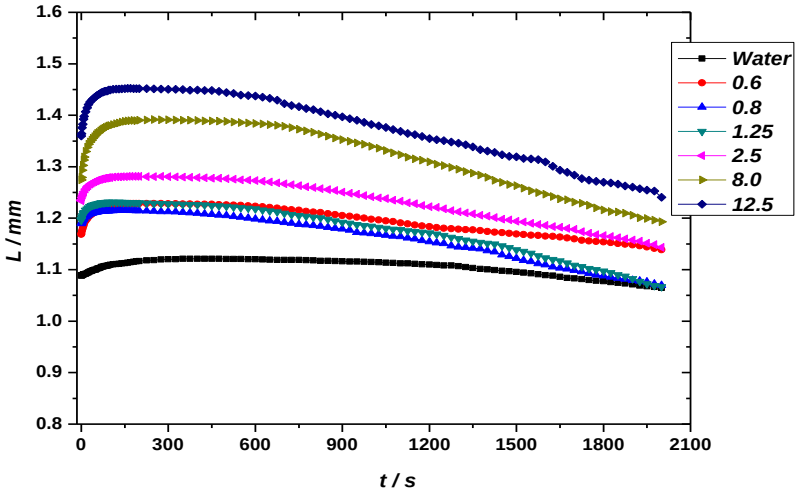

A.6: Measurements for (a) θ , (b) V and (c) L at 90% RH and 30ºC

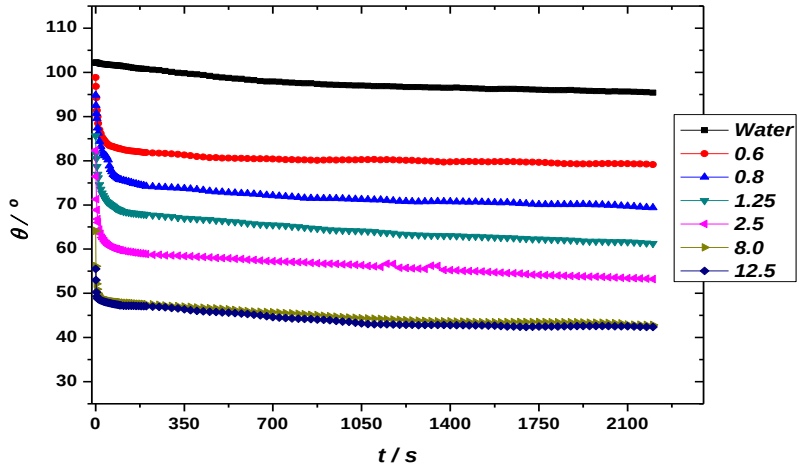
θ / °
t / s
Water
0.6
0.8
1.25
2.5
8.0
12.5

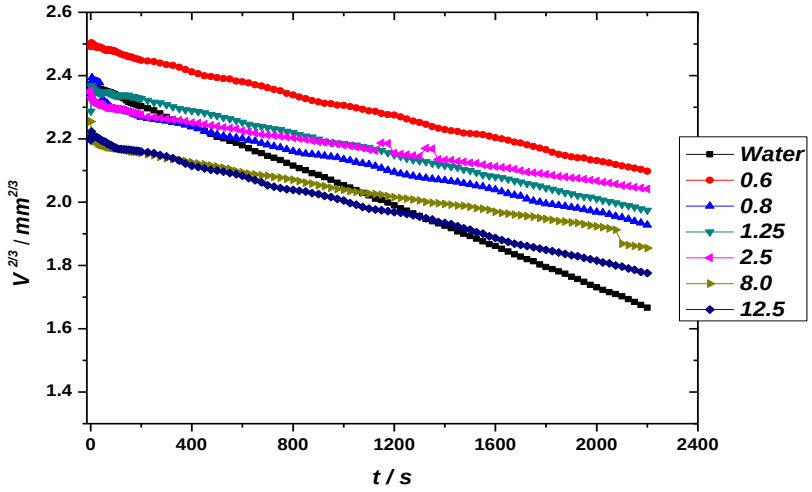
V^2/3 / mm^2/3
t / s
Water
0.6
0.8
1.25
2.5
8.0
12.5

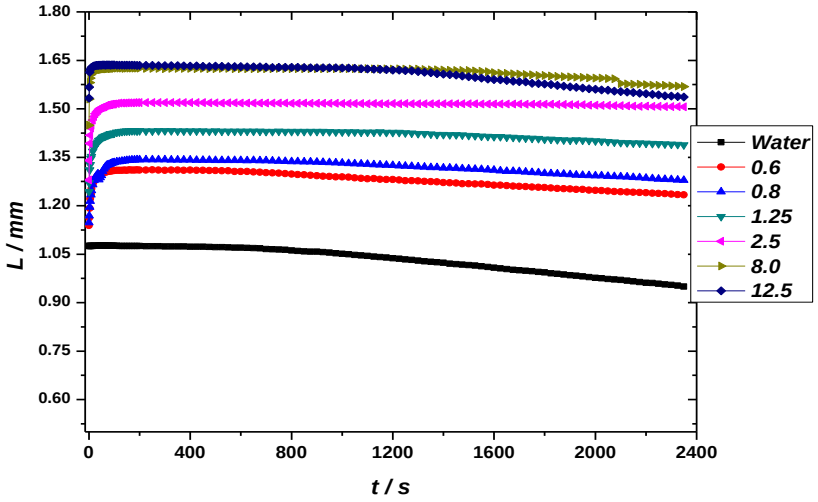
L / mm
t / s
Water
0.6
0.8
1.25
2.5
8.0
12.5

A.7: Measurements for (a) θ , (b) V and (c) L at 90% RH and 24ºC